GRAPHENE SYNTHESIS ON A SURFACE BY MOLECULAR BEAM EPITAXY USING A CARBON-SOLID SOURCE

Memoria presentada para optar por el grado de Doctor en Física por

Irene Hernández Rodríguez

Dirigida por el Dr. Javier L. Méndez Pérez-Camarero y el Dr. Jorge M. García Martínez

Madrid, Junio 2017

A mis padres y Guille

A Javier

Agradecimientos

Me gustaría agradecer a mucha gente, pues son muchos los que han contribuido a la realización de esta tesis. No solo desde el punto de vista científico, sino también haciendo que este proceso de varios años fuera más cómodo y agradable.

Primero de todo, debo de agradecer a Javi, por todo su apoyo, tanto en el plano científico como en el personal. No solo has sido mi director de tesis, sino también un amigo, una persona comprensiva que me ha ayudado y dado ánimos todas las veces que lo he necesitado.

También a Jorge, que te has mantenido a lo largo de estos años ayudándonos, dando nuevas ideas, e incluso añadiendo resultados tuyos para enriquecer esto. Además, al final, a pesar de estar en contra del tiempo, has aceptado la codirección, con todo lo que eso conlleva. Muchas gracias.

Agradezco a todos los que forman el grupo ESISNA, por acompañarme en todo este proceso, y por todos los momentos que hemos pasado (congresos, cenas, barbacoas, reuniones…y muchas horas de laboratorio).

En especial, a los grandes amigos que he hecho en el ICMM: a Rebeca, mi amiga inseparable que tanto extrañare vaya a donde vaya; a Leandro, nunca olvidaré lo inmensamente feliz que fui al verte en EEUU, tras un mes sola allí; a Jose, cuando llegué ya estabas, y durante todo este tiempo siempre me has acompañado, comprendido y apoyado; a Leo, me he reído tanto contigo…; a Enrique, haces que la vida de los demás sea más entretenida con tu peculiaridades; a Adri, estuviste poco tiempo, nos conquistaste…y te fuiste, así

que solo te agradezco a medias. También a Anna y Manu, que con Jose me acogieron al llegar y me hicieron el comienzo más agradable. Por supuesto, a Dulce y Leti, con las que pasé tan buenos momentos, dentro y fuera del instituto, y con las que espero seguirlos pasando, aunque sean distanciados en el tiempo; y a Norberto, que aunque no se de ti hace mucho, tampoco me olvido. También a las nuevas incorporaciones como Unai, Sandra, Rafa, Juan Jose…que aunque tampoco he coincidido mucho con ustedes, ayudan a renovarnos, que siempre es bueno.

Me gustaría agradecer a toda la gente del Instituto de Materiales que me han acompañado y me han hecho más cómodo todo este tiempo. Estar rodeada de gente tan agradable hace que el día a día sea mejor.

I would like to thank to Michael F. Crommie to give me the opportunity to be in your group for three months. It was a great experience for me and I felt like one more of your group; and thank you to all people of the Crommie's group who accompanied me during that time. Specially, I thank to Zahra Pedrahmrazi for all the time we were together, the plans we did and we could not do and the walk through SF; and Chen Chen, thank you very much for all, you are very nice and it was a pleasure work with you.

También agradecer a toda la gente con la que he coincidido de manera reincidente en los congresos, y con la que he pasado tan buenos momentos. En particular, gracias a Miguel Ugeda por toda la ayuda para que realizara la estancia y todos los consejos.

Muchas gracias a mi Yani. Lo nuestro fue un flechazo. Fuiste mi familia la primera vez que salía de Canarias, me convenciste para que buscara becas fuera de allí, y aquí estoy…

A Erney, Adan, Ailyn, Carlos, Amalia, Jorgito, Adi, Josue, Roger...que me acogieron desde que llegué como una más.

Gracias a Caty, por darme la oportunidad de entrar en su laboratorio al terminar la carrera; y a Jorge, Mariadel, Pau, Carla, Diego y Ander, por acompañarme durante ese año y medio, hacerme amar la cristalografía, ayudarme a darme cuenta que me gustaba estar en un laboratorio y que quería hacer el doctorado. Todo empezó ahí, gracias a ustedes.

A todos los buenos profesores que he tenido durante mi vida, y han sido muchos.

A mis padres y mi hermano, por su apoyo, su compañía a pesar de la lejanía. Por siempre estar ahí. Al principio, haberme venido a Madrid fue complicado, pero ahora, con nuestros cafés, a veces ni noto la distancia. Gracias por todo.

A Javier, gracias por estos más de cinco años. Por tu apoyo, toda la ayuda que me has dado en la tesis, tu compañía, tu temple. Gracias por esta vida a tu lado, que tanto me gusta.

Contents

Abstract

Until now, the direct growth of graphene on a material is limited to metal transition substrates. It is because the most frequently used methods need of the catalytic properties of these materials to favor the formation of graphene, such as CVD. Focusing on that idea, we decided to cross this barrier and establish as the aim of this work the synthesis of graphene on an insulator; and to do this, we have used a MBE solid carbon source.

We have developed and adapted the MBE method to work in our UHV chamber. The combination of a UHV environment and the use of a MBE method allow us a greater control of the growth conditions and it helps to elucidate the process of growth graphene on surfaces. Moreover, using this method we can synthetize graphene in large areas and we are not limited by the nature of the substrate so, we can growth directly on insulating or semiconductor materials.

We have done several steps before to grow graphene on a non-metallic substrate. In this work we present all this process: the assembly of the method to grow graphene, the synthetize of graphene (G) on a well-known surface as platinum (111), and on a less common substrate as gold (111); and finally, the growth of graphene on an insulator (diamond). Diamond is a material made of the same atoms of graphene. It has interesting properties as the highest hardness and thermal conductivity than any bulk material, so the graphene-diamond system can have high technological interest. Here, we have used two different surfaces (C (111) and C (100)) doped with boron or nitrogen so, the diamond has a semiconductor behavior. It is needed to use the scanning tunneling microscopy (STM) (the main technique used in this work).

For the characterization of the graphene layers we have used in situ surface science techniques, e.g. low energy electron diffraction (LEED), Auger electron spectroscopy (AES) and scanning tunneling microscopy (STM), quadrupole mass spectroscopy (QMS). Moreover, we have used, ex situ, Raman spectroscopy for the graphene-diamond characterization.

The results obtained from the different surface techniques prove the formation of graphene with different characteristics. For example, long-range ordering with moiré patterns that correspond to a monolayer of G/Pt (111), dendritic islands of graphene pinned to atomic step edges on Au (111), or nano-islands with different orientations on the diamond. Therefore, we have proved that the MBE growth method based on the direct sublimation of carbon atoms on a surface opens up new possibilities for the formation of graphene on very different substrates with potential technological applications.

Furthermore, at the end of the dissertation, we take the last chapter of results for a different issue. It is based in the direct sublimation of a huge molecule under UHV conditions; and the transformation of its structure due to the sublimation of water molecules.

In surface science, the use of UHV conditions is a good approach to control the functionality, size, and shape of the grown nanostructures by the sublimation of molecules. However, it is limited by the stability of the molecule because it can suffer structural damage during that process. For that reason, in most of the previous studies related to complex molecules on surfaces, the molecules were transferred from a solution or by a dry imprint technique to the substrate, as an attempt to preserve the weak core.

In the six chapter, we show the results about the manipulation of a transition metal complex with a robust structure $[Cu_4(m_3\text{-}Cl)_4(m\text{-}pym_2S_2)_4]$ (pym_2S_2= di-

pyrimidine disulfide) (named Cu_4Cl_4). We have been able to sublimate it keeping its molecular integrity and then, we have studied how these molecules self-assemble without being disrupted by the surface of Cu (110). Then, we have taken a further step observing in situ how the self-assembled structure transforms into other one in the presence of water. Thus, we have been able to analyze in detail the chemical and physical processes that involve the transformation and to determine the final structure obtained by the combination of surface techniques and DFT calculations. Our experimental results reveal that the substrate played an important role. The interactions of the Cu (110) surface with the water molecules and the atoms of the Cu_4Cl_4 cluster induce the transformation. Accordingly, we propose a model for the resultant assembled molecules after the reaction.

Resumen

Hasta ahora, el crecimiento directo de grafeno sobre un material ha estado limitado a los metales de transición. Esto es debido a que los métodos más usados, como el CVD, necesitan de las propiedades catalíticas de estos materiales para favorecer la formación de grafeno. Esta limitación nos ha conducido al objetivo de este trabajo: sintetizar grafeno sobre un aislante; y para hacerlo, hemos usado la técnica de crecimiento epitaxial de haces moleculares (MBE) con una fuente de carbono sólida.

Hemos desarrollado y adaptado este método (el MBE) a nuestra cámara UHV. La combinación de las condiciones de ultra alto vacio y el uso del MBE nos permite un gran control de las condiciones de crecimiento y ayuda a elucidar el proceso de crecimiento de grafeno en superficies. Además, usando esta técnica, podemos sintetizar grafeno en grandes áreas y no estamos limitados a la naturaleza del sustrato pues, podemos crecerlo directamente sobre materiales aislantes o semiconductores.

Antes de llegar a nuestro objetivo, tuvimos que realizar varios pasos previos. Todo este proceso es presentado en este trabajo, desde el ensamblaje del método para crecer grafeno, la síntesis de grafeno en una superficie conocida (platino (111)) y en otra menos habitual (oro(111)), hasta finalmente, el crecimiento de grafeno sobre un aislante (diamante). El diamante es un material hecho de los mismos atomos que el grafeno. Tiene interesantes propiedades como la dureza y la conductividad térmica más alta a la de cualquier otro material. Por tanto, el sistema grafeno-diamante puede tener un alto interés tecnológico. Aquí, hemos usados dos superficies diferentes (C(111) y C(100)) dopados con boro o nitrógeno, por lo que el diamante se comporta

como un semiconductor. Esto es necesario para poder usar el microscopio efecto túnel (STM), el cual es la principal técnica utilizada en este trabajo.

Para la caracterización de las capas de grafeno se han utilizado técnicas de física de superficies in situ como difracción de electrones a baja energía (LEED), espectroscopía de electrones Auger (AES), espectroscopía de masas (QMS) y microscopía túnel (STM). Además, hemos usado ex situ, espectroscopía Raman para la caracterización de grafeno-diamante.

Los resultados obtenidos de las diferentes técnicas de superficies demuestran la formación de grafeno con diferentes apariencias. Por ejemplo, grandes áreas ordenadas con patrones de moiré que corresponden a una monocapa de G / Pt (111), islas dendríticas de grafeno fijadas a aristas atómicas en Au (111) o nano-islas con diferentes orientaciones sobre diamante. De esta manera, nuestro método basado en la sublimación directa de átomos de carbono en una superficie abre nuevas posibilidades para la formación de grafeno en muchos sustratos diferentes con aplicaciones tecnológicas potenciales.

Por otra parte, al final de esta disertación, hemos dedicado el último capítulo de resultados para un tema diferente. Éste está basado en la sublimación directa de una molécula de gran tamaño bajo condiciones de ultra alto vacío, y la transfomación de su estructura debida a la sublimación de moléculas de agua.

En la ciencia de superficies, el uso de condiciones de UHV es un buen enfoque para el control de la funcionalidad, el tamaño y la forma de las nuevas nanoestructuras por la sublimación de moléculas. Sin embargo, la estabilidad de estas moléculas presenta una limitación que no permite la sublimación sin que haya daño estructural durante ese proceso. Por esta razón, en la mayoría de estudios previos, de moléculas complejas y grandes sobre superficies, las

moléculas fueron transferidas de una solución, o por una técnica de impresión en seco en el sustrato para preservar el núcleo frágil.

En el capítulo seis, mostramos los resultados de la manipulación de un compuesto de metal de transición con una estructura robusta [$Cu_4(m_3\text{-}Cl)_4(m\text{-}pym_2S_2)_4$] ($pym_2S_2$= di-pirimidina disulfuro) (llamado Cu_4Cl_4). Hemos sido capaces de sublimarlo manteniendo su integridad molecular y estudiamos cómo se autoensamblan moléculas sin que la superficie de Cu (110) las rompa. Luego, observamos in situ cómo la estructura autoensamblada se transforma en presencia de moléculas de agua. Así, analizamos en detalle los procesos químicos y físicos que implican la transformación y determinamos la estructura final obtenida con la combinación de técnicas de superficie y cálculos de DFT. Nuestros resultados experimentales revelan que el sustrato ha desempeñado un papel importante en esta transformación. Las interacciones de la superficie Cu (110) con las moléculas de agua y los átomos del grupo Cu_4Cl_4 inducen el cambio. En consecuencia, proponemos un modelo para las moléculas ensambladas resultantes después de la reacción.

1. Introduction

Nanotechnology refers to the sciences and techniques dedicated to the manipulation of matter on an atomic, molecular o supramolecular scale. The final purpose is to design and to build systems for the ultimate benefit of human kind, for example in industrial or medical applications. This concept is based on the idea to use atoms or molecules as the building blocks to make a final object. The first time this concept has been used was in the famous talk “There is plenty of room at the bottom” of Prof. Feynman in 1959[1]. There, he talked about the possibility to decrease the size of the circuit of a computer until the atomic limits, and he speculated about the multitude of applications once the methodologies to handle individual atoms could have been dominated. At present, Feynman’s request for the tools to handle atoms has been realized, although their full potential has not yet been achieved. In the last decades, new methods have been developed that allow the manipulation of the individual atoms, as is the case of scanning tunnel microscopy. One of the most famous cases was the manipulation of Xe atoms to write IBM in 1990 by Don Eigler and Erhard Schweizer[2]. This way, the invention of the STM[3] gave a great tool for atomic manipulation and visualization. The subsequent birth of AFM[4] further opened countless possibilities to handle biological systems as DNA.

Nanotechnology is also a multidisciplinary field that can contribute to face many challenges in medicine (e.g. the search for nanoparticles for the transportation of drugs into the human body), power storage (e.g. the design and the develop of materials to build cheap, ecologic and efficient solar cells), electronic devices (e.g. the develop of nano-circuits to build multimedia systems with much memory and processing that occupy less space), environment problems (e.g. the develop of biodegradable plastics or devices for purification of water), food or textile industry(e.g. improving the packacking and the food process or the develop of nano-fibers to regulate the temperature, the odors, modify the colors and to avoid immflamations), and even, in areas of the primary sector, such as agriculture and livestock (e.g. for the treatment of plant diseases or the control

of pests). In our case, we use the nanotechnology in the field of material sciences, and more specifically, surface science.

The possibility of separate single graphene flakes is an impressive case of scientific ingenuity using, what probably will be the simplest, most unexpected nanotechnology[5] tool: scotch tape. This work led to the experimental confirmation of the possibility of insolation of a single graphene flake and to the demonstration of its unique properties.

Graphene is a 2D carbon pure composite with a honeycomb structure (Fig 1.1). It has many interesting properties like a high electrical and thermal conductivity, and extremely high mechanical strength[6,7]. These characteristics have attracted the attention of the scientific community because the combination of these properties in one single material has boosted a plethora of promising practical applications such as nanocomposites, sensors, energy storage devices, and transparent conducting films.

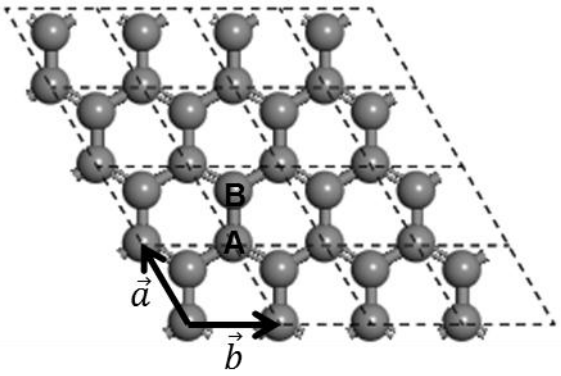

Fig 1.1: Representation of the graphene structure. It is a 2D carbon pure composite formed by a honeycomb lattice. The unit cell and lattice vectors are represented by dashed lines and the arrows $\vec{a}$ and $\vec{b}$ respectively. Each unit cell is defined by two carbon atoms with non-equivalent positions; the labels A and B indicate this.

These properties are the result of the particular electronic structure of graphene. In Fig 1.2 we show the energy band dispersion of graphene, as a function of the momentum k. It exhibits a muffin-tin shape with six Dirac points (the points where the conduction and valence bands touch); because graphene symmetry, the six Dirac points are paired too. Near these points the energy band adopts a cone-shape called Dirac's cone where the energy dispersion is linear. Linearity in these points implies that the effective mass of the electrons is zero, since it is related to the second derivative of the energy[6]. This way, electrons in that region have a behavior similar to the Dirac fermions[6]. This amazing electronic structure is characteristic of materials formed by a 2D honeycomb, and it is the reason why many scientists look for new, cheap and scalable methods to grow graphene or new alternative materials as TMDs (transition metal dichalcogenide)[8].

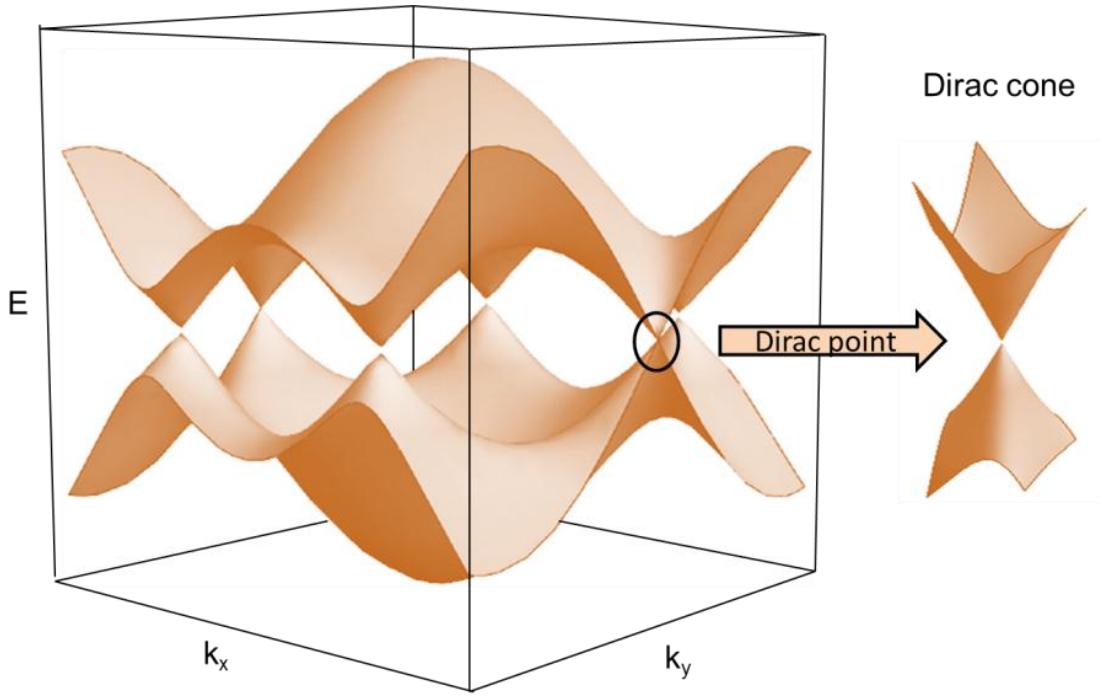

Fig 1.2: Energy band dispersion model for the graphene electronic structure with respect to the momentum (k). It looks like a muffin-tin. At the right side, a closer view of the energy band in the Dirac point exhibits the Dirac cone.

Preparation methods of graphene greatly vary. One part of this work, we focus on the growth of graphene using a solid carbon source. The growth of graphene based on the direct sublimation of carbon composites on a surface in a vacuum environment is usually known by the name of MBE and the efficiency of these type of methods have been previously demonstrated[9–11]. However, these methods depend on various parameters such as the substrate quality, the temperature of the substrate and the temperature of the source, the time of sublimation, etc. We remark that the flexibility that can be obtained with MBE can be difficult to obtain by other methods, but most importantly MBE is not limited to metallic substrates.

Furthermore, surface science techniques have allowed the characterization of many systems with high technological impact based on the organization of molecules on surfaces. This is because molecules or nanoparticles can modify the properties of the substrate[12] regarding electric or optical characteristics, changing the resistance or altering the response of the substrate to an external molecule forming sensors. Furthermore, the development of molecular electronics to replace the inorganic semiconducting technology has been a priority for surface science. Molecular electronics allow the building of electronic circuits more functional, cheaper, smaller, and open to more changes than the traditional technologies.

In this area, the choice of the molecule to be deposited plays a fundamental role. It is needed to find a molecule that is adequate to achieve our objectives. For example, molecules that are good electron acceptors or donors, or that can be covalently bonded to itself to form COFs (covalently organic frameworks) [13–15]. Until now, the main limit is, most of the times, the size of the molecule. Huge molecules tend to be more unstable, and the deposition on a surface without disrupting the molecule becomes a problem. In the second part of this thesis, we have successfully used a large molecule on a metallic surface; we hope this work could open the door to future studies in this field.

Another important issue is the choice of the substrate; the catalytic properties of the transition metals have been exploited. So, they are well-known to favor the connection of organic molecules or the induction of chemical reactions[14]. The electronic structure of this group on the periodic table promotes the catalytic activity, so the metallic substrate has a different activity for each reaction, and it depends on the electron occupancy of the last bands. In consequence, some authors have compared the catalyst effects of different substrates with a specific molecule[16,17]

Most surface science works are developed in vacuum environments, or in our case in Ultra High Vacuum (UHV). It is due to the need to approach an ideal system. The UHV allows using substrates atomically clean, and offers an excellent control of the system to be studied and the characterization techniques. This way, it makes the understanding easier of how the chemical and physical processes happen.

1.1 Outline of this thesis

This thesis is divided into seven chapters:

1. **Introduction and motivation.** This is an introductory chapter to explain the importance of the topics that will be approached in this work: Graphene growth by MBE and by using a metal-organic complex deposition (MOD) technique on a suitable surface.

2. **Methods.** Detailed description of the experimental and theoretical methods used throughout the thesis. Moreover, in this chapter, it will be shown the UHV system in which the MBE and the MOD techniques have been implemented in this thesis.

3. **Molecular Beam Epitaxy solid carbon source.** This chapter explains the design, development, and implementation of the carbon evaporator in the ultra-high vacuum chamber. It also described our characterization system in which graphene is grown onto various substrates.

4. **Graphene by MBE on metallic substrates.** Growth of graphene on Au (111) and Pt (111) single cristal substrates using a MBE solid carbon source. A detailed characterization of the graphene using STM, LEED and AES is showed in this part. Moreover, It will also be shown a theoretical description of the formation on graphene on these two substrates; from the deposition of one carbon atom until the formation of a graphene monolayer, and analysis about the moirés observed in the experimental results.

5. **Graphene by MBE on insolation substrates: diamond C (111) and C (100).** In this chapter, we demonstrate the growth of graphene on two different faces of diamond. The characterization is carried on with the surface techniques of the UHV chamber and Raman spectroscopy. The theoretical part supports the existence of graphene on the surfaces.

6. **Metal-organic complex deposition.** This part is about a different issue than the growth of graphene. Here, we show the study of self-assembling processes of a huge metal-organic complex to form graphene and its reaction induced by water molecules.

7. **Conclusions**. This chapter summarizes the main results obtained in this work.

2. Methods

Experiments have been performed in Ciclope chamber (Fig 2.1) at the ESISNA laboratories (ICMM-CSIC). It consists of an ultra-high vacuum (UHV) chamber equipped with a Variable Temperature Scanning Tunneling Microscopy (STM-VT, Omicron), Low-Energy Electron Diffraction (LEED), Auger Electron Spectroscopy (AES), and Quadrupole Mass Spectrometer (QMS). Taking advantage of the LEED and Auger apparatuses, we have carried out Electron Energy Loss Spectroscopy (EELS).

We have implemented an in-house evaporator of metal-organic complex molecules and a home-made Molecular Beam Epitaxy solid carbon source. This evaporator uses a piece of pure glassy carbon, Sigadur ® G-type from HTW Hochtemperatur-Werkstoffe GmbH[18] which is resistively heated.

Furthermore, the chamber includes some other facilities, namely: (1) A sputtering ion gun to facilitate the cleaning of surfaces. (2) A manipulator with two sample stages where the sample can be cooled down or heated it up (until 1473 K). (3) A home-made tip manipulator to prepare STM tips either by heating or by field emission. (4) Two Bayard-Alpert type ionization gauge to measure the pressure in the chamber. (5) Valves to keep isolate the preparation chamber from the STM chamber. For example, it is possible to vent the fast-load-lock while the rest is kept in UHV conditions

The STM measurements have been taken using Dulcinea's and the WSxM software[19] electronic from Nanotec. Both, tungsten tips or Kolibri sensors adapted for our STM have been utilized in the experiments.

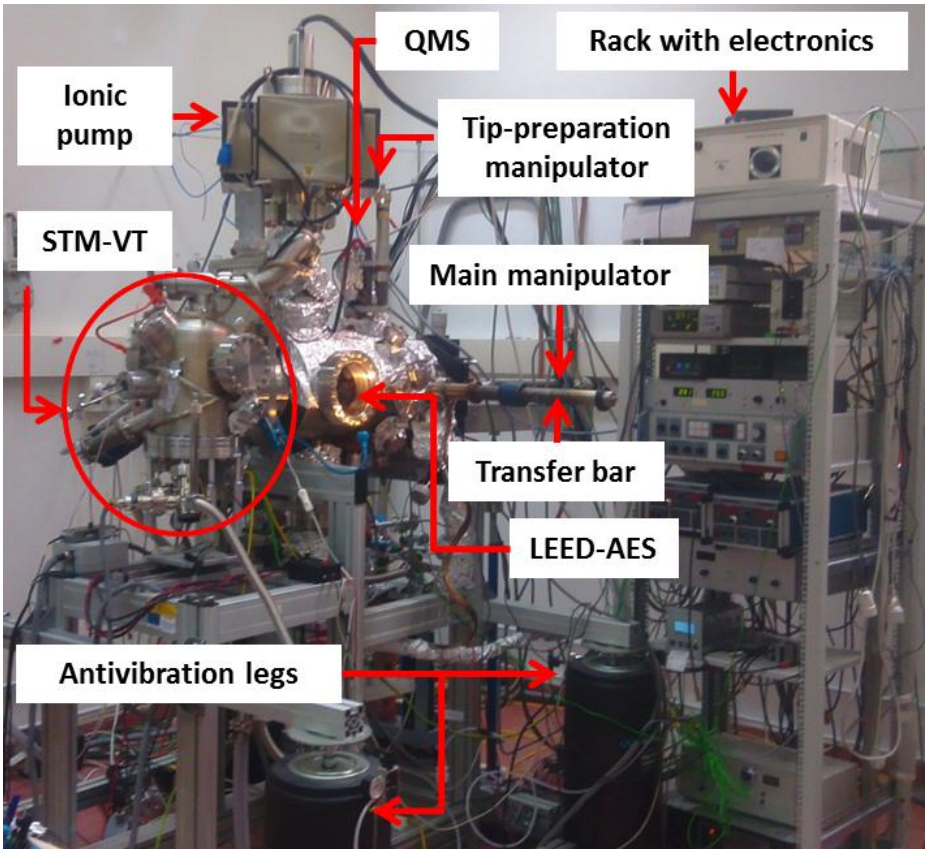

Fig 2.1: The Ciclope chamber in ESISNA's laboratory. The different parts of the chamber are identified with labels.

A base pressure of 1×10^{-10} mbar can be routinely attained in the chamber. The pumping stages consist on: a small turbo molecular pump (67 l/s) and the main turbo molecular pump (235 l/s) which are backed by a membrane pump. First, the membrane and the small turbo molecular pump help to get pre-vacuum conditions (~ 10^{-6} mbar). Then, the main molecular pump takes on the control until obtain a good UHV. Moreover, we have an external pumping-system (turbomolecular + membrane) to improve the vacuum in other parts of the chamber when it is needed, e.g. in the transfer bar, in distinct areas of the chamber, etc.

Aside from the turbo molecular pumps, this system has an ionic pump, a Titanium Sublimation Pump (TSP), and a non-evaporation getter (NEG) to maintain the base pressure in the 10^{-10} mbar range, during, for example, STM vibration free operation.

Other techniques have been used ex-situ: (1) Raman Spectroscopy and micro-Raman Spectroscopy at the Instituto de Ceramica y Vidrio (ICV-CSIC) and (2) Surface X-Ray Diffraction at BM25-SpLine Beamline (ESRF, Grenoble, France).

Theoretical calculations have been carried out using density functional theory (DFT) with CASTEP program and Materials Studio 6.1/8.0 software. All calculations have been performed in high-performance computer clusters TRUENO (CSIC) and HADES (ICMM-CSIC).

2.1 Scanning tunneling microscopy (STM)

Scanning tunneling microscopy is a technique developed in the 1980s [3] by Binning and Rohrer and based on the quantum-mechanical tunnel effect that allows electrons to tunnel through otherwise classical forbidden potential regions.

It has become one of the most powerful techniques in surface science, providing images of clean surfaces and species adsorbed on them with atomic or molecular resolution.

Since it is the primary tool used in this thesis, a thoroughly description has been incorporated to help interpret the results. The technique, however, is nowadays very well understood, and there are many good reviews on the subject [20–23].

STM

The STM consists of a sharp metallic tip that we can be approached to the surface of a conductive sample using piezoelectric actuator until a tunneling current is detected (see Figure 2.2). The current depends on the tip-sample distance according to the Eq(2.1)

$$I_t \propto NV_S e^{(-\mathrm{k}d\sqrt{\bar{\varphi}})} \qquad \text{Eq(2.1)}$$

where N is the density of states, V_s is the voltage applied between the tip and the sample, k is a constant, d is the distance between the tip and the sample and $\bar{\varphi}$ is the average of the work-function.

The Eq(2.1) indicates that the tunneling current is proportional to the voltage applied (it is applied to favor the tunneling current in only one direction; in our case, it is applied to the tip) and that the current decays exponentially with the distance between the tip and the sample. So, a small change in the distance between them causes a big change in current. The piezoelectric actuators are used to move the tip scanning over the surface and the computer system based closed loop measures the current and can generate a topographic image based on the tunneling intensity

Acquisition of images proceeds most commonly in a constant-current mode. A feedback loop is used to maintain the tunneling current constant as we scan the tip back and forth. The piezoelectric materials extend or compress as appropriate to keep the current constant, so the color map of the images encode how much the tip has moved vertically. These movements are recorded by the computer system and translated as an STM image. Every pixel in this image corresponds to the distance moved to maintain the tunnel current constant. Different chemical species adsorbed on the surface can also induce variations in the tunneling current because differences in the electronic structure can also translate as differences in the tunneling current. Therefore, the

simplest interpretation of an image regarding only topology and variation of distances might not be correct.

The second mode of image acquisition is the constant-height mode. Here, the current is allowed to vary and the feedback is used to preserve the same height between the tip and the sample. The images show a map of relative distances via the measured currents, which again can be affected by electronic effects.

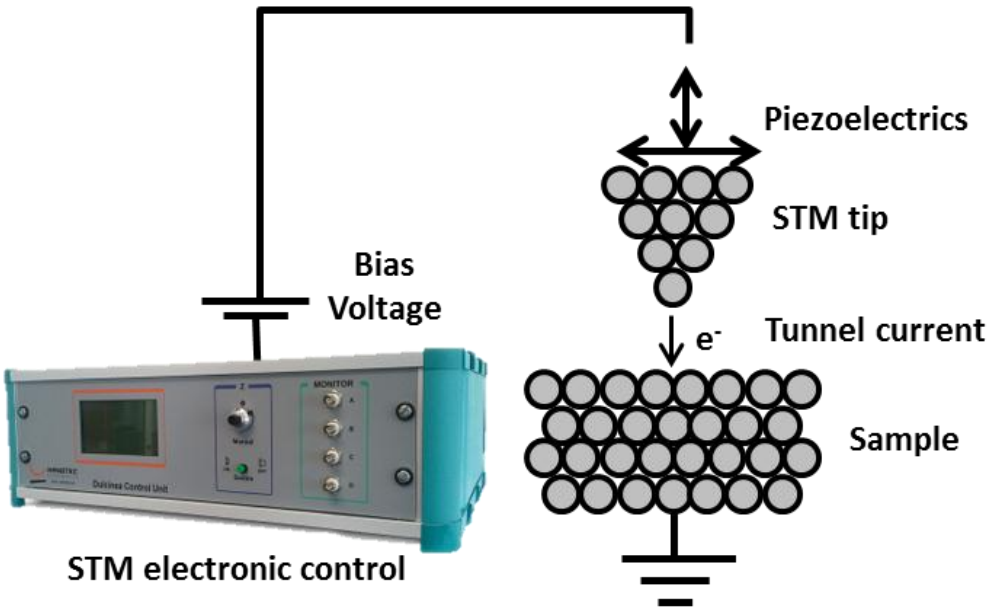

Figure 2.2: Schematic representation of the STM. The voltage is supplied to the tip and the sample is grounded to earth. The tip is moved in x,y and z directions by piezoelectrics. Dulcinea's control unit arranges the movement of the z piezoelectrics to maintain the constant-current or constant-height and the x,y piezoelectrics serve to scan the surface as required by the software. The sharp tip scans the surface of the sample and the control unit translates the signal as an image in the computer.

2.1.1 Quantum Mechanical Tunneling effect

The quantum tunneling effect is related to the capability of an electron (described by its wave function ψ(r)) to overcome a barrier even if it has not enough classical energy to do it (Figure 2.3). The quantum particle has a nonzero probability of tunneling through a potential barrier of height $V_0<\infty$ and width d. If the electron would be described in a classical approximation, it would have a zero probability through a barrier with a height $V>E_{electron}$.

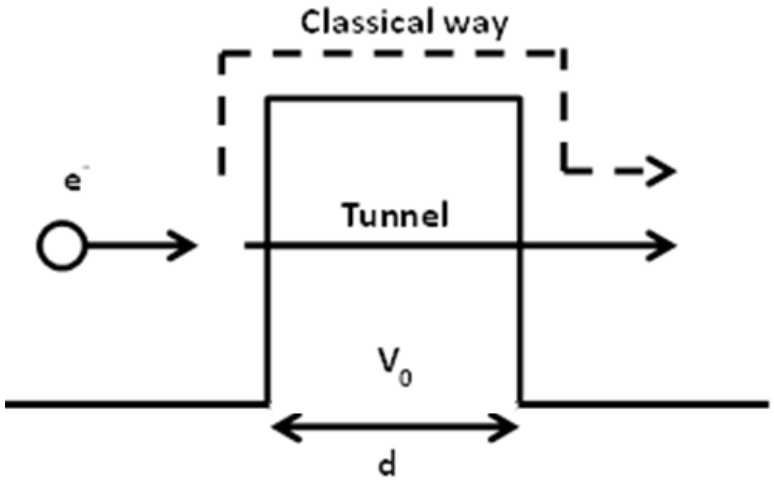

Figure 2.3: An electron in front of a barrier $V_0<\infty$ with a weight d can describe a classical path that overcomes the barrier only if its energy $E>V_0$ .On the other hand, to the quantum theory it has a non-zero probability of crossing the barrier even if it has not enough energy.

In the literature, two main formalisms have been developed to explain the STM experiments: Bardeen's formalism and Tersoff-Hamman approximation.

i. Bardeen's formalism

Bardeen's tunneling formalism (1961)[20] is the base for many theories of STM, but the predictions of this formalism are usually applicable when the tip-sample distance is big enough and the bias voltage is adequately small.

Bardeen's approach separates the tip and the sample on independent systems. The tunneling current is the result of independent scattering events that transfer electrons through the barrier. Schrödinger's equation can be solved in each separate region when the electronic states of the sample and the tip have been separately obtained; then time dependent first-order perturbation theory is used to estimate the rate of electron transfer between the two regions.

Alex Goettlieb and Lisa Wesoloski[24] have discussed Bardeen's theory as applied to STM. The theory is based on several assumptions:

a) The electron-electron interaction can be ignored
b) The occupation probabilities for the tip and sample are independent of each other and don't change in the process of tunneling
c) The tip and sample are in electrochemical equilibrium.
d) The tunneling is weak enough to justify that the first-order approximation is valid
e) Tip and sample states are orthogonal.

Considering these presumptions we can write the single-particle Hamiltonian that describes the electrons behavior. Since we are assuming independent electrons, the problem of the electronic dynamics in the STM focuses the analysis on the single-electron Hamiltonian:

$$H\psi(\boldsymbol{r}) = -\frac{\hbar^2}{2m}\nabla^2\psi(\boldsymbol{r}) + V(\boldsymbol{r})\psi(\boldsymbol{r}) \qquad \text{Eq. (2.2)}$$

where V(**r**) is the electrostatic potential energy that an electron would have at position **r**. We must take into account that the samples that exhibit single-electron charging effects cannot be treated by Bardeen's tunneling theory (assumption a).

The Hamiltonian must be applied to the tip and sample separately. Bardeen defines tip's and sample's Hamiltonians as follows.

Sample states are given by:

$$H_{sample}\psi(\boldsymbol{r}) = -\frac{\hbar^2}{2m}\nabla^2\psi(\boldsymbol{r}) + V_{sample}(\boldsymbol{r})\psi(\boldsymbol{r}) \qquad \text{Eq. (2.3)}$$

And tip states by:

$$H_{tip}\psi(\boldsymbol{r}) = -\frac{\hbar^2}{2m}\nabla^2\psi(\boldsymbol{r}) + V_{tip}(\boldsymbol{r})\psi(\boldsymbol{r}) \qquad \text{Eq. (2.4)}$$

V_{sample} and V_{tip} are the potential for the sample and the tip respectively. The space containing the STM is divided into three regions: the barrier region, the sample region, and the tip region.

V_{sample} is defined as:

$$V_{sample}(\boldsymbol{r})\begin{cases} V(\boldsymbol{r}) & if\ \boldsymbol{r}\ is\ inside\ the\ sample\ and\ barrier\ regions \\ 0 & if\ \boldsymbol{r}\ is\ in\ the\ tip\ region \end{cases}$$

And V_{tip} as:

$$V_{tip}(\boldsymbol{r})\begin{cases} V(\boldsymbol{r}) & if\ \boldsymbol{r}\ is\ inside\ the\ tip\ and\ varrier\ regions \\ 0 & if\ \boldsymbol{r}\ is\ in\ the\ sample\ region \end{cases}$$

The boundaries between the barrier region and the tip and sample regions are drawn arbitrarily and it is necessary to divide the space between the tip and the sample regions.

The tunneling current is the result of the electron transfer between the tip and the sample. At that point, the assumptions that and the tip and sample states are occupied by electrons are required to compute the current. The density of states (DOS) in the tip and the sample are given by $\rho_{tip}(E)$ and $\rho_{sample}(E)$ and occupations are determined by Fermi Dirac statistics:

$$F_{\mu,T}(E) = \frac{1}{e^{E-\frac{\mu}{k_B T}} + 1} \qquad \text{Eq. (2.5)}$$

μ is the chemical potential
T is the temperature
E is the energy
k_B is the Boltzmann constant

The tunnel current can be written as a sum of all possible processes, considering that the electrons can tunnel out from occupied tip states to unoccupied sample states and from occupied sample states to unoccupied tip states:

$$I = \frac{2\pi e}{\hbar}\sum_{n}\Big\{F_{\mu_{tip},T}(E_n)\Big(1 - F_{\mu_{sample},T}(E_n)\Big) - \Big(1 - F_{\mu_{tip},T}(E_n)\Big)F_{\mu_{sample},T}(E_n)\Big\}\rho_{tip}\,(E_n)M^2(\psi_n) \qquad \text{Eq. (2.6)}$$

To obtain the above equation we have used the Fermi's golden rule[24], where the rate of tunneling from an occupied sample state (ψ_{sample}) into a tip state is shown as

$$\frac{2\pi}{\hbar}(1 - F_{\mu_{tip},T}(E))\rho_{tip}(E)M^2(\psi_{sample}) \qquad \text{Eq. (2.7)}$$

Assuming that the occupation statistics of the tip are those of Fermi-Dirac equilibrium at temperature T (B and C assumptions). M^2 is the square amplitude

of the scattering matrix element which connects the sample and the tip states $\left(\left|\langle \Phi | H - H_{sample} | \psi \rangle\right|^2\right)$

In the particular case for the current at low temperature (T=0), the Fermi-Dirac function becomes a Heaviside function:

$$F_{\mu,0}(E)\begin{cases}1\ if\ E < \mu \\ 0\ if\ E > \mu\end{cases}$$

And the above tunnel current formula Eq. (2.6) is summarized in:

$$I = \pm \frac{2\pi e}{\hbar} \sum_{n:\ \mu_a < E_n < \mu_b} \rho_{tip}(E_n) M^2(\psi_n) \qquad \text{Eq. (2.8)}$$

where μ_a = min {μ_{sample},μ_{tip}} and μ_b = max {μ_{sample},μ_{tip}}; ± depends if $\mu_{tip} > \mu_{sample}$ or vice versa.

The current Eq. (2.8) can be approximated by an integral where T(ε) corresponds to the average value of $M^2(\psi_n)$ over all states of the sample for an energy E_n ranged in a small interval centered at ε:

$$I = \pm \frac{2\pi e}{\hbar} \int_{\mu_a}^{\mu_b} \rho_{tip}(\varepsilon) T(\varepsilon) \rho_{sample}(\varepsilon) d\varepsilon \qquad \text{Eq. (2.9)}$$

This Eq. (2.9) can be further simplified for the low bias case, because if μ_{sample} and μ_{tip} are close, the $\rho_{tip}(\varepsilon)$ and $\rho_{sample}(\varepsilon)$ are practically constants in the integral range, and the formula is reduced to:

$$I = \pm \frac{2\pi e}{\hbar} (\mu_b - \mu_a) \rho_{tip}(\mu) \rho_{sample}(\mu) T(\mu) \qquad \text{Eq. (2.10)}$$

and

$$T(\mu) = \frac{1}{(\mu_b - \mu_a)\rho_{sample}(\mu)} \sum_{\psi_n:\, \mu_a<\varepsilon_n<\mu_b} M^2(\psi_n) \qquad \text{Eq. (2.11)}$$

μ is any number between μ_a and μ_b

So, if we substitute T(μ) Eq. (2.11) into the last current formula Eq. (2.10), we obtain,

$$I = \pm\frac{2\pi e}{\hbar}\rho_{tip}(\mu) \sum_{\psi_n:\, \mu_a<\varepsilon_n<\mu_b} M^2(\psi_n) \qquad \text{Eq. (2.12)}$$

At the time Bardeen published his theory, he did not have in mind the STM since it only would be invented twenty years later. The formulas above have been taken from the nice review by Alex Goettlieb and Lisa Wesoloski[24].

An important point is about the Scattering Matrix elements determination ($M^2(\psi_n)$) because Eq. (2.12) depends on the matrix elements. Moreover, these matrix elements will also appear in the next alternative approach of Tersoff-Hamman. In Eq. (2.7) we have

$$M^2(\psi) = \left|\langle \Phi | H - H_{sample} | \psi \rangle\right|^2 \qquad \text{Eq. (2.13)}$$

where,

$$\langle \Phi_j | H - H_{sample} | \psi_n \rangle = \int (H(\boldsymbol{r}) - H_{sample}(\boldsymbol{r}))\, \overline{\Phi_j(\boldsymbol{r})}\psi_n(\boldsymbol{r}) d\boldsymbol{r} \qquad \text{Eq. (2.14)}$$

From Eq. (2.13), if we approximate the volume integral by a flux through a surface of separation in the barrier region, a more symmetric Bardeen's expression will be obtained below Eq. (2.17).

Considering any smooth surface in the barrier region, the operator H-H_{tip} and H-H_{sample} are zero on the tip side of the separation surface and on the sample side of the surface respectively. So, in the tip region, the operator H-H_{sample} is evaluated as Eq. (2.14) and H-H_{tip} as

$$\langle \Phi_j | H - H_{tip} | \psi_n \rangle = 0 \qquad \text{Eq. (2.15)}$$

Developing those two expressions (Eq. (2.14) and Eq. (2.15)) we can obtain[24],

$$\begin{aligned} &\langle \Phi_j | H - H_{sample} | \psi_n \rangle \\ &\quad = \int_T \overline{\Phi_j(\boldsymbol{r})} \left(-\frac{\hbar^2}{2m} \Delta \psi_n(\boldsymbol{r}) - \varepsilon_n \psi_n(\boldsymbol{r}) \right) d\boldsymbol{r} \\ &\quad - \int_T \psi_n(\boldsymbol{r}) \left(-\frac{\hbar^2}{2m} \Delta \overline{\Phi_j(\boldsymbol{r})} - E_j \overline{\Phi_j(\boldsymbol{r})} \right) d\boldsymbol{r} \end{aligned} \qquad \text{Eq. (2.16)}$$

Remaining the Fermi's Golden Rule where we only consider the elements with $\varepsilon_n \approx E_j$, the matrix elements can be written through the Divergence Theorem as

$$\langle \Phi_j | H - H_{sample} | \psi_n \rangle \approx -\frac{\hbar^2}{2m} \int_{dT} \left[\overline{\psi_n(\boldsymbol{r})} \boldsymbol{\nabla} \Phi_j(\boldsymbol{r}) - \Phi_j(\boldsymbol{r}) \boldsymbol{\nabla} \overline{\psi_n(\boldsymbol{r})} \right] d\boldsymbol{n} \qquad \text{Eq. (2.17)}$$

n is the normal vector to the surface dT, oriented external from T, and the integral is over any surface lying entirely within the barrier separating the two sides. This barrier will be the vacuum region between the tip and the sample.

ii. Tersoff-Hamman approximation

Twenty-two years after Bardeen's formalism was published, J. Tersoff and D.R. Hamman applied those results to the STM[23]. First, they assumed the tip wave functions had to be radially symmetric. Using this approximation they deduced that the tunneling current is directly proportional to the sample electron density at the center of the tip (Fig 2.4).

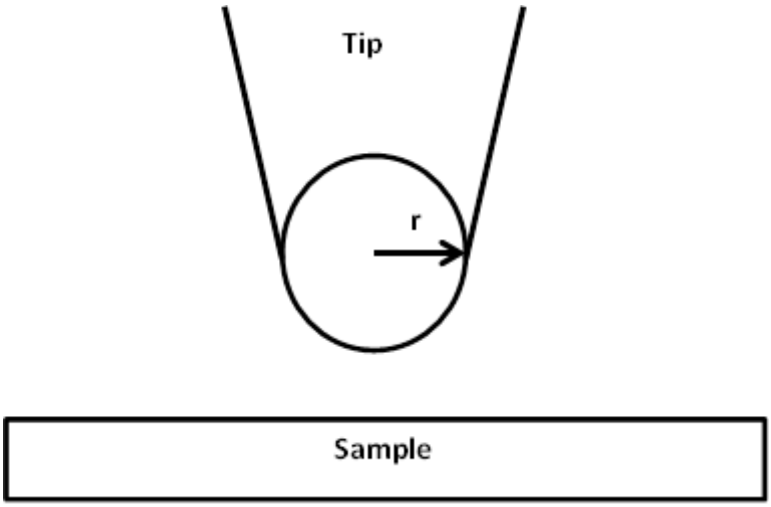

Fig 2.4: Tersoff-Hamman approximation assumes the Bardeen's results considering a spherically symmetric tip.

The approximation draws from the Bardeen's results Eq. (2.17). Considering a spherically symmetric tip, the tip states can be modeled as $\Phi_j(\boldsymbol{r}) \approx A_j \frac{e^{-k_j r}}{r}$ where r corresponds to the distance to the center of the tip, $k_j = \frac{\sqrt{2m|E_j|}}{\hbar}$ and A_j is a constant.

$\Phi_j(\boldsymbol{r})$ satisfies the independent Schrödinger's equation for r>R because the radially symmetric potential is $V_{tip}(\mathbf{r})=0$ for those r values.

Using Eq. (2.16) and approximating $\Phi_j(\boldsymbol{r}) \approx A_j \Phi_j(\boldsymbol{r})$ only outside of the tip region,

$$M(\psi_n) = \langle \Phi_j | H - H_{sample} | \psi_n \rangle \approx \langle A_j \Phi_j | H - H_{sample} | \psi_n \rangle = -\bar{A}_j \int_T \psi_n(\boldsymbol{r}) \left(-\frac{\hbar^2}{2m} \Delta \Phi_j(\boldsymbol{r}) - E_j \Phi_j(\boldsymbol{r}) \right) d\boldsymbol{r} \quad \text{Eq. (2.18)}$$

C.J Chen[21] showed that $\Phi_j(\boldsymbol{r})$ has to satisfy at all points the equation:

$$-\frac{\hbar^2}{2m} \Delta \Phi_j(\boldsymbol{r}) - E_j \Phi_j(\boldsymbol{r}) = \frac{\hbar^2}{2m} 4\pi \delta_0(\boldsymbol{r}) \quad \text{Eq. (2.19)}$$

If we subtract Eq. (2.19) from Eq. (2.18)

$$M(\psi_n) = \langle \Phi_j | H - H_{sample} | \psi_n \rangle \approx -\bar{A}_j \frac{\hbar^2}{m} 2\pi \psi_n(0) \quad \text{Eq. (2.20)}$$

So, the formula for tunneling current at low bias and low temperature Eq. (2.12) can be summarized in

$$\begin{aligned} I = \pm \frac{2\pi e}{\hbar} \rho_{tip}(\mu) \sum_{\psi_n:\, \mu_a < \varepsilon_n < \mu_b} M^2(\psi_n) \\ = \pm \frac{2\pi e}{\hbar} \rho_{tip}(\mu) \left(\frac{\hbar^2}{m} 2\pi \right)^2 A^2 \sum_{\psi_n:\, \mu_a < \varepsilon_n < \mu_b} |\psi_n(0)|^2 \\ = \left(\mu_{tip} - \mu_{sample} \right) \frac{e h^3}{m^2} A^2 \rho_{tip}(\mu) \rho_{sample}(0, \mu) \end{aligned} \quad \text{Eq. (2.21)}$$

with

$$\rho_{sample}(0, \mu) = \frac{1}{\left| \mu_{sample} - \mu_{tip} \right|} \sum_{\psi_n:\, \mu_a < \varepsilon_n < \mu_b} |\psi_n(0)|^2 \quad \text{Eq. (2.22)}$$

Obtaining Eq. (2.21) as the Tersoff-Hamann formula for the current and Eq. (2.22) as the local density of sample states per unit volume near the point r=0 near the quasi-Fermi energy μ.

From Eq. (2.21) and Eq. (2.22) we can deduce that the conductance at low bias and low temperature is directly proportional to the local density of sample states at the center of the tip in an STM, as we have advanced in the first paragraph of this part.

2.1.2 Scanning Tunneling Microscope-Variable Temperature (STM-VT)

In this thesis, we have used an Omicron's Scanning Tunneling Microscope of Variable Temperature (Fig 2.5). This Microscope operates in a range of temperature from 25K until 500K. In the process to cold down the system or to measure at low temperature we use Liquid Nitrogen or Liquid Helium. However, most experiments of this work have been realized at room temperature.

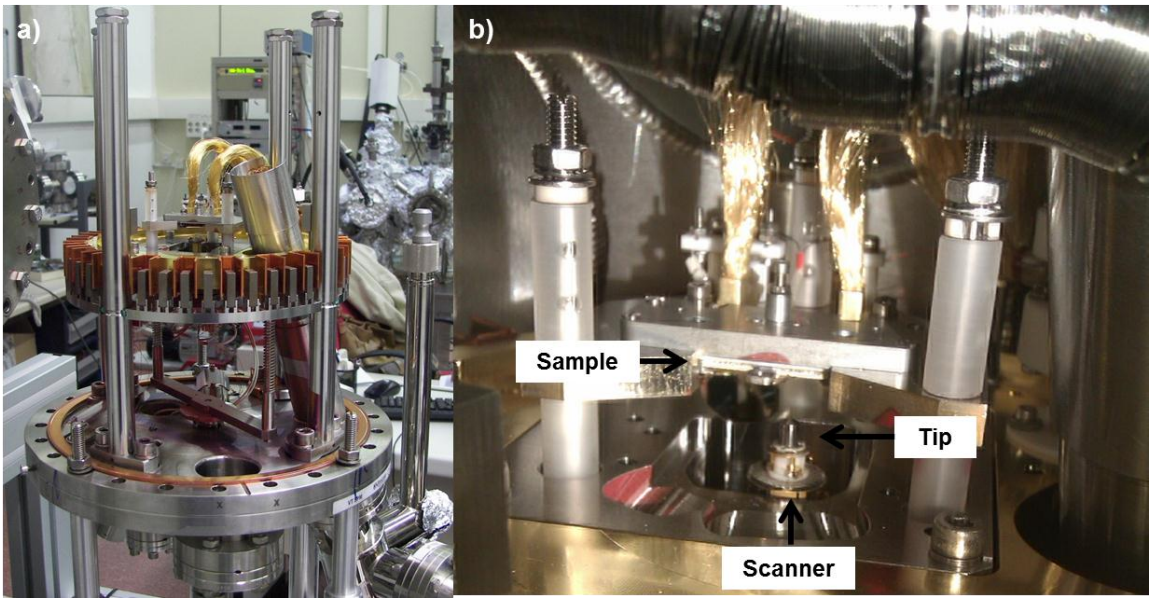

Fig 2.5: a) Omicron's STM-VT. The picture shows the STM used in this thesis; b)

Picture of the head of our STM. The sample, the scanners and the tip are indicated on it.

2.2 Tip preparation

An ideal tip to be used in STM would terminate in only one atom at the edge. In practice, this is very difficult to obtain. However, it is important since it influences the resolution of images. With this goal in mind we have used two different kinds of tips: (1) homemade tungsten tips and (2) Kolibri sensors (commercial tips of SPECS).

2.2.1 Tungsten tips

The set up to make this type of tips is shown in Fig 2.6a. It is based on the electrochemical etching of a tungsten wire. With this purpose, a tungsten wire is introduced in a metallic ring covered with a droplet of KOH solution. The droplet is made by introducing the ring into a 2.5M KOH so that the solution remains on the hoop. A voltage has been applied between the ring and the tungsten wire until obtain an emission current between 15-40 mA. The K^+ ions from the KOH membrane react with the tungsten in such a way that they etch the wire. This process takes places only at the part of the wire in contact with the droplet thinning the wire until it forms a sharp tip. Then the wire is carefully cut by the other end and introduced into an Omicron's tip-holder (Fig 2.6b).

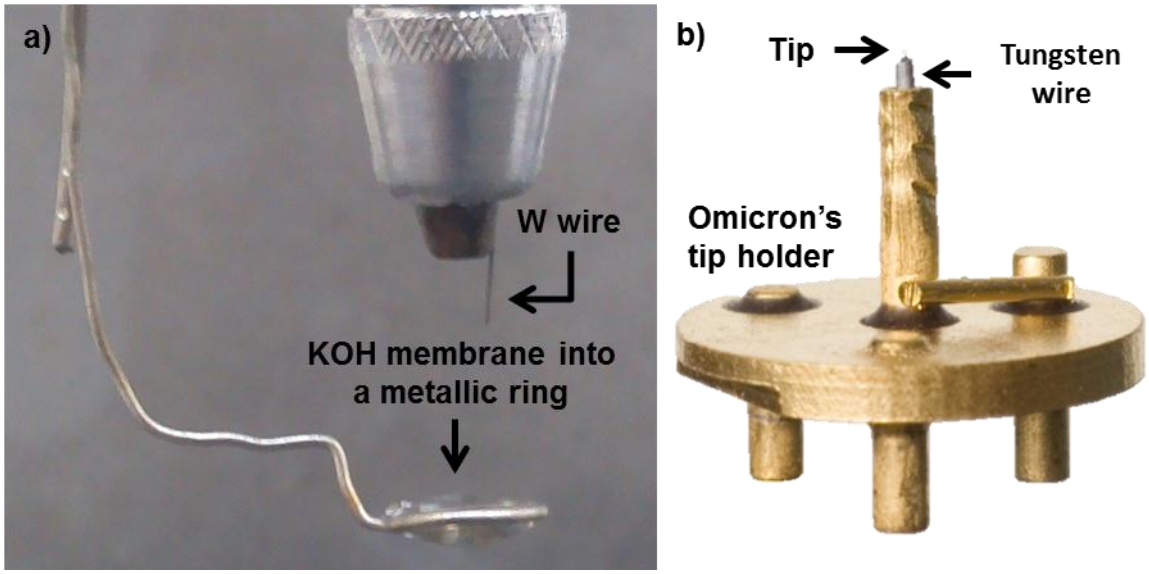

Fig 2.6: a) Image of the set up to make tungsten tips. The W wire will be introduced into the KOH membrane to realize the described process above; b) Picture of a tungsten tip into an Omicron's tip holder.

2.2.2 Kolibri sensors

Kolibri sensors are commercial SPECS tips based in a quartz sensor used for non-contact AFM (Fig 2.7). These sensors are based on a symmetrical length extension resonator with a very thin metallic tip with a weight of about 1µg meant to do not disturb the symmetry of the quartz oscillator. We have worked to adapt these tips to the STM-VT, connecting them with the Omicron's tip holders.

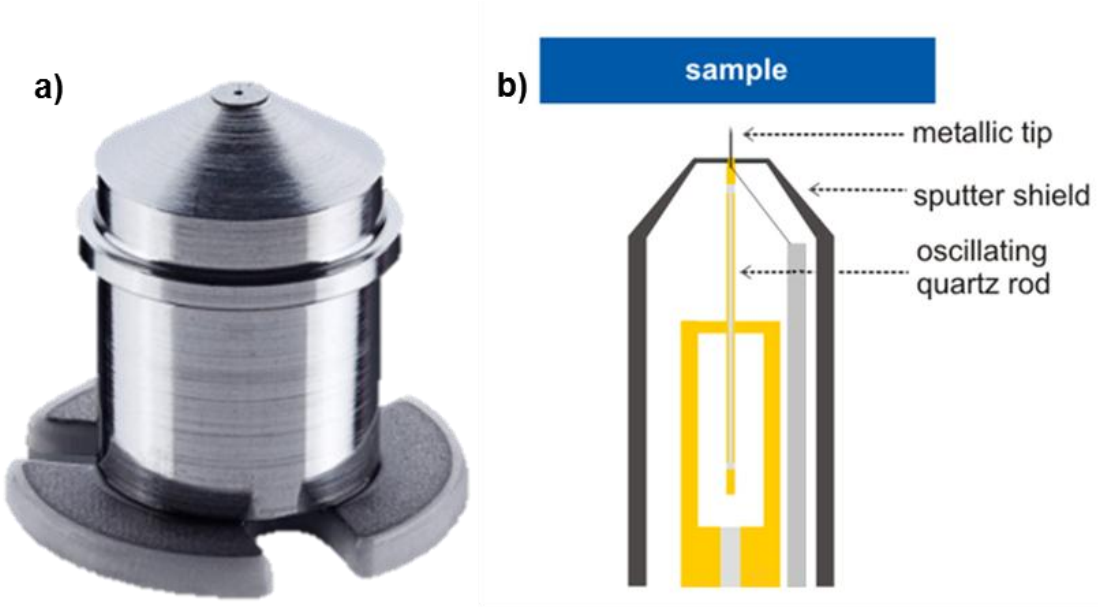

Fig 2.7: These two images have been obtained from the specs website. a) External appearance of a Kolibri sensor. The metallic tip is so small and it is very difficult to observe; b) Schematic representation of the Kolibri's internal structure. The oscillating quartz rod is in charge to move the metallic tip. The sputter shield protects the internal structure of we use Ar^+ sputtering to make better the tip.

2.3 Low-energy electron diffraction (LEED)

Low-energy electron diffraction is a useful technique for the determination of the surface structure (Fig 2.8). This technique allows the structural determination of the surface by bombardment with a collimated beam of low energy electrons from 20 eV to 500 eV. The diffracted electrons are collected on a fluorescent screen forming a pattern which is a reciprocal image of the atomic structure of the surface.

The LEED system is formed by an electron gun, a hemispherical fluorescent screen, which is positively biased with +6 kV and a series of grids towards the screen. The grids are used to slow down the inelastically scattered electrons.

The electron gun emits electrons by a cathode filament which is at a negative potential while the sample is grounded. The electrons are accelerated and focused into a beam and, some of them are backscattered elastically by the surface. A good quality diffraction pattern is detected if the surface is atomically ordered and clean. The image on the screen corresponds to the reciprocal space map of the structure of the surface.

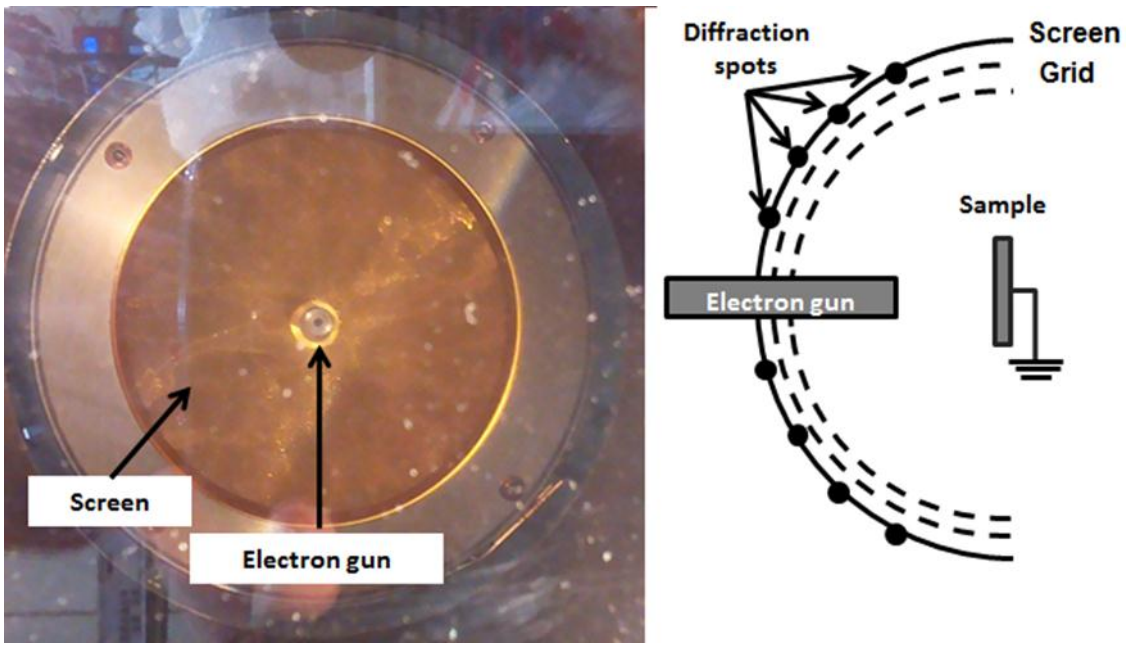

Fig 2.8: a) The LEED apparatus. It is possible to observe the screen where the spots appear forming the reciprocal space map, and the electron gun which emits the electrons. b) Schematic representation of the LEED system. The sample needs to be grounded. The electron emitting the electrons is located in front of the sample. The scattered electrons are filtered by the grids and are detected in the screen showing the formed LEED pattern.

2.3.1 LEED patterns: Interpretation

In the LEED technique, the pattern observed on the screen corresponds to the reciprocal lattice of the surface. The incident electron energy let to control the number of diffraction spots and additionally, the size of the Ewald's sphere. The

real space lattice can be obtained from the reciprocal lattice and the surface can be characterized qualitatively, for example, the periodicity. In the Fig 2.9, the periodicity of the Cu(110) surface is observed, in such a way, we can deduce the structure of the substrate surface is rectangular. As the LEED pattern corresponds to the reciprocal lattice, the distance between the spots is related to the inverse distance in the real lattice. Comparing the LEED pattern with the corresponding model in the corner, we can deduce these relations.

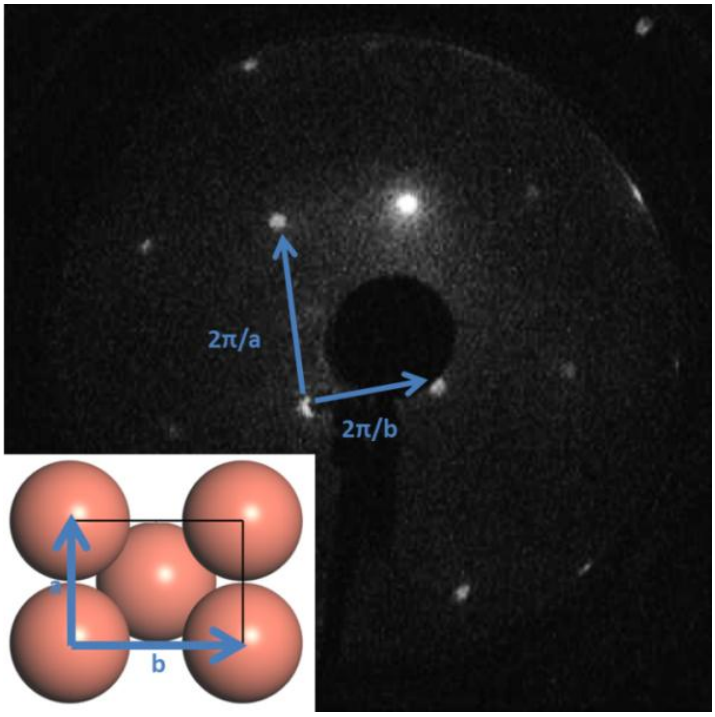

*Fig 2.9: LEED pattern of the Cu (110) surface at 108eV. In the corner, a representation of the Cu(110) unit cell with the **a** and **b** distances marked.*

2.4 Auger Electron Spectroscopy (AES)

The LEED optics can be used like an Auger electron spectroscopy system. We use this technique to determine if the sample is clean enough. Moreover, we can check after a deposition if we have specific type of atoms on our surface.

For example, the first time we sublimated Cu_4Cl_4 (see section 2.9), we tested if the AES spectrum showed peaks in the chlorine, sulfur, carbon and nitrogen areas to make sure that the sublimation had been successfully.

This technique is based on the Auger effect. The Auger effect consists on an electronic process resulting from electron transitions in an excited atom. The process is illustrated for a Nitrogen atom with three energy levels (1s 2s 2p) in Fig 2.10. The atoms on the surface are excited by the beam of electrons with energy in a range from 0.2keV until 50keV. 1s level electrons from these atoms are removed leaving 1s level holes which can be filled by 2s level electrons. In this process, the electrons moved to lower energy level and lose energy. That energy is in correspondence with the orbital energies difference and is imparted to 2p level electrons. These electrons are emitted. Considering that orbital energies are specific and characteristic of every element, if we collect the emitted electrons with an electron detector we can obtain information about the chemical composition of the surface.

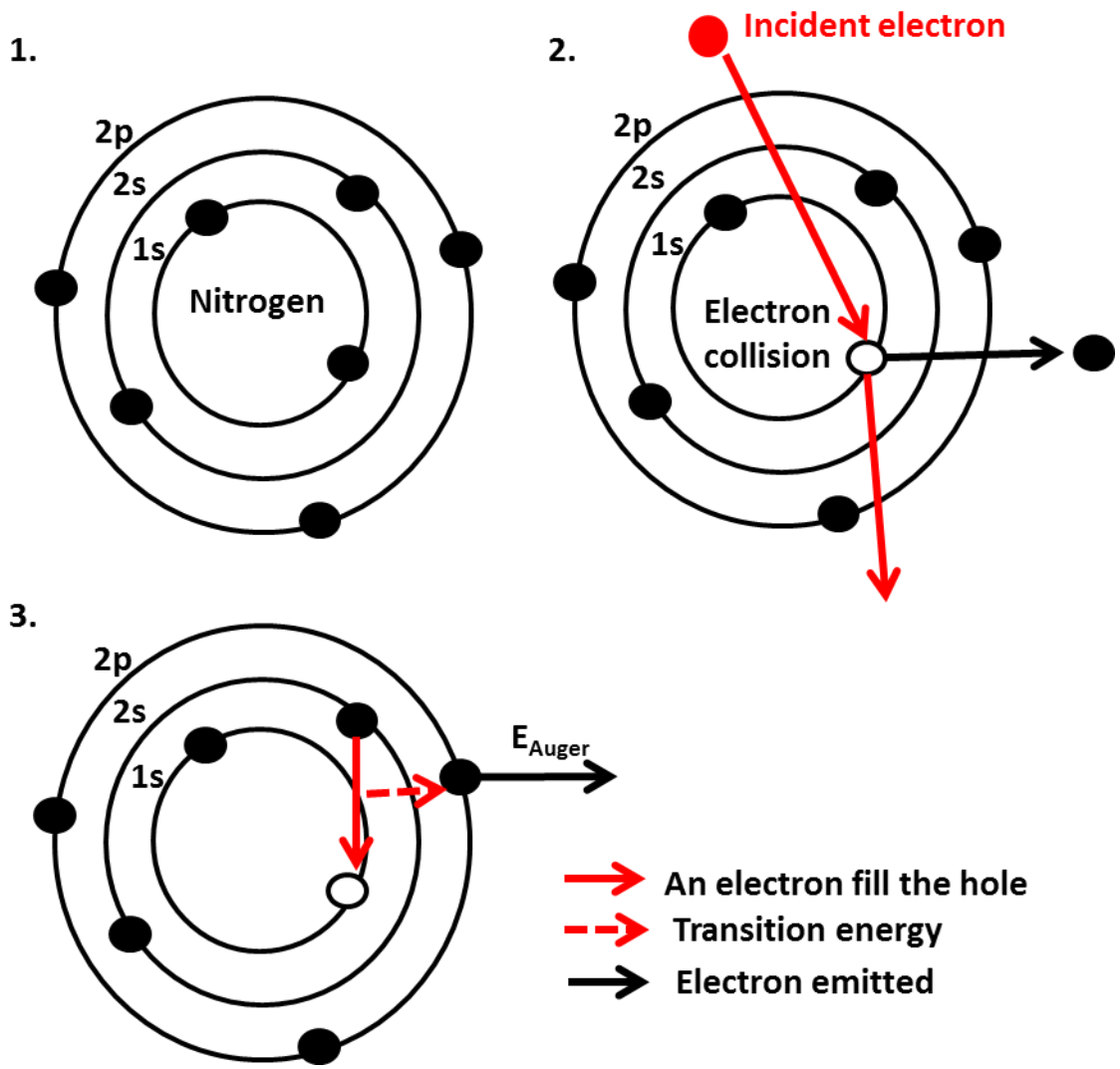

Fig 2.10: Auger effect summarized in three steps. First, Nitrogen atom structure used this explanation. Second, an incident electron from the beam of electrons collides with a 1s electron. The red and black arrows show the incident and 1s electron trajectories respectively. The white circle marks the hole resulted. Third, a 2s electron fill the 1s hole, the transitions energy resulted from this causes the emission of a 2p electron.

2.4.1 Electron Energy Loss Spectroscopy (EELS)

Electron energy loss spectroscopy consists on the exposure of a sample to a beam of electrons (such as in LEED or in AES) to obtain the spectrum of energy loss of the electrons scattered inelastically with respect to the intensity.

This spectrum contains information about the physical properties of the material. So, the amount of energy loss can be interpreted in the way of what caused it, for example, inelastic interaction, Plasmon-excitations, inter- and intra-band transitions…

Using AES technique, we obtain the elastic peak in the excitation energy value. This means that all the electrons are emitted elastically at this energy value. In other words, this peak corresponds to the zero loss scattering. For that reason we have used AES like EELS with particular attention to the region near the elastic peak (Fig 2.11).

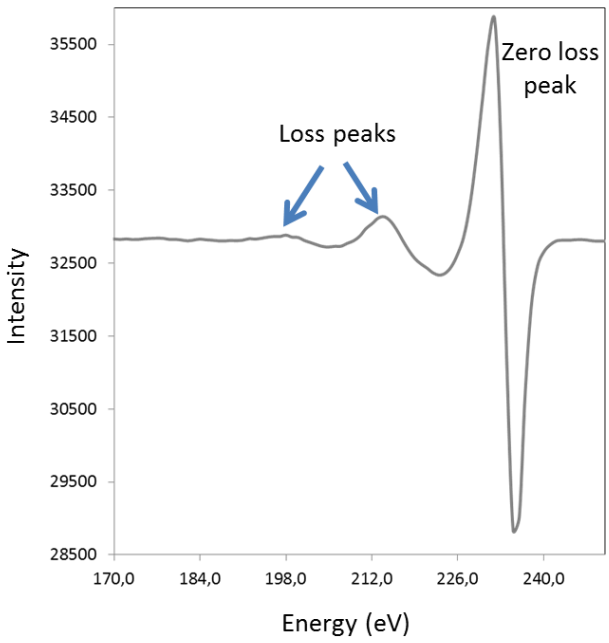

Fig 2.11: An AES spectra used as EELS plot. The zero loss peak corresponds to the elastic peak at 235eV. In the picture appears two loss peaks as consequence of the inelastic scattering of the electrons.

2.5 Quadrupole Mass Spectrometer (QMS)

The QMS is a powerful tool to obtain the mass to charge ratio so we can monitor our experiments. The most common use is as a residual gas analyzer (RGA) that let us knows, for example, sublimating molecules and to monitor deposition or sample's cleaning process.

The Quadrupole Mass spectrometer consists of a mass analyzer formed by four parallel cylindrical rods enquired to filter the environment ions into the ultra-high vacuum chamber by their mass respect their charge ratio (m/Z). An RF oscillating electric field is applied to the rods separating the ions as a function of the stability of the ions trajectories. This ionization is translated as a mass spectrum formed by a plot of the mass with respect to the ion current (Fig 2.12b) or different masses are represented in a plot of the time with respect to the ion current (Fig 2.12a), letting us determine the mass of the particles, ions or molecules in the chamber.

In Fig 2.12a is possible to observe the masses involved in a cycle of cleaning of a metallic surface. The Ar^+ sputtering is performed from 17:37h to 17:48h. In these 11 minutes the main masses are 40 a.m.u. and 20 a.m.u, both related with the Argon atom; the follow higher masses are 36, 28, 2, 18, 44 a.m.u., all of them are related with compounds of carbon, molecular nitrogen, hydrogen, water molecule or carbon dioxide, and they are the common masses observed into the chamber. Then, the annealing process is observed between 17:49 to 17:59h. The desorption shows a peak of argon (40 and 20 a. m. u.) with the maximum at 17:52h. The 28 a.m.u. (corresponding to CO) describes the same behavior than argon.

In other hand, in Fig 2.12b, we can to see the amount of each mass between 0 to 50 a.m.u. at logarithmic scale. Our QMS let us extend the range until 200 a.m.u.

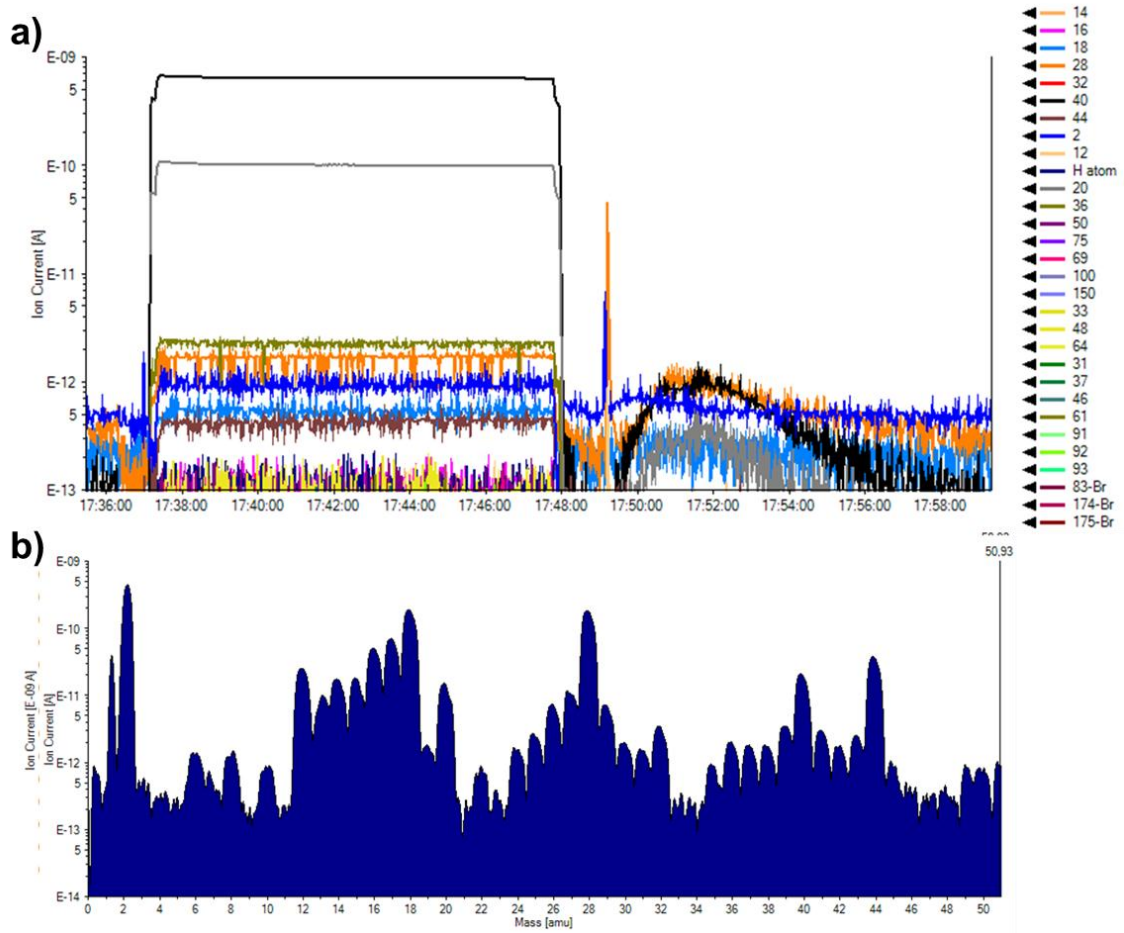

Fig 2.12: a) Example of the ion current plot respect of a period of time. This plot is useful to observe the fluctuations of selected masses along the time. The masses are represented with different colors according with the color legend at the right side. In that case, it is possible to observe the masses during a Ar^+ sputtering (from 17:37 to 17:48h) and an annealing (from 17:49 to 17:59h); b) Example of a sacn barrier form the 0 to 51 u.m.a. The amount of the elements or compounds into the chamber is related with the height. In this case, the scan is in logarithmic scale, so the height can confuse.

2.6 Surface preparation

The surface preparation should be divided in two parts in accordance with the type of sample nature, i. e. metallic and insulating samples. Along this work we have used different substrates: on one side we have used copper, gold and platinum single crystals as metallic samples, on the other side we have worked with diamond as insulating samples. The preparation of the two groups of samples is very different, most especially for the diamond particularities.

2.6.1 Metallic samples

The procedure with the metallic samples consists of cycles of Ar^+ sputtering and annealing. The Ar^+ sputtering is realized at different energies, varying from 1,5KV until 0,6KV (usually we start from the highest value and we finish at the lowest) during 10 min. The annealing temperature is different in every substrate, the most common values we use are: copper at 773-823K , gold at 873-923K, platinum at 1173-1223K. The annealing in needed to achieve a good pressure (lower than $5 \cdot 10^{-9}$mbar) to maintain the sample as clean as possible.

The cleaning of the samples is monitored with the QMS: we check that the Ar gas is clean from the gas cylinder before the sputtering starts, and the Ar desorption from the sample surface during annealing. The annealing can vary from 10-30 min depending when the Ar peak decreases on the mass spectrum. The cycles are repeated until we observe sharp spots with the LEED technique and the lack of the peaks related with contamination in the AES spectra (carbon, sulfur or chlorine peaks).

Occasionally, we perform an annealing of the Platinum single-crystal in an oxygen environment into the chamber ($P \approx 1 \cdot 10^{-7}$mbar) to remove the contamination from the carbon on the surface. In this process, the oxygen reacts with the carbon forming CO and CO_2 gasses which are pumped away. This process is needed because Platinum is a very hard crystal which needs higher sputtering energies and temperatures to clean than other substrates.

2.6.2 Insulating samples

The preparation of the diamond surface has some disadvantages: i) We cannot use Ar^+ sputtering to prepare the surface because the collision of Ar^+ ions form holes and the surrounded regions to them graphitized; ii) The annealing of the diamond in an oxygen environment is not adequate because the diamond is formed by carbon atoms which react with the oxygen destroying the surface. Thus, establishing a method of surface preparation involves considerable time and effort.

So after several attempts using a homemade Hydrogen cracker (we mounted in our chamber) without success because we don't obtain LEED patterns from the single-crystals, we got a protocol to use outside the ultra-high vacuum chamber.

This protocol starts by introducing the diamond in a mix of sulfuric acid with potassium nitrate held at boiling point. Ten minutes later, we put the sample into an ultrasonic wash of deionized water and then, another wash of acetone. After that, we flush the sample with methanol and isopropanol and blow with nitrogen gas. At this point we can introduce the diamond into the chamber. In good pressure conditions, we have to degas the substrate at 1000°C. The

pressure increases very much and the annealing has to be maintained until ≈$5 \cdot 10^{-9}$mbar.

2.7 Raman spectroscopy

Raman spectroscopy consists of the illumination of a sample with a laser beam. When the photons are scattered, most of them are elastically scattered (Rayleigh scattering) with the same energy as the incident photons. A small part of them are scattered by an excitation with a different frequency used to be lower than the incident ones. This inelastic scattering is the Raman Effect. It is based on the incident photons generating an oscillating polarization in the molecules of the sample. This polarization can link to other polarizations of the molecules as vibrational or electronic excitations. If the polarization doesn't couple to other polarizations, the vibrational state of the molecules does not change and the scattered photon ends with the same energy achieved an elastic scattering, however, if the polarization matches to a vibrational state with higher energy, the started and the scattered photons differ in an amount of energy forming the Raman Effect. This amount is the energy required to excite a molecule to a higher vibrational mode. Thus, the Raman spectroscopy let us observe the molecular vibrations trough the inelastic scattering process. The electromagnetic radiation is collected through a monochromator and the elastic scattered radiation is filtered out while the inelastic photons are dispersed onto a detector. This part of the collected light provides a fingerprint (*Fig 2.13*) of the molecules.

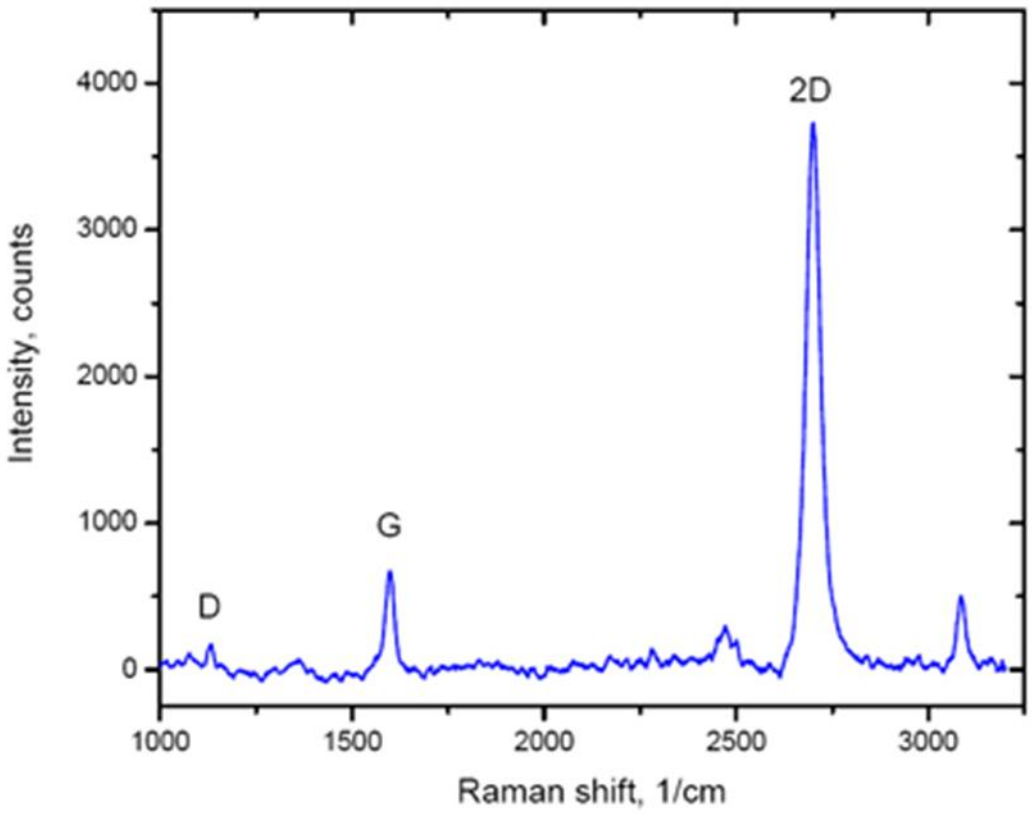

Fig 2.13: Example of a Raman spectrum of graphene. It has been extracted from http://www.sciencefacts.net/raman-spectroscopy.html. There, it is possible to observe the characteristics peaks related to Graphene (D, G and 2D).

2.8 Molecular beam epitaxial growth

In the main body of this work is dedicated to the synthesis of graphene on different substrates by MBE using a homemade molecular beam epitaxial carbon source. MBE is a technique to grow films epitaxially (it is referred to the deposition of a crystalline overlayer) in an ultra-high vacuum environment in such a way with the absence of carrier gases

An advantage of this method is that it eliminates the process of transferring the graphene from the metal or bulk graphite to the substrate on which the graphene will ultimately be used. Molecular beam epitaxy (MBE) is a well-known and widely used technique for the production of high quality and homogeneous wafer-scale epitaxial layers. It is highly reproducible with atomic layer control of thickness and composition. These properties make MBE an attractive growth method for graphene films. There have been only a few experimental attempts to grow the graphene by the evaporation of carbon. We also show that thickness, structure, and electronic properties can be controlled by carbon flux, the types of carbon source, and substrate temperature.

In a solid source as our case, the element to be evaporated is heated until the atoms begin to sublimate. The term “beam” refeers to the fact that sublimated atoms don’t interact with other gases or with each other until the deposition on the sample.

2.8.1 Graphene growth

We achieved the graphene growth with a homemade molecular beam epitaxy solid carbon source (Fig 2.14). It consists of two tantalum bars connected through a glassy carbon filament. By passing a DC current of 14A (7.9V, 110W) through the filament, it reaches 2273 K obtaining the needed conditions for the evaporation to take place. The filament temperature is measured with a two-color optical pyrometer IRCON MODLINE 5, series 5R, model 5R-3015-0-0-0-2B and the emissivity used was 1.00 (the emissivity of a back body).

Once we have obtained the filament temperature necessary for graphene growth at a pressure lower pressure than 1×10^{-8} mbar, the substrate is placed in front of the filament with a distance of 20mm. Graphene growth takes place

for 30 min to cover a half of a monolayer. After deposition, the substrate is annealed. The temperature annealing depends of the substrate; in this thesis we have used platinum (T = 923 K), gold (T = 823 K) and diamond (T= 1473 K). The deposition rate of carbon depends on the DC current. The calibration methods will be discussed next.

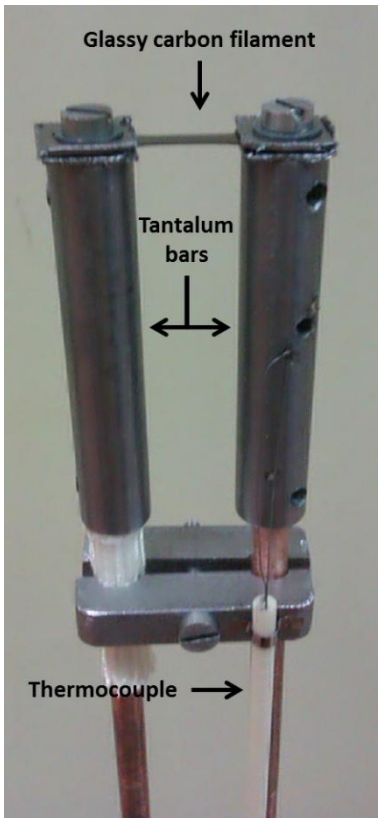

Fig 2.14: Appearance of the Homemade MBE solid carbon source.

2.9 Molecular deposition

One part of this dissertation is the deposition of organic molecules on Copper (Cu(110)). The sublimation was performed in ultra-high vacuum environment from a home-made Tantalum crucible filled by powder molecules (Fig 2.15a).

By passing a current through the envelope, the molecules are heated and sublimated. The base pressure of the chamber was 10^{-10}mbar but during deposition it increased up to $7 \cdot 10^{-10}$mbar. The sublimation temperature was controlled with a K-type thermocouple spot-welded to the envelope base.

The crucible was degassed until the pressure was lower than 1×10^{-9} mbar at a temperature below the deposition temperature (370 K) to desorb the water molecules and the contamination. The molecules used in this work are $[Cu_4(\mu_3\text{-}Cl)_4(\mu\text{-}pymS_2)_4]$ (named Cu_4Cl_4), synthetized by the Felix Zamora's group in the Universidad Autónoma de Madrid (Fig 2.15b). The molecules sublimation's rate is 0,017 monolayer/min at 370 K. This estimation was performed using the STM images.

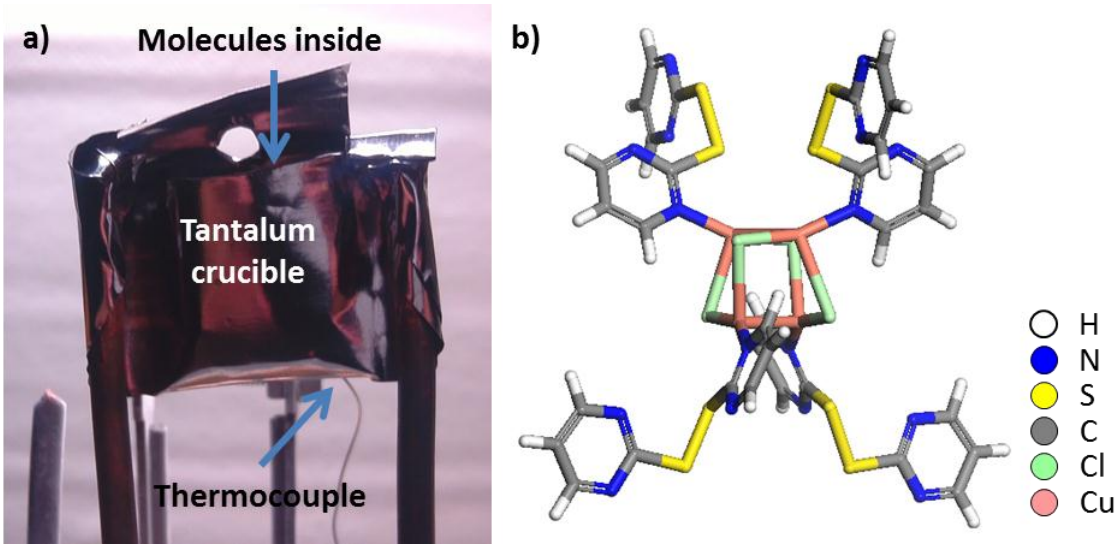

Fig 2.15: a) Picture of a homemade Tantalum crucible used to the molecules evaporation. The crucible shows a circular opening that lets the evaporated material to flow out. This particular picture shows the crucible lid open, during refilling the Ta pocket with more material; b) Representation of $[Cu_4(\mu_3\text{-}Cl)_4(\mu\text{-}pymS_2)_4]$ structure.

2.10 Density Functional Theory (DFT)

Theoretical simulations have been performed using DFT. It is a common computational and versatile method used in material science, physics and chemistry. It is commonly used for calculations in solid-state physics but it has some limitation to describe intermolecular interactions like van der Waals forces due to the approximations made for exchange and correlations interactions. However, in our case, this method can provide us a reasonable access to the properties of different systems of interest.

DFT is supported by the Hohenberg-Kohn theorems[25] although its basis departs from the Thomas-Fermi model. The H-K theorems tell us that: i) For two systems of electrons that have the same ground-state density, if one feels a potential $v_1(\mathbf{r})$ and the other a different one $v_2(\mathbf{r})$, it is necessarily $v_1(\mathbf{r}) - v_2(\mathbf{r}) =$ constant; ii) A density functional F[n] exists such that the total energy of a system can be written as $E_{(v,N)}[n] = F[n] + \int v(\boldsymbol{r})n(\boldsymbol{r})d^3r$, in such a way that the minimal value of $E_{(v,N)}[n]$ is the ground state energy of this system for N electrons (so it is a positive integer value) and potential $v(\mathbf{r})$.

These theorems apply only for non-degenerate ground states in the absence of a magnetic field; consequently they needed to be generalized to include these cases. For example, the first theorem determines that the ground-state properties of a system of electrons are determined by an electron density; this one is extended to the time-dependent domain that is needed to describe excited states resulting in time-dependent density functional theory (TDDFT).

With that in mind, the many-body problem of interacting electrons in a static external potential can be reduced to a problem of non-interacting electrons

moving in an effective potential which includes the external potential and the effects of the Coulomb interactions between the electrons (the exchange and correlation interactions). The simplest approximation to model the exchange and the correlation interactions is the local-density approximation (LDA) functional where exchange and correlation is computed using the local value of the electronic density at a given point alone. The exchange and correlation energy to be used is obtained for a uniform electron gas with a given density. LDA has the tendency to over-estimate the exchange-correlation energy, so it is common to expand the energy using gradients of the density to correct this tendency, an approximation that is known under the name of generalized gradient approximations (GGA). These are the two functional used in this work.

We have optimized the geometry of different systems to obtain the correct electronic structure by solving the Schrödinger equation

$$\hat{H}\Psi = \left[\hat{T} + \hat{V} + \hat{U}\right]\Psi = E\Psi \qquad \text{Eq. (2.23)}$$

where $\hat{H}$ is the Hamiltonian, E is the total Energy, $\hat{T}$ is the kinetic energy, $\hat{V}$ is the potential energy from the external field and $\hat{U}$ is the electron-electron interaction energy.

As the Schrödinger equation cannot be solved exactly for a many-body system (the many-particle equation cannot be separable into single-particle equations because of the $\hat{U}$ interaction term), the DFT provides an appealing alternative because tell us how to map the many-body problem to a one-body problem with the same particle density n(**r**).

2.10.1 LDA and GGA

Therefore, Local-density approximations (LDA)[26] and Generalized Gradient Approximations (GGA) [27] are used to obtain the electronic. We have used these approximations incorporated into CASTEP simulation package [28,29]. We briefly sketch a few important features regarding both approximations:

i. Local-density approximation (LDA)

LDA is the simplest approximation to model the exchange-correlation (XC) energy functional in DFT and it only depends on the value of the electronic density at each point in space. This approximation has been derived from the homogeneous electron gas model.

Generally, the local-density approximation for the exchange-correlation energy is written as

$$E_{XC}^{LDA}(n) = \int \in_{XC} (n) n(\boldsymbol{r}) d^3 r \qquad \text{Eq. (2.24)}$$

where n(**r**) is the particle density and $\varepsilon_{XC}(n)$ is the exchange-correlation energy per particle. The functional depends only on the density at the coordinate where the function is evaluated.

ii. Generalized gradient approximation (GGA)

GGA is another functional which corrects the xc-energy by using the gradient of the density. In such a way, within this approximation, the molecular geometries and the ground-states energies obtained are usually more adequate.

The Generalized Gradient approximation for the exchange-correlation energy is written as

$$E_{XC}^{GGA}(n_\uparrow, n_\downarrow) = \int \in_{XC} \left(n_\uparrow, n_\downarrow, \vec{\nabla} n_\uparrow, \vec{\nabla} n_\downarrow\right) n(\boldsymbol{r}) d^3 r \qquad \text{Eq. (2.25)}$$

where $\in_{XC} \left(n_\uparrow, n_\downarrow, \vec{\nabla} n_\uparrow, \vec{\nabla} n_\downarrow\right)$ is the exchange-correlation energy density and includes the spin density and the gradient of the spin density. This approximation is a variation of the Local Spin Density approximation (LSD) which corresponds with the incorporation of the spins to LDA.

However, the $\in_{XC}^{LDA} (n)$ and $\in_{XC}^{LSD} (n_\uparrow, n_\downarrow)$ (corresponding exchange-correlation energy density to LSD approximation) are well established to difference of $\in_{XC} \left(n_\uparrow, n_\downarrow, \vec{\nabla} n_\uparrow, \vec{\nabla} n_\downarrow\right)$. For that reason, there are different derivations of GGA to parameterize that term as an analytic function. More precisely, in our work we have used Perdew-Burke-Ernzerhof (PBE) GGA[30,31].

3. Molecular Beam Epitaxy (MBE) carbon solid-source

3.1 Introduction

Preparation methods of graphene are various: mechanical exfoliation of graphite[5,7], chemical reduction of graphene oxide (RGO)[32,33], Chemical Vapor Deposition (CVD)[34,35] or carbon segregation from volume[36], among others. Moreover, other innovative techniques have appeared as the case of the use of a mixer to obtain graphene in large quantities from a non-expensive mechanical method[37]. Some of them have clear advantages to others. For example, the CVD is easily up-scalable for industrial applications and the RGO method is adequate for wet chemistry techniques. However, these methods show some limitations too. For example, focusing on CVD, the graphene synthesis by decomposition of organic precursors depends on the catalytic properties of metallic substrates because they play a fundamental role during cracking processes of C–H bonds. Thus, a method with the possibility of growing graphene in a high-quality large-area and with a transfer-free process represents a significant advance in research.

That objective has inspired the use of a Molecular Beam Epitaxy (MBE) method to synthesize graphene on a surface. It allows in-situ characterization with surface science techniques as LEED, RHEED, STM, XPS in a highly controllable growth environment (growth rate, substrate type, substrate temperature, chamber pressure) that greatly help to understand the formation mechanisms of graphene[38,39]. .

Moreover, this methodology requires lower substrate annealing temperature than other reported methods[40–43]. For example, low-temperature MBE growth of Graphene on Copper has been reported by Meng Yu-Ling et al.[44] Their work shows atomic-resolution STM images of graphene on Copper between RT to 573K, demonstrating the capacity of this method to form graphene at low

temperatures. Despite that, the direct deposition of carbon atoms on a substrate using an MBE has rarely been reported[10,11,44–47].

Up to date, most articles report methods for synthesizing graphene using high temperatures of the substrates. Some of them employ a method similar to ours, using an electron beam evaporator, or a resistively-heated piece of graphite[42,43]. In these cases, the substrate has needed a temperature of 1223K. The use of these temperatures avoids it to be compatible with other processing techniques because the substrate temperature used is high. For example, the graphene made by decomposition of irradiated ethylene is formed annealing the substrate up to 1223K[40]. That temperature is close to the roughening transition temperature of the gold substrate used. Typically the roughening transition takes place at 0.75 times the bulk melting temperature. So for a gold single-crystal, where the melting temperature is 1337K, forming graphene by this method can easily produce a deterioration of the substrate. Another example is the decomposition of polycyclic aromatic precursors on platinum, which needs a temperature of 1000K in order to get graphene formation[41]. In contrast, the growth of graphene with our method requires a temperature around 823K for gold and 923K for platinum. This is a significant reduction in temperature.

Along with this dissertation, we prove the efficiency of growing graphene by using a MBE carbon source on various substrates with two main advantages added: a) to synthesize graphene on an insulating substrate independently of its catalytic properties; and b) the substrate temperature needed to grow graphene is significantly reduced.

3.2 MBE carbon solid-source assembly

The carbon solid-source[48] consists of a glassy carbon filament connected by two refractory metal bars (Tantalum in our case) to a DC source. The glassy carbon is a pure carbon material made of randomly oriented fragments of carbon planes as broken fullerenes[49]. This material has interesting properties as low oxidation rates, high chemical inertness and a resistivity 10 times bigger than graphite. This last property let us flow moderate electrical current[50] and makes it an ideal option for constructing heating elements[51]. Moreover, it is simple and easy to install in a UHV system, and the contamination drawback problems are reduced.

The main elements needed to mount it appear in Fig 3.1. The filament appearance has been cut from a glassy-carbon sheet of 0.3 nm by laser or water-jet cutting, so the shape and efficiency can vary.

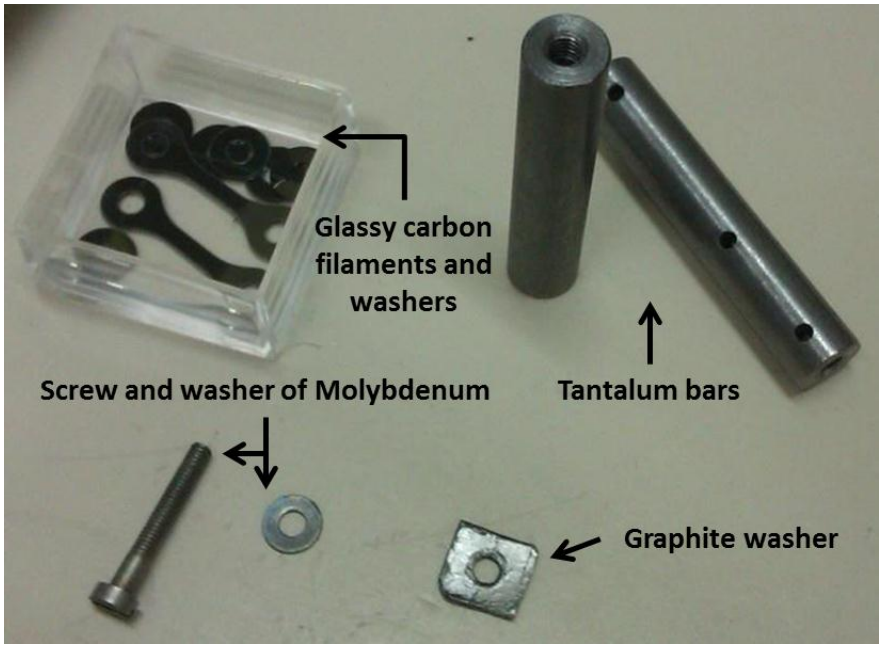

Fig 3.1: The different elements used in the carbon source assembly appear in the picture. All the elements used are made of refractory materials. The glassy carbon filament, molybdenum screws, molybdenum washers and graphite separators.

After assembly, the carbon source had an appearance as Fig 3.2. There, it is possible to identify the elements of Fig 3.1 in Fig 3.2a. The thermocouple was fixed to a tantalum bar, so the temperature is measured far from the filament. The carbon source length (from DN40CF flange to glassy carbon filament) is 300 mm. The long length allows for being close to the sample during sublimation. In our case, the separation between the sample and the filament is 20 mm. This is illustrated in Fig 3.3. We have used three fixing clamps to give mechanical stability to the evaporator (Fig 3.2b). We have used fiberglass in order to electrically isolate the clamps from the copper leads. The clamp (and its screw) closer to the carbon source is fabricated in tantalum to avoid degassing. The two others are made of stainless steel. We have used two consecutive edge-welded bellows with a total effective traveling length of 300 mm.

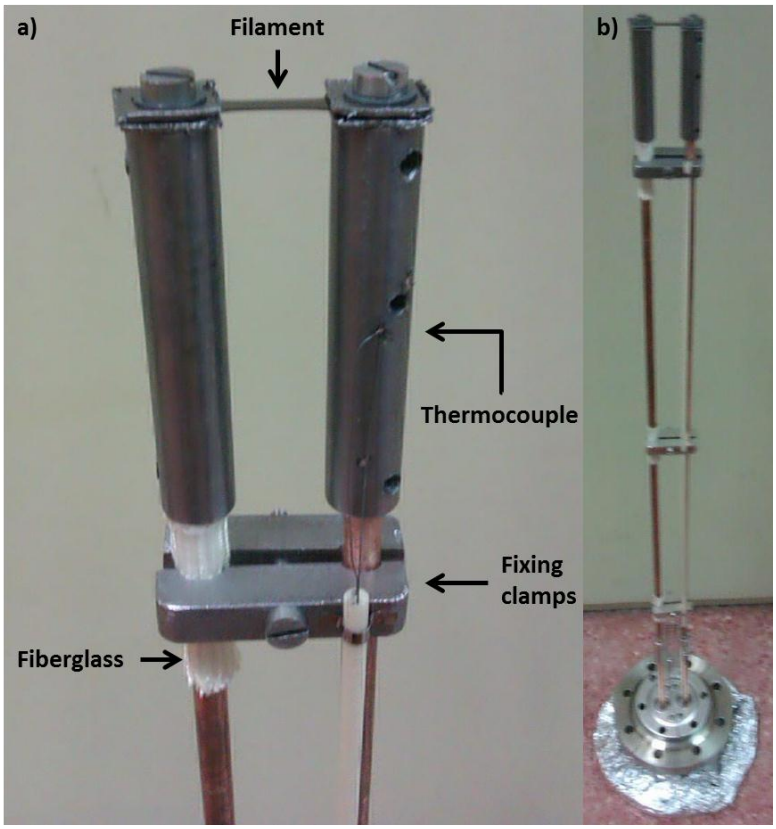

Fig 3.2: a) Image of the solid carbon source. The labels identify different components of it; b) The picture shows the whole source. It lets give an idea of the size.

The solid carbon source is a simple method to install in a UHV chamber not requiring any water cooling for filament working temperatures of 2273ºK. This is possible thanks to an approximately 10 time higher resistivity of glassy carbon vs. graphite. For example, commercially available carbon sources (SUKO cell from MBE-Komponenten) use currents in the 100-200A requiring complex vacuum and cooling system.

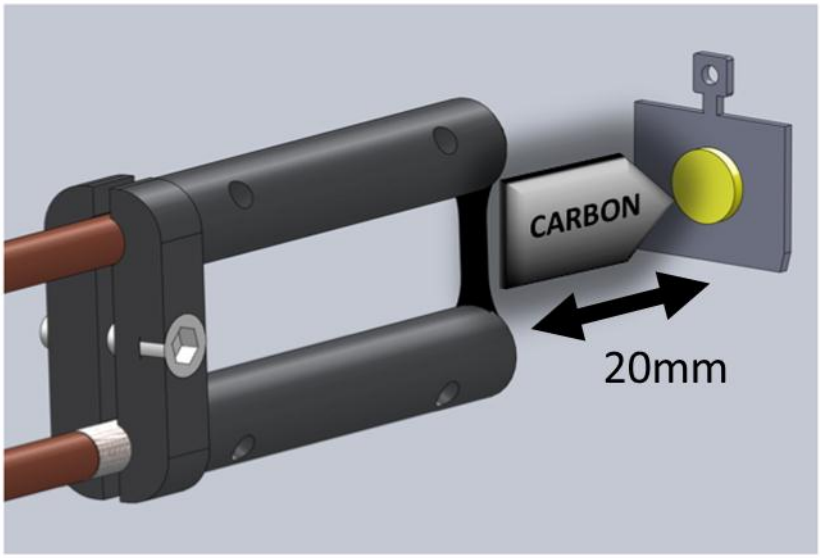

Fig 3.3: Scheme of the solid carbon source. There, it is possible to observe the head of the source at a distance of 20 mm from the sample holder with the shape of Omicron. Between them, an arrow indicates the direction traveled by carbon, from the filament to the sample.

3.3 Calibration and characterization of operating parameters.

Once the system is mounted into the ultra-high vacuum chamber, we have to perform a calibration to establish the parameters of the growth of graphene. The choice of parameters to the growth is an important issue, because they affect to the growth rate and the compounds sublimated from the filament (the glassy carbon filament is a mix of randomly oriented fragments of carbon compounds).

So first, we need to know what temperature is related to the current which we supply to the carbon filament. Then, it is important to determine the growth rate and which compounds are the main sublimated substances at various temperatures of the filament. The type of sublimated substances can affect to the quality of the graphene growth, in a way that a graphene growth by the sublimation of compounds with one or two carbon atoms can have less impurities than a graphene obtained from substances of three or four carbon atoms. Using a QMS we can study what species are sublimated at various temperatures. However, the sublimation of them depends on the specific latent heat, because that parameter determines the facility for a substance to be sublimated. Thus, to obtain a good characterization of our method and to know the conditions of our growth, we have done the curve of calibration current vs. temperature, the deposition rate vs. temperature and we have analyzed with the QMS the sublimation of different masses (a.m.u.) in a range of temperatures between 2200 to 2550 K approx.. Finally, we have calculated the specific latent heat (L) for sublimated main masses (a.m.u.).

We have calibrated the temperature of the filament vs. DC in two different systems (Fig 3.4). On one hand, we have measured the temperature of the carbon filament with a single color optical pyrometer (the adjusted emissivity value was 1.0, corresponding to the emissivity of a black body) in the Cyclope chamber in the ESISNA lab (ICMM). This calibration was done to the carbon source used in this thesis, and the range of current used is 5.5 A to 15.5 A (black squares). On the other hand, a calibration curve of current vs. temperature was performed in the MBE lab (IMM) using a dual-color optical pyrometer and a similar carbon source (the carbon source was assembled with the same characteristics as the Cyclope one). Here, the curve was performed in a current range between 8.0 A and 16.5 A (white squares).

A two-color pyrometer measures the radiation using two different wavelengths. Then, it calculates the ratio from the signals, and finally determines the temperature. When forming the ratio, the emissivity is eliminated as part of the calculations; in other words the temperature measurement becomes independent of the emissivity of the object. The wavelengths are close together in order to equalize, as much as possible, emissivity (for example 0.95 μm and 1.05 μm). The output signal will not change when the object does not fully cover the spot size, or when the UHV window becomes slightly covered with carbon, providing they occur equally in both wavelengths. If the emissivity is different at the two wavelengths, then it is possible by setting the ε-slope to give an input to the instrument of the ratio of the emissivity at the two wavelengths.

In Fig 3.4, it is possible to observe a difference between the temperatures for the same current range. The difference between them is 115 K on average. For example, at 14 A (the current used in the sublimations for growth graphene), the temperature for the infrared pyrometer is lower than 2273K (it is 2203K), and the temperature for the dual-color pyrometer is 2289K. However, considering that both curves were performed in two different systems, and using two different pyrometers, we can conclude that the temperature difference is not high.

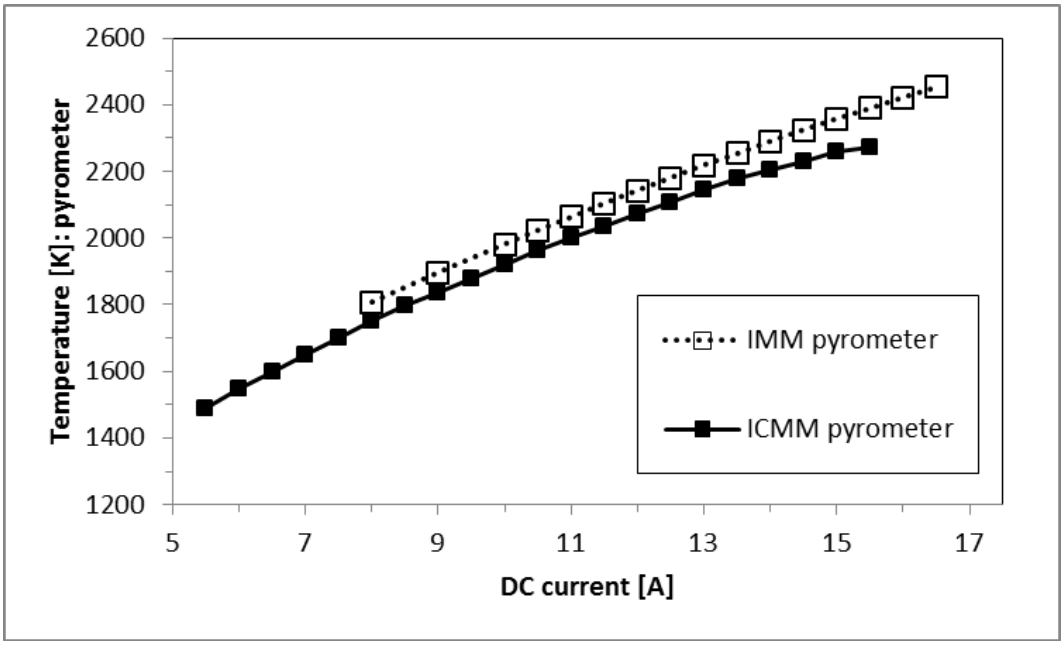

Fig 3.4: Calibration of the temperature *vs. DC in two different labs. The ICMM pyrometer (black squares) corresponds to a one-color pyrometer with the emissivity adjusted to 1.0 (black body), and took the temperatures between 5.5 A and 15.5 A. The IMM pyrometer (white squares) corresponds to a dual-color pyrometer and the current range varies from 8 A to 16.5 A.*

Before starting to growth graphene on a surface, it is needed to forming the carbon filament for working conditions. This process consists of a reshaping of the filament and the remove of material, and it requires heating the filament above the temperature of the working conditions. In Fig 3.5 we show a SEM (scanning electron microscopy) image of the filament before (a) and after (b) of the tuning forming. Both images were measured with the same parameters and correspond to the same scale (the parameters can be observed below each one). Fig 3.5a corresponds to the filament with the commercial appearance and it seems flat. However, Fig 3.5b shows an appearance completely different and very porous. This image is taken after the filament is annealed between 2600 K-2800K.

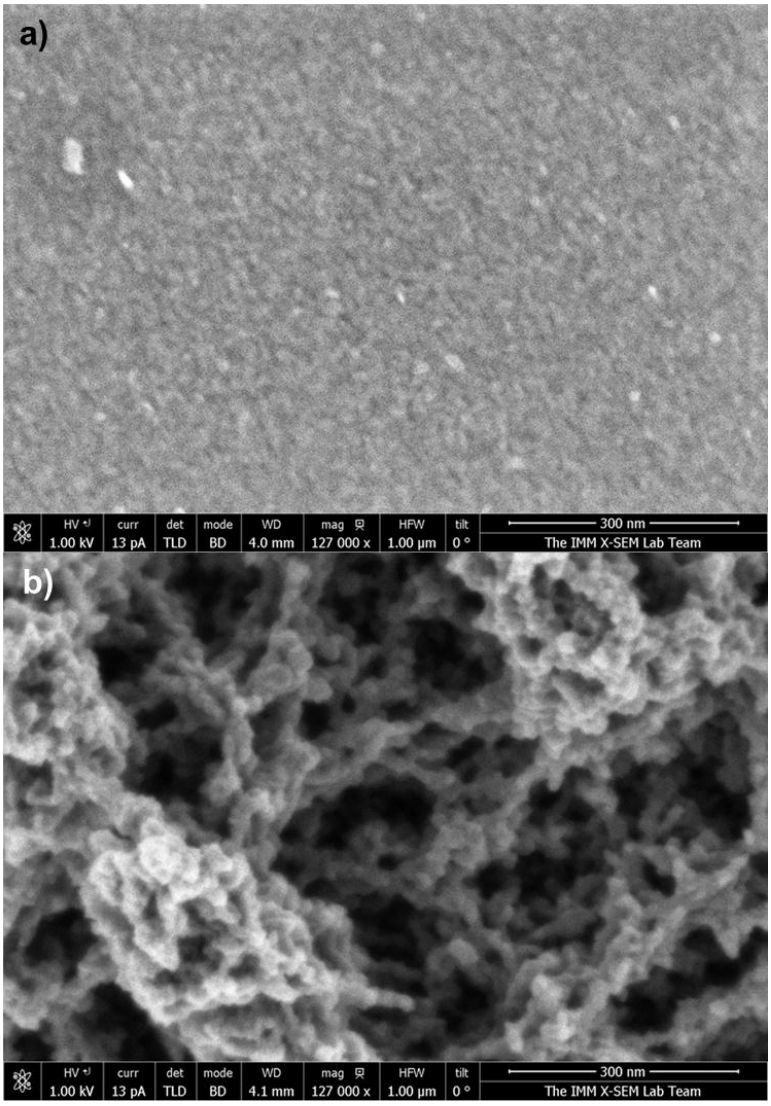

Fig 3.5: SEM images of the glassy carbon filament before annealing a) and after annealing b). The surface of the filament seems flat before annealing and very porous after that.

Another important point is to know the deposition rate at various temperatures. We have done a graph of deposition rate vs. temperature (Fig 3.7) with a mix of data obtained from the ESISNA and the MBE laboratories. These data is obtained in a different way, so it is necessary to explain them first.

In the Cyclope chamber (ESISNA lab), we estimate the amount of material deposited on a surface using the STM images. A good estimation is easier to

realize when the material deposited on a surface is less of a monolayer. Comparing several images of different parts of the surface, we can obtain an average of the amount of deposition.

However, the estimation of the deposition rate in the MBE lab is different. First, we have used a polished silicon wafer as a substrate. In the middle of the surface, we have put a reversed strip of silicon (the polished face against the surface) to act as a shadow mask. This is illustrated in Fig 3.6a. Then, we sublimate carbon material using the carbon source. Finally, we remove the mask and we use an AFM to estimate the height of the step between the part of the surface with sublimated material and the part covered by the mask (Fig 3.6. That height let us estimate the amount of material sublimated on the surface.

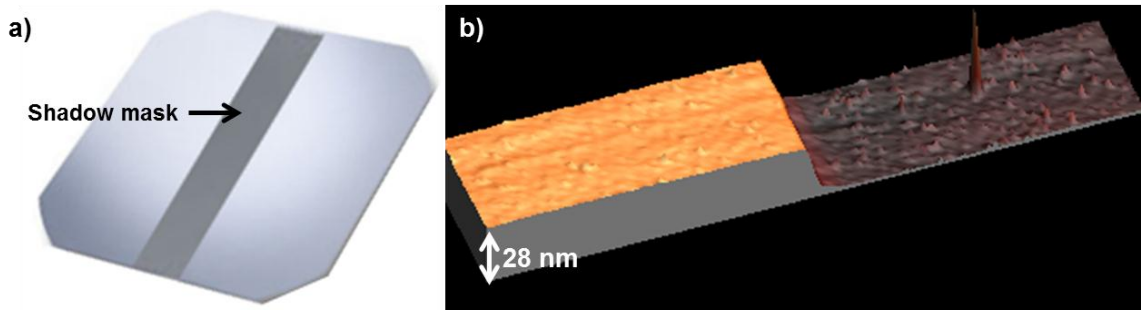

Fig 3.6: a) Illustration of a silicon wafer with a shadow mask on it. The shadow mask is a reversed strip of silicon with the unpolished face up; b) AFM image of the step between the silicon surface with carbon material sublimated (clearer part) and the silicon part covered by the mask during sublimation (darker part). In that case, the height of the step is of 28 nm.

These estimations let us obtain the Fig 3.7, where the point at lower temperature was obtained in the ESISNA lab and the two ones at the higher temperatures were performed in the MBE lab using the shadow mask. Trying to reproduce the same conditions in both laboratories, the sample was placed at 20 mm from the filament of the carbon source during sublimation. In the graph,

it can be seen that there is a relationship, such that a higher temperature increases the deposition rate.

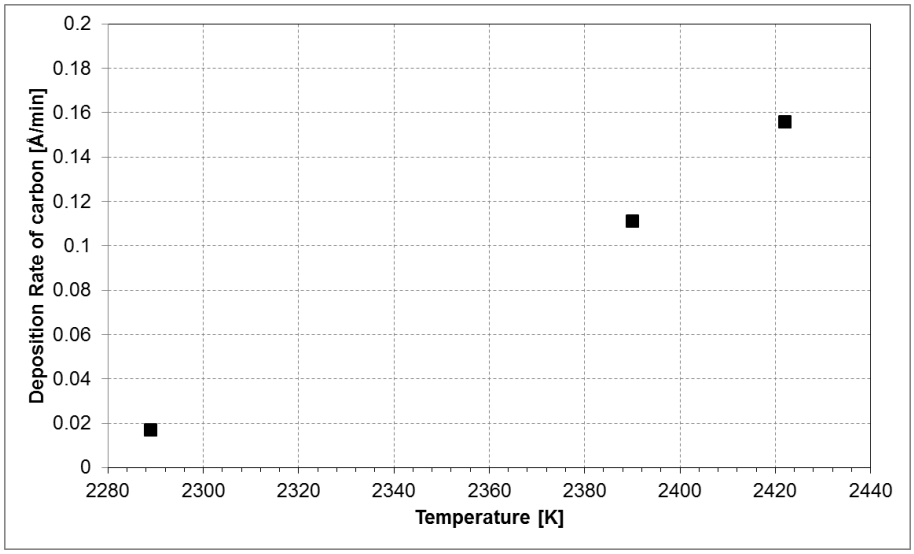

Fig 3.7: Experimental values for the deposition rate of carbon at different temperatures. In the three cases, the sample was placed at 20 mm. The experimental values indicate a relationship between the deposition rate of carbon and the temperature. The deposition rate at lowest temperature was measured at ESISNA lab (ICMM-CSIC) and the other two points were measured at MBE lab (IMM-CSIC).

In consideration of these calibrations, then, we have varied the DC from 18.5 A (2567K) to 13.5 A (2254K) staying in each one for 40 seconds approx. to observe the behavior in a residual gas analyzer (QMS). We have selected atomic equivalent masses (a. m. u.) that are multiples of the atomic mass of carbon: 12 (1C), 24 (2C), 36 (3C), 48 (4C) and 60 (5C) (Fig 3.8). In the Fig 3.8 is plotted the partial pressure (ion current) of the selected masses respect to the time. We observe a stair-like behavior (Fig 3.8) in which each step correspond to a DC current value. The supplied DC in each moment to the carbon source is indicated on the figure. We can observe as the carbon source sublimates a stable rate of each carbon masses at different DC and, the higher masses have a lower sublimation rate. In such a way, the masses 48 and 60 are overlapped in the low part of the graph. This stair-like behavior is observed in several

masses related with carbon, even the masses 48 and 60 (it is possible observe in a zoom). On the other hand, the Fig 3.8 exhibits as the atomic mass of carbon is the mass with highest partial pressure in all DC range, followed by 24 and 36.

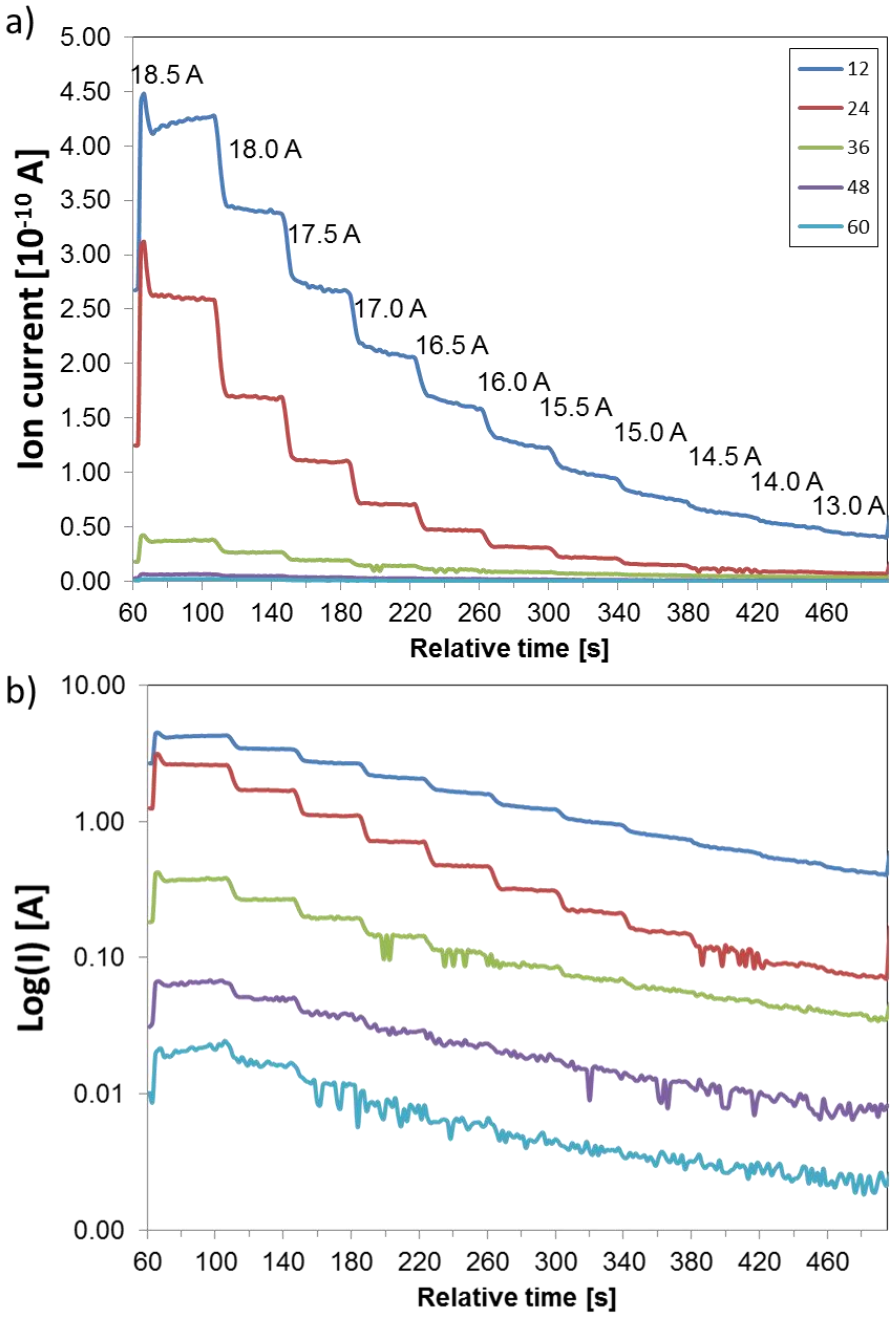

Fig 3.8: a) Comparison of the partial pressure of multiples of the atomic mass of

carbon. The 48 a.m.u. and the 60 a.m.u. are stacked near the relative time axe, so they are difficult to observe; b) The same graph of (a) at logarithmic scale. There, the behavior of the masses with lower partial pressure is easier to observe. To perform these graphs, the DC is varied in a range between 18.5 A to 13.5 A in steps of 0.5 A for 40 seconds approx. The DC used in each step is indicated on the figure (a) because the steps are more accentuated. The masses show a behavior like a stair.

After the general analysis of Fig 3.8, we have focused on the different sublimated masses at each temperature. With this objective, we have used a range between 2217 K (13 A) and 2540 K (18 A) and we have focused on the masses of pure carbon compounds from 1C (12) until 6C (72) (Fig 3.9). In the comparison between them, the mass of atomic carbon increases too much at higher temperatures in respect to the other masses. The mass related to two carbon atoms can be easily identifiable too. It increases, but less than atomic carbon. The other masses, however, are stacked in a low range of the ion current. For that reason, each one is plotted below separately keeping the markers. There, it is possible to observe that the bigger masses (60 or 72 a.m.u.) show a partial pressure at a lower scale than the smaller ones (12 or 24 a.m.u). This fact indicates that the compounds formed by more number of carbon atoms are harder of sublimate.

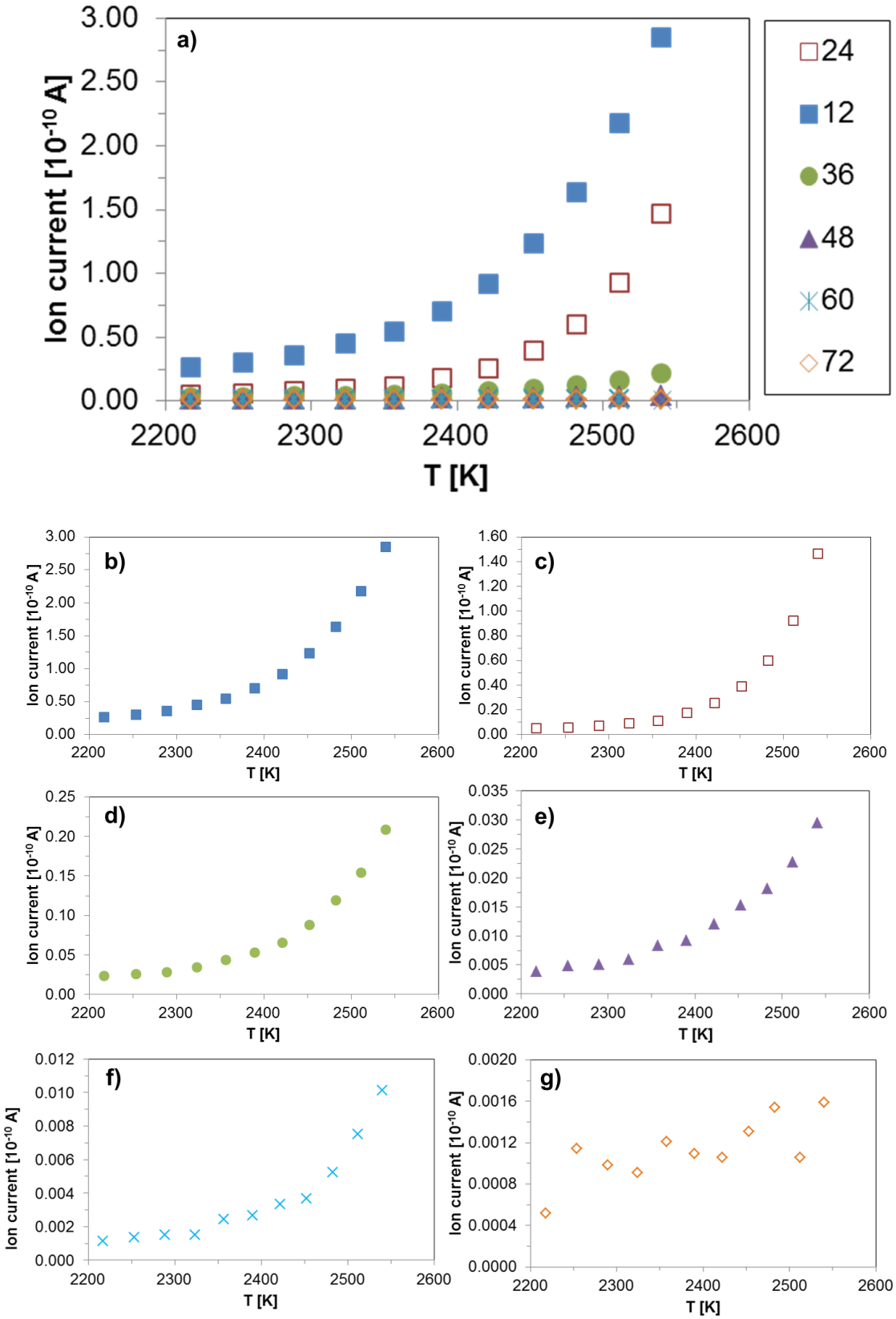

Fig 3.9: a) Partial pressure of various substances made of carbon atoms vs T are

showed at the left side. Below, every mass is plotted independently((b)-(g)). The markers are the same for every mass in both parties for better identification. The values of the masses in the legend correspond to a.m.u.

For a better comparison, we sum the ion currents of these six species as the total of the evaporation, so we can establish the relative percentage of presence in respect of the other five of everyone at a specific temperature. Thus, we have realized the table of Table 3.1 using two different temperatures, 2289.5K and 2540.4K. The first corresponds to a DC of 14 A, that is the temperature used for graphene growths, and the second is the higher temperature used in Fig 3.9. It corresponds to a DC of 18 A.

At 14 A, the atomic carbon is the 77.5 % of the sublimated species with respect to the other carbon species, however, at 18 A, the rate proportion decreases to 62.4 %, despite observing the higher level of sublimation in Fig 3.9a. Furthermore, two carbon atoms have an inverse behavior, this rate increases with the temperature. The other four species reduce their percentage, so at 14 A, we are mainly sublimating monoatomic carbon, and at 18 A, two-thirds is monoatomic carbon, and one-third is two carbon atoms.

Temperature [K] / Masses [a. m. u]	12	24	36	48	60	72
2289.5	77.51 %	14.56 %	6.26 %	1.12 %	0.33 %	0.22 %
2540.4	62.40 %	32.10 %	4.60 %	0.65 %	0.22 %	0.03 %

Table 3.1: Percentage of every mass made of carbon respect to the others at two different temperatures: the temperature used to growth graphene and the highest temperature used with this method.

Apart from these masses, there are other ones very presents during sublimation. They can be collected in two groups: molecules with one carbon atoms and molecules with two. The molecules with one carbon are formed by a

carbon with hydrogen or oxygen atoms. That is the case of the masses: 13 (CH), 14 (CH_2), 15 (CH_3), 16 (CH_4), 28 (CO) and 44 (CO_2). The 28 mass is particular because it can correspond to two different molecules: CO and C_2H_4 so, it can be added to the two groups. Furthermore, it has one of the most intensity signals. In the group of two carbon atoms are selected the masses of 25 (C_2H), 26 (C_2H_2) and 28 (C_2H_4). Other compounds have not been collected because their signal was pretty low. However, some of them are gathered in the table (Table 3.4) at the end of this chapter, which their percentage of presence is showed with respect the whole of the signal obtained by the sum of all masses. The threshold used to be collected there has been to have at least a 0.1% of presence at some temperature.

In Fig 3.10 two graphs are showing the ion current signal of species with one carbon atom (Fig 3.10a) and two (Fig 3.10b). The main mass is 28 in both cases, but surely it has a contribution from two different compounds (CO and C_2H_4). Beyond this, in the first graph, the mass for atomic carbon is the one that increases the most, and the mass of CH_4 (16 a.m.u.) keeps one of the highest levels of the signal during all sublimation and showing a different behavior than the other masses: it does not increase as the temperature does. In fact, the signal decreases at the highest temperatures. It is due because this a. m. u. (16 a.m.u.) is the same for CH_4 and atomic oxygen, so it has two different contributions (as the case of 28 a.m.u). Despite realizing the experiment in an ultra-high vacuum chamber, there are some masses usually remains (hydrogen, water, oxygen). At the experiment conditions (pressure and temperatures), the atomic oxygen contribution is higher than the quantity of sublimated CH_4, so the corresponding curve has an entirely different appearance.

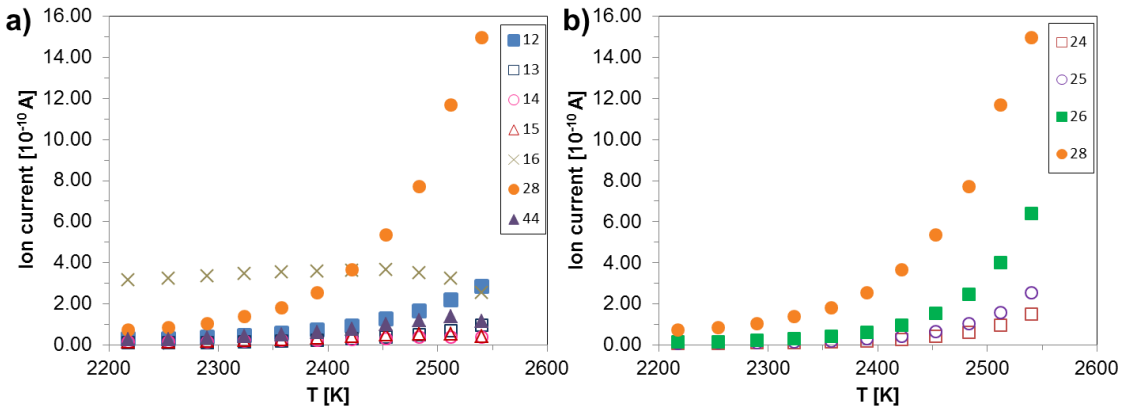

Fig 3.10: a) Partial pressure of different substances formed by one carbon (C = 12 a.m.u.), one carbon atom combined with hydrogen atoms (CH = 13 a.m.u., CH_2 = 14 a.m.u., CH_3 = 15a.m.u., CH_4 = 16 a.m.u.), or one carbon with oxygen atoms (CO = 28 a.m.u. and CO_2 = 44 a.m.u.) at different temperatures; b) In this case the four compared masses are made of two carbon (C_2 = 24 a.m.u.) or compounds formed by two carbon atoms and hydrogen atoms (C_2H = 25 a.m.u., C_2H_2 = 26 a.m.u. and C_2H_4 = 28 a.m.u.). The species formed only by one and two carbons are added respectively for a better comparison. In both cases, the values of the legend correspond to the masses in a.m.u. The mass of 28 a.m.u. appears in two graphs because it has the contribution of two different substances (CO and C_2H_4)

In Fig 3.10b, all masses show the same behavior but a different scale. C_2 has the lowest signal, so we are sublimating more quantity of another species as C_2H and C_2H_2 than two carbon atoms (C_2).

To allow better comparison of the presence of the different compounds, Table 3.2 collects the relative percentage of the masses of Fig 3.10 at two different temperatures: 2289.5K (the temperature used for growth of graphene) and 2540.4K (the highest temperature we used). That percentage of presence is respect to the other masses of the group; it means we consider that the 100% is the sum of the ion current signal of the species in Fig 3.10a in one case, and in Fig 3.10b in the other.

In Table 3.2a at 2289.5K, the main mass is 16 (CH_4) as we observe in Fig 3.10a, and it has a different behavior than other masses, 28 is almost the 20%, and atomic carbon represents the 6% approx. However, at the higher temperature, the presence of CH_4 decreases a lot indicating that the quantity of 28 and 12 have risen much (because CH_4 keeps a steady signal). Atomic carbon has duplicated the relative presence, and 28 mass is the 65%. CH increases in a lower scale, from the 2% until the 4% and 14, 15 and 44 show a relative presence more constant. The percentages decrease slightly, but they show in Fig 3.10a a behavior of rising.

In Table 3.2b, 28 a.m.u. predominates at all temperatures, but it has almost a 15% of relative presence less at 2540 K than at 2289 K, however, the 26 mass (C2H2) increases the percentage of relative presence at the highest temperature (it increases around a 12%). The other two masses (24 and 25) enhance their relative presence a little too.

A: Species of one carbon atom							
Temperature [K] / Masses [a. m. u]	12	13	14	15	16	28	44
2289.5	6.54 %	1.83 %	2.45 %	2.92 %	61.74 %	18.94 %	5.58 %
2540.4	12.29 %	4.04 %	1.56 %	1.69 %	10.84 %	64.65 %	4.93 %

B: Species of two carbon atoms				
Temperature [K] / Masses [a. m. u]	24	25	26	28
2289.5	4.84 %	6.70 %	13.73 %	74.73 %
2540.4	5.77 %	9.98 %	25.21 %	59.04 %

Table 3.2: a) Percentage of every mass formed by one carbon and hydrogen or oxygen atoms respect to the others at two different temperatures; b) Percentage of the presence of different substances with two carbon atoms respect to the total of themselves.

The Ion current vs. Temperature curves can be used to obtain the specific latent heat for these masses. The specific latent heat (L) of a substance is the needed energy required to produce a phase change in heat form (Q). It characterizes that mass and does not depend on the shape, size or extend of the sample. We can obtain that property using the Clausius-Clapeyron relation, which is used to describe a phase transition between two states of the matter of substance. This relation has huge importance because it allows determining the vaporization enthalpy at a specific temperature with the slope of the saturation curve (Eq. 3.1) in a pressure - temperature diagram.

In our case, every mass change from a solid state as a constituent of the glassy carbon filament to a gas phase into the UHV chamber. On a pressure-temperature diagram as above (Fig 3.9, Fig 3.10), this relation let us obtain the slope of the tangents to those curves:

$$\frac{dP}{dT} = \frac{L}{T\Delta v} \qquad \text{Eq. 3.1}$$

Where dP/dT is the slope of a curve in a pressure-temperature diagram, L is the specific latent heat, T is the temperature and Δv is the specific volume change of the phase transition.

The Eq. **3.1** can be re-written for transitions between a condensed phase and gas as

$$ln\, P = -\frac{L}{R}\left(\frac{1}{T}\right) + c \qquad \text{Eq. 3.2}$$

Where L is the specific latent heat of sublimation, R is the gas constant; c is a constant and the relationship between lnP and 1/T is linear so, L/R corresponds to the slope of that regression.

This way, we have calculated the specific latent heat of sublimation (L) (Table 3.3.) for the collected masses in Table 3.4 (masses with a presence more than the 0.1% of the total ion current) with some exceptions. We have excluded some masses attending three reasons: 1. the presence is not due to the heating of the glassy carbon filament: molecular hydrogen (2), OH^- (17), water (18), molecular oxygen (32); 2. The ionization surely is realized in the QMS filament: C^{2-} (6) and O^{2-}(8); and 3. The mass is not related to the source: masses 19 and 20. On the other hand, we have included other masses in Table 3.3, and they do not have more than 0.1% of presence at some temperature. That is the case of C_4 (48), C_5 (60) and C_6 (72). We compare their behavior above, and it is good to know the needed energy to change the phase from solid to gas of these three species.

Mass [a. m. u.]	**12**	**13**	**14**	**15**	**16**
Substance	C	CH	CH_2	CH_3	CH_4 / O
Marker in Fig 3.10	■	□	□	□	
L [eV/K]	3.68	3.99	1.98	2.46	-0.09

Mass [a m. u.]	**24**	**25**	**26**	**7**	**29**	**30**
Substance	C_2	C_2H	C_2H_2	C_2H_3	C_2H_5	C_2H_6
Marker in Fig 3.10	●	○	○	○	○	○
L [eV/K]	5.29	5.73	6.17	2.60	2.82	2.79

Mass [a. m. u.]	**36**	**37**	**38**	**39**	**41**
Substance	C_3	C_3H	C_3H_2	C_3H_3	C_3H_5
Marker in Fig 3.10	♦	◊	◊	◊	◊
L [eV/K]	3.32	.14	2.24	2 2	2.36
Mass	**48**	**60**	**72**	**28**	**44**

[a m. u.]					
Substance	C_4	C_5	C_6	CO / C_2H_2	CO_2
Marker in Fig 3.10	▲	×	+	*	*
L [eV/K]	3.05	3.20	1.02	4.79	2.94

Table 3.3.: The table shows the values of the latent heat of sublimation for different masses. Moreover, they are related to the formulas of their corresponding substances and the markers of Fig 3.11.

On the other hand, we can deduce from the Latent heat values that the masses with higher L will need more energy to be sublimated. So, the cases with a negative values indicate that there are sublimated spontaneously and they do not need external energy.

The specific latent heat of sublimation (L) is plotted in Fig 3.11 for a better visualization. The marker of every mass is indicated in Table 3.3. The mass of 16 does not have a marker because it is not included in Fig 3.11. As we observe in Fig 3.10a, the behavior of that mass is completely different to the others because it has the contribution of CH_4 and atomic oxygen. Atomic oxygen is not produced by the carbon source, so it keeps practically constant its level of partial pressure. Thus, the slope of the curve to obtain L is negative; as it is indicated above, it means this mass does not need external energy to change from solid to gas, and it is according to the Fig 3.10a where that mass has a pretty high partial pressure at any temperature.

The masses for four (48 a. m. u.), five (60 a. m. u.) and six (72 a. m .u) carbon atoms do not have big values of the latent heat of sublimation (L) so, they are substances easy to sublimate. However, their partial pressure is low. Thus, we conclude that the glassy carbon filament does not produce them in a significant quantity.

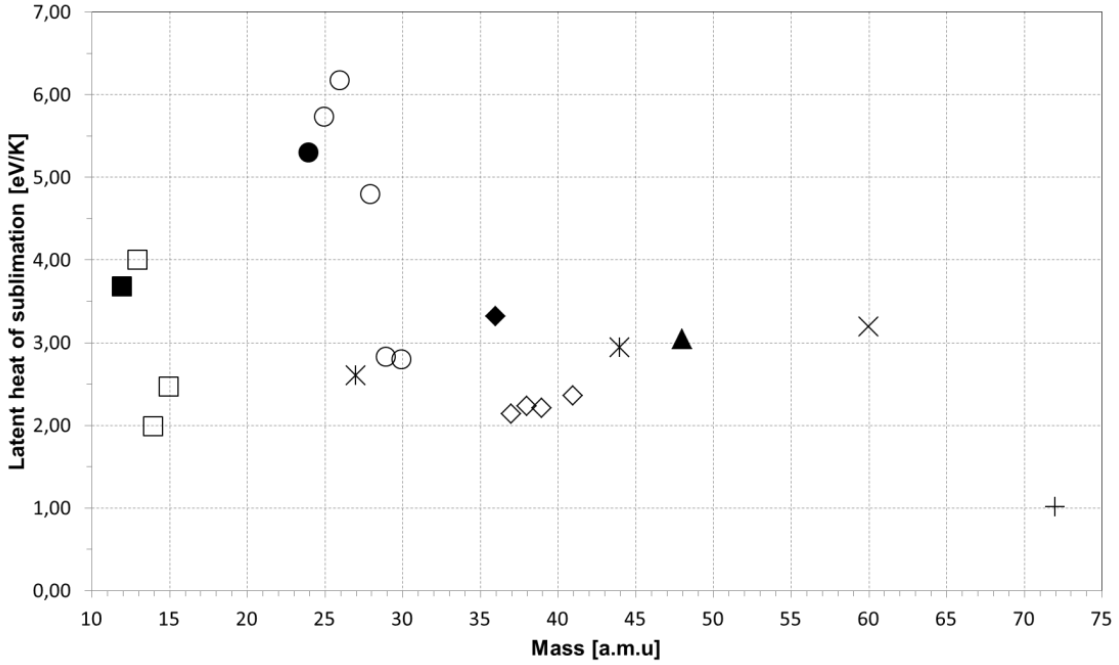

Fig 3.11: Representation of the latent heat of sublimation for different masses (these values are collected in Table 3.3). A low value of L indicates that mass needs less energy to change from solid phase to gas.

In fact, the masses formed by only carbon atoms (1C-6C) have a lower value of latent heat of sublimation as the number of carbon atoms increases; with two exceptions, two carbon atoms which have a pretty high value of L, and five carbon atoms with a L value a little higher than the one for four carbon atoms, so it appears slightly out of the tendency line.

The substances with two carbon atoms are the hardest to sublimate, especially for those with less number of hydrogen atoms (25-27 a. m. u.). Accordingly, the percentage of presence of these masses increase at the highest used temperature (2540K; Table 3.4).

On the other hand, the species with three carbon atoms (37-41 a. m. u.) show a very similar and low value for L, but their percentages are low too (Table 3.4).

The percentages of Table 3.4 and their values for latent heat of sublimation give us relevant information. It helps to conclude that the glassy carbon filament mainly sublimates substances with one and two carbon atoms, but moreover, it has in smaller quantities other different substances with a higher number of carbon atoms.

Several works about the vaporization of Carbon have characterized the sublimation of graphite or carbon molecules[52–56] with different techniques. In these cases, the temperatures used during sublimation are between 2400 K and 3000 K and the main and analyzed masses are C_1, C_2 and C_3. Our analysis is performed at lower temperatures (between 2217 K and 2540 K), but we find a similar behavior of the heats of vaporization. For example, the latent heat value is highest for C_2[54,55]. In another hand, we obtain that there are many different masses than C_1, C_2 and C_3 that has allowed us to make a more complete comparison.

Temperature [K]/Mass [a. m. u]	Percentage of presence [%]																							
	2	6	8	12	13	14	15	16	17	18	19	20	24											
2540.45	8.40	0.15	0.09	3.61	1.19	0.46	0.50	3.19	11.13	33.45	0.38	0.10	1.86											
2512.18	8.35	0.09	0.10	2.58	0.79	0.43	0.63	3.83	14.52	41.51	0.56	0.12	1.09											
2483.02	8.15	0.07	0.12	2.06	0.62	0.42	0.63	4.40	16.72	46.67	0.70	0.14	0.75											
2452.98	7.83	0.06	0.15	1.64	0.47	0.39	0.61	4.83	18.41	50.17	0.80	0.13	0.52											
2422.06	7.50	0.05	0.15	1.31	0.38	0.37	0.55	5.20	19.80	52.64	0.88	0.15	0.36											
2390.25	7.29	0.04	0.18	1.09	0.31	0.34	0.48	5.59	20.93	54.00	0.93	0.14	0.27											
2357.55	7.08	0.03	0.17	0.92	0.25	0.31	0.42	5.96	21.73	55.01	0.94	0.14	0.18											
2323.97	6.93	0.03	0.19	0.81	0.20	0.29	0.38	6.28	22.45	55.35	0.96	0.15	0.16											
2289.51	6.83	0.02	0.21	0.70	0.20	0.26	0.31	6.64	23.01	55.57	0.95	0.15	0.13											
2254.15	6.73	0.02	0.26	0.64	0.17	0.26	0.29	6.99	23.56	55.41	0.92	0.15	0.12											
2217.92	6.68	0.03	0.24	0.60	0.16	0.27	0.24	7.25	23.88	55.33	0.92	0.15	0.10											

Temperature [K]/Mass [a. m. u]	Percentage of presence [%]																							Total Ion current signal [10^{-10} A]
	25	26	27	28	29	30	32	36	37	38	39	41	44											
2540.45	3.21	8.12	0.71	19.01	0.58	0.14	0.10	0.27	0.18	0.13	0.33	0.28	1.45	78.49										
2512.18	1.87	4.74	0.63	13.89	0.52	0.11	0.09	0.18	0.15	0.12	0.29	0.26	1.61	83.84										
2483.02	1.26	3.09	0.57	9.71	0.45	0.09	0.08	0.15	0.13	0.11	0.28	0.24	1.49	78.98										
2452.98	0.85	2.02	0.52	7.13	0.39	0.08	0.08	0.12	0.12	0.11	0.25	0.21	1.30	74.68										
2422.06	0.58	1.36	0.47	5.21	0.34	0.06	0.08	0.10	0.11	0.09	0.23	0.17	1.07	69.32										
2390.25	0.41	0.91	0.42	3.94	0.30	0.06	0.08	0.08	0.10	0.08	0.21	0.15	0.92	63.84										
2357.55	0.29	0.65	0.37	3.04	0.26	0.05	0.08	0.07	0.10	0.08	0.20	0.16	0.78	58.88										
2323.97	0.22	0.49	0.34	2.48	0.22	0.05	0.08	0.06	0.09	0.08	0.19	0.15	0.70	54.80										
2289.51	0.18	0.37	0.30	2.04	0.22	0.04	0.08	0.06	0.09	0.07	0.17	0.13	0.60	50.07										
2254.15	0.16	0.30	0.28	1.80	0.19	0.04	0.09	0.06	0.08	0.06	0.16	0.13	0.54	46.05										
2217.92	0.14	0.27	0.25	1.62	0.18	0.04	0.08	0.06	0.08	0.06	0.15	0.12	0.51	43.24										

Table 3.4: The table summarizes the percentages of the masses with more quantity than 0.1% respect to all masses for the temperatures between 2217.92K and 2540.45K. The total pressure for each temperature is indicated.

4. Graphene on metals

4.1 Introduction

The growth of graphene on transition metal substrates is a well-studied subject[57–61]. The catalytic properties of this type of substrates help the growth of graphene with a high structural quality. Even among the methods that employ a catalytic effect to synthesize graphene, it can be found that the graphene/metal interface interaction depends strongly on the substrate material. For example, meanwhile a deep modification of the electronic structure occurs on G/Ni(111)[62,63] and on G/Ru(0001)[64,65] almost no interaction is present of G on Ir(111)[66,67]. This variety of G-on-metal properties shows the relevance of studing in detail several metals. In some cases, it has been proposed that the hybridization of carbon with the metal can affects contact transmittance [68,69] or produce local doping of graphene[70,71]. In all these cases, graphene has been grown using CVD or deposition of aromatic precursors and its properties and interaction with the substrate has been well studied. All these previous works have led to the first attempts to graphene synthesis by MBE have been made on metals, as a natural way of comparing the differences in the results obtained with this new method and others well established.

Among the metal substrates, Copper and Nickel are commonly used in the literature for the growth of graphene by CVD. In Fig 4.1 we show all transition metals, and we have highlighted with blue circles the substrates used more often[40,42–44,61,62,65,67,72–79].

As it is apparent in Fig 4.1 the most popular substrates correspond with the most electronegative atoms. The electronegativity is the chemical property that describes the tendency of an element to attract electrons. In Fig 4.1 we show Pauling's values (an adimensional number). It is observed that substrates employed for CVD have an electronegativity value 1.9 or higher. We have chosen to grow G, among the transition metals, on two materials showing

higher electronegativity (Pt and Au), taking advantage of the hexagonal symmetry of their (111) surfaces.

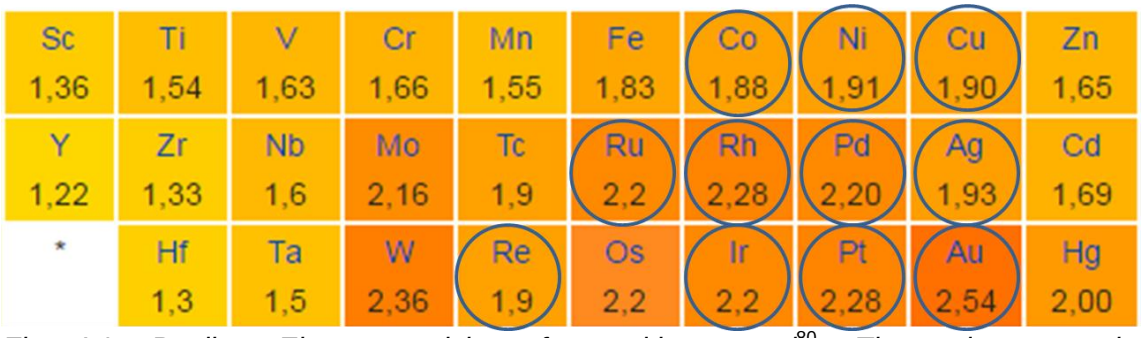

Fig 4.1: Pauling Electronegativity of transition metal[80]. The colors are in correspondence with the number in such a way the higher numbers are darker and more electronegativity elements than elements with brighter and lower numbers. All the elements surrounded by blue circles correspond to substrates reported in the literature used to grow graphene on them.

While platinum (111) has been commonly used to grow graphene[41,57,79,81–88], not so many works can be found using gold (111)[40,42]. A possible reason is that during growth of graphene on a metal by CVD, the appropriate conditions for cracking the precursor molecules (C_2H_2 or CH_4,) require the use of a high substrate temperature. For example, a gold single-crystal needs to be annealed to temperatures close to its roughening transition (Note: Roughening transition means a transition from smoothness to roughness undergone by a surface of a crystal when the temperature exceeds a certain critical value). The temperature for a roughening transition to occur T_R is a fraction of the bulk melting temperature T_B. It is commonly accepted that $T_R \approx 0.75 \cdot T_B$. So, the temperature of the roughening transition is for gold $T_R \approx 1073$ K and for platinum $T_R \approx 1598$ K. For example the formation of graphene on Au(111) by decomposition of ethylene[40] or using an electron beam carbon evaporator[42] requires that the substrate is annealed at 1223 K, a temperature clearly above T_R, that can easily let he gold single crystal surface to become amorphous..

However, as we will explain in the third chapter, one of the main advantages of the MBE method developed in this thesis is that graphene can be grown at much lower temperatures.

4.2 Graphene on platinum (111)

The platinum surface cleaning procedure is described in section 2.6.1. The process of growing graphene on platinum has been described in subsection 2.8.1. Sample's exposure to the carbon beam was 30 minutes. Simultaneously, the sample was annealed at 923 K. However, the procedure works equally well if the sample is annealed after growth. The temperature was measured using a commercial one-color IR pyrometer.

After growth, the LEED pattern (Fig 4.2) shows a distinctive graphene ring (near the corners of the black hexagon) surrounding the spots corresponding to the Pt(111) surface (blue hexagon). The lattice constant of the platinum is 2.75 Å and of the 2D rhombohedral unit cell of graphene is 2.46 Å. Therefore, in reciprocal space, the graphene spots appear at a larger distance than the platinum ones, as it is seen in the figure.

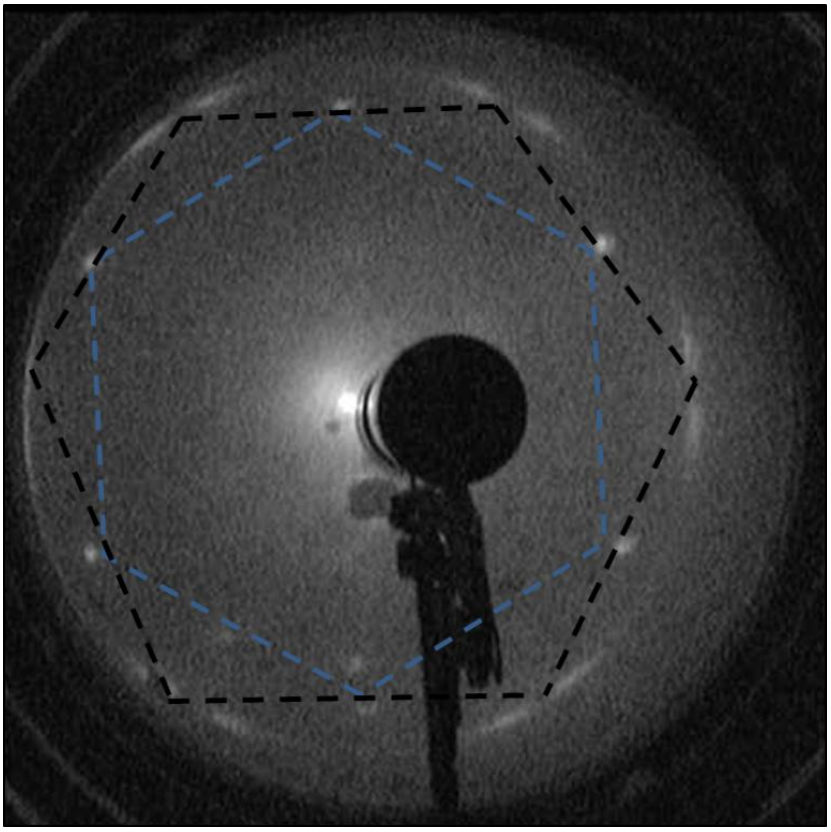

Fig 4.2: LEED pattern taken at 57.4 eV of a Pt (111) crystal after deposition during 30 min. of carbon from a MBE source. Spots related to Pt(111) form the characteristic hexagonal pattern (blue dashed hexagon) surrounded by a discontinuous ring marked by the black dashed hexagon corresponding to graphene.

The presence of a ring corresponding to graphene indicates the formation of graphene domains rotationally disordered respect to the substrate. Furthermore, it is discontinuous with some spots brighter than others indicating some preferential orientations. In this case, the ring is brighter in places forming an angle of 19° with respect to the platinum spots. Therefore, this angle is the dominant orientation of the graphene patches. This result is in good agreement with the literature[81].

Additionally, the AES spectra provide an independent verification of the existence of carbon on the surface (Fig 4.3). We observe a new peak at 272 eV; this value corresponds to the energy position of the highest intensity peak for

carbon. The main intensity peaks for platinum are in the energy values of 43eV, 64 eV, 168 eV and 237 eV, so they are far away enough from the main energy value for carbon.

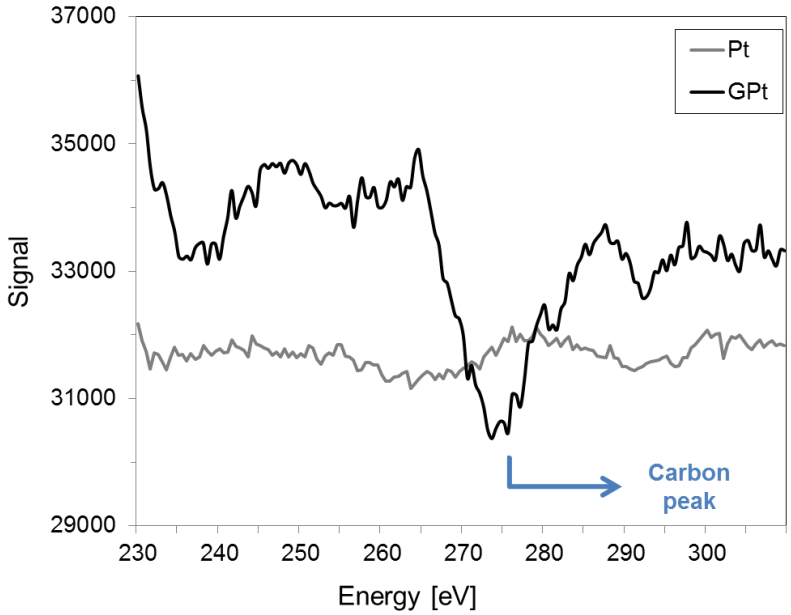

Fig 4.3: Comparison between the AES spectra for clean Pt (111) surface (gray line) and platinum after growth (black line). The gray line shows a flat tendency, however, the black line exhibits a peak in the region of 272 eV in correspondence with the value of the Carbon peak.

STM images show extensive areas of the surface covered by graphene with a surface morphology similar to that reported in the literature by thermal decomposition of hydrocarbons[41] (Fig 4.4). Analyzing different regions up to 1μm × 1μm we have concluded that graphene coverage is about 50% of the surface. STM images show several Moiré's patterns separated by domain boundaries that appear as bright features together with a dark seam line (Fig 4.4a). Moreover, some 3D nucleated protrusions can also be observed and are tentatively attributed to amorphous carbon.

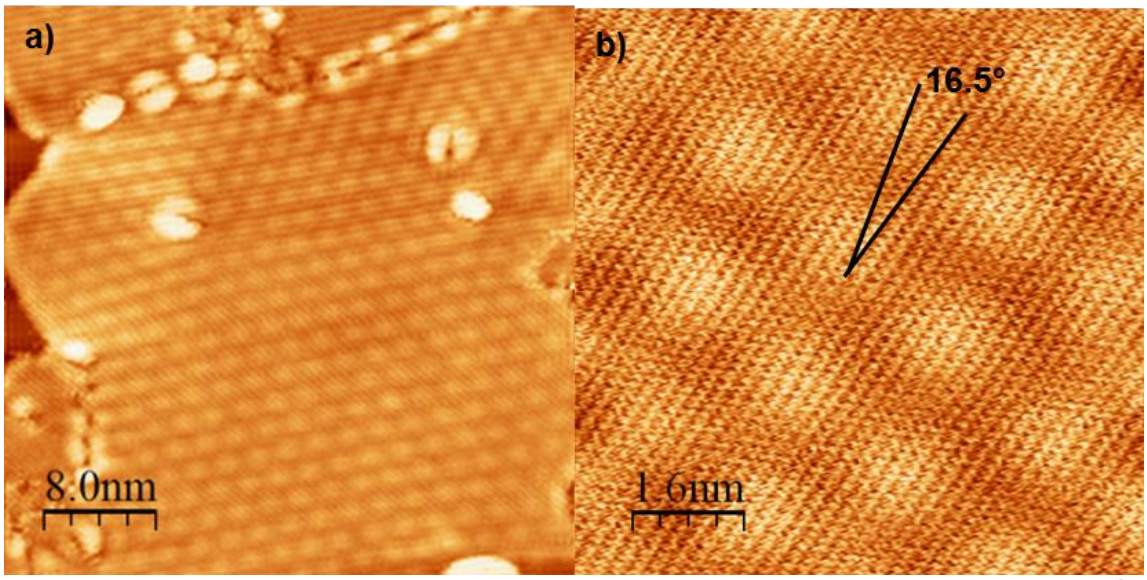

Fig 4.4: a) STM picture showing several of the characteristic graphene moirés separated by grain boundaries visualized as brighter areas. Size: 65 nm × 65 nm, V = -35.7 mV, I = 0.04nA; b) Atomic resolution image of graphene on platinum (111). The angle between the moire bumps and the atoms line is 16.5°. Size 8 nm × 8 nm, V = -3507 mV, I = 0.04 nA.

Atomic resolution images (Fig 4.4b) clearly show a Moiré pattern obtained at low bias voltages and typical values for the tunneling current. A Moiré is the visual pattern created when two regular patterns interfere. In this case, the two hexagonal structures (graphene (0001) and Pt(111)) with a similar lattice constant. This one shows an apparent angle (angle between the carbon atoms and the moiré bumps) of 16.5° indicated in the image with a periodicity between the bumps of 2.1 nm. However, the actual rotation angle between the graphene and the underlying Pt (111) surface (in correspondence with the apparent angle and the bumps periodicity) is 2° (see Fig 4.18b).

To explore the minimum temperature for graphene formation using our MBE solid carbon source we have also performed carbon evaporation on platinum at 823 K. In this case, no ordered graphene layer has been obtained, but an unordered carbonaceous growth on the surface. This attempt was made with

the goal to find the lowest temperature to grow graphene on a given surface using this method.

4.3 Graphene on gold (111)

Graphene on gold has been successfully grown using a similar protocol as on the platinum substrate. Here, the time of sample exposure in front of the carbon source was 30 and 45 minutes. Simultaneously, the sample was annealed at 823 K. Before growth, the gold was cleaned using the procedure described for the preparation of metallic substrates (2.6.1 section).

Platinum and gold single crystals have a FCC structure. However, in both cases, the (111) surface has a 2D rhombohedra unit cell that shows an hexagon in the LEED pattern. After growth, the LEED pattern exhibits graphene diffraction spots around the hexagon related to the Au (111) (Fig 4.5). These spots are in correspondence with the lattice parameters of 2.46 Å and 2.88 Å for graphene and gold respectively.

The graphene spots are brighter at zero (black dashed hexagon) and thirty (gray dashed hexagon) degrees respect to the gold spots (yellow dashed hexagon). This result indicates that graphene is either aligned with the substrate or with the atoms along (110) direction. These systems are further studied in the theoretical part.

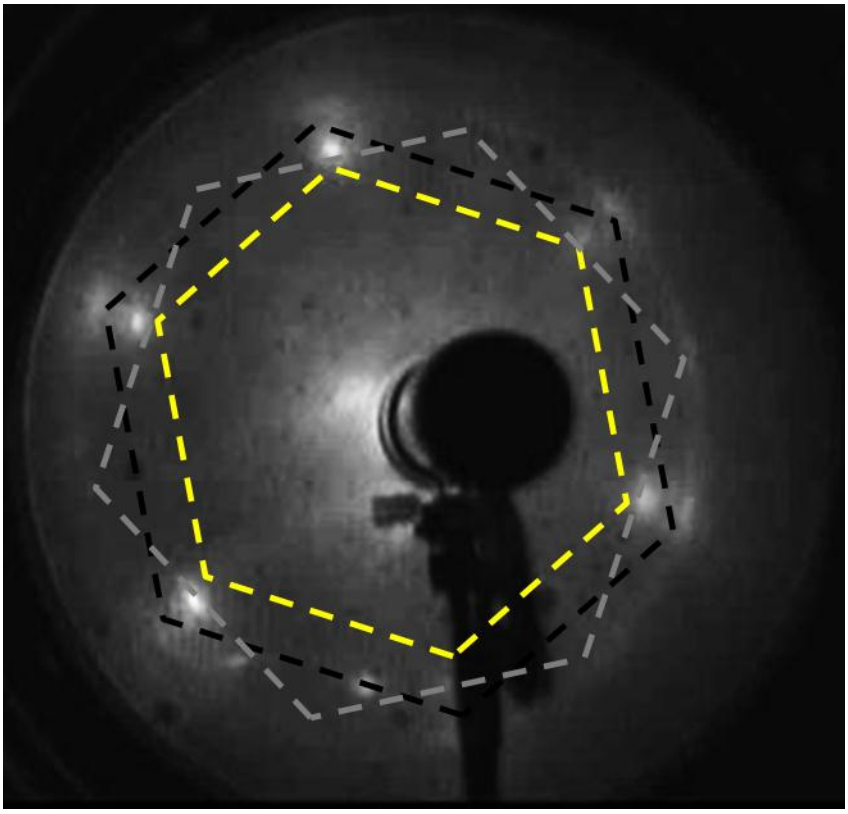

Fig 4.5: LEED image took at 55.1 eV for gold after growth of graphene. Spots associated with Au(111) form an hexagonal pattern in correspondence with the corners of the yellow dashed hexagon which is surrounded by a characteristic graphene diffraction pattern. The graphene diffraction spots are brighter at 0° and 30°. Both types of graphene spots are in the corners of the black and gray hexagons respectively.

The AES spectra verify the existence of carbon on the surface (Fig 4.6). We have compared the spectra just after cleaning and after graphene growth. The clean spectra show two peaks that correspond to gold peaks (239 eV and 257 eV). On the other hand, the after growth spectra has a new peak in 272 eV. It is the value for the carbon peak as I have commented in the previous section (4.2).

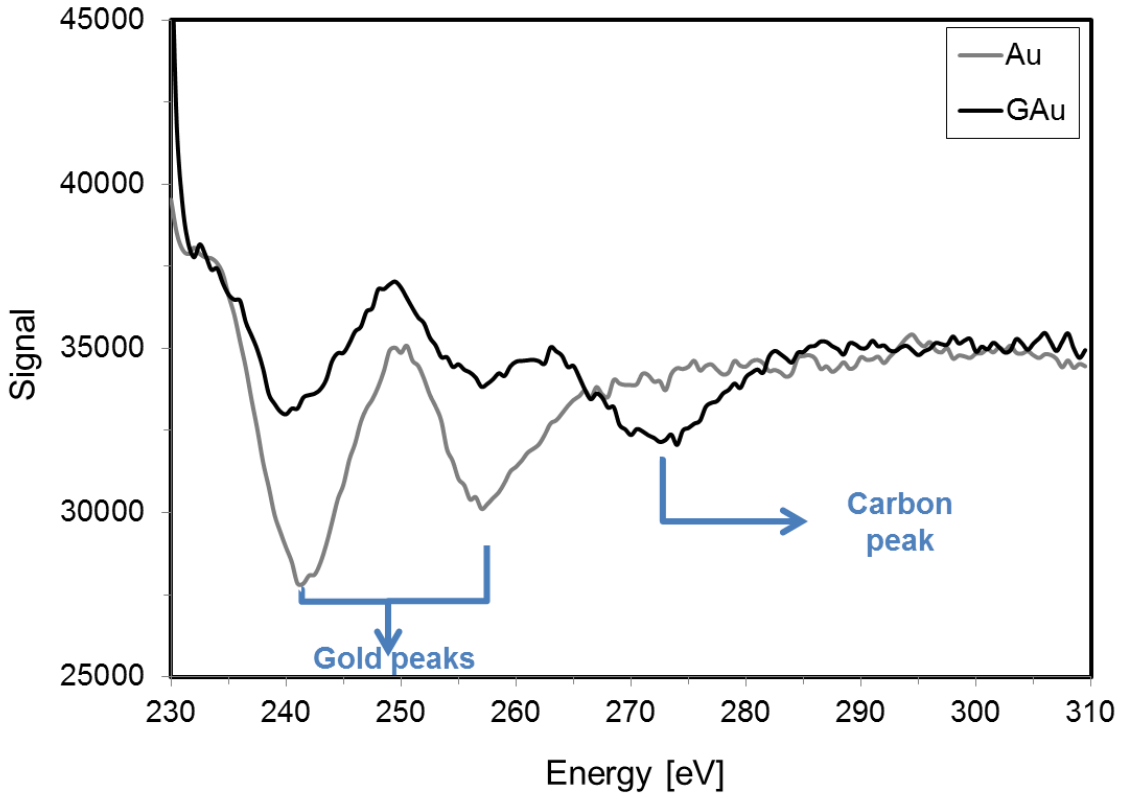

Fig 4.6: Comparison between the AES spectra for clean Au (111) surface (gray line) and Au (111) after graphene growth (black line). The gray line shows a flat tendency in the carbon peak region (272 eV), unlike the black line. Both lines show two peaks related with the gold (indicated in the graph).

The STM images of graphene on gold show dendritic islands growing either on both sides of the gold step edges, or pinned by defects (Fig 4.7a). In many cases graphene can be clearly distinguished by analyzing STM current images (Fig 4.7b); the graphene-covered areas correspond to dark regions, while bright areas correspond to uncovered gold.

Fig 4.7a corresponds to an evaporation of 30 min, obtaining approximately a 0.5 monolayer of graphene on gold. Thus, it would be possible to consider that the dendritic islands can be smoothed if we would have covered almost the entire surface.

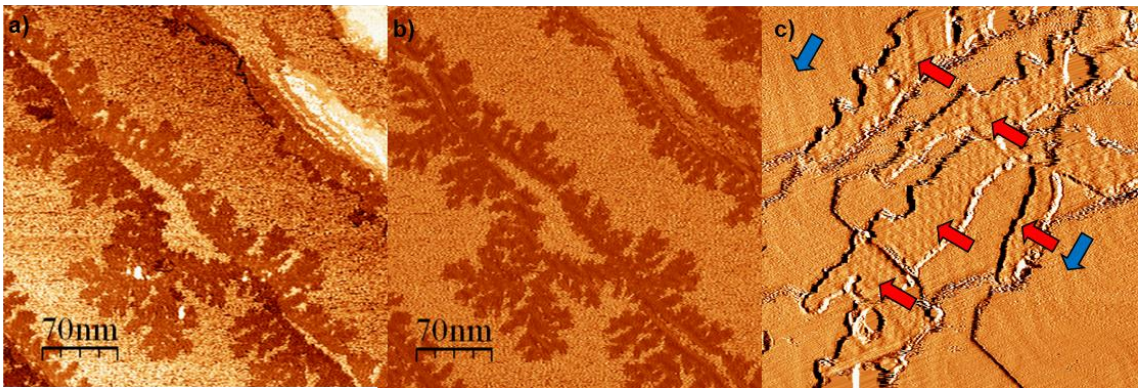

Fig 4.7: a) STM topographic image in correspondence with b) STM current image. Two pictures show graphene growth on Au(111). Graphene areas are clearly distinguished in the current picture (b), as substrate appears noisy and lighter. a) and b) are obtained after 30 minutes of evaporation, so they are covered by a 0.5 graphene monolayer approx. Size: 350 nm × 350 nm, I = 4 pA, V = −1241 mV;c) STM image in derivative mode showing graphene areas as dendritic branches (red arrows) with several types of moirés. The gold herringbone reconstruction is viewed on some of the uncovered areas (blue arrows). Size of the image: 67 nm × 67 nm, I = 1 pA, V = −107.8 mV.

A closer view on graphene allows us to recognize several Moiré's (Fig 4.7c and Fig 4.8a). These Moirés (red arrows) are in good agreement with other works in the literature[42] and confirm that the dendritic islands (Fig 4.7c) correspond to graphene.

In Fig 4.7c, the Au (111) reconstruction (blue arrows) can be used to deduce the orientation of the moiré on the crystallographic directions of gold. Thus, the middle graphene patch is oriented along the gold atom's direction. This alignment is in agreement with what is observed in the LEED diagram (spots at 0°). The periodicity of the moiré corresponds to 1.9 nm (distance between moiré bumps)

Fig 4.8 shows two STM images with graphene on gold where almost a full monolayer has been completed (0.8ML). The image illustrates how the

graphene sheets (dark regions) terminate in rounded fingers while approaching others, but we do not see them coalesce.

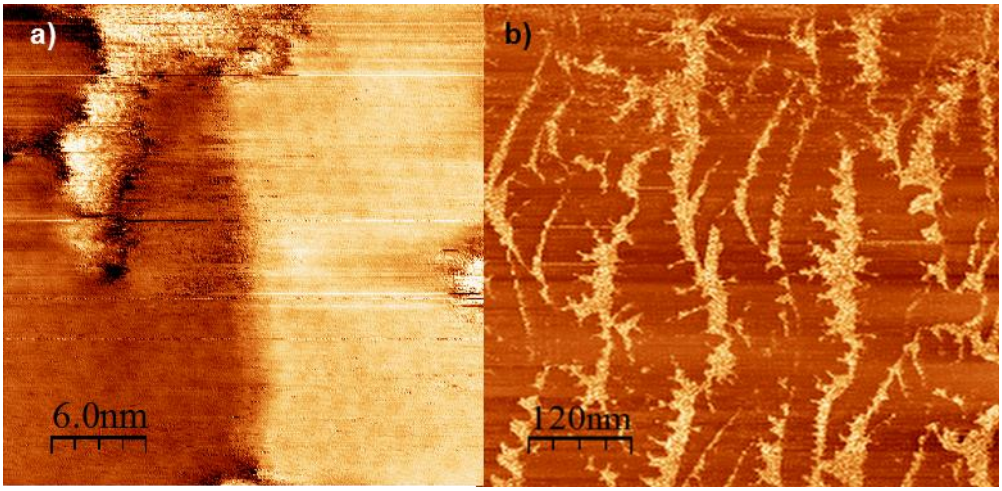

Fig 4.8: a) STM image showing a characteristic moiré pattern of graphene in the branches of a dendritic region. The gold seems noisy as other images. Size: 30.0 × 30.0 nm, I = 5 pA, V = −558.2 mV; b) STM current image after 45 minutes of evaporation. Graphene (dark areas) covers the 80% of the gold surface (noisy regions between the dark graphene fingers). Size: 600 × 600 nm, I = 5 pA, V = −558.2 mV

Furthermore, STM topographic images of graphene on gold are usually revealed as depressions. This fact can be related to a smaller electrical conductivity in the layer of graphene on gold than the gold itself. It could also be related to adsorbates on the STM tip that will induce a reversed contrast [89]. Fig 4.9 is a schematic representation of a constant-current topographic scanning profile over the sample. Over graphene regions, the STM tip must approach the surface to maintain a constant tunneling current. This procedure has inverted contrast on the apparent topography: graphene appears dark (depressions) and bare gold appears bright. In comparison to G/Au, uncovered gold region are visualized by STM as noisier patches (Figure 4.8a), which may be due to the presence on the surface of fast diffusing carbon species, as it has been previously reported for organic molecules on gold [90].

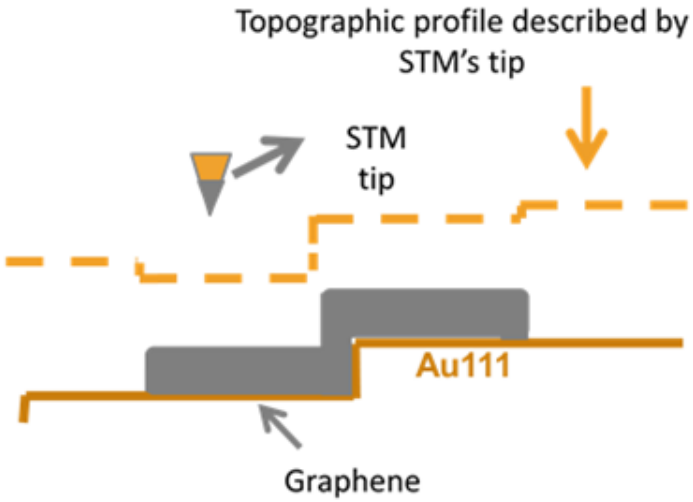

Fig 4.9: Scheme showing the topographic constant-current profile describe by STM tip. Tip gets closer over the graphene islands, even when the tip-surface distance is reduced, inducing a reverse effect and making the graphene to be viewed as depressions.

4.4 Formation of graphene on Pt(111) and Au(111): Theoretical part

In this section, we study the formation of graphene from a theoretical point of view. Having this goal in mind, we look at systems formed by one, two three, four, six and eight carbon atoms (a graphene monolayer) on a 2×2 unit cell of Pt(111) and Au(111).

The exchange-correlation functional employed was the Generalized Gradient Approximation proposed by Perdew-Burke-Ernzerhof (GGA-PBE). I have used ultrasoft pseudopotentials and 300 eV as the energy cutoff that determines the number of plane-waves in the models. The electronic minimization is considered to have converged when the total energy changes less than 1×10^{-5} eV per atom in three consecutive iterations. Geometric optimizations were performed using a force threshold of 0.03eV/Å acting on each atom, and a final change in any atomic position smaller than 0.002 Å. Finally, the maximum stress on the unit cell is kept below 2.0 eV/Å^2. All calculations were performed without polarization of spin. The Monkhorst-Pack grid employed was 5 × 4 × 1 for Pt(111) and Au(111). All calculations have been performed with the CASTEP code as provided in the Materials Studio simulation suite (v 8.0, [28,29]).

The procedure we have used is as follows: First of all, we create the surface of interest from a bulk unit cell always optimized with the same parameters and thresholds. Next, we optimize the 2×2 cell with four layers of substrate to allow for relaxation of the distance between layers. Therefore, I have started with **a**,**b** = 5.65 Å, **c** = 16.92 Å; α,β = 90°, γ = 120° and **a**,**b** = 5.76 Å, **c**= 20.00 Å; α,β = 90°, γ= 120° for Pt(111) and Au(111) respectively, and I have optimized these values for the surface to get for Pt (111): **a**,**b** = 5.53 Å, **c**= 16.92 Å; α,β = 90°, γ = 120°, and for Au(111): **a**,**b** = 5.90 Å, **c** = 20.00 Å; α,β = 90°, γ = 120°. These last values indicate that the 2x2 surface system supports a surface stress compression in the Pt (111) case while for Au (111) is the other way around.

These final values for the 2D unit cell where the surface stress has been relieved are then used in all calculations of this section.

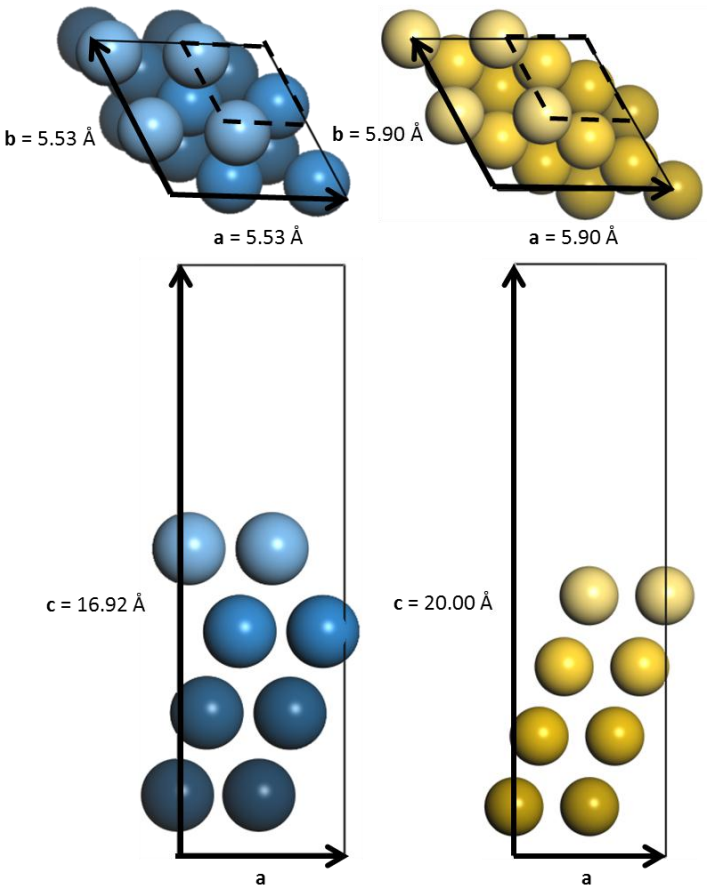

Fig 4.10: In the picture is represented the optimized cells which have been used in the calculations of this section. The cell parameters are marked. In the calculation, we have used a 2x2 cell, thus, the unit cell is marked with dashed lines in the image. The image with blue balls corresponds to Pt (111) and the one with yellow balls to Au (111). In both cases, the layers progressively become darker to facilitate the visualization of the top views (above).

4.4.1 One carbon atom on Pt (111) and Au (111) surfaces.

We have added carbon atoms to form a graphene monolayer on the surface. First we have considered adsorption of one carbon atom in four different positions on the substrate surfaces: top, bridge and the two hollow sites (HCP

and FCC). In all calculations, we have fixed the positions of the bottom layer (represented in darkest colors in Fig 4.11.).

HCP hollow site corresponds to place the carbon atom on the hollow coinciding with an atom of the second layer. In FCC hollow site, the carbon atom is also on a surface hollow, but in this case, the atom is on top of an atom of the third layer. In the top position, the carbon atom is placed over an atom of the surface and in the bridge position the carbon atom is on the bridge formed by two atoms on the surface. Initially, the carbon atoms are placed at a surface distance of 3.0 Å approx.

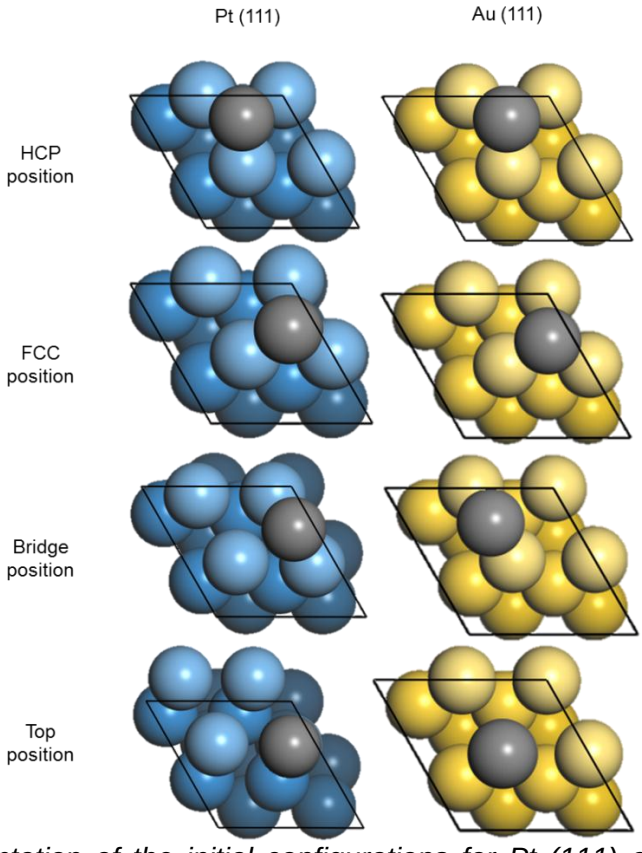

Fig 4.11: Representation of the initial configurations for Pt (111) and Au (111). We have continued using the same color settings than above (upper layers of the substrates lighter than lower layers).

Independently from the starting position carbon atoms show a tendency to move to the two hollow sites. These results are summarized in Fig 4.12.

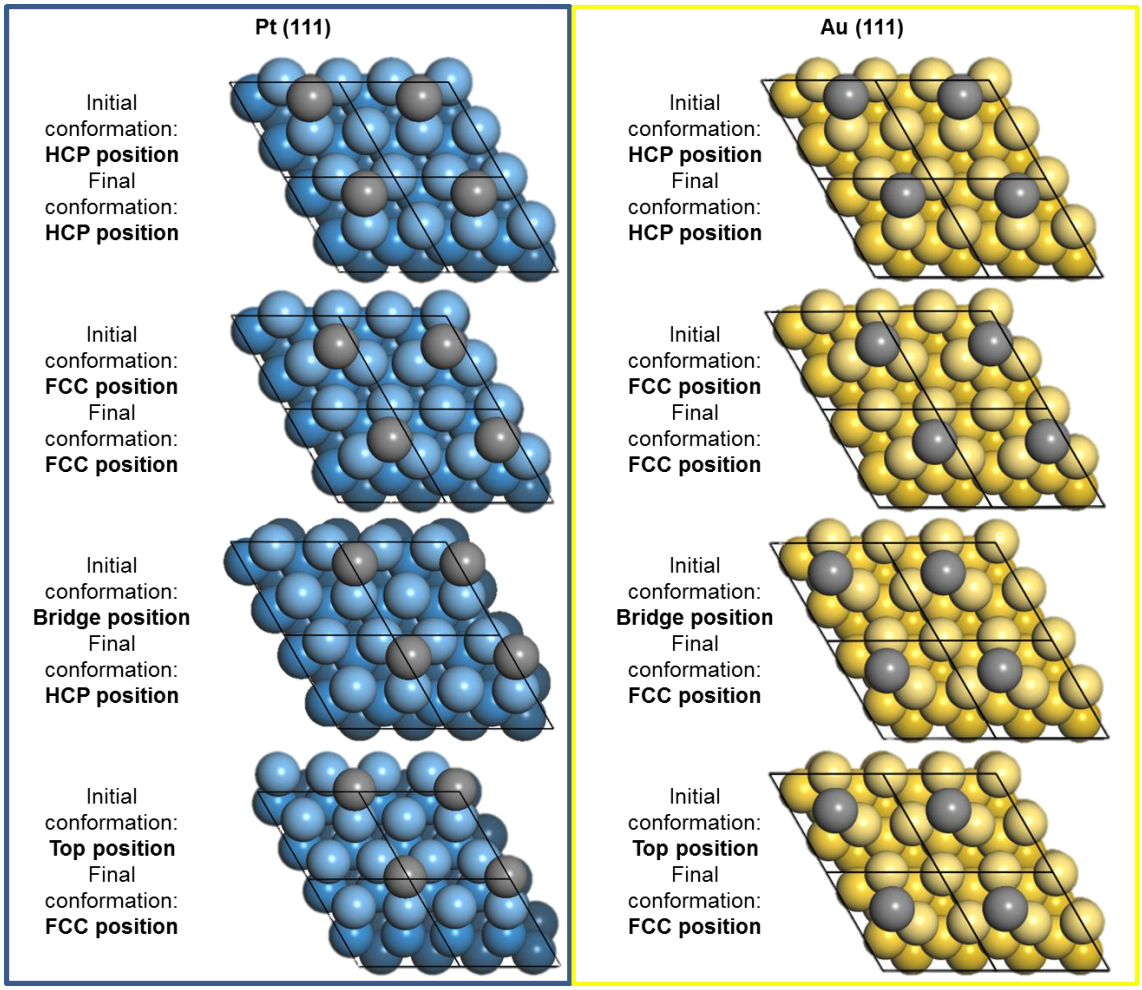

Fig 4.12: Every case shows the initial conformation (illustrated situation in Fig 4.11) and the obtained situation at the end of the geometry optimization. The images correspond to the left-side final structures of the different cases. The pictures correspond to a 4 × 4 unit cell with the 2 × 2 cell marked by black lines (they are the cell used in these calculations).

The adsorption energy (E_{ads}) of these systems have been calculated as

$$E_{ads} = E_{1C/Sub} - (E_{1C} + E_{Sub}) \qquad \text{Eq (4.1)}$$

where $E_{1C/Sub}$ corresponds to the energy of the one carbon atom on the substrate in the different positions, E_{1C} the energy of one carbon atom calculated in the vacuum and E_{Sub} the energy of the relaxed substrate (four layers of the 2 × 2 unit cell). Therefore, a negative value for E_{ads} denotes a favorable adsorption (exothermic process).

All the E_{ads} values are collected in Table 4.1. All cases show negative values and the most favorable case correspond to FCC hollows in both substrates. The next more favorable case is the HCP hollow. The maximum difference energy between the most and the less favorable cases are 0.28 eV and 0.14 eV for Pt (111) and Au (111), respectively. In Table 4.1 the energy values are exhibited as the whole energy value of the system and as the energy value per carbon atoms. This last form of expression can help to a better comparison between different systems, most especially if they are formed by a different number of atoms. In this case, the number of carbon atoms is one, so the two energy values are the same.

Initial position\Substrate	**Pt (111)**	**Au (111)**
	E_{ads}/N_C [eV]	E_{ads}/N_C [eV]
HCP position	-7,576	-5,691
FCC position	-7,702	-5,835
Bridge position	-7,424	-5,819
Top position	-7,462	-5,759

Table 4.1: Energy adsorption values (E_{ads}) and energy adsorption values by carbon atoms (E_{ads}/N_C) for the different systems described above.

As we explain above, in every case, the carbon atoms start at 3.0 Å from the surface in the geometry optimization. At the beginning, each carbon atom goes straight down until it reaches the interaction distance with the surface. This way, the adsorbed carbon atom interacts directly with three substrate atoms. In that moment, these three atoms of the surface change their initial positions and move in the **z**-direction to adapt to the adsorption of the carbon atom at each

position. The fourth atom, on the other hand, does not interact directly with the carbon atom and the surface becomes corrugated. Then, the carbon atom moves on the surface to find the position of minimum energy (that is the FCC position), but the atoms of the surface maintain the displacement from their initial positions, so they undergo different corrugations. The difference of these values in **z**-direction is collected in Table 4.2. In any case, the values for the metallic corrugations are fairly small (the highest value is 0.7 Å). A value of atomic displacement lower than 1 Å is not relevant because the atomic vibrational movement and the electronic density are higher than that threshold.

Initial position\Substrate	**Pt (111)**		**Au (111)**	
	Metallic surface corrugation [Å]	$D_{C\text{-}Pt}$ [Å]	Metallic surface corrugation [Å]	$D_{C\text{-}Au}$ [Å]
HCP position	0.10	1.14	0.17	1.22
FCC position	0.12	1.12	0.17	1.26
Bridge position	0.21	1.17	0.25	1.30
Top position	0.22	1.18	0.70	1.46

Table 4.2: The table summarizes the metallic surface corrugation values due to the adsorption of one carbon atom and the z-direction distances between the lowest platinum ($D_{C\text{-}Pt}$) or gold ($D_{C\text{-}Au}$) atom in the surface and the adsorbed carbon atom.

The largest corrugation is obtained with gold, especially in the top case with 0.7 Å. Comparing the values for the two substrates in the same initial position, the corrugation is always higher with gold, but the difference is not very significant except in the case Top. Moreover, observing the different cases for the same substrate, the corrugation increases in the same order. On the other hand, the distance between the carbon atom and the metallic surface ($D_{C\text{-}Sub}$) is similar in platinum, unlike gold. On Pt (111) the carbon atom is placed at similar height (the z distance differs in 0.06 Å), and on Au (111) the difference of the carbon atom height reaches 0.24 Å.

On balance, the most favorable adsorption is starting from the FCC position on both substrates. Thus, we have performed following calculations with the carbon atoms from the FCC positions at a surface distance around 3.0 Å.

4.4.2 Two carbon atoms on Pt (111) and Au (111) surfaces.

In this part, the initial configuration consists of two carbon atoms in FCC position. The final situation of the two carbon atoms is the same as the initial one (FCC position for both substrates). Carbon atoms only change the distance from the metallic surfaces. The carbons are located closer to them and are linked with three atoms of the surface (Fig 4.13). In both cases, the two carbon atoms are placed at the same distance from the surface (the difference between them is practically zero, see Table 4.3)

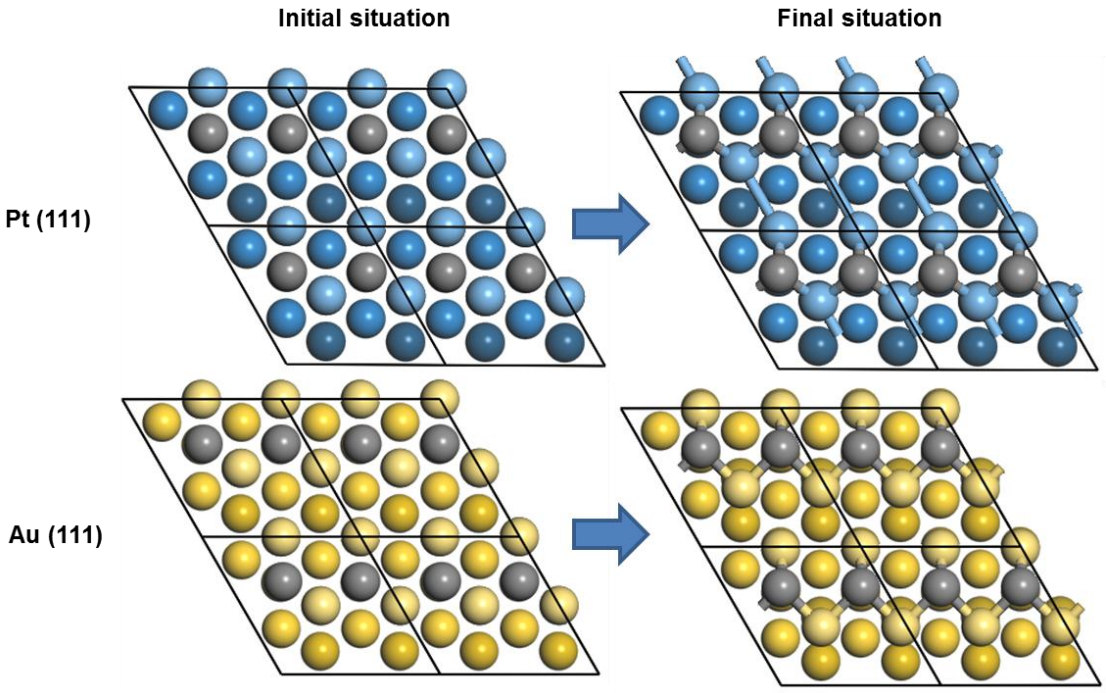

Fig 4.13: 4 ×4 c view representation of the system formed by two carbon atoms in a 2×2 unit cell of Pt (111) and Au (111) (the 2 × 2 unit cells are marked by black lines). The color settings are the same then the above sections. The picture shows the initial and the final carbon positions.

The carbon adsorption changes the position of platinum first layer atoms, in such a way that platinum atoms get closer in **b** direction. That is the reason why they appear linked in the Fig 4.13 with a 2.78 Å distance in contrast to the other platinum atoms in the cell with an average distance of 2.83 Å. This fact is observed also for the gold atoms in the x-y plane. The final carbon position

picture for gold shows the gold atoms displaced in the **y** direction, so it is possible to see the fourth layer of gold atoms. The distance between the gold atoms linked through a carbon atom is 3.73 Å and the value for the distance between the gold atoms without a carbon atom in the middle is 2.85 Å. However, the average of the distance of gold atoms is usually 2.89 Å. So carbon atoms extend the distance between the gold atoms and compress the gold atoms without carbon in the middle.

On the other hand, the **z** direction for the platinum substrate is much less modified than gold. The gold surface suffers a large corrugation when the carbon atoms move close to them. The z-distance between the highest and lowest gold atoms from this layer is 1.18 Å, which is very high in comparison with the platinum corrugation (Table 4.3). This z position difference is observed two to two in the four atoms of the surfaces. In other words, two atoms from the first layer are in the higher z position and the other two ones in the lower z position for both substrates, being very remarkable in the gold case.

	Pt (111)	**Au (111)**
E_{ads} [eV]	-2.00	-5.64
E_{ads}/N_C [eV]	-1.00	-2.82
Metallic surface corrugation [Å]	0.17	1.18
D_z(C-Sub) [Å]	1.19	1.53
$D_z(C_1\text{-}C_2)$ [Å]	$2\cdot10^{-5}$	$16\cdot10^{-5}$

Table 4.3: The table collects the main values for this part. Energy adsorption values (E_{ads}) and energy adsorption values by carbon atom (E_{ads}/N_C) on Pt (111) and Au (111), the metallic surface corrugation as the difference between the highest and lowest metallic atom of the first layer, the z-direction distances between the lowest platinum ($D_{C\text{-}Pt}$) or gold ($D_{C\text{-}Au}$) atom in the surface, the highest adsorbed carbon atom D_z(C-Sub) and the z-position difference between the two carbon atoms $D_z(C_1\text{-}C_2)$.

Finally, the z-position difference between the two carbon atoms (Table 4.3) is not significant (2·10-5 or 16·10-5 Å), so both are placed at the same distance from the substrate for platinum and gold.

In these systems, the adsorption energy (E_{ads}) is calculated by adapting the definition given by equation 4.1.

$$E_{ads} = E_{2C/Sub} - (E_{2C} + E_{Sub}) \qquad \text{Eq (4.2)}$$

where $E_{2C/Sub}$ is the energy of two carbon atoms on the substrate with the final configuration and E_{2C} the energy of two carbon atoms calculated in the vacuum.

In both cases, the E_{ads} corresponds to a negative value, so it denotes that the adsorption is favorable (Table 4.3). The energy for platinum is lower than the one carbon atom adsorption, however, in the gold case, the energy is similar to the previous values.

4.4.3 Three carbon atoms on Pt (111) and Au (111) surfaces.

To build the graphene monolayer, we added another carbon atom in the 2×2 cells. All carbon atoms begin with a FCC position, but in this case, they have a different behavior depending on the substrate (Fig 4.14).

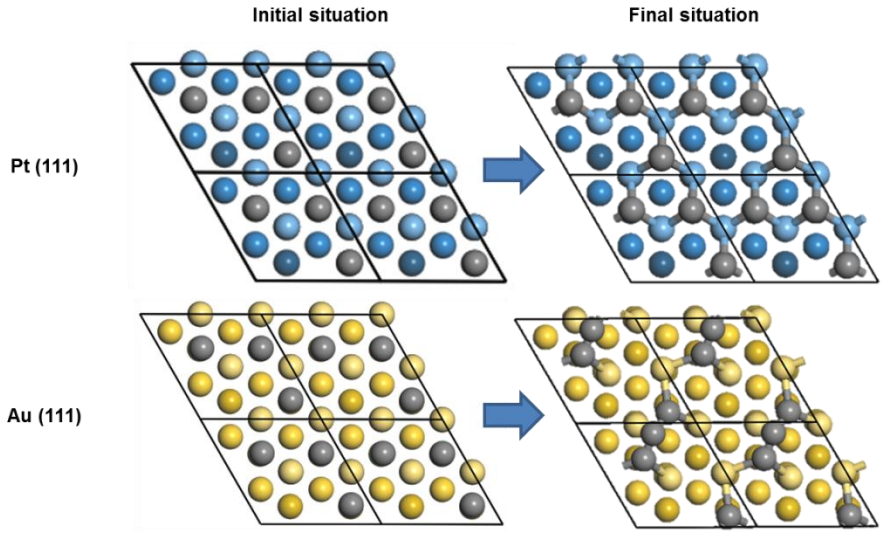

Fig 4.14: Initial and final appearance of the structures for the adsorption of three

carbon atoms on Pt (111) and Au (111).

On Platinum, the three carbon atoms go down in the same x-y position until they get very close to the substrate, so they bind with the platinum atoms. In some way, the carbon atoms are occupying the x-y position of the platinum atoms from a new layer and consequently, the platinum atoms from the first layer try to continue with their crystal structure with the carbon atoms. This way, the last situation is a framework of alternate carbon-platinum atoms forming hexagons and dodecagon structures. This framework induces a small surface corrugation (0.2 Å approx.; Table 4.4) because the carbon atoms form an angle between 85° and 97° with the platinum. Thus, they maintain their x-y coordinates in the fictitious position of the platinum atom with a C-Pt bond distance (the typical value for C-Pt distance is 1.98 Å, and the carbon atoms are bonded to the platinum at a distance between 1.97 and 1.99 Å in this structure). Due to this geometry, the z-distance between the planes formed by the carbon atoms and the platinum atoms from the surface is approx 1.2 Å. In this case, we are talking about planes formed by carbon atoms and platinum because the metallic corrugation is very low and the z position difference for carbon atoms is not significant (Table 4.4) due they are occupying equivalent positions (fictitious platinum positions.)

However, on gold is different (Fig 4.14). One of the three carbon atoms moves from its initial position until a place in the middle between the two another ones at 1.3 Å (this value corresponds to the C-C double-bond distance). This way, the final structure is formed by a chain of three carbon atoms linked at the ends with gold atoms. The gold is well-known by the facility to bond with organic molecules, especially, forming metal-organics structures with carbon as that [91–94]. The main reason is due to the association energy difference between C-C (-6.4 eV) and C-Au (-4.7 eV) since, although the both bonds are energetically favorable, the C-C bond is easier to form spontaneously.

	Pt (111)	Au (111)
E_{ads} [eV]	-1.40	-2.74
E_{ads}/N_C [eV]	-0.47	-0.91
Metallic surface corrugation [Å]	0.17	1.56
$D_z(C_{Zmin}$-Sub) [Å]	1.17	1.77
$D_z(C_{Zmax}$-$C_{Zmin})$ [Å]	$5 \cdot 10^{-5}$	0.47

Table 4.4: The table summarizes the main values to characterize these systems. $D_z(C_{Zmin}$-Sub) corresponds to the z-distance between carbon and the atom from the first layer with lower z position and $D_z(C_{Zmax}$-$C_{Zmin})$ is the z difference between the higher and lower carbon atoms.

As we mentioned before, carbon atoms are linked at both side with gold atoms. This way, from the four gold atoms of the first layer, one of them is not linked with carbons, two of them are linked with one carbon atom and the other gold atom is linked to two carbon atoms at the same time (the two different ends of the chains). This last gold atom is displaced to higher z position than the others, the two gold atoms bonded to one carbon atom are displaced to a z intermediate position, and the one not bonded stays at its initial coordinate. This re-configuration of the first layer of gold is the reason for the high values for metallic surface corrugation and the distance between the lowest z value for carbon and gold atoms (Dz(CZmin-Sub); Table 4.4.).

Adapting the Eq (4.1) to calculate the adsorption energy for this case, we obtain

$$E_{ads} = E_{3C/Sub} - (E_{3C} + E_{Sub}) \qquad \text{Eq (4.3)}$$

where $E_{3C/Sub}$ is the energy for the final configuration of this section and E3C the energy of three carbon atoms calculated in the vacuum.

The energies show that the two adsorptions are favorable (Table 4.4) but less spontaneous than the cases of the previous sections (the absolute value is

lower than the others). To compare them it is needed to use the Eads/NC because the previous systems have a different number of carbon atoms. This way, for platinum the energy value decreases as we increase the number of carbon atoms, however, for gold, in the previous sections, the energy value was stable (-0.3 approx) but in this case, it decreases with the C-C bond formation. On the other hand, if we compare the adsorption of the three carbon atoms in both substrates, the gold case is easier to occur than the platinum one.

4.4.4 Four carbon atoms on Pt (111) and Au (111) surfaces.

In this section, we have started with four carbon atoms in FCC position in both substrates. The behavior of these systems is different from the case of three carbon atoms (Fig 4.15).

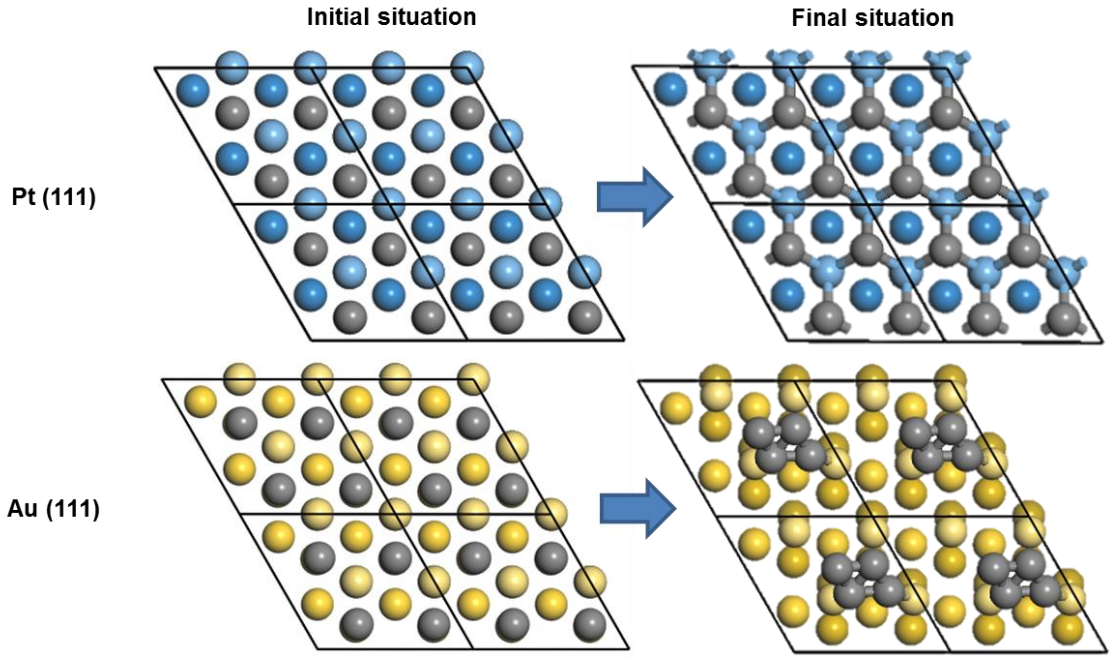

Fig 4.15: Initial and final appearance of the structures for the adsorption of four carbon atoms on Pt (111) and Au (111). The carbon atoms start on FCC positions on both substrates but, they have different behavior after the geometric optimization.

On platinum, the carbon atoms are placed in an equivalent x-y position (FCC) of the platinum lattice (Fig 4.15), so the first layer of platinum atoms is completed with carbon atoms. As the C-Pt bond (1.98 Å) is shorter than the Pt-Pt bond (2.42 Å), the carbon atoms move closer to the surface until they link with platinum atoms forming an hexagonal structure. However, to maintain the x-y position and the 1.98 Å of distance, the carbon atoms form an angle with the platinum ones of almost 90° (from 90.3° to 90.5°) as the case of the 4.4.3. section. In this case, the main difference is that the carbon atoms complete the fictitious layer of platinum (four atoms in a 2 × 2 cell), forming a complete monolayer of a carbon-platinum material. Thus, the distance between the carbon atoms and the substrate is similar to the three carbon case (1.14 Å for four carbon atoms and 1.17 Å for three carbon atoms, see Fig 4.15) and the z difference between the carbon atoms is not significant ($3 \cdot 10^{-4}$ Å).

On gold, the C-C interaction continues to dominate with respect to the C-Au. Thus, the carbon atoms move until they link between themselves (Fig 4.15). The C-C distances between the linked atoms vary from 1.39 to 1.53 Å. At the top view it cannot be fully appreciated, but the structure is formed by two carbon atoms linked with two gold atoms and the two other ones are placed with a pyramidal appearance (the z difference between the higher and lower carbon atom is 1.34 Å, Table 4.5). This configuration is due to that the four carbon atoms form a cycle-butane with a torsional effect with carbon atoms confined to their positions by the C-Au bond.

	Pt (111)	**Au (111)**
E_{ads} [eV]	-15.18	-17.73
E_{ads}/N_C [eV]	-3.80	-4.43
Metallic surface corrugation [Å]	$3 \cdot 10^{-4}$	0.46
$D_z(C_{Zmin}\text{-Sub})$ [Å]	1.14	2.31
$D_z(C_{Zmax}\text{-}C_{Zmin})$ [Å]	$9 \cdot 10^{-4}$	1.34

Table 4.5: The table summarizes the main characteristics for four carbon atoms. The meaning of the parameters are similar as the described in previous subsections.

The metallic corrugation of platinum is almost zero (Table 4.5.). The carbon atoms do not induce any displacement in the platinum because they move until they complete a new layer of the platinum lattice. On the other hand, the corrugation of the gold surface is because two of the four gold atoms from the first layer are linked to two carbon atoms. In this manner, these two bonds C-Au are the reason for the modification of the gold atoms position and the twisting of the cycle-butane.

The E_{ads} has been calculated as in previous sections. In these cases, the energy is really high. It is because in both substrates new species are formed and therefore, new links, dropping the energy.

4.4.5 Six carbon atoms on Pt (111) and Au (111) surfaces.

In this section, we start with six carbon atoms forming a ring. The ring goes down in both cases (Fig 4.16.). The final situation is similar as it does not happen in the two last sections. For platinum, six carbon atoms are much more than the needed to form a new layer of the platinum lattice, for this reason, the opposite effect occurs. In this case, two platinum atoms from the surface get included in a hexagonal structure on the substrate (as the carbon atoms try to form a similar structure than graphene) preserving the C-Pt distance (1.98 Å). On gold, a similar effect occurs. The carbon atoms are already linked, but they have more capability to create bonds. Thus, they link with gold atoms attracting them from the surface. Thus, a metal-organic structure of a six-carbon ring linked with gold atoms is formed. The structure has an hexagonal appearance in top view as in the platinum case. However, the structure maintains the carbon-gold bond distance.

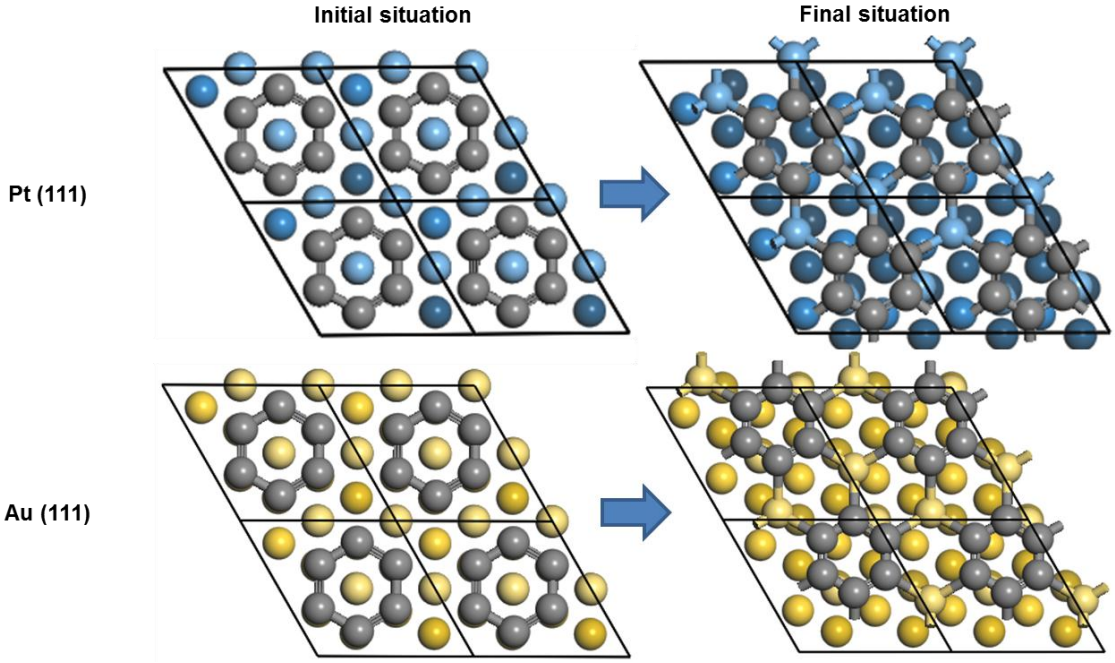

Fig 4.16: In the original situation, a six carbon ring has in the middle a platinum atom from the surface. Then, in both cases, they have formed a metal-organic structure with an hexagonal appearance in top view.

Considering the structure explained above, the atoms from the substrate included in the metal-organic structure generates large corrugations if we continue taking them as part of the metallic surface at the same time. The value for the corrugation varies from 1.9-2.0 Å approx. (Table 4.6). On the other hand, the z distance of the lower carbon and the lower metallic atom from the surface is 2.1 and 2.8 Å for platinum and gold respectively. So, the carbon atoms attract the metallic atoms until a z distance of 0.2 and 0.8 Å for Pt and Au on lower carbon atoms of the hexagonal structure.

	Pt (111)	**Au (111)**
E_{ads} [eV]	-4.91	-3.00
E_{ads}/N_C [eV]	-0.82	-0.50
Metallic surface corrugation [Å]	1.88	2.00
$D_z(C_{Zmin}\text{-Sub})$ [Å]	2.12	2.82
$D_z(C_{Zmax}\text{-}C_{Zmin})$ [Å]	0.76	0.11

Table 4.6: Here the main points are collected to describe the structures from this subsection. The meaning of every point is defined in the first subsections.

The hexagonal structure needs to preserve the typical values for bond distances, so the carbon ring tilts to fit in the 2 × 2 cell of the substrate. As the cell parameters for gold are bigger, the ring needs a lower tilt, so the z difference value for carbon atoms is less for gold (0.1 Å for Au and 0.8 Å for Pt approx.; Table 4.6).

The adsorption energy values have been calculated adapting the equation explained in the previous sections (Table 4.6). The energy values are negative, so they mean that these adsorptions are energetically favorable. The absolute value indicates that the formation of this hexagonal structure releases more energy with platinum as substrate. Moreover, the adsorption energy value per carbon atom is moderate comparing with other sections.

4.4.6 A graphene monolayer (eight carbon atoms) on Pt (111) and Au (111) surfaces.

The last structure of this part is the eight carbon atoms in the 2 × 2 cell forming a monolayer of graphene. This case will be explained in depth in the section 4.5 with the different moirés. Here, we start with an initial situation of eight carbon atoms. In the platinum case they do not form a graphene layer (Fig 4.17). However, the carbon atoms organize on the platinum surface until forming graphene. For the gold case, in the original situation, the carbon atoms are already close enough to form a graphene layer, so they maintain their x-y positions.

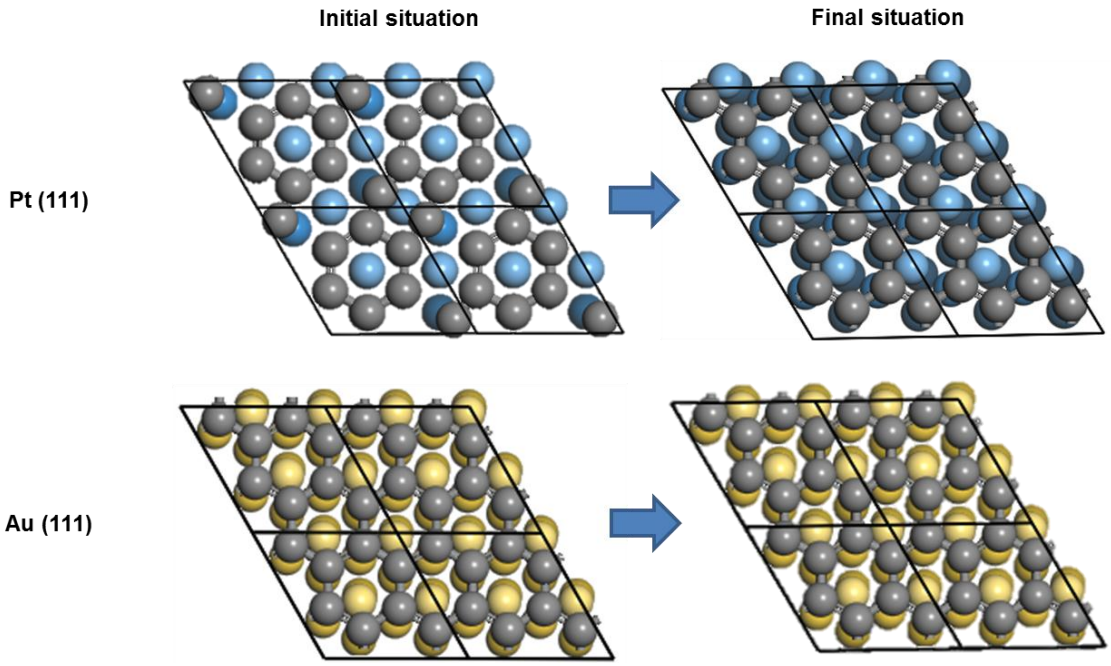

Fig 4.17: Eight carbon atoms are placed on two metallic substrates. On platinum, the carbon atoms don't form a graphene monolayer as it's possible to see in the picture, but at the end, the graphene monolayer is obtained on both substrates.

In both cases, the eight atoms start at a distance around 3.1 Å from the substrate and then, the graphene layer moves up until 3.8 and 3.2 Å for platinum and gold respectively. This distance is measured considering the z difference between the lowest carbon a substrate atoms, but in these cases, the graphene doesn't induce significant corrugation in the metallic surfaces (Table 4.7), and it is showed flat (the z difference between carbon atoms is negligible ; Table 4.7).

	Pt (111)	**Au (111)**
Metallic surface corrugation [Å]	$7 \cdot 10^{-4}$	$22 \cdot 10^{-4}$
$D_z(C_{Zmin}\text{-Sub})$ [Å]	3.84	3.21
$D_z(C_{Zmax}\text{-}C_{Zmin})$ [Å]	$2 \cdot 10^{-4}$	$14 \cdot 10^{-4}$

Table 4.7: In this table are collected geometric characteristics of the systems (a graphene monolayer on metallic substrates). These points indicate the distance at the graphene layer places and the low corrugation induced on the metallic surface and the graphene layer.

The energy is not showed in the Table 4.7 because we talk about it in different systems formed by graphene and platinum or gold in the 4.5 section. This part serves mainly to observe the organization of the carbon atoms and how the graphene layer separates from the substrate until a preferred distance.

To conclude, the Table 4.8 summarizes the values of the section 4.4. There, we have considered that the displacements of atoms lower than 1 Å are not significant. These values are indicated in the table with a “no”. On the other hand, the E_{ads}/N_C, the metallic surface corrugation and the distance between the carbon atoms and the substrate are plotted in Discussion (Section 4.6) for a better visualization (Fig 4.23). There, the tendency is easier to observe. The difference of z distance between the carbon atoms is not plotted because most of these differences are lower than 1 Å, and the only case higher (1.3 Å for 4C/Au (111)) is not a big value.

In the most of the cases for Pt (111), the surface does not corrugate with the adsorption of carbon atoms, except for the case of 6 carbon atoms. However, the displacement of the platinum atom is due to the formation of a hexagonal structure by the combination of them with carbon atoms. In the gold case, the metallic corrugation of the surface is higher than Pt (111). The reason is the formation of carbon-gold compounds as we observe in the images (Fig 4.13-Fig 4.16). On the other hand, it is possible to see the tendency to increase the distance between the carbon atoms and the substrates as the number of adsorbed atoms increase.

	Pt (111)					
	1C	2C	3C	4C	6C	8C
E_{ads}/N_C [eV]	-7.58	-1.00	-0.47	-3.80	-0.82	-
Metallic surface corrugation [Å]	No	No	No	No	1.9	No
$D_z(C_{Zmin}$-Sub) [Å]	1.1	1.2	1.2	1.1	2.1	3.8
$D_z(C_{Zmax}$-$C_{Zmin})$ [Å]	-	No	No	No	No	No
	Au (111)					
	1C	2C	3C	4C	6C	8C
E_{ads}/N_C [eV]	-5.83	-2.82	-0.91	-4.43	-0.50	-
Metallic surface corrugation [Å]	No	1.2	1.6	No	2.0	No
$D_z(C_{Zmin}$-Sub) [Å]	1.3	1.5	1.8	2.3	2.8	3.2
$D_z(C_{Zmax}$-$C_{Zmin})$ [Å]	-	No	No	1.3	No	No

Table 4.8: A summary of the different values for the six systems analyzed in the section 4.4. For the case of 1C atom, we have indicated the values of FCC position.

4.5 Graphene on metallic substrates: Moires

As mentioned above, the moiré is a super-structure formed as the result of placing two hexagonal structures with different angles or periodicities. In the sections 4.2 and 4.3, we observe the existence of several moirés formed by rotations of graphene on Pt (111) or Au (111).

On platinum, the LEED pattern shows a super-periodicity at 19° (Fig 4.2) indicating the main orientation of the graphene patches. The angle corresponds with one of the most common moirés of graphene on platinum, however, in the STM images, we observe more graphene orientations as the Fig 4.4b (the atomic resolution image). This image shows a moire with an apparent angle of 16.5°, which is obtained by rotation of the graphene 2° respect to the platinum surface.

On the other hand, on gold, the LEED pattern shows two main orientations at 0° and 30° (Fig 4.5.). In the STM image, we verify the existence of the moire of 0° (Fig 4.7c). In these pictures (in Pt (111) and Au (111)), Moirés can give a misleading impression as that graphene is corrugated, however, our calculations determine that graphene is mainly flat.

Therefore, we have performed DFT calculations of graphene on Pt (111) and Au (111) collecting the moirés observed in the above sections, in such a way, the same moires have been studied with Pt (111) and Au (111) to a better comparison: (i) **0°:** Graphene is rotated at an angle of 0° with respect to the substrate, and the moire is observed as a 7 × 7 super-cell of the substrate; (ii) **2°**: graphene is rotated at an angle of 2° with respect to the substrate, the moire is represented by the

matrix $\begin{pmatrix} 3 & -1 \\ 1 & 2 \end{pmatrix}$ forming a cell close to 7 × 7; (iii) **19°:** graphene is rotated at an angle of 19° with respect to the substrate. This moire shows the smallest super-periodicity corresponding to √7 x √7 and (iv) **30°:** Graphene has rotated at an angle of 30° respect to the substrate forming a moire of 3 × 3 unit cells of the substrate.

In these calculations, the moirés have been studied using the super-cells related with their periodicities. The computational details are mainly the same as in section 4.4 with some exceptions: in this part, we have used local density approximation (LDA) as exchange-correlation functional and the energy cutoff is 300 eV in all models except in the case of 0° for Pt (111) with an energy cutoff of 350 eV.

The Monkhorst-Pack grid employed to get the convergence in each moire of Pt or Au varies according to the type of structure. In Table 4.9, they are summarized and related to the kind of moire, the super-cell employed in the geometric optimization and the cell parameters used after the cell optimization of the bare substrate for every case. In this section, we have used three layers of the substrate for every case. Some of the moirés are huge, and we had to decrease the number of atoms, therefore we have used one layer less than in the previous section (4.4)

Type of moire	Super-cell	Number of atoms	Cell parameters		Monkhorst-Pack grid	
			G-Pt	G-Au	G-Pt	G-Au
0°	7 x 7	275	a,b = 18.9 Å c = 20.0 Å α,β = 90° γ = 120°	a,b =19.8 Å c = 20.0 Å α,β = 90° γ = 120°	1 × 1 × 1	1 × 1 × 1
2°	7 x 7	269	a,b = 18.7 Å c = 24.0 Å α,β = 90° γ = 60°	a,b = 19.9 Å c = 24 Å α,β = 90° γ = 60°	2 × 2 × 1	1 × 1 × 1
19°	√7 x √7	39	a,b = 7.2 Å c= 20.0 Å α,β = 90° γ = 120°	a,b = 7.4 Å c = 20.0 Å α,β = 90° γ = 120°	4 × 4 × 1	4 × 4 × 1
30°	3 x 3	51	a,b = 8.1 Å c= 20,0 Å α,β = 90° γ = 120°	a,b = 8.5 Å c = 20,0 Å α,β = 90° γ = 120°	2 × 2 × 1	3 × 3 × 1

Table 4.9: The table collects the cell parameters used for the four moires with the Graphene-Platinum (111) [G-Pt] and Graphene-Gold (111) [G-Au] systems, the number of atoms and the size of the super-cells corresponding with each ones and the Monkhorst-pack grid used in the different calculations.

The final appearance of the systems after the geometric optimization is shown in Fig 4.18. The pictures are ordered increasing the rotation angle of the graphene. The observed super-periodicity of the moiré for Fig 4.18a is remarkably visible because the graphene corrugates a lot forming large bubbles (it is observed in detail in Fig 4.19). In the bibliography [81] it seems that this moire on platinum (0°) can be given experimentally from a geometric point of view, however, it is not reported. The reason why it appears here is because we have obtained it for gold as substrate. However, the behavior of this structure in Pt (111) and Au (111) is completely different.

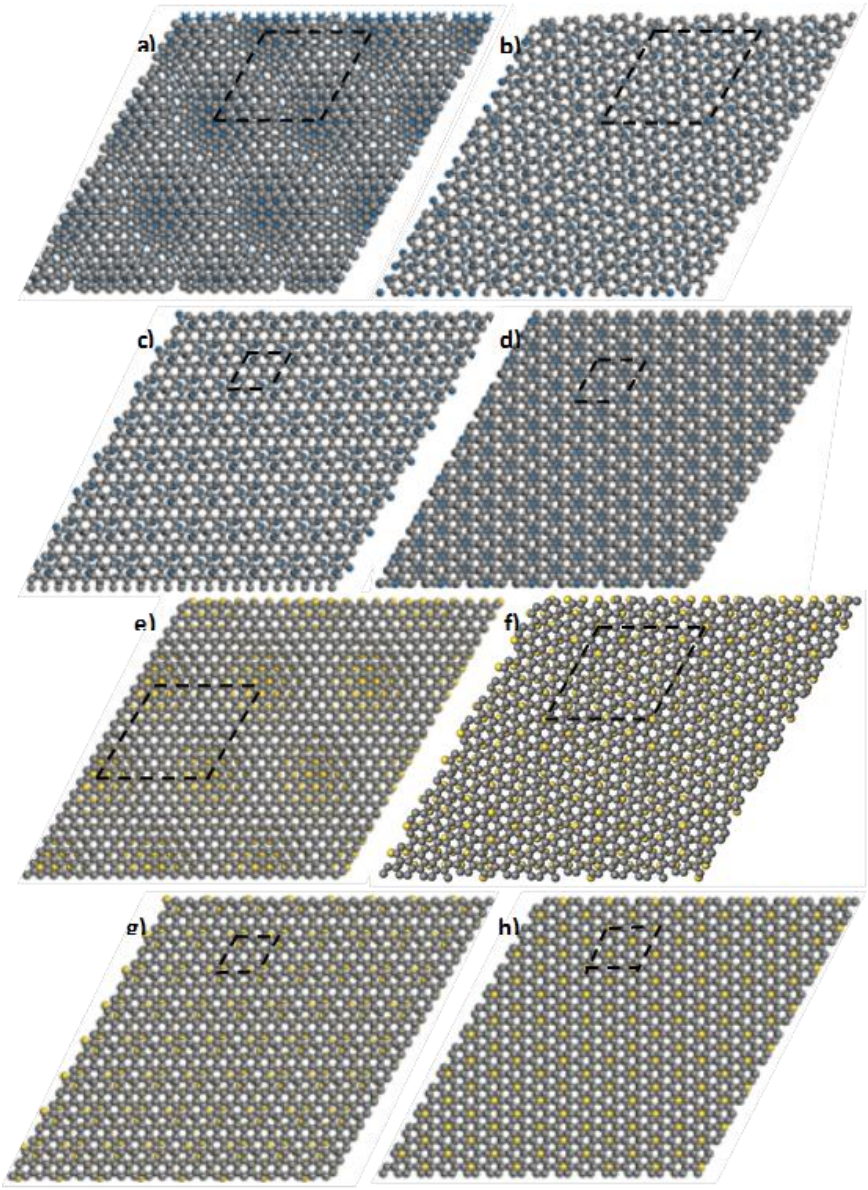

Fig 4.18: Top views of the various systems compared in this section. The images are formed with the graphene layer and the last layer the substrate. In the upper side (a - d) the final structures for the moires with platinum as substrate are showed (platinum atoms correspond to the blue balls) and on the lower side (e - h) the same cases with gold as substrate are presented (gold atoms are the yellow balls). Graphene is represented with a gray color and the black lines indicate the supercell of the moires. The type of the moire in each figure is: a) and e) are the moire of 0°; b) and f) correspond to the moire of 2°; c) and g) show the moire of 19° and d) and h) are the moire of 30°.

The distances between the graphene layer and the substrate and the graphene corrugations of the Fig 4.18 are collected in the Table 4.10. The 0° case for G-Pt shows a large corrugation due to the large bubbles mentioned above. In the other situations, the corrugation is much smaller; one reason is that graphene is maintained at a minimum distance of 3 Å of the substrate, so the interaction between them should be weak. In these structures, the substrates (platinum and gold) have not suffered deformations (excluding the 0° for platinum).

	G-Pt		**G-Au**	
Moire\Substrate	Distance [Å]	Corrugation [Å]	Distance [Å]	Corrugation [Å]
0°	3.45	2.52	3.23	0.01
2°	3.17	0.10	3.09	0.09
19°	3.39	0.03	3.21	0.005
30°	3.23	0.01	3.22	0.006

Table 4.10: Graphene-to-substrate distances and graphene corrugation. Distances are measured in the z direction, thus it is equivalent to consider the distance in z-direction between two planes: one plane defined by the graphene layer and the other one forming by the topmost layer of the substrate. In the particular case of 0° G-Pt, the distance corresponds to the average distance between the carbon and platinum atoms, and the corrugation is the distance between the highest carbon atom and the lowest in the layer of graphene.

The corrugations and the distances observed in the Table 4.10 are lower on the gold substrate than on platinum for the same moire (excluding the 0° for the platinum case). Moreover, the minor value for the corrugation corresponds to the moires of 19° and 30° on both substrates, it seems a tendency that moires with a lower periodicity show a lower corrugation in the graphene layer.

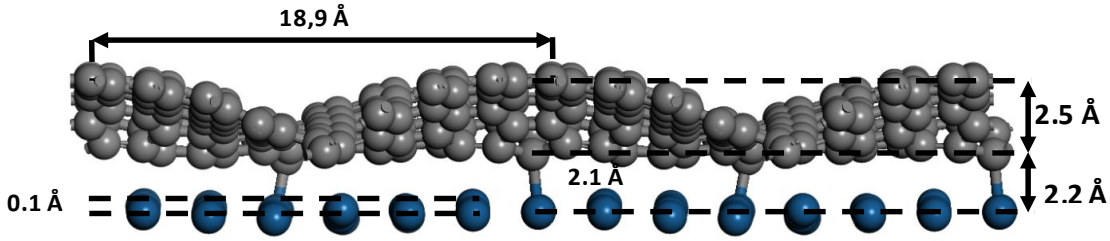

Fig 4.19: Picture shows graphene on the last layer of platinum forming the moire of 0°. The periodicity of moire corresponds to 7x7 cell of the substrate (18,9 Å). Graphene is deformed during the geometry optimization showing a huge corrugation. The platinum surface is corrugated in the opposite direction (anti-corrugation) making the closer distance to be 2.1 Å to the graphene. Bond distance corresponds to the distance between these two atoms, and the distance graphene-to-platinum is the separation in the z-direction.

All graphene layers are at a distance between 3,1 to 3,4 Å approx of the substrate. In the case of G-Pt for 0°, the value of the Table 4.10 indicates the average distance between the carbon and the platinum atoms. In that case, the value is 3.4 Å because the graphene shows large ripples. Thus, as shown in Fig 4.19, the corrugation of this system corresponds to 2.5 Å indicating that the nearest carbon atom to the platinum is at 2.2 Å and the farthest atom at 4.7 Å approx. On the other hand, the z distance of 2.2 Å (actually, the bond distance is 2.1 Å; Fig 4.19) indicates that at least, this carbon atom is at a distance to bond with the platinum atoms of the surface. It is the reason that these carbon atoms appear linked to the platinum ones in the Fig 4.19[95].

In Fig 4.18 it is very complicated to observe the moire pattern. So we have simulated the STM images of the eight systems using CASTEP (Fig 4.20). These simulations make the comparison easier with the experimental STM pictures and let us analyze the main difference between the moirés and the substrates.

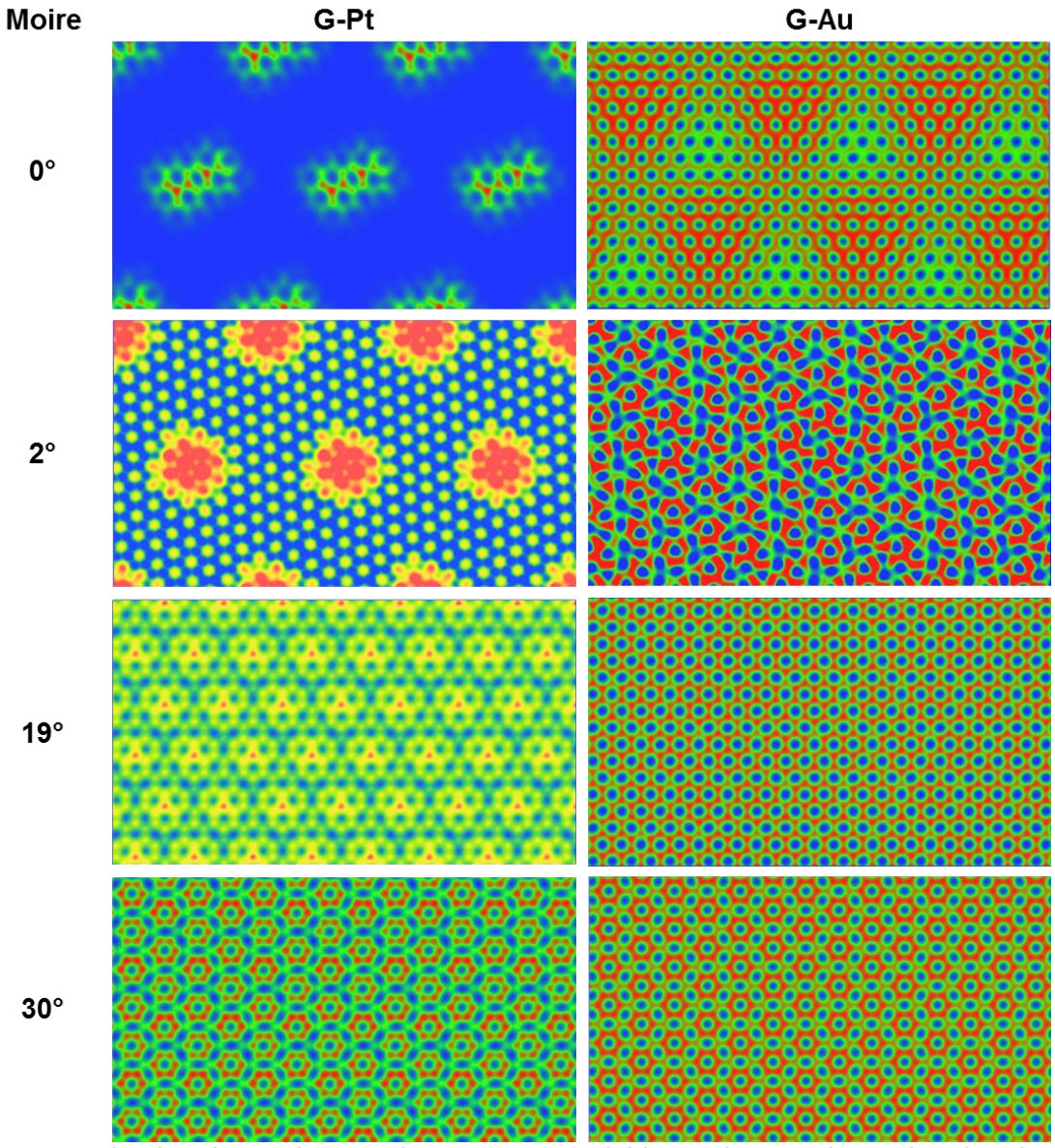

Fig 4.20: Simulated STM images for every case of this section. Each one is related to the type of moire and the substrate when increasing the rotation angle of the graphene.

In all the images for G-Pt we have established an STM bias of 3.5 V, and for gold, we have used 0.11V. These values have been chosen because they are the bias values of the experimental images Fig 4.4b and Fig 4.7c. The color settings indicate that the blue areas are the deepest zones and the red regions correspond to the highest zones.

For G-Pt, the images show a clear moire pattern in all cases, especially for 2°. The 0° case only shows a non-zero signal in the upper carbon atoms of the graphene areas. This is due to the large corrugation explained above. However, for G-Au there is definitively a moire pattern for 0° and 30° in correspondence with the experimental part. As an example, 2° for G-Au does not exhibit any clear pattern, and 19° does not show a super-periodicity, so the STM simulation image presents the structure related to a graphene layer.

In these systems, the adsorption energy (E_{ads}) has been calculated following the Eq. 4.3.

$$E_{ads} = E_{G/Subs} - (E_G + E_{Subs}) \qquad \text{Eq (4.4)}$$

where $-E_{G/Subs}$ corresponds to the total adsorption energy of the system, E_G the energy of a graphene layer calculated at the same geometry of the total system without substrate and E_{Subs} the energy of the relaxed substrate, either Pt (111) or Au (111). Therefore, the definition of E_{ads} denotes that a negative value is in agreement with a favorable adsorption.

The adsorption energies of the different systems are contained in Table 4.11. Every described system is formed by several number of atoms so, for a better comparison, the adsorption energy per atom (E_{ads}/N_{atoms}) is more adequate. The adsorption energy by atom can be used because the number of carbon atoms is proportional to the number of substrate atoms, moreover, in all cases, we have used the same number of layers for each substrate.

Moire\Substrate	Platinum (111)		Gold (111)	
	E_{ads} [eV]	E_{ads}/N_{atoms} [eV]	E_{ads} [eV]	E_{ads}/N_{atoms} [eV]
0°	-6.03	-0.02	-4.45	-0.02
2°	-2.82	-0.01	-8.73	-0.03
19°	-0.57	-0.01	-0.71	-0.02
30°	-1.16	-0.02	-0.79	-0.02

Table 4.11: Values of adsorption energy and adsorption energy per atom according to the type of moire. Bold letters emphasize the energy values for the experimental cases.

The negative values mean that the formation of these structures is energetically favorable. Bigger absolute values indicate that the systems release more energy. As a reminder, we obtain experimentally the moirés of 2° and 19° for Pt and 0° and 30° for Au. Their energies correspond to the lower absolute values of adsorption energy per atom, so the adsorption energy values indicate that the moirés not observed in the experimental part can be formed experimentally and they release more energy during the geometry stabilization. On the other hand, LEED pattern provides an average of the contributions of the different moirés formed on the surface and the brightest areas of the graphene ring indicate the orientations of the most common moirés obtained, but more types can be formed on the surface. Therefore, we can deduce that adsorption energy per atom (Table 4.11.) can establish the possibility of the formation of a kind of moire (by the sign), but it is not definitive to conclude which (one) is the most common moire.

The stress of the systems can give us another perspective of the trend of the formation of these moires on platinum and gold. The values for each are in Table 4.12. In platinum, lower stress corresponds to the moire of 0° but, in that case, the graphene has a strange behavior forming large ripples, whereby the carbon atoms have been placed in positions where they are more relaxed reducing the stress of the system. On the other hand, other values for G-Pt vary between 0.4 to 1.1eV/Å^2 approx and they correspond to the two lowest moirés obtained experimentally (2° and 19°). The same behavior is observed in G-Au, the moires of 0° and 30° are

experimentally showed, and the stress values are the lowest with -0.03 and 0.04 eV/Å^2 respectively. Thus, we can conclude that the lowest absolute values of stress are related to the possibility to appear experimentally if the geometry of the system is adequate. The sign of stress indicates if the system extends or not.

Moire\Substrate	G-Pt [eV/Å^2]	G-Au [eV/Å^2]
0°	0.11	-0.03
2°	0.58	-0.19
19°	0.39	-0.20
30°	1.10	0.04

Table 4.12.: Stress values for the graphene-substrate structures for the four moiré

4.6 Discussion

We have grown graphene on two metals with different properties. For that reason, graphene appears with different appearance and forming different moirés. During the process, we have adapted the system to the substrate used. This way, we have annealed the substrates at different temperatures and reported the lower temperature to achieve graphene formation. As a reminder, for Au, the temperature is 823 K, and at this temperature, on Pt, we only obtain a disorder carbon layer. In fact, to get an ordered graphene sheet on Pt, we need to increase the temperature up to 923 K.

This difference can be understood with the calculations of the diffusion barriers for C on both substrates. By using a Linear Synchronous Transit Method, we find that the diffusion barrier for C on Au is 61 meV lower than on Pt.

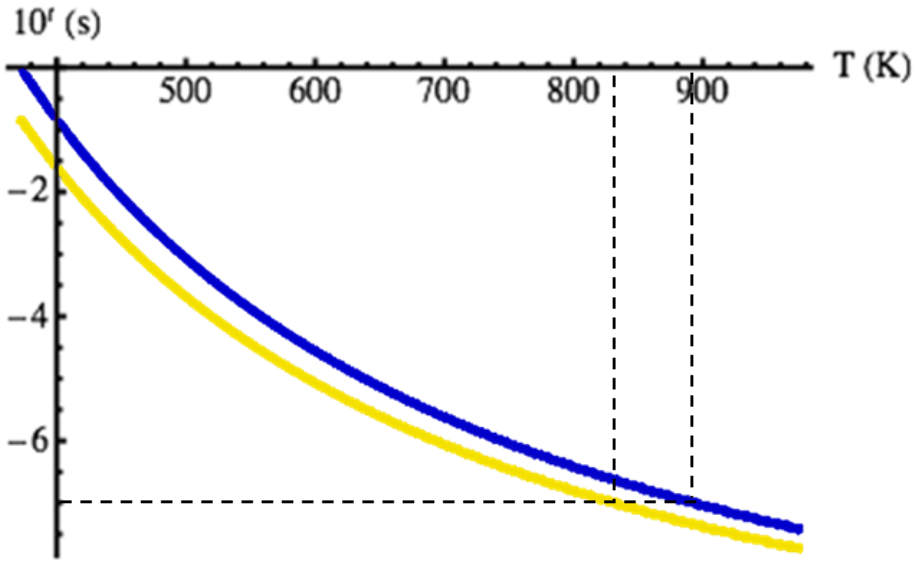

Fig 4.21: Diffusion barrier for one carbon atom on platinum (blue) or gold (yellow) as a function of the temperature. The dashed lines highlight the different temperature needed in each substrate for the same time period.

The Fig 4.21 represents an estimation of the time needed as a function of temperature for a carbon atom to jump from one cell to a neighbor one for both substrates: platinum (blue) and gold (yellow).

By observing the graph, at a given temperature, e.g. 823 K, it takes about 100 ns for a C atom on Au (yellow) to jump from one cell to a neighboring one. Tracing an horizontal line (dashed line in the figure), we observe that a temperature higher by approximately 60 K is needed to get the same rate on Platinum. This is in reasonable agreement with the experimental part in which we increase 100 K approximately for platinum. Moreover, it is interesting to notice that the lower diffusion barrier on Au is partly due to the higher mobility of Au atoms on the last surface plane (ductility).

On the other hand, it is important to understand that the difference between the graphene formed on gold or platinum is coming from the diffusion of carbon atoms at the edge of graphene sheets. Once the graphene is formed, the carbon-carbon interaction dominates as the graphene sheets are located far away from both substrates (more than 3 Angstroms). The higher temperature formation for the platinum substrate results in a higher carbon diffusion at the graphene islands perimeter, producing a rounded shape for graphene on platinum. On the other hand, carbon atoms forming graphene on gold diffuse slower, as the temperature is almost 100 K lower (823 K), and the shape of the islands remains close as the one first formed, showing a dendritic shape.

Moreover, taking account the section 4.4, the bonding energy for C-C (-6.4 eV) is more favorable than C-Au (-4.7 eV) (the energy value for C-Au was calculated using a singlepoint with CASTEP code). However, this difference is not so big respect with platinum (-5.9 eV). So a carbon atom on gold, with a lower diffusion, easily bonds with another carbon atom resulting in a fractal shape. However, on platinum, the carbon atom links with three platinum atoms in most of the cases, as it is placing the platinum lattice positions (from 4.4.2 to 4.4.4 subsections). Thus, the adaptation of the carbon atoms to the platinum lattice, the low energy difference between the C-C and C-Pt bonds (0.5 eV) and the bigger diffusion of carbon on the platinum surface due to the higher temperature used makes the C-Pt bond be more possible than a C-C link. This way, the Fig 4.22 shows the energy by adsorption of a new carbon atom in a system. The energy values has been calculated by

$$E = E_{nC/Pt} - (E_C + E_{(n-1)C/Pt}) \qquad \text{Eq (4.2)}$$

In such a way, we obtain the energy by adsorption of a new carbon atom in a 2×2 cell of platinum with at least, one carbon atom on the surface. So $E_{nC/Sub}$ is the adsorption energy of the final system formed after the adsorption (we have calculated for 2C, 3C, and 4C), $E_{(n-1)C/Pt}$ corresponds to the energy before adsorption (1C, 2C or 3C respectively) and E_C is the energy for one carbon atom. These values have been obtained from the table of the 4.4 section. For the case of the adsorption of the second carbon atom, we start with the energy of one carbon atom in B position on Pt (111).

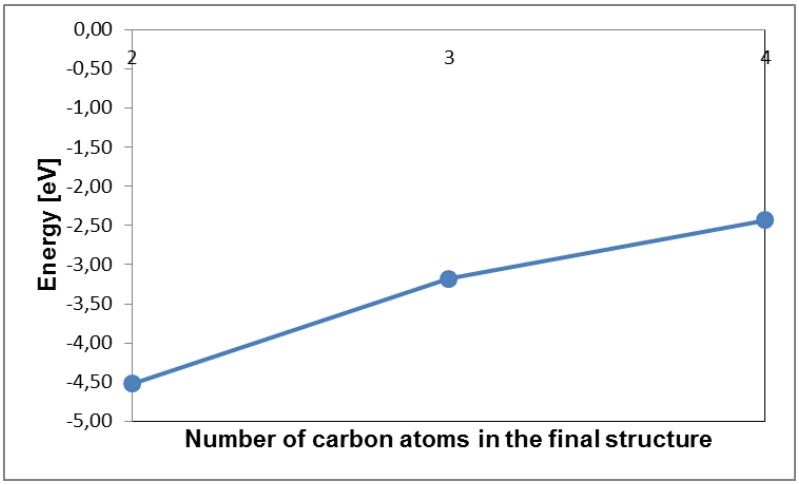

Fig 4.22: Representation of the adsorption energy by adding one carbon atom more on a platinum 2×2 cell with one, two or three carbon atoms on it.

In the Fig 4.22, the absolute value of the energy decreases as the number of carbon atoms increases. It is because the adsorption of a new carbon atom is more difficult as it increases the number of them. The carbon atoms place in platinum position (from 4.4.2 to 4.4.4 subsections) forming a fictitious platinum layer until they are too much. At that moment, the C-C bond prevails forming a ring and, the platinum atoms are included in a hexagonal framework as a fictitious graphene layer (4.4.5 subsection).

On gold, as the C-C bond is dominant, the structures are different and show a trend to form carbon species (a chain in 4.4.3 and a cycle-butane in 4.4.4. subsections) linked with gold by the ends.

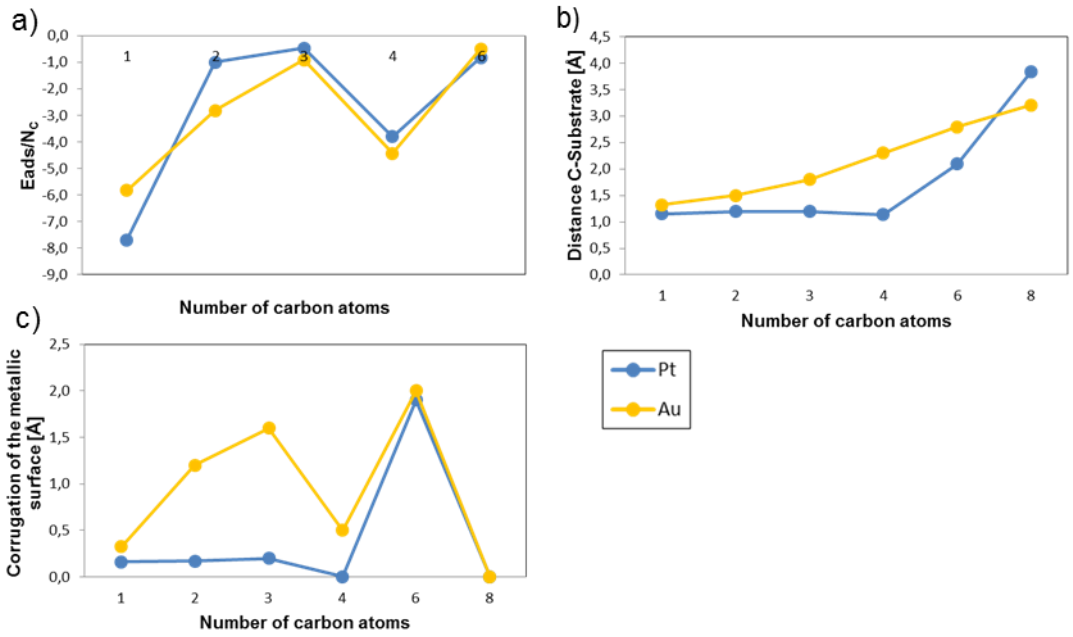

Fig 4.23: Visual summary of section 4.4. a) Evolution of the adsorption energy by atom from one to six carbon atoms on platinum (blue) and gold (yellow) b) Plot of the distance between the carbon atoms until a graphene layer and platinum or gold c) representation of the induced corrugation of the metallic surface as the number of carbon atoms increase.

In Fig 4.23 a summary appears of the values of section 4.4. It is possible to observe a change in the trend for the adsorption energy by atom and for the corrugation of the metallic surface for the case of four carbon atoms on both substrates. However, the distance to the substrate increases with the number of carbon atoms, showing an almost linear behavior for the gold case and an exponential appearance for platinum.

In the four carbon case (4.4.4 subsection) the adsorption energy increases. On platinum, four carbon atoms link with three platinum atoms completing the positions of a first layer of the platinum surface. From that perspective, the first layer of platinum atoms is comfortable because the atoms are acquiring a place in good correspondence with a second layer, so they move slightly from their initial positions and they don't produce any corrugation. On gold, the four carbon atoms try to form a cycle-butane creating different bonds between them and with the gold atoms of the surface. The gold atoms force the cycle-butane to be in torsion and at the same time, the carbon atoms attract the gold atoms to change their initial positions, but less than other structures.

The corrugation of the gold surface increases with the number of carbon atoms in the system. In that process, different structures are formed by the combination of carbon and gold atoms until the graphene layer be built. Once the graphene layer is formed, the corrugation decreases dramatically because the carbon atoms are comfortable forming graphene and therefore they stop forming links with the gold atoms of the surface. On platinum, to a lesser extent, the behavior is similar.

Finally, we can compare de STM images obtained experimentally with the ones calculated using the CASTEP simulation of the moiré models (4.5 subsection). As a reminder, we observe the moirés of 2° and 19° for Pt (111) and 0° and 30° for Au (111). It is easier to compare the G/Pt images because we obtained larger moirés areas and atomic resolution. This way, the Fig 4.24a shows different moirés of G/Pt (111) separated by boundaries in the same image. These moirés are placed individually next to the corresponding simulated image in Fig 4.24b or Fig 4.24c. The Fig 4.24b corresponds to 19° moiré, and it is possible to observe in the simulated image a small periodicity of the moiré bumps and low contrast between

the intensity of the picture. For these reasons, the corresponding STM image (placed at the same scale than the simulated one) doesn't let us observe the moiré pattern. The Fig 4.24c (moiré of 2°) shows a bigger periodicity for the moiré bumps (almost three times larger than the moiré of 19°) and the contrast is higher, so it is easier to observe the similarity between the simulated and the experimental pictures. For that purpose, the experimental one is superposed to the simulated. There, the experimental distance between the moiré bumps is 2.1nm approx., however, the theoretical distance is 1.9 nm (marked in Fig 4.24c), so the difference is 0.2 nm. That value is low enough to be within the experimental error of the STM measurements.

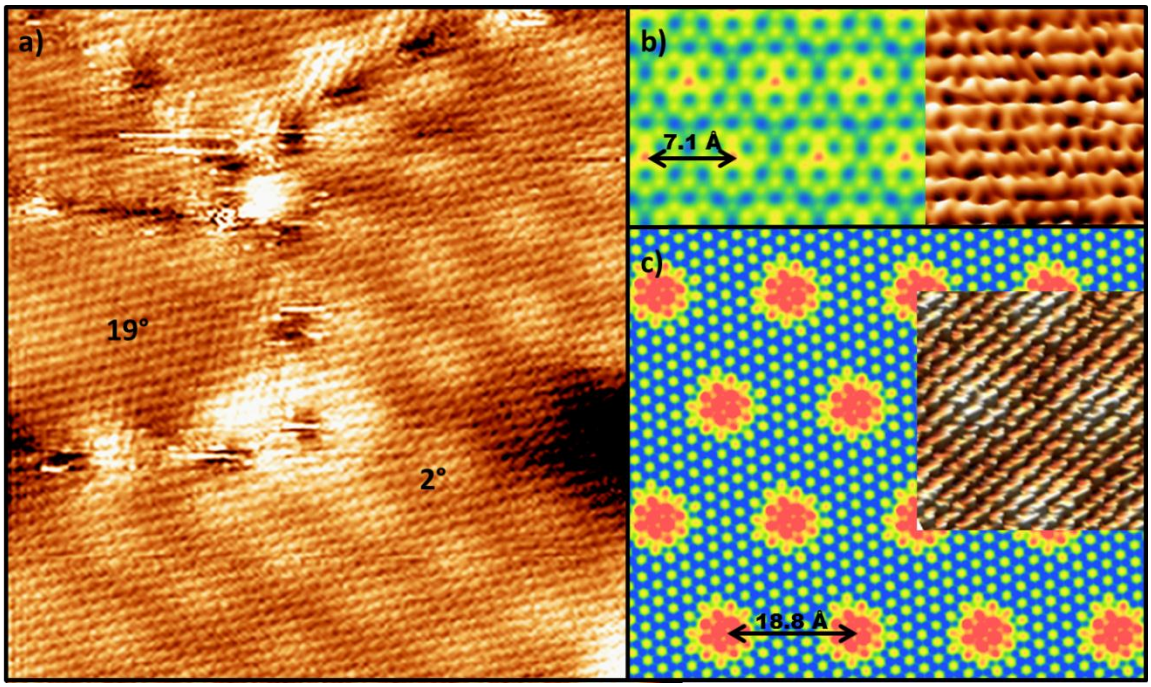

Fig 4.24: a) The STM image shows two different moirés of G/Pt separated by boundaries. Each type is labeled on their area. At the right side the two are placed separately beside the corresponding simulated image; b) The STM simulated image of the moire of 19° next to the experimental one at the same scale; c) a small experimental image of the moiré of 2° inserted into the simulated at the same scale to observe the adequate comparison between them.

Discussion

On gold, we have a similar situation. The moire of 0° has larger periodicity than the moire of 30°. In fact, the second one shows the smallest periodicity between the four types (Fig 4.25b). Thus, it is too small to be observed in STM images, although it is visible in LEED pattern (Fig 4.5). However, the moire of 0° has a bigger periodicity (similar to the moire of 2° for platinum) and enough contrast to be observed with both techniques. In Fig 4.25a an STM image of 12x12nm is presented. Besides, we show the corresponding simulated image with the same scale. There, it is possible to observe that both show a moire of similar size. The distance between the experimental moiré bumps is 1.9 nm approx in agreement with the almost 2.0 nm of the simulated image.

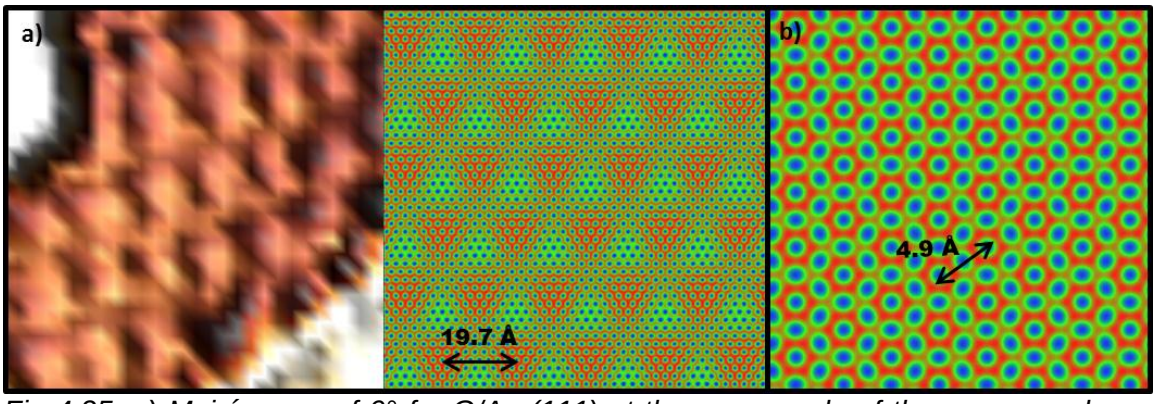

Fig 4.25: a) Moiré zoom of 0° for G/Au (111) at the same scale of the correspondence simulated image at the right side; b) Simulated image of the moire of 30°. The periodicity is too small and with low contrast to observe experimentally. However, the LEED pattern indicates that it is one of the most common moirés obtained.

5. Graphene on Diamond

5.1 Introduction

Graphene is a promising material for the performance of electronic devices. However, those devices have to be supported by a substrate which does not modify the graphene properties. In most cases, it is necessary to transfer the graphene from the substrate where it is grown to another substrate for the application. However, the transference of graphene has many disadvantages, as the graphene properties can be altered or diminished[96,97]. So it is necessary to find an adequate substrate to grow graphene directly on it.

Up to date, different substrates have been used to growth graphene, as metallic substrates or semiconductors. The main problem of the metallic substrates is the strong interaction between the graphene and the metal, so the transport properties are altered. The semiconductors more used are carbides as SiC[97–99] or oxides as SiO_2[100–102], but the graphene growth on them suffers additional scattering from charged surface states and impurities[103,104], the roughness of the substrate surface [105] and surface optical phonons[106]. All this involve a deterioration of the devices.

Diamond, however, is a natural candidate to be an adequate substrate because it has excellent properties, such as low charged surface states, unparalleled hardness, chemical inertness, few impurities, high phonon energy, thermal conductivity, and electron mobility[107]. For these reasons, graphene on diamond have attracted much attention[96,102,108–114].

In this work, we have used two different surfaces of single diamond crystals: diamond C (111) and diamond C (110). Diamond C (111) is a synthesized and Boron doped single-crystal. The graphitization of this surface by annealing is well

known[115–118]. In fact, the diamond C (111) and graphene lattice closely match (projected carbon-carbon bond in diamond is 2% bigger than graphene), so this diamond surface is the most used to have graphene on it[108,110,111,117,119–121]. On the other hand, we have used two synthesized diamonds with a (100) surface, the first doped with boron and the second with nitrogen. This surface is completely different to the graphene lattice, so it has not been used before to grow graphene on it, and the graphitization of the surface is not reported.

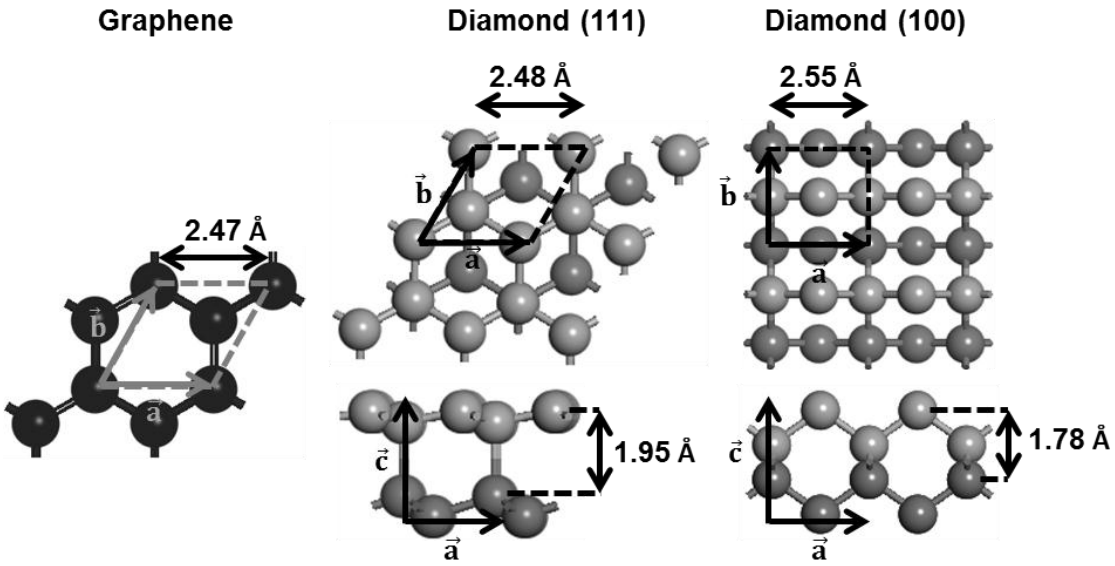

Fig 5.1: Representation of graphene, diamond C (111) and diamond C (110) structures. Dashed lines represent the unit cell. The carbon-carbon distances corresponding with the $|\vec{a}|$ and $|\vec{b}|$ cell values and the distances between diamond planes are indicated on the picture. The second layer of diamond is darker for a better visualization.

As we mention above, in Fig 5.1 it is possible to observe the similar structure of graphene and diamond C (111) from a $\vec{c}$ view. They are entirely different to the diamond C (100) structure which it is square, so at first, it is easier combine the graphene and diamond C (111) structures than graphene and diamond C (100). On the other hand, in the across view, we can see how every diamond layer is

formed by two different heights. In other words, every diamond layer is a bilayer preserving the sp^3 structure.

Few articles have reported the growth of graphene on diamond. The most common method is the diamond C (111) graphitization as we mention above. In fact, it has been used an iron layer on the diamond to favor the graphitization at lower temperatures[121]. Other authors have also reported the use of CVD method to obtain graphene on diamond C (111)[122,123] or the graphite exfoliation and the subsequent deposition on diamond C (100)[102]. The diamond C (111) surface graphitizes easily. For example, the argon ion bombardment damages the surface and the surrounded areas are partially graphitized, or the heating of the diamond up to 1773K at 1.3×10^{-10}mbar produces graphitic carbon on the surface[107] . That reason limits the way of cleaning the surface, so we find the better way of cleaning the diamond surface is ex-situ using the procedure described in section 2.6.2.

5.2 Graphene on Diamond (111)

After cleaning the diamond surface, we introduce it in the Ultra High Vacuum chamber, and then the sample is annealed at 1273K until the pressure is lower than 1×10^{-9} mbar. The LEED in Fig 5.2a corresponds to the clean diamond C (111). The corners of the red hexagon indicate the spots of the unit cell.

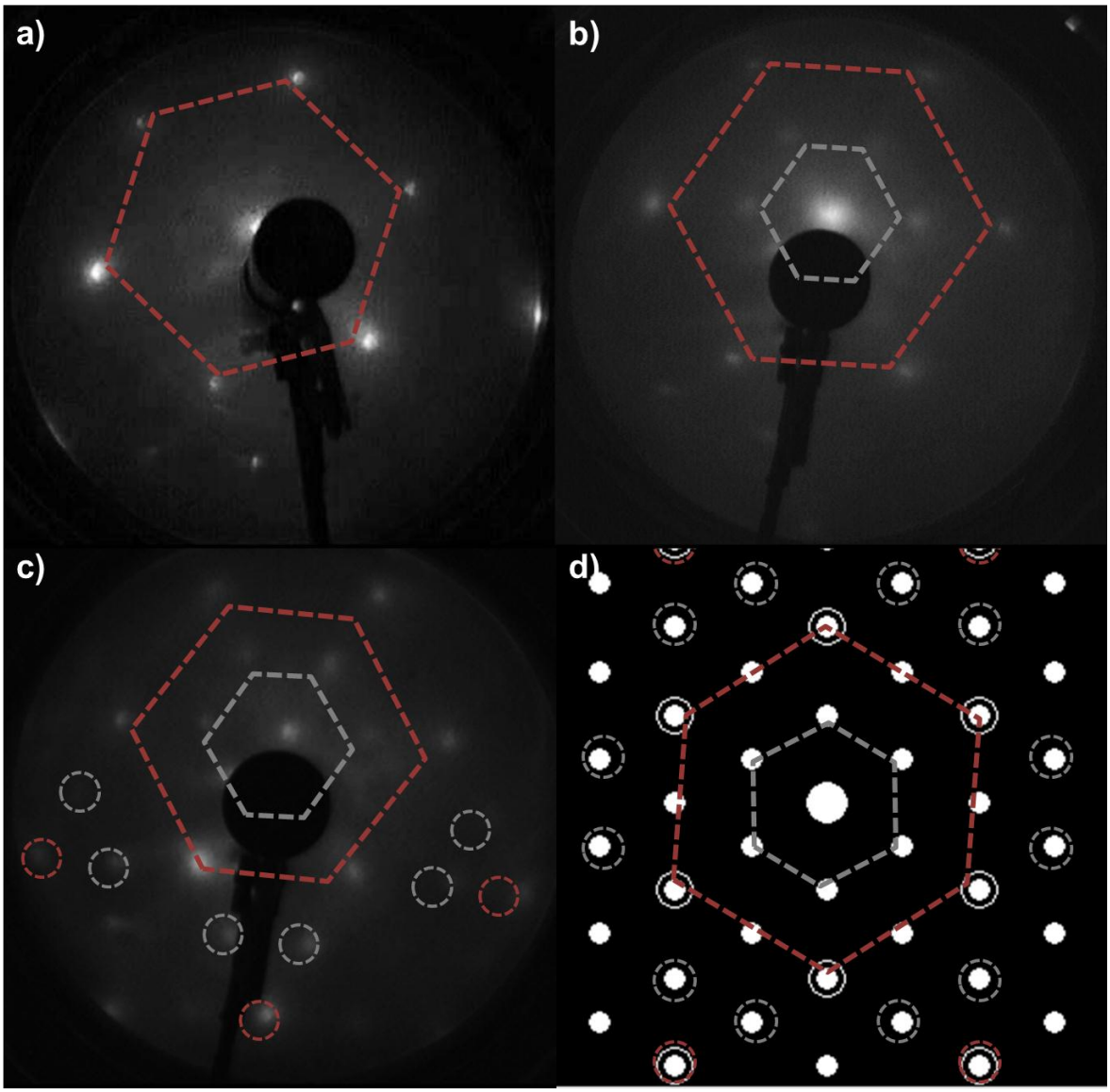

Fig 5.2: a)LEED pattern of the clean diamond C (111) surface. It was taken at 105 eV; b)

LEED image after graphene growth (104eV) forming a p(2x2) pattern. New spots are indicated with a gray hexagon; c) p(2x2) pattern at higher energy (139 eV) showing the spots of second order marked by circumferences; d) LEEDpat representation of a p(2x2) LEED pattern of an hexagonal lattice. The same code is used in the four pictures: red for diamond, gray for graphene, a hexagon for the spots of first order and circumferences for the second ones.

The graphene growth was performed for 30 minutes. Simultaneously, the diamond was annealing at 1473K. That heating is maintained until recovering a pressure lower than 5×10^{-9}mbar, so the diamond cools down better the lower the pressure. The LEED pattern has changed to a p (2×2) (Fig 5.2b/c). The Fig 5.2b indicates the spots related to the diamond C (111) surface with the red hexagon and the new ones corresponding with the graphene with the gray hexagon. The same colors are used in Fig 5.2c. That LEED pattern is at a higher energy to obtain the spots of the second order. They are surrounded by circumferences. In both schemes, the spot corresponding to (0,0) is off-axis to observe better the new spots of the p(2x2). Fig 5.2d is a representation of a p (2x2) cell made with the LEEDpat software[124]. The pattern is similar to Fig 5.2c except for some spots that can not be observed in the experimental image. The main reason of this effect is the bad quality of the old LEED screen, making the experimental contrast to be not so good in some regions.

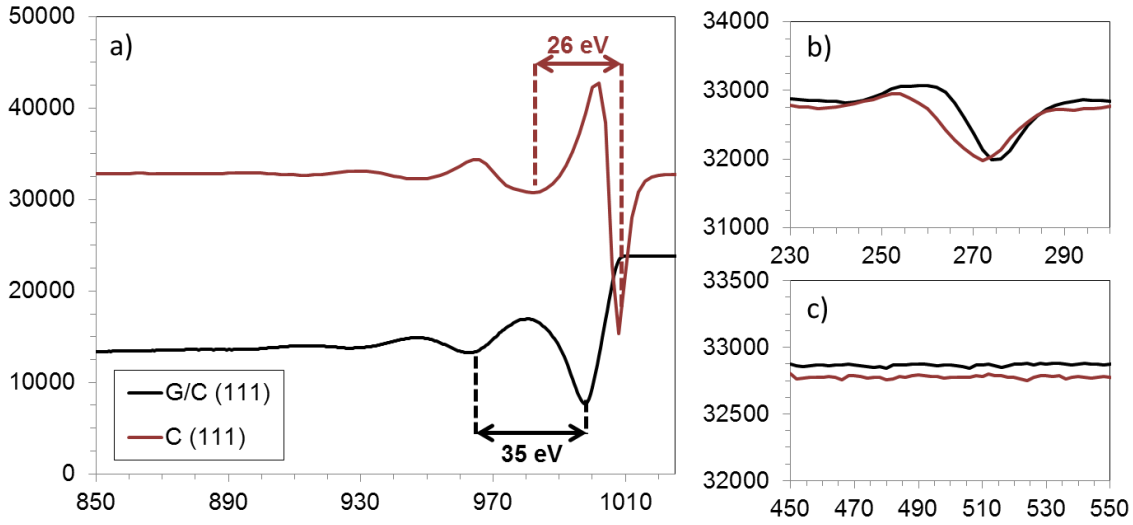

Fig 5.3: AES spectra comparison of clean diamond C(111) (red) and graphene on diamond C (111) (black) in different regions: a) elastic peak around 1000 eV and electron energy losses peaks; b) carbon peak at 272 eV; c) oxygen area (510 eV) exhibiting that the sample does not have that substance on the surface.

The AES spectra indicate that the sample is made of carbon and it does not have another substance. The peak related with Boron (the dopant) does not appear, so it must be lower than the limit sensitive of the AES system (around 5% of the surface). In Fig 5.3 we have compared the spectra before and after growth. Fig 5.3b and Fig 5.3c show the region of the carbon and oxygen peak respectively. There, we observe the existence of the carbon peak (272 eV) in the diamond (red) and the graphene/diamond (black) spectra, however, in the oxygen range peaks do not appear (the oxygen peak should be at 510 eV). We exhibit this oxygen range because it is one of the more common peaks to determine that the surface is dirty. Based on the EELS technique, the AES spectra of Fig 5.3a exhibit the elastic and the energy loss peaks. The difference between them determines a change in the surface structure[125]. Here, the energy loss peak after growth has moved away from the elastic peak so, the energy difference increases from 26 ± 1 eV to 35 ± 1 eV as it is indicated in the picture. The error is estimated from the step interval of energy used in these scans (1 eV). Several studies have been reported about the use of EELS technique to obtain information of sp^2 and sp^3 carbon hybridizations in thin

films[125–127]. Between them, one article[125] compares the wide of the plasmon losses peak of bulk graphite (27.5 eV), a graphitic film (25.5 eV) and a CVD diamond (22eV). Despite having different values to ours, the peak of electron energy losses changes from diamond to graphite moving away from the elastic peak. This fact is also observed in the literature as a displacement due to the change from the initial sp^3 structure to a sp^2 one[126].

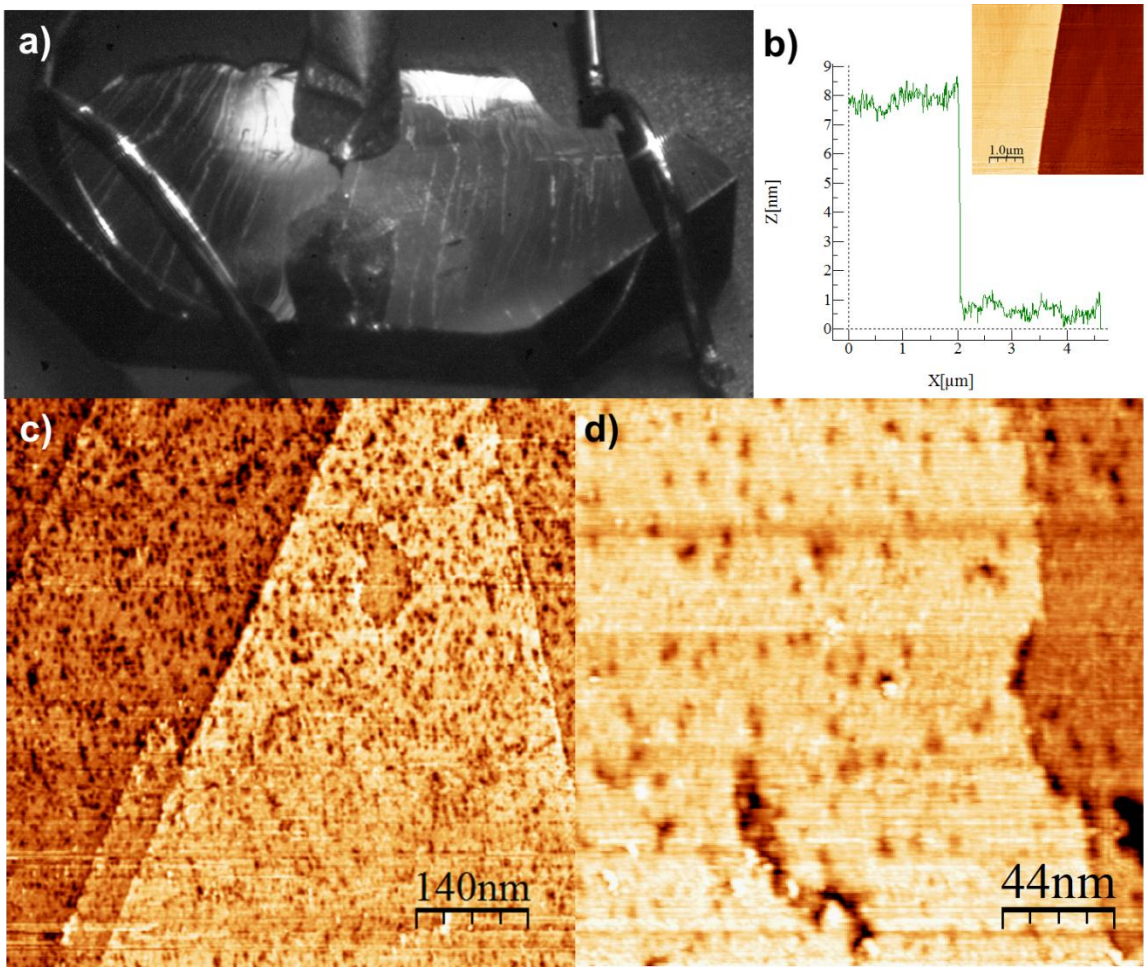

Fig 5.4: a) Picture of the diamond single crystal into the STM. The single crystal is fixed to the sample holder with two Tantalum wires. The STM tip is very close to its reflection, so it is near to tunnel range. The sample is stepped; b) Profile an image of 5 × 5 µm. A step of 8nm is showed. The image related with this profile is in the right corner. There. It is possible to observe more steps with a triangular shape in both terraces; c) STM image

of the clean diamond surface. The clean was checked before with LEED and AES techniques. Size: 700 × 700 nm. Bias Voltage = -2.93 V; Set point current = 5 μA; d) Smaller STM picture of the clean diamond surface. There it is easier observe the roughness. Size: 219.1 × 219.1 nm. Bias Voltage = -3.90 V; Set point current = 15 μA.

Obtaining the STM images of the diamond sample has been a difficult task. The diamond is an insulator, and although this substrate is doped with Boron, it was not conductive enough to get good measures. Moreover, the clean diamond surface has big steps as it is showed in Fig 5.4a. These steps are much higher than typical ones of metallic surfaces. A profile of one step of 8 nm is exhibited in Fig 5.4b, and the corresponding image is on the right corner. Beside these steps before growth graphene, we observed smaller steps with a triangular shape and a rough surface (Fig 5.4c and Fig 5.4d). The clean diamond surface has an appearance with a lot of black areas and white mounds over regions of 700 × 700 nm (Fig 5.4c) and 220 × 220 nm (Fig 5.4d). The black areas could be related with the dopant. However, they cover around 10% of the surface (measured with the WSxM), and we do not observe the Boron peak in the AES spectra (or any other contaminant), so at least part of them are not Boron islands. They also could be surface holes at most.

Additionally, we found a bigger problem. Every cleanness process attack the diamond surface and the annealing at such high temperatures cause a degradation of the single diamond crystal and a reduction of the boron doping. This way, in every new trial, it was difficult to perform the STM measurements because the tip not entering in range or crashing directly (the diamond surface does not conduct). This fact was observed too with the LEED technique because the screen charges faster with each test.

We can measure STM images at negative Voltages (in our STM the voltage is applied to the tip) due to the doping with Boron (p-type diamond). However, after

graphene growth, we can use this technique for positive and negative bias voltages. Moreover, the sample conducts better than before growth.

STM images after graphene growth show an ordered structure covering the rough surface. One of these images are showed in Fig 5.5a. The ordered structure covers different areas forming patches with different orientations. The Fig 5.5b shows a zoom of 3 × 3 nm. The Fourier Transform of the Fig 5.5b image exhibits a clear hexagonal structure (Fig 5.5c) with a distance between the spots of 2.47 Å. That distance corresponds to the graphene lattice as we indicate above (Fig 5.1).On the other hand, the Fourier Transform exhibits in some cases a distance between the spots of 4.96 Å (Fig 5.5e). This distance is approximately twice the graphene lattice, so it corresponds to a 2×2 moiré in good agreement with the LEED pattern. The Fig 5.5e is obtained from Fig 5.5d. There, the distance between the bumps is 5.0 Å approximately, and it is obtained from a profile traced over the moire bumps. An example of a profile is placed in the right corner of Fig 5.5e. This way, the STM helps to conclude we have covered the diamond surface with a hexagonal structure after growth graphene. It has the lattice parameter of graphene, and it shows a super-periodicity with a double value (moiré).

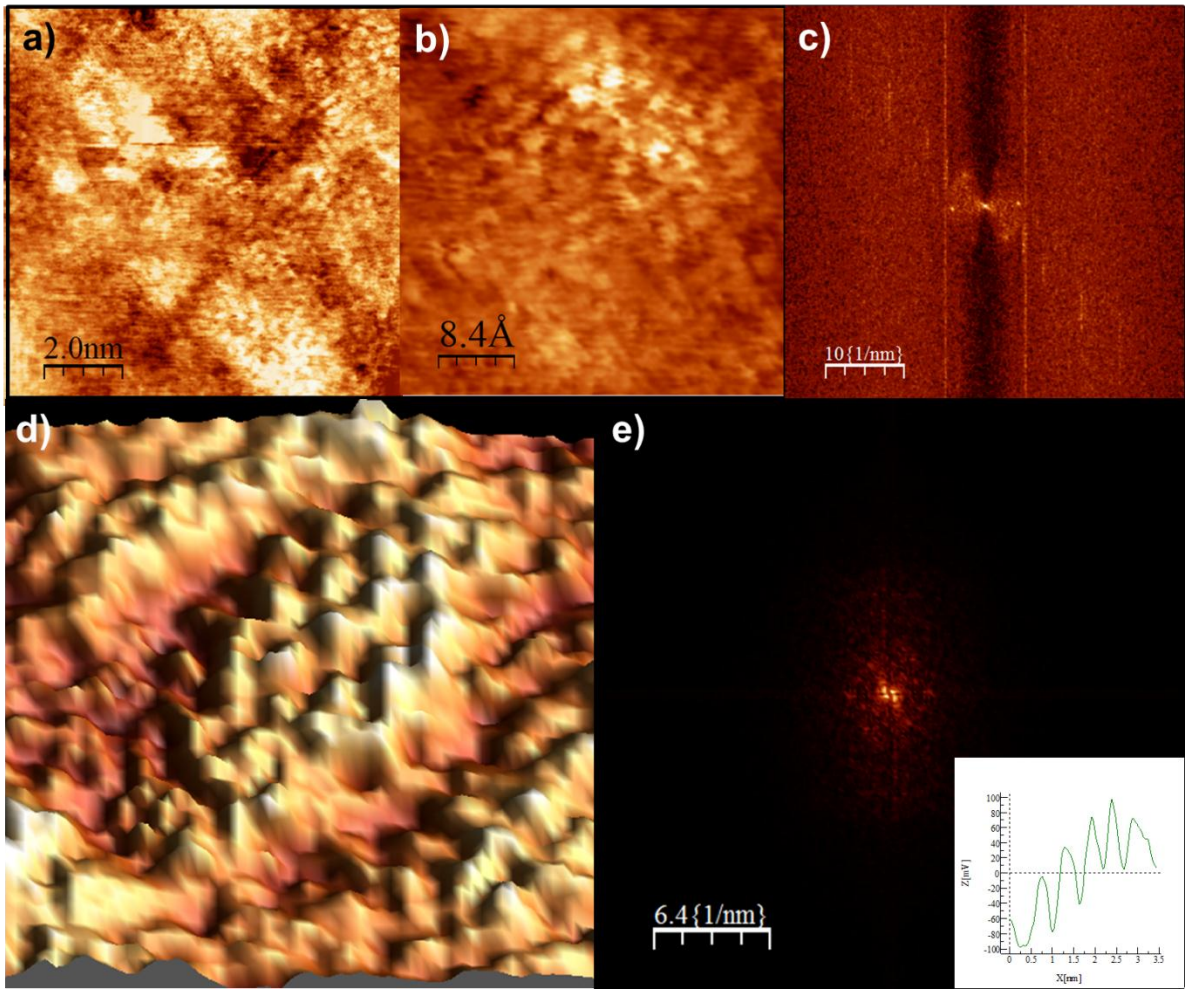

Fig 5.5: a) Graphene on Diamond C (111). Size: 10.0 × 10.0 nm. Bias Voltage: -1.9 V, Set point current: 1.0 nA; b) STM image of hexagonal structure with the same lattice parameter of graphene. Size: 3.0 × 3.0 nm. Bias Voltage: -1.88 V, Set point current: 0.95 nA; c) Fourier Transform of 5.5b. The image shows a hexagonal structure with a distance between the spots of 2.47 Å. The vertical lines represent the noise of the corresponding STM image; d) STM image with 3D representation. The moire bumps are easily identifiable in small patches. Size: 4.4 × 4.4 nm. Bias Voltage: -1.0 V, Set point current: 0.76 nA; e) Fourier Transform of 5.5d. The distance between the spots is 5.0 Å. In the right corner a profile of Fig 5.5d is placed with a distance between the moiré bumps of 5.0 Å approx.

Fig 5.6 shows several Raman spectra represented in 3D for an easier comparison. The spectra were taken going from outside to inside the sample, from 1.9 µm up

until -2 µm inside. The colored base of the spectra represents the region where the spectrum was performed. Thus, the front dark area is referred to the Raman over the surface. The clearest region corresponds to the surface, and the dark region at the bottom is the area inside the diamond.

The full Raman is also placed in the inset right corner. There a strong peak is observed at 1332 cm^{-1}, corresponding to optical vibrations of the diamond crystal. The peak decreases going out of the substrate. The intensity and thickness of the peak confirm that the substrate is a single crystal.

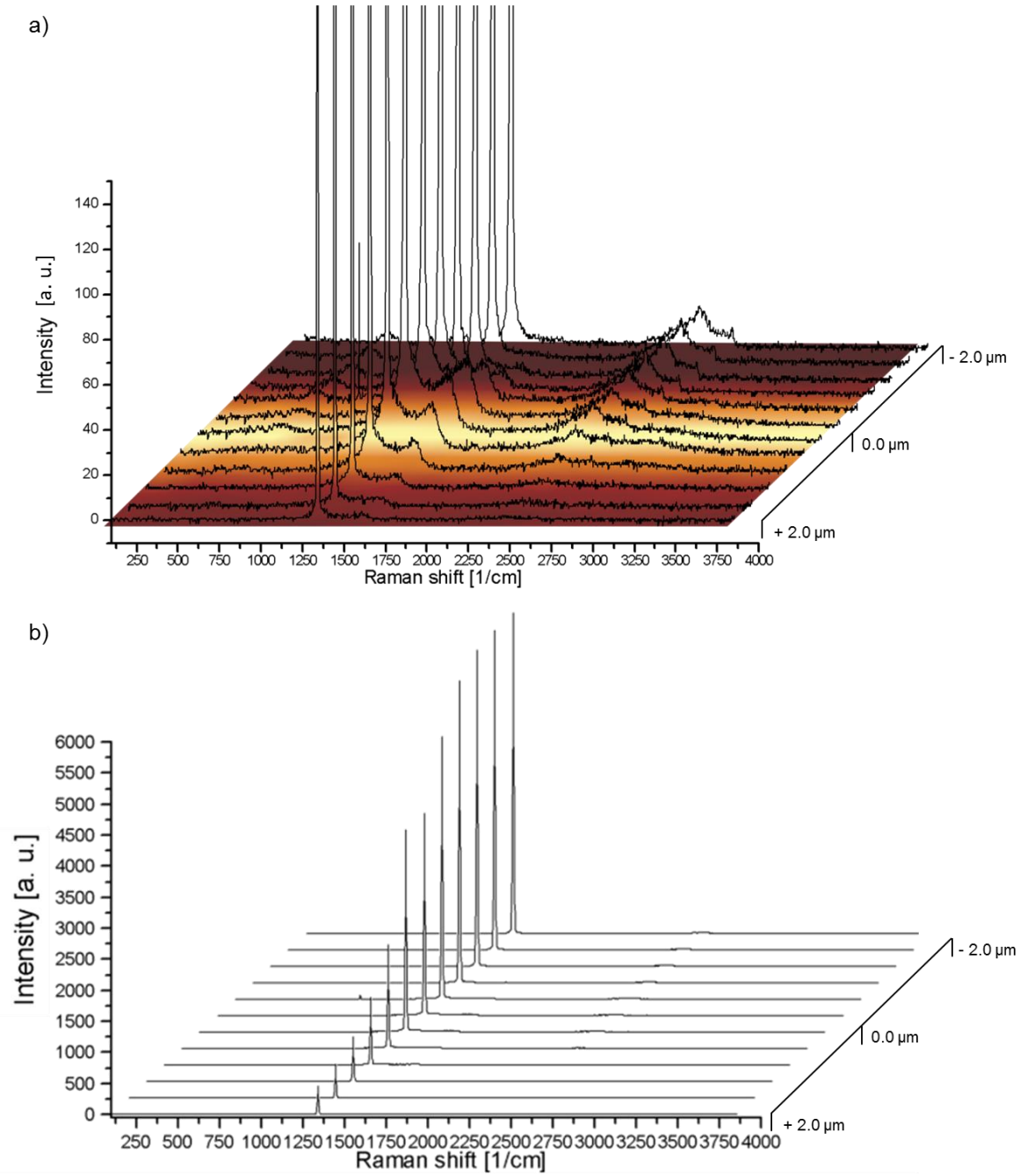

Fig 5.6: a) Zoom of Raman spectra after growth graphene on diamond C (111). The base picture represents the region where each Raman was taken, so the lightest region corresponds to the surface, the backside dark area is a zone inside the diamond crystal (from 0.0 µm to -2.0 µm), and the dark front area was taken over the sample (from +2.0 µm to 0.0 µm). The Raman spectra were performed from -2.0 until 1.9 µm; b) Complete Raman spectra.(a) is a zoom of this. The peak related with the diamond crystal (1270 cm^{-1}) decreases in the zone over the sample (from +2.0 µm to 0.0 µm).

In the main image of Fig 5.6, the zoom helps to observe new peaks related with graphene. In the image, it is possible to observe the increase of some peaks in the surface region. That is the case of one in the 1580 cm^{-1} region. It corresponds to the G peak. Moreover, in the picture it is possible to observe that the width of the diamond peak increases (1332 cm^{-1}) in the surface. The D peak of graphene is located at 1360 cm^{-1}, so it is overlapped to the diamond peak. It is due to the out-of-plane vibrational mode of sp2 carbon atoms and it activates in the presence of defects, for example, small regions of graphene with different orientations. The 2D peak of graphene is situated at 2668 cm^{-1}. However, it is difficult to identify in Fig 5.6 because there are two peaks in this region from the diamond crystal.

We have performed the difference between two Raman spectra (Fig 5.7). They are placed in the right-up corner and correspond with the innermost Raman of Fig 5.6 (red line) and the one centered in the light region (black line). This way, the difference corresponds to the contribution of graphene grown on the surface. We have removed the negative part coming from the huge diamond peak at 1332 cm^{-1}.

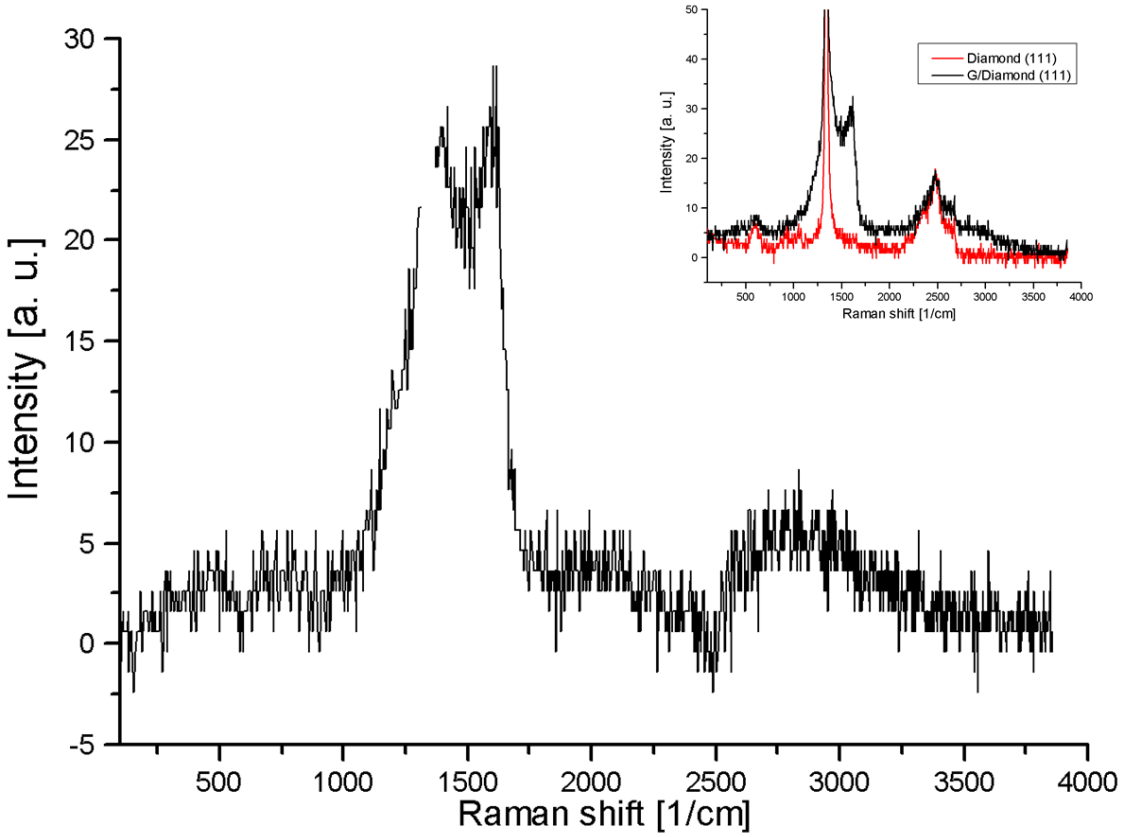

Fig 5.7: Difference of the two Raman spectra represented at the right corner: the red line is a Raman inside the Diamond crystal and the black line is a Raman on the Diamond surface after growth. The main graph (the difference) corresponds to the graphene contribution.

The difference indicates the broadening of the D region (1360 cm $^{-1}$), and the appearance pf a new peak, the G peak (1580 cm $^{-1}$). Moreover, a hill is observed from 2550 to 3250 cm^{-1} occupying the 2D and D+G peaks (the positions are 2668 and 2947cm^{-1} respectively). This Raman spectrum demonstrates the existence of carbon sp^2 at the surface, and the wide of the peaks indicates that this graphene is in the form of patches, in good agreement with the STM images.

5.3 Graphene on Diamond (100)

Diamond C (110) has a square surface structure as we indicate above (Fig 5.1). In this part, we have used two types of diamonds: one doped with boron and another one doped with nitrogen. The main difference between these dopants is that a diamond with boron becomes a P-type semiconductor, however, with nitrogen, the diamond converted into an N-type semiconductor. It is because the number of electrons in these three involved atoms is: Boron (5) < Carbon (6) < Nitrogen (7), so a diamond doped with nitrogen means that in the crystal structure of the carbon, some of them have been substituent by nitrogen atoms. Thus, this semiconductor has a larger electron concentration, and the electrons are the majority carriers (N-type). However, the opposite effect occurs with boron as the dopant (P-type).

The type of semiconductor affects to the STM measurements. Our STM apply the voltage to the tip so, using a P-type semiconductor (C (110) doped with Boron), we can use only negative voltage values, so that we injects electrons to the sample because, in this type of semiconductor, the holes are the majority carriers. On the other hand, in the N-type semiconductor (C (110) doped with Nitrogen), we use positive voltage values, so we attract the negative charges from the sample.

In our case, the diamond C (110) doped with Nitrogen has less density of dopant than the diamond C (110) doped with Boron, so it was more difficult to observe the LEED pattern because of a faster screen charging. Moreover, we cannot measure with the STM the clean surface of diamond with nitrogen, so we had to use AFM (Atomic Force Microscopy) to observe it.

Fig 5.8 shows the LEED patterns before and after growth graphene. Fig 5.8a corresponds to the clean diamond C (110) surface. The spots form a square structure indicated by red dashed lines. Fig 5.8b and Fig 5.8c is the LEED pattern obtained after growth graphene of diamond doped with Boron and diamond doped with Nitrogen respectively. In both cases, the corners of the gray dashed lines indicate new spots related to the graphene growth. The new spots indicate the emergence of a new cell: a 2×1. We have made a representation of a p (2 × 1) cell with the LEEDpat software[124] in Fig 5.8d. There, we can observe how this picture corresponds to our experimental results. In this representation, we have included the domains, so it means that we have ordered structures in the two crystallographic directions of the diamond C (110), so it forms the p (2 × 1) and p (1 × 2).

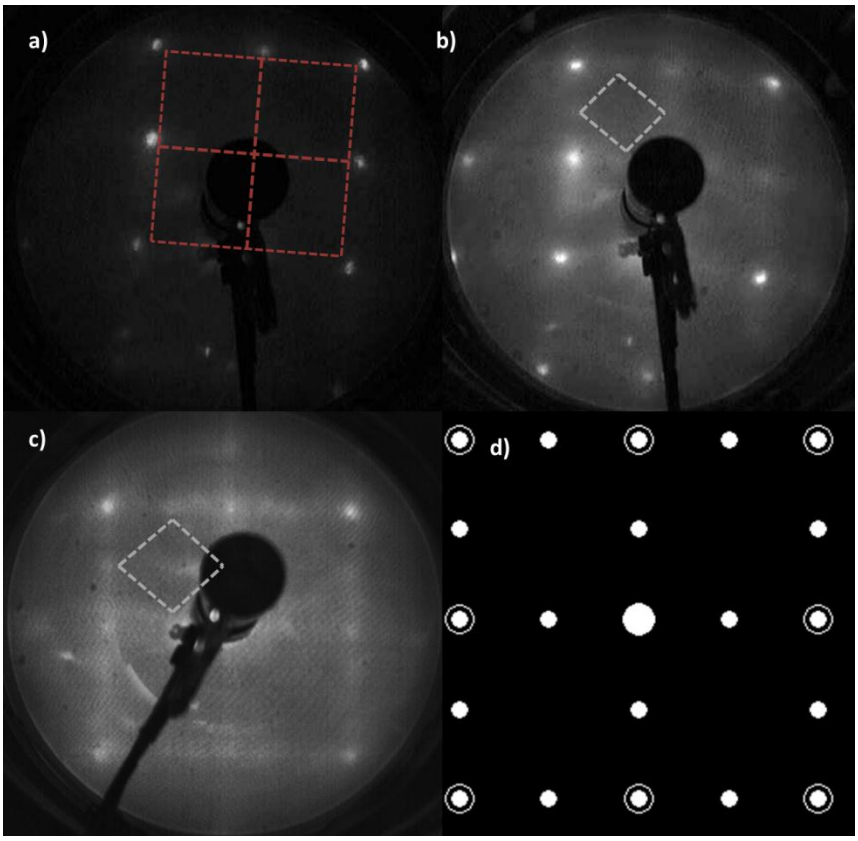

Fig 5.8: a) LEED pattern of clean diamond C (110). Red dashed lines indicate the

spots and the square structure of this surface. It was taken at 130 eV; b) LEED picture of diamond C (110) doped with Boron after growth graphene for 30 minutes. The corners formed by gray dashed lines indicate the new spots related with graphene. This pattern corresponds to an energy of 131 eV; c) LEED image of diamond C (110) doped with Nitrogen after growth graphene for 30 minutes. The corners of the gray dashed lines indicate the new spots form a p (2 × 1) structure with two domains. The picture was taken at 90 eV; d) Representation of a p (2 × 1) structure on a square surface LEED pattern with two domains. One domain is related to the horizontal spots (p (2 × 1)) and the other one with the vertical spots (p (1 × 2)).

Fig 5.9 shows the AES spectra performed in these samples. Here, we observe the difference of energy between the energy loss peak and the elastic peak of the clean (red line) and after growth graphene (black line) of the diamond C (110) (Fig 5.9a). Similarly as observed for the diamond C (111) surface (Fig 5.3), the energy loss peak after growth graphene has moved away from the elastic peak. The energy difference varies from 28 ± 2 eV to 32 ± 2 eV. Here, the error is bigger because we have used a different step interval of energy (2 eV). Thus, this surface reproduces the same behavior observed before, and the energy difference is into the measurement error. Moreover, on both surfaces an attenuation of the elastic peak is observed after growth graphene.

On the other hand, the AES spectra show we have only carbon in the sample. The peaks related with the dopants (boron (180 eV) or nitrogen (381 eV)) or with contamination (oxygen (510 eV)) do not appear. The carbon region is showed in Fig 5.9b. There, we compare the carbon peak (272 eV) before (red) and after growth graphene (black) and in both cases the peak is clearly indicated.

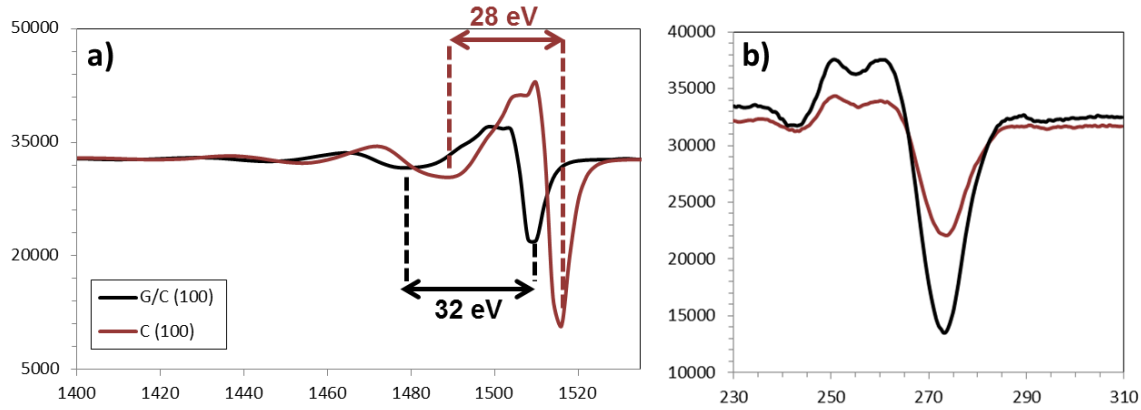

Fig 5.9: Comparison of AES spectra. The red line corresponds to the clean diamond C (110), and the black line is the spectra obtained after growth graphene for 30 minutes; a) The spectra show the elastic peak region. The difference between the energy loss and the elastic peak is indicated on the image. That difference increases after growth and the elastic peak attenuate; b) Spectra in the AES carbon peak region. In both cases, the carbon peak is identified (272 eV).

Fig 5.14a and Fig 5.14b exhibit two pictures of the diamond crystal. The first corresponds to the diamond doped with Boron, which makes the crystal dark. However, the diamond doped with nitrogen (Fig 5.10b) keeps the transparency. In both pictures, the crystals are fixed to the sample holder by two tantalum strings, and a tungsten tip approaching to the surface can be observed. The diamond doped with boron has a square shape, and the one doped with nitrogen is rectangular. Moreover, the first one is thinner than the second one.

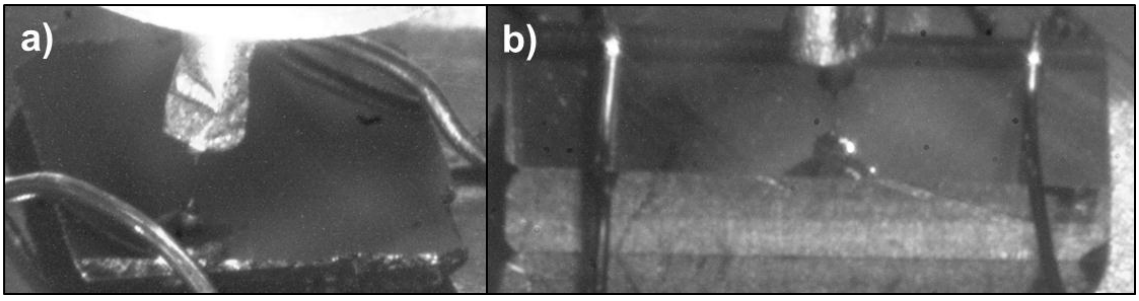

Fig 5.10: a) Diamond C (110) doped with Boron; b) Diamond C (110) doped with

Nitrogen

The STM images of the clean diamond C (110) doped with Boron show a very rough sample. The steps have a shape likes fingers and do not have flat regions. An image of the clean surface is the Fig 5.11. The significant roughness (much bigger than the diamond C (111)) of the surface prevents an observed change attributable to graphene after growth.

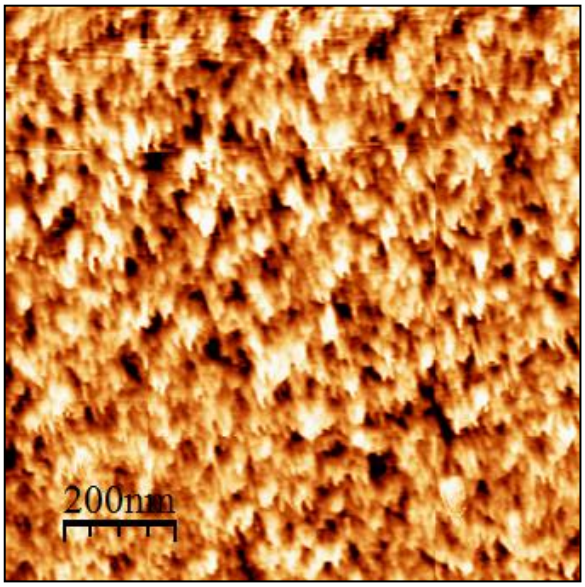

Fig 5.11: STM image of the clean surface of diamond C (110) doped with Boron. Size: 1.0 × 1.0 µm. Bias Voltage = -2.00 V. Set Point = 37.00 pA

On the other hand, the clean diamond C (110) doped with Nitrogen has a low density of dopant, so we cannot measure STM because the sample does not conduct enough. We have used AFM to observe the clean surface (Fig 5.14). The AFM technique does not need that the sample is conductive because it is based on measuring the forces between the cantilever and the sample. The obtained images of the clean surface show long and tight steps. The pictures of the two clean

diamonds (Fig 5.12 and Fig 5.13) are the same size (1.0 × 1.0 µm) for a better comparison although they have been measured by different techniques.

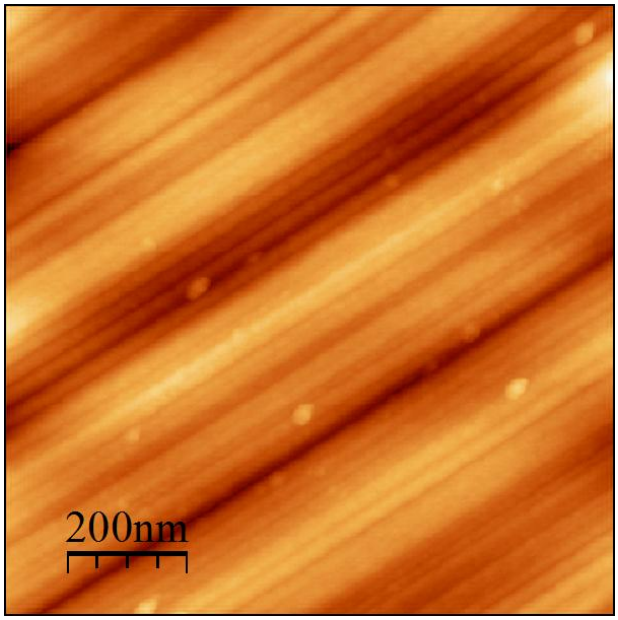

Fig 5.14: AFM image of the clean surface of diamond C (110) doped with Nitrogen. Size: 1.0 × 1.0 µm. Dynamic AM. Amplitude = 0.35 V. Set Point = -1.25.

After growth graphene for 30 minutes, the diamond C (110) doped with Nitrogen conducts well so that we can use the STM technique. The images (Fig 5.15a and Fig 5.15b) show the same staggered substrate with a shadow forming islands linked together. The islands grow with a hexagonal shape, and a path between the bigger regions confirms we have growth graphene on the surface. The graphene has a low coverage, but it is in agreement with our estimations performed in the fourth chapter. Here, we have growth graphene for 30 minutes, so we have around half monolayer.

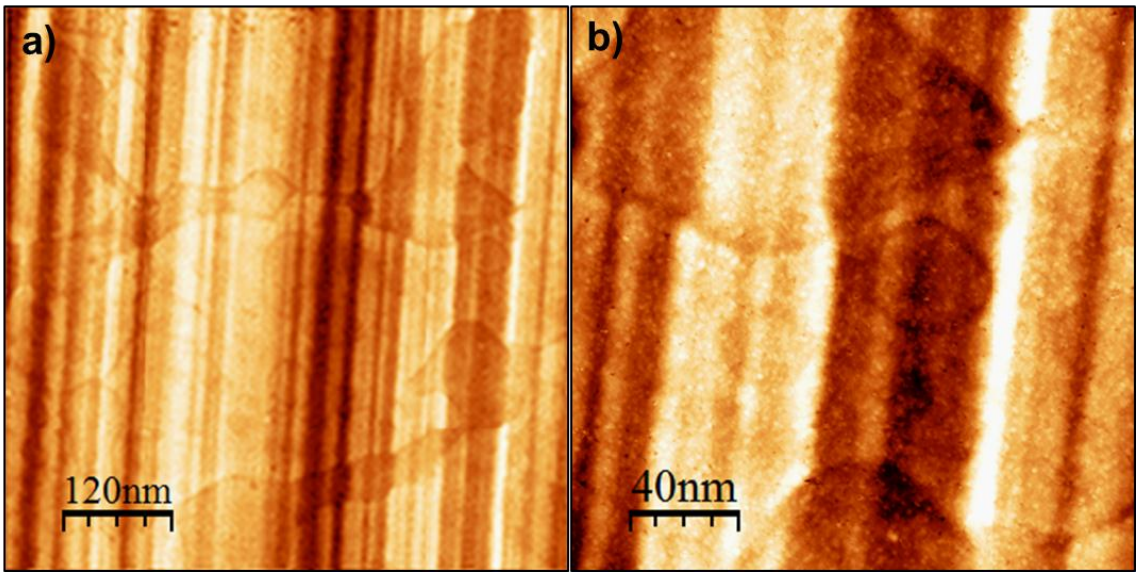

Fig 5.15: a) STM image of diamond C (110) doped with Nitrogen after growth graphene for 30 min. The shadows correspond to graphene regions. Size: 600.0 × 600.0 nm. Bias Voltage = -2.54 V. Set Point = 5.00 pA; b) Smaller STM image of diamond C (110) doped with Nitrogen after growth graphene for 30 min. Here we have a closer view of the steps and the diamond and graphene zones. Size: 200.0 × 200.0 nm. Bias Voltage = -2.54 V. Set Point = 5. 00 pA.

5.4 Calculations

The procedure used in this part is similar to the one described in section 4.4 with a few exceptions. The convergence parameters are the same, but the exchange-correlation functional employed is Local Density Approximation. We talked about this in section 2.10.1. The Monkhorst-Pack grid employed was 6 × 6 × 1, and the calculations have been performed with the CASTEP code too.

First of all, the surface is created from a bulk unit cell always optimized with the same parameters and thresholds. Next, the 2 × 2 cell has been optimized with five

layers of the substrate to allow for relaxation of the distance between layers. Therefore, the original 2 × 2 cell have as cell parameters **a**,**b** = 5.03 Å, **c** = 26.48 Å; α,β = 90°, γ = 120° for diamond C (111) and the cell parameter values after optimization are: **a**,**b** = 4.98 Å, **c**= 26.48 Å; α,β = 90°, γ = 120° (Fig 5.16). These last values have been used in all calculations of this part. The cell parameters are smaller because the system supports a surface stress compression.

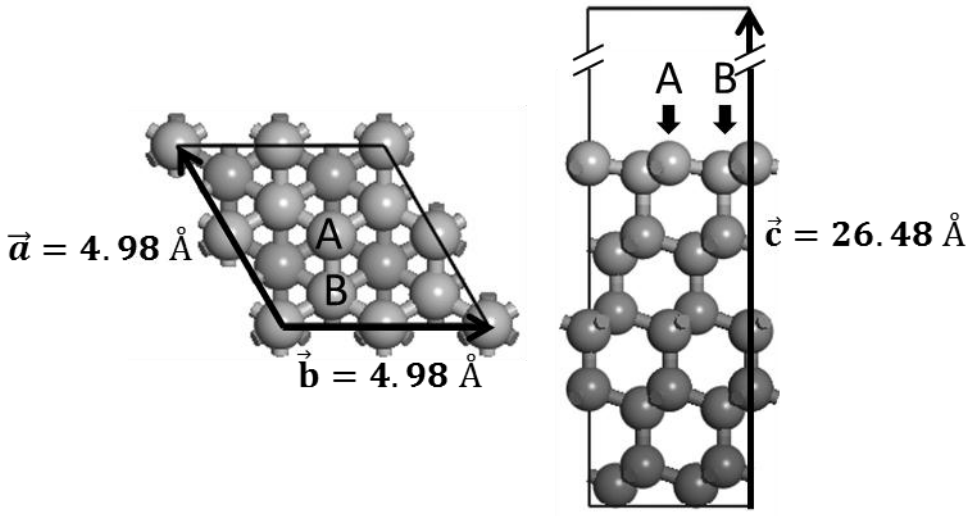

Fig 5.16: Two views of the 2 × 2 cell used in this section. The cell parameters and the A and B atoms of the surface are marked on them.

We have looked for a system to reproduce the 2 × 2 pattern observed with LEED and STM techniques in section 5.2. Thus, we have designed a system formed by a buffer layer of one carbon atom between the graphene layer and the diamond C (111) surface.

For this purpose, we have added a carbon atom on the surface with an initial distance of the surface of around 3.5 Å. The carbon atom is placed in four different positions: hollow, bridge, top A and top B. The two different top positions are

because every layer of diamond C (111) is formed by a bilayer, it means the carbon atoms have two separate z positions, so an A atom is the highest atom and the B atom is the lowest carbon atom of the bilayer.

The initial and final positions obtained in the adsorption of one carbon atom on a diamond C (111) surface is observed in Fig 5.17. There, the carbon atom is adsorbed in top B or hollow position. The carbon atom goes down, and it links to another three carbon atoms of the diamond surface.

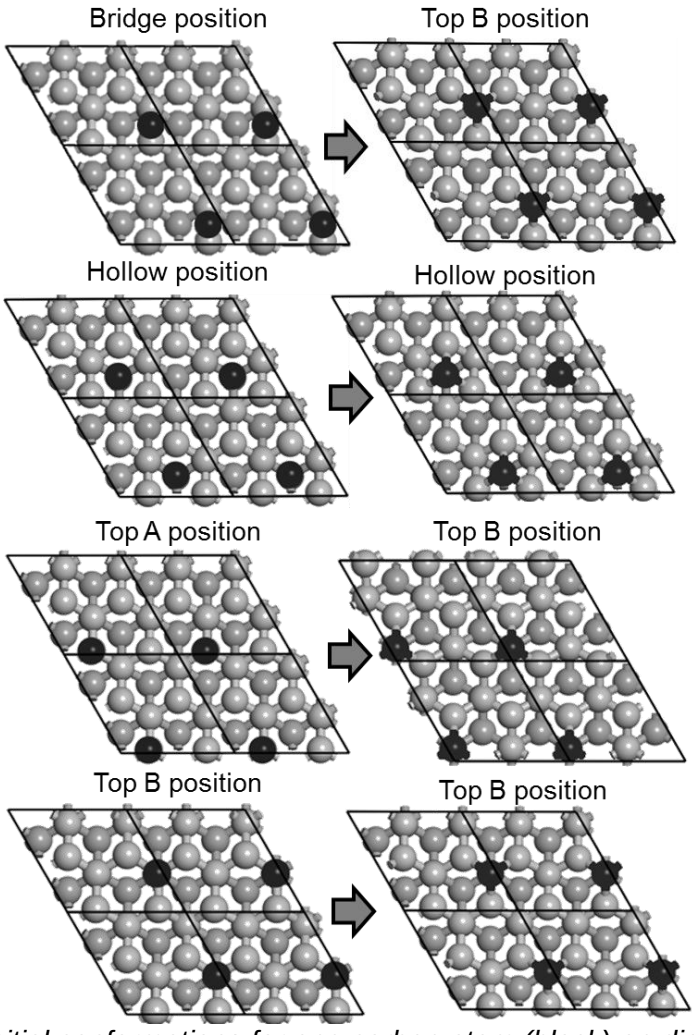

Fig 5.17: Four initial conformations for one carbon atom (black) on diamond C (111) at

the left sides and the four corresponding final structures after geometry optimizations (right sides). Every picture is a 4 × 4 unit cell with the 2 × 2 cell marked by black lines (the cell used in these calculations).

The adsorption energy of the carbon atom is calculated from:

$$E_{ads} = E_{C/C(111)} - (E_C + E_{C(111)}) \qquad \text{Eq (5.1)}$$

where $E_{C/C(111)}$ corresponds to the energy of the one carbon atom on the diamond C (111) in the final position, E_C the energy of one carbon atom calculated in the vacuum and $E_{C(111)}$ the energy of the relaxed substrate (five layers of the 2 × 2 unit cell).

The adsorption energies for the four cases are collected in Table 5.1. All of them are negatives, so it means that all processes are exothermic. Thus, the adsorption of the one carbon atom is favorable. Moreover, the adsorption energy values are the same, so the initial position of the carbon atom does not have much importance.

Initial position\Substrate	**C (111)**
	E_{ads} [eV]
Bridge position	-11.54
Hollow position	-11.46
Top A position	-11.61
Top B position	-11.56

Table 5.1: Energy adsorption values (Eads) of one carbon atom on C (111) starting from the different positions described in Fig 5.17.

On the other hand, the carbon atom is linked to three other carbons in either of the two final positions. The association energy for two carbon atoms (C-C) is -6.40 eV

and the association energy for two carbon atoms with one of them linked at the same time with another two carbons is -3.47 eV (the association energy of two atoms change if one of them is related to other species). These values give us an idea of what means -11 eV because the carbon atom makes three links with three atoms of the surface.

Once it has been established the carbon atom adsorption at the Top B position of the diamond C (111) as the buffer layer, we added a single layer of graphene on it. The graphene layer is placed at 3.3 Å of the buffer layer. After geometry optimization, the graphene layer has gone down until link with the carbon atom of the buffer layer. Fig 5.18 shows the final situation of the system. There, the carbon atom of the buffer layer is orange to observe easier from the top view.

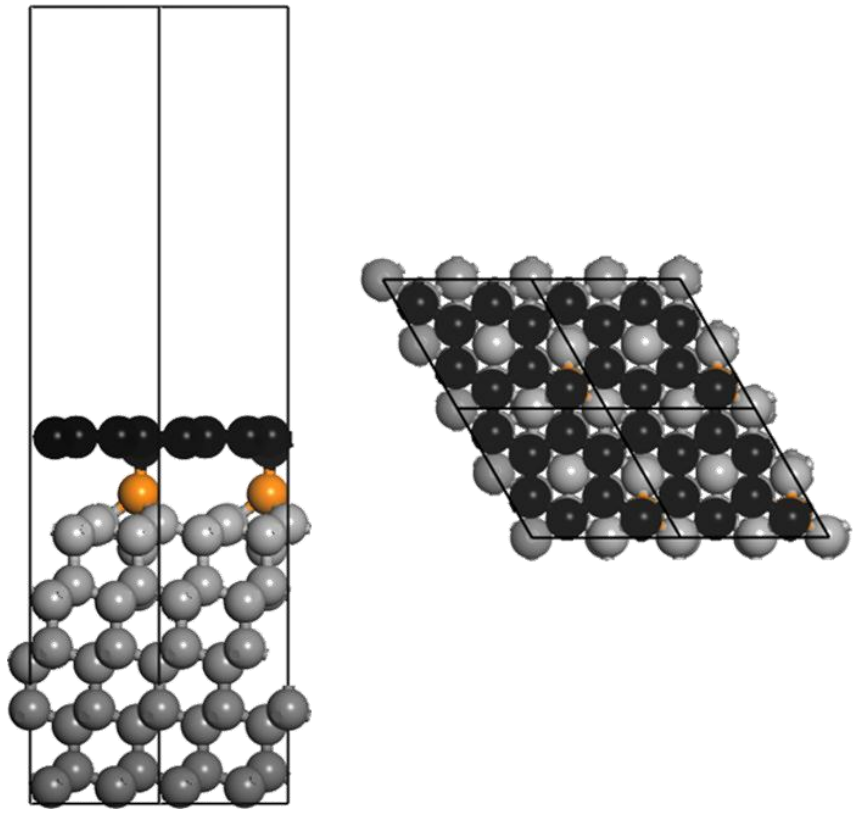

Fig 5.18: Two views of the final structure after geometry optimization. Every layer of

the diamond C (111) is colored with a different gray tone to an easier visualization, the buffer layer formed by a carbon atom is orange, and the graphene layer is black.

The adsorption energy of the graphene layer is needed to deduce if this system can be formed, so the eq. (5.1) is adapted to this new structure as:

$$E_{ads} = E_{G/C/C(111)} - (E_G + E_C + E_{C(111)}) \qquad \text{Eq (5.2)}$$

where $E_{G/C/C(111)}$ is the total energy of the whole structure, E_G the energy of a graphene layer into a 2×2 diamond C (111) cell, E_C the energy of one carbon atom calculated in the vacuum and $E_{C(111)}$ the energy of the relaxed substrate (five layers of the 2 × 2 unit cell).

Thus, the adsorption energy is E_{ads} = -12.24 eV. The graphene layer is formed by eight carbon atoms in the 2×2 diamond C (111) cell, so the adsorption energy per surface carbon atom is E_N = -1.11 eV, considering the surface carbon atoms are the eight atoms of the graphene layer. The negative value indicates a favorable adsorption as the result of an exothermic process.

We have simulated the corresponding STM image of this structure (Fig 5.19) using CASTEP as the same way than the pictures of chapter 4 (section 4.5). The dashed lines indicate the 2×2 diamond C (111) cell we have performed the calculation of this chapter. The simulated image indicates a 2×2 pattern which corresponds to the experimental results obtained with the LEED and STM.

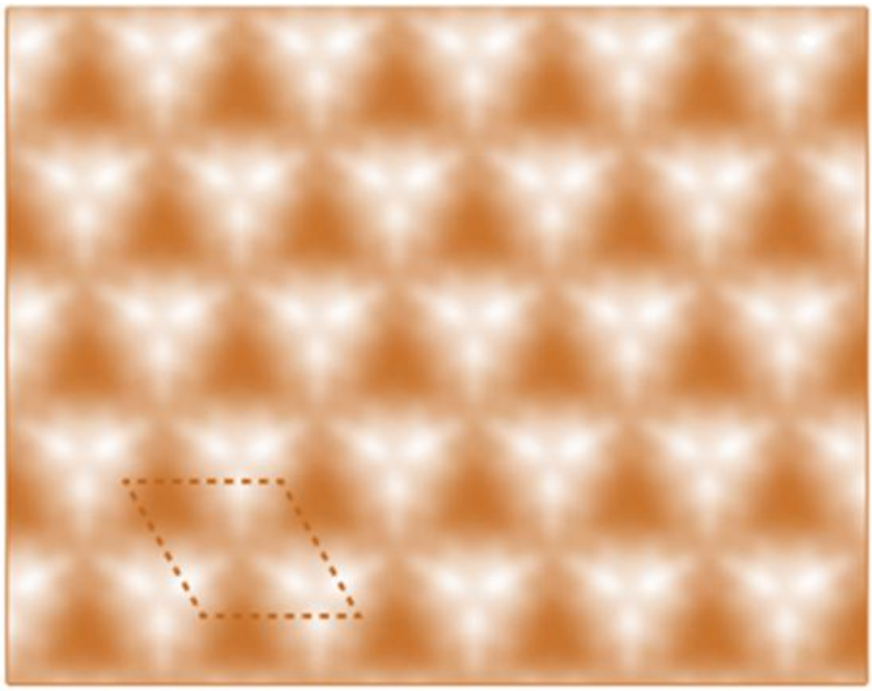

Fig 5.19: Simulated STM image of the structure formed by graphene on diamond C (111) with a buffer layer of one carbon atom in top B position. Bias Voltage = +2.0 V.

Before that, we performed the calculation for a single monolayer on diamond C(111). The geometry optimization indicates that the graphene layer is placed at 3.66 Å on the surface and the final configuration of the graphene on the diamond without a buffer layer is showed in Fig 5.20a. We apply the Eq (5.1) to obtain the adsorption energy of the graphene layer on diamond, in a way that the adsorption energy is defined by:

$$E_{ads} = E_{G/C(111)} - (E_G + E_{C(111)}) \qquad \text{Eq (5.3)}$$

In this case, the adsorption energy per surface carbon atom is E_N = -1.72 eV, so that structure is more favorable energetically that the buffer layer structure.

We have simulated the STM image for this structure (Fig 5.20b), and that image corresponds to a 1×1 pattern. So, the experimental results do not match with the formation of graphene on diamond C(111) without a buffer layer between them. It does not mean that we have regions with this configuration, but, in the LEED results, the 2x2 signal would be superimposed to the 1x1, and, in the STM technique, this structure is much harder to observe in the images.

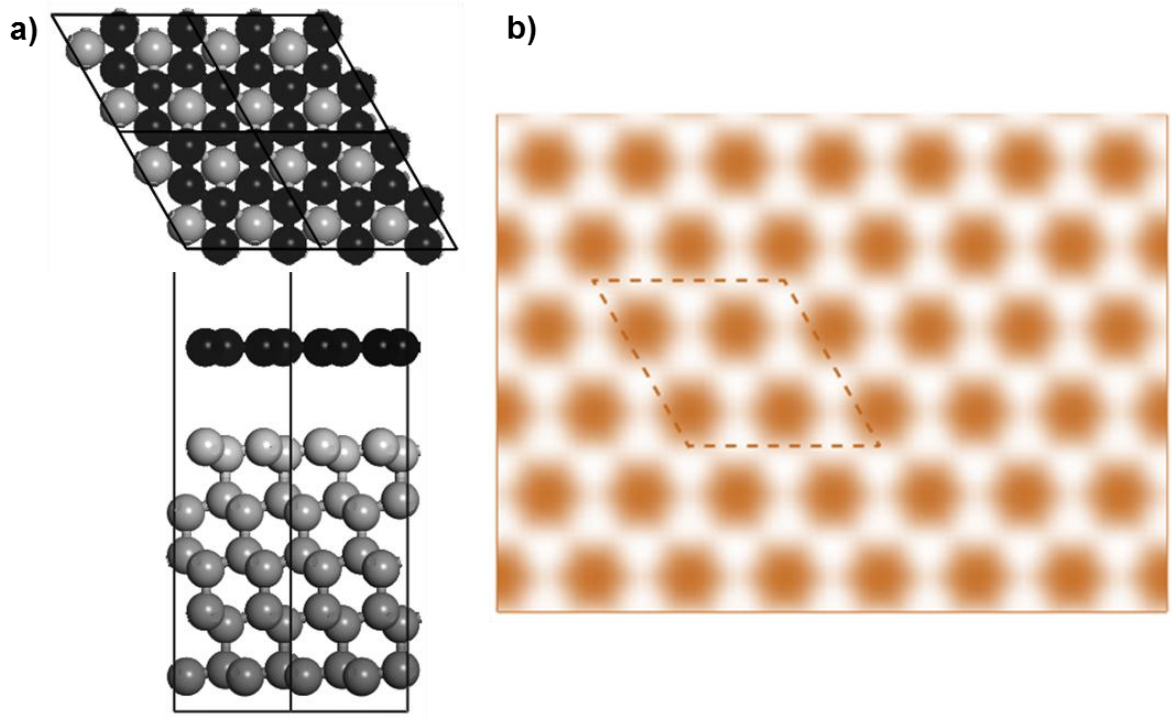

Fig 5.20: a) Two views of the final structure after geometry optimization. Every layer of the diamond C (111) is colored with a different gray tone, and the graphene layer is black; b) Simulated STM image of the left configuration.The image corresponds to a 1×1 structure. Bias Voltage = +2.0 V

5.5 Discussion

The aim of this chapter is growth graphene on diamond. For this purpose, we have used the MBE solid carbon source described in Chapter 2 and several techniques to verify the existence of graphene on the surface. LEED technique indicates we have ordered structures after graphene growth on the both diamond surfaces. These structures change the LEED patterns of the clean diamond surface to two different periodicities (p (2×2) for C (111) and p (2×1) for C (110)). On the other hand, AES confirms that the ordered structures are made of carbon and the distance between the energy loss and the elastic peaks change in the same direction and value.

Furthermore, STM images let observing the 2×2 ordered structure in C (111) in agreement with the LEED pattern and islands with hexagonal shape in C (110). The model to explain the 2×2 structure is showed in section 5.4. The calculation indicates that the existence of this structure is energetically favorable and the STM simulated image matches with the experimental one.

The model is based on the existence of a buffer layer between the graphene and the diamond C (111) surface. First, we tested if it is possible to obtain the buffer layer by adsorption of one carbon atom on the diamond surface. The carbon atom could be close to the surface at different positions but, as the carbon atom approaches towards to the surface, it changes the initial x-y position and it tends to move to Top B position.

In the calculation part (section 5.4) we have also check that the adsorption of a graphene layer on diamond C (111) is energetically favorable, but the simulated

STM image shows a different structure to the experimental results (a 1×1 structure). So, both structures (with and without buffer layer) can co-exists on the surface, and the second one would not observed by the experimental limitations.

Raman spectroscopy shows that the related peaks to graphene appear in the diamond C (111) surface and this graphene is made of patches. These are regions of graphene with different orientations and with a 2 × 2 periodicity as we observe in the STM images. Moreover, we have growth less than a graphene monolayer. We have growth graphene for 30 minutes and considering the estimated ratio for the MBE solid carbon source (3×10^{-4} ML/s), in that period we growth half graphene monolayer.

On the other hand, despite the diamond crystals are doped, the cleaner process or the low density of dopant (in the case of the diamond C (110) doped with nitrogen) makes every trial harder to test the graphene existence with our experimental techniques. For example, the STM technique is limited to conductive samples, so we cannot use it to observe the clean diamond C (110) surface doped with diamond. Thus, this technique is better to be used after growth graphene because this material conducts well. Moreover, we can only use the STM at determined bias voltages with the doped diamond (the dopant type affects if we can use positives or negatives bias voltages). However, the existence of graphene let us using both voltages ranges. Moreover, the diamond surfaces are too rough in comparison with the usual surfaces used with STM. It makes it harder to verify the graphene existence on the surface. Trying to prevent all these difficulties, we use X-Ray at low angle in the ESRF, BM-25 (Spline): However, the obtained results were not good to analyze, despite reproducing the 2×2 structure.

6. Reaction of a metal-organic complex on Cu (110)

6.1 Introduction

The control over the functionality, size, and shape of new nanostructures is a major goal in nanoscience[128,129]. The bottom-up strategies for forming on surface nanostructures by direct sublimation of their building blocks under UHV conditions has been shown as an excellent approach to this goal[130]. However, the stability of the molecule to allow sublimation without structural damage presents a limitation, so there are few nanostructures formed by a combination of metal and organic molecules[131,132]. Moreover, these metal-organic structures have been obtained by subsequent sublimation of both building blocks or by the reaction of the organic molecules with the metal atoms form the substrate[133,134].

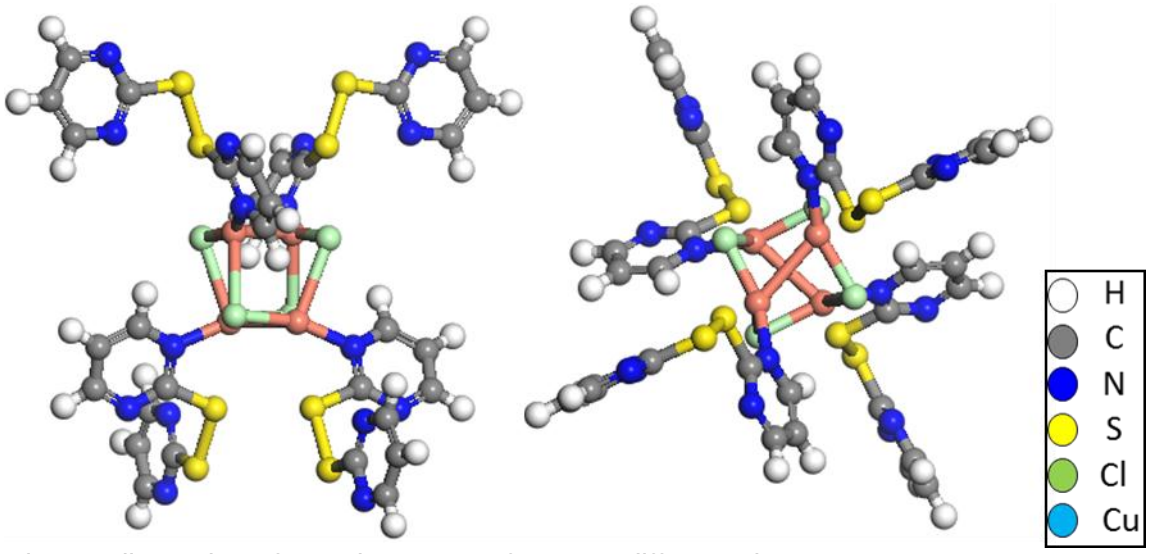

Fig 6.1: Illustration of Cu_4Cl_4 structure from two different views.

For this reason, in most of the previous studies of major complex molecules on surfaces, the molecules were transferred from a solution[135–140] or by a dry imprint technique to the substrate[141] to preserve the weak core. In this section we focus on a transition metal complex $[Cu_4(m_3\text{-}Cl)_4(m\text{-}pym_2S_2)_4]$ (pym_2S_2= di-pyrimidine disulfide) (named Cu_4Cl_4) with a robust structure[142] (Fig 6.1). We have shown that

we are able to sublimate them keeping its molecular integrity and how they self-assemble without being disrupted by the surface (section 6.2).

The sublimation has been performed in UHV conditions, allowing the formation of new nanostructures on the Cu (110) surface (the chosen substrate in this chapter) and the use the surface techniques of our chamber.

On the other hand, the synthesis and characterization of Cu_4Cl_4 (Fig 6.1) complex have been reported[142] showing interesting physical and chemical properties. This molecule has the capability to change its structure from a 3D robust structure to a 2D-coordination polymer $[Cu(\mu\text{-}pym_2S_2)(\ \mu\ \text{-}Cl)]_n{\cdot}nS$ (S = H2O or EtOH) when exposed to water or ethanol. However, the transformation of these big metal-organic molecules in solution is clearly altered by the role of the substrate (in this case Cu (110)), so we have observed in situ how the self-assembled molecular chains transform into other smaller chains induced by water (section 6.3).

6.2 Self-organization of Cu_4Cl_4 metal-organic cluster on Cu (110)

The sublimation procedure is described in section 2.9. Before that, the Cu (110) surface was clean as it is explained in section 2.6.1 (Surface preparation - Metallic samples).

After sublimation, the LEED pattern has changed from a rectangular unit cell corresponding to the clean Cu (110) surface (Fig 6.2a) to a p (5×3) (Fig 6.2b). The new spots indicate that an ordered superstructure cover the surface. To obtain this

LEED scheme, we sublimate the molecules approximately for 30 minutes, so for a rate of 1 ML/hour the molecules coverage corresponds to a 0.5 ML.

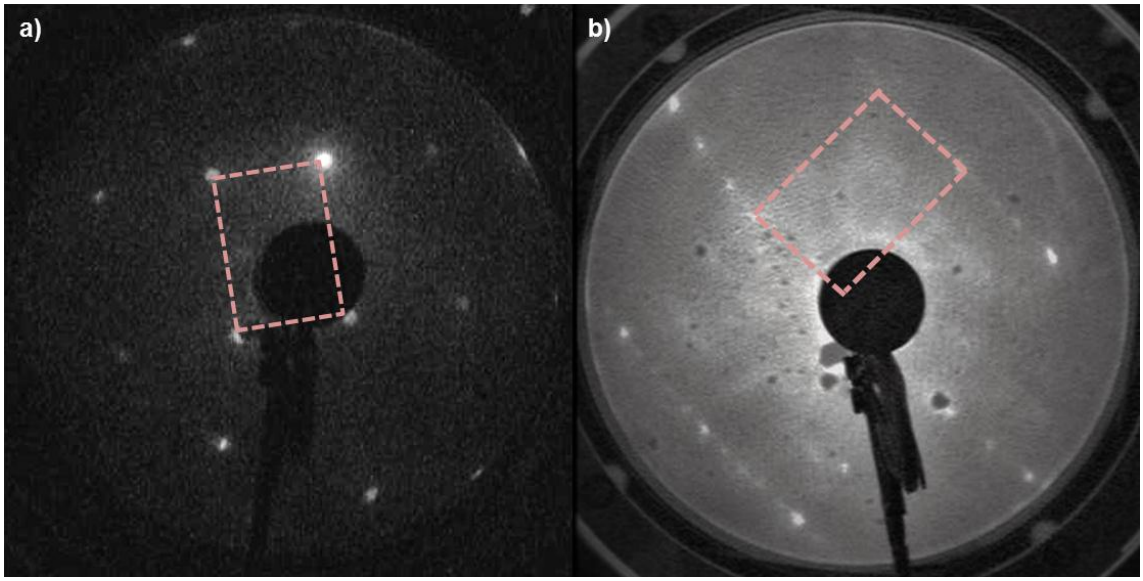

Fig 6.2: LEED patterns: a) clean surface of Cu (110) at 108 eV; b) LEED scheme after depositing 0.5 ML of Cu_4Cl_4 molecules on the copper surface. The pattern corresponds to a p (3×5) superstructure. The image is taken at 95 eV.

The STM images show a self-organized structure on Cu (110) surface. The complex structure of Cu_4Cl_4 molecules allow a high level of interconnections, so any particular motif in the STM images can be related to the Cu_4Cl_4 molecules. In this case, a molecular network is observed. It is formed by a double-bumped row surrounded by dark, undulating stripes (Fig 6.3). These lines are placed along the [1 1 0] surface crystallographic direction.

The surface coverage can be modulated by the deposition time (Section 2.9). This way, Fig 6.3a corresponds to a low coverage of molecules (30 minutes of sublimation, half monolayer). In the case of high coverage (Fig 6.3b, 60 minutes of sublimation) the stripes are much longer than at low coverage, and the chains are

stacked. On the other hand, we observe that the stripes morphology does not depend on the bias voltage in the range on ±2.0 V.

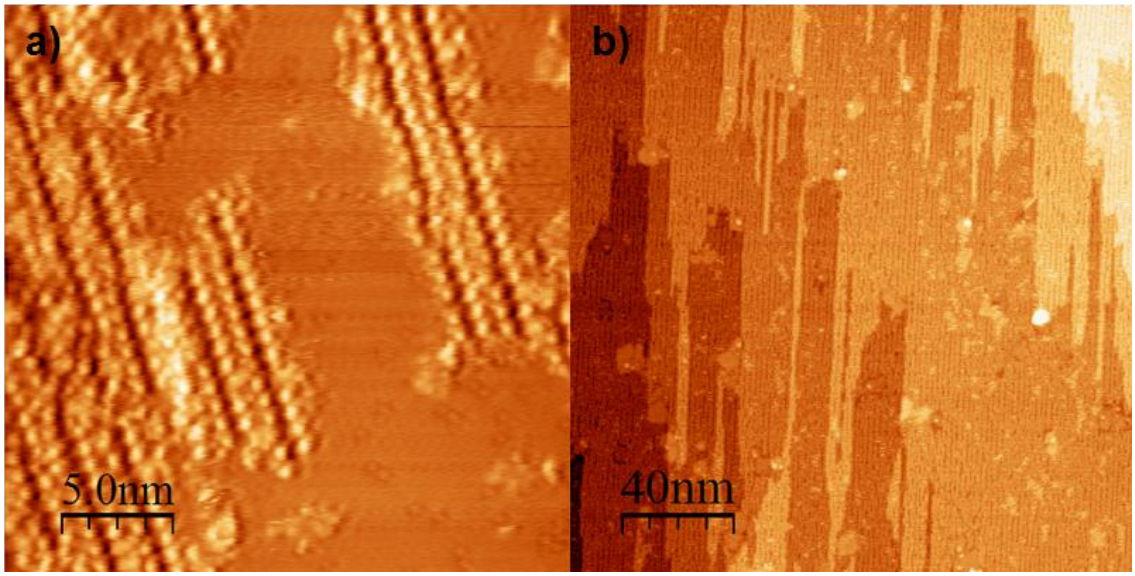

Fig 6.3: a) STM image of low coverage of Cu_4Cl_4 assembled stripes (30 min, 0.5 ML) on Cu (110). Size: 25 × 25 nm; Bias Voltage: -1.0 V and Set Point: 2.0 µA; b) Picture of high coverage of self-assembled molecules (60 min). The chains are very long and filled the entire surface. Size: 200 × 200 nm; Bias Voltage: -0.8 V and Set Point: 33.0 µA

In a closer view of the stripes (Fig 6.4a) we observe small defects along the molecular array, as missed bumps in some cases, but generally, the lines show a pretty regular appearance. Even so, the most probable defect is the result of a lack of local order between two molecules. On the other hand, an analysis of the STM images let us estimate the number of defects to be smaller than 5%.

In the Fig 6.4a, we have indicated the distance between the ends of two consecutive lines formed by bright bumps with a dark stripe in the middle (1.8 nm) and the distance between the center of the bumps (0.9 nm) with the same orientation. The 1.8 distance corresponds to the width of the chain. On the other

hand, the distance between two consecutive bumps in the [110] crystallographic direction is 0.76 nm. These two values characterize the molecular assembly and are in good agreement with the distance between five and three copper atoms of the substrate in the same directions. A representation of the Cu (110) surface with the distances on it is placed in Fig 6.4b. The high level of the molecular organization detects by STM is reflected in the 5×3 diffraction pattern obtained by LEED (Fig 6.2b). These observations indicate that the interaction of the molecules with the metal surface plays a major role in the stabilization of the macromolecular assembly. Moreover, sometimes we observe in the STM images with a medium coverage that the molecules diffuse on the copper surface and change their positions. This fact indicates that the interaction between the molecules and the substrate is not so high.

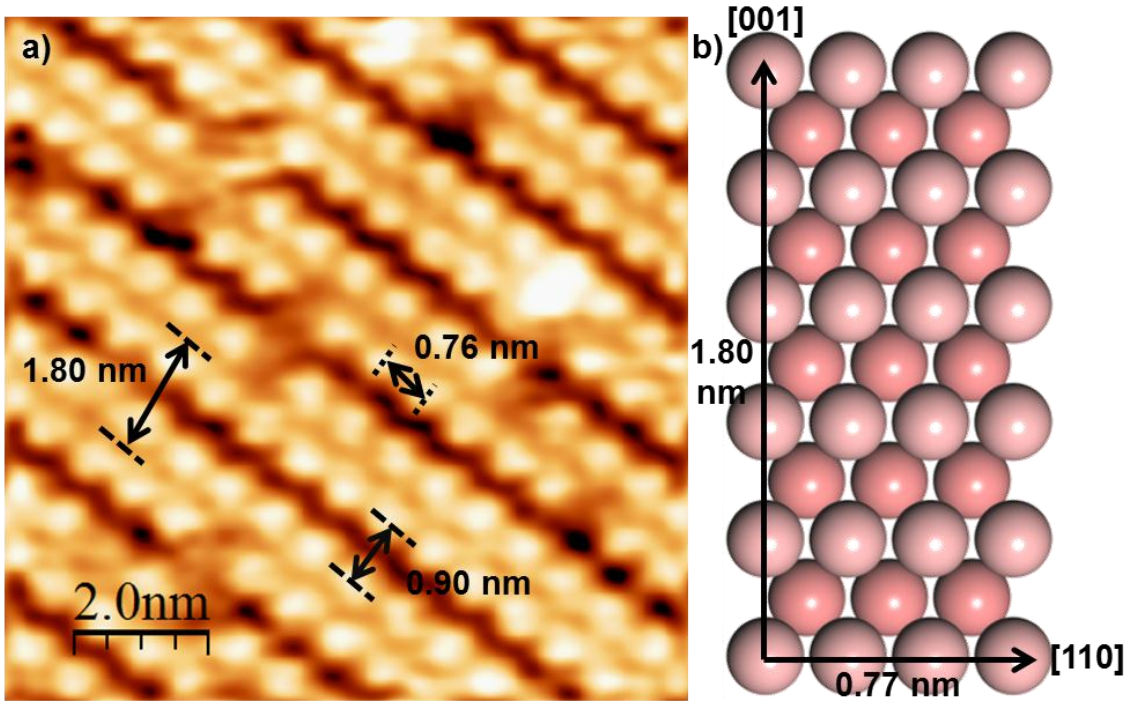

Fig 6.4: a) STM image of the molecular array. The width of the chains and the periodicity are indicated on it. The Cu_4Cl_4 structure shows several defects, but the amount of them is not significant. Size: 10 × 10 nm; Bias Voltage: -0.75 V and Set Point: 0.2 nA; b)

Representation of the Cu (110) surface. In the figure the corresponding distances is indicated to five and three copper atoms in each direction. The use of two pink tones marks out two different layers of the substrate.

To go from the STM images to the molecular structure when complex molecules are involved is a hard task. To overcome this problem, Jose Ignacio Martinez (theoretic scientist of our group) has carried out ab-initio atomistic and molecular dynamics simulations STM-DFT on different possible organizations of Cu_4Cl_4 on the copper surface surface[143].

He combined the localized-basis-set and plane-wave schemes as implemented in the FIREBALL[144] and PWSCF[145] simulation packages, respectively. A perturbative van der Waals (vdW) correction was used to check the reliability of the adsorbed adlayer configuration, as well as the adsorption distance and energy. Additionally, in our STM approach, tunnelling currents for the STM images were calculated using a Keldysh–Green function formalism, together with the first-principles tight-binding Hamiltonian obtained from the local-orbital DFT-FIREBALL method[144,146,147].

The theoretical calculations indicate the geometrical structure for the gas-phase molecule change when it is adsorbed on the Cu (110) (Fig 6.5a). The molecule suffers an accommodation on the surface, and the initial leg positions are modified, so the metallic-core of the molecules is displayed as a depression in the STM images (Fig 6.5b). In the figure, it is possible observe the STM simulated image next to the experimental one. There, the molecular model is drawn on the calculated STM image and it supports that the metallic-core of the molecule is displayed darker at the STM images.

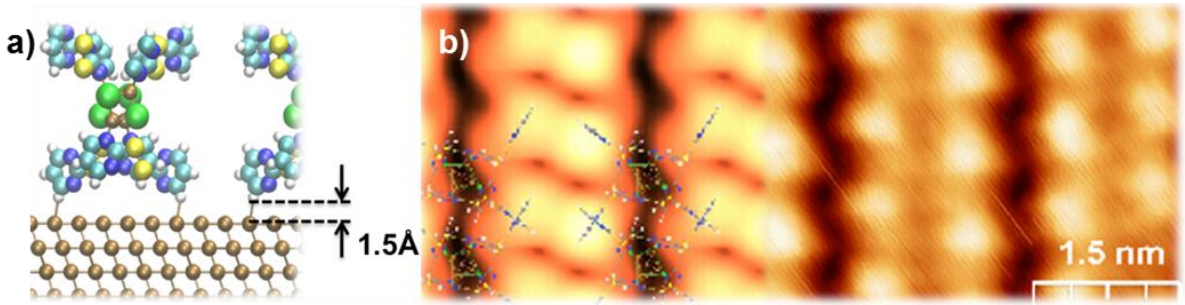

Fig 6.5:a) Schematic model of the molecule on Cu(110). The geometry optimization indicates that the molecule is placed at 1.5 Å on the copper; b) STM images with the [001] surface direction corresponding to the horizontal axe; left side: simulated STM image obtained for the same conditions than in the experiment. In that part, it is possible observe the structural model represented in Fig 6.6 overimposed to the STM image; right-side: experimental STM image of the self-organized compound. Set Point=0.25 nA and Bias Voltage=-0.75 V.

The assembly of the molecules is the result of p-p interactions between the di-pyrimidine rings of the Cu_4Cl_4 legs. In this way, a parallel-displaced π-π stacking of the rings create this intermolecular bonding (Fig 6.6) and form the supramolecular array along [110] direction. The calculations verify that the structural and chemical integrity of the metal-organic core is preserved. The Fig 6.6 shows the molecular assembly schematically.

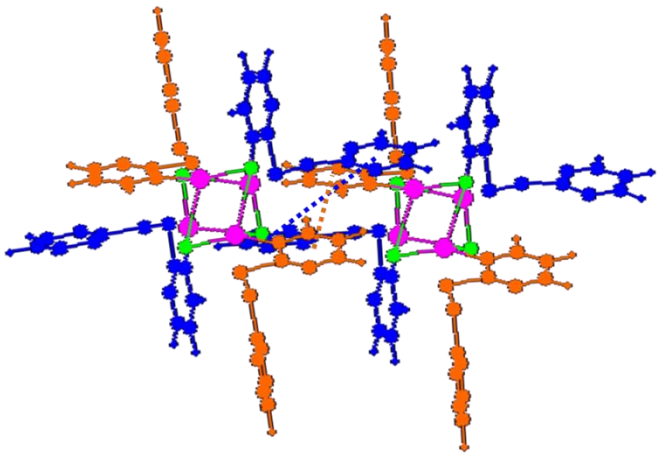

Fig 6.6: Schematic representation of the molecular assembly. The molecule keeps the pink and green colors for copper and chlorine atoms respectively. The blue color corresponds to the legs of the molecule closer to the substrate (down part of the Cu_4Cl_4), and the orange color identifies the legs farther to the Cu (110) surface (in the up part of the molecule). The dashed lines mark out the displaced π-π bonds between the legs of the same color. Moreover, the stacking is also formed by other weak interactions as Hydrogen bonds.

6.3 Reaction induced by water

As we indicate above, the Cu_4Cl_4 structure suffers changes in a water environment[142]. This idea conducts the experiment to observe what happen after the self-organization of the molecule on a Cu (110) surface in a pure-water environment. For this purpose, we have introduced mili-q water in the ultra-high vacuum chamber using an increasing flux until 2×10^{-9} mbar. The water is introduced via a water vessel and a leak valve. The water has been pre-purified by several pumping cycles when the water is frozen.

The LEED pattern after the pure water exposure has changed from a p (3×5) (Fig 6.2b) to a p (2×1) (Fig 6.7a). This new structure corresponds to the LEED pattern of oxidized copper[148,149]. The Fig 6.7b illustrates the positions of the oxygen atoms on the copper surface. This way, the copper unit cell is indicated by a black line, and the corresponding cell to the new LEED pattern (p (2×1)) is marked by dashed lines.

This transformation implies that the water molecules (or part of them) break up. The capability of the copper to broke water molecules is a controversial issue.

Several works about water adsorption in copper surfaces has been published[150–159] reporting two main lines of opinion. Some authors have reported that water molecules do not break on copper at any temperature, but small amounts of oxygen promoted the decomposition[152]. On the other hand, organized structures of water on copper at temperatures below 195 K have been reported[151,159] and the partial decomposition of water molecules occur between 170-190 K[155–158], so a consensus developed that this temperature is the lower limit for the water dissociation on copper.

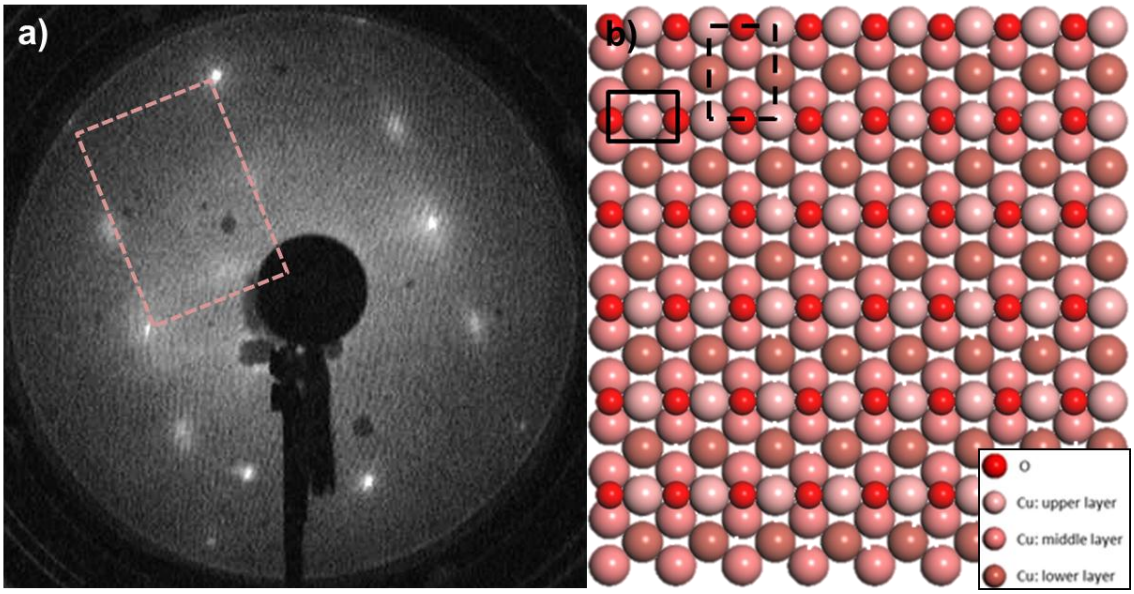

Fig 6.7: a) LEED pattern of a p(2×1) structure. It corresponds to the reconstruction of Cu (110) with oxygen. The pink dashed lines indicate the Cu (110) unit cell. E= 44 eV; b) Representation of the atoms positions in the reconstruction of Cu (110) with oxygen. Black solid lines indicate the Cu (110) unit cell and black dashed lines mark out the 2×1 cell related to the reconstruction.

Our experiments have been performed at room temperature, so in any case the temperature was above 195 K. Thus, the water molecules dissociate on the copper surface. Then, the oxygen or the OH^- re-organized on the surface as it is illustrated in Fig 6.7b.

At the moment we are introducing water molecules in the ultra-high vacuum chamber we can measure the copper surface with the STM simultaneously (the STM let us observe the changes in the surface). The images show new black areas (Fig 6.8a) and new shorter and less bright chains aligned with the original ones. Progressively, a number of black regions increase (Fig 6.8b) and the long stripes formed by Cu_4Cl_4 molecules are shortened. This way, these images show the etching process due to the water exposure.

Among these new elements, it is possible to observe the 2×1 reconstruction covering the surface (Fig 6.8c). There, the long original stripes are shortened and intercalated with the new ones. The reconstruction is also showed in a closer image in Fig 6.8d. It is formed on the entire surface, so it has enough presence to give the Fig 6.7a pattern. Moreover, in Fig 6.8d, the black and bright new areas are also observed.

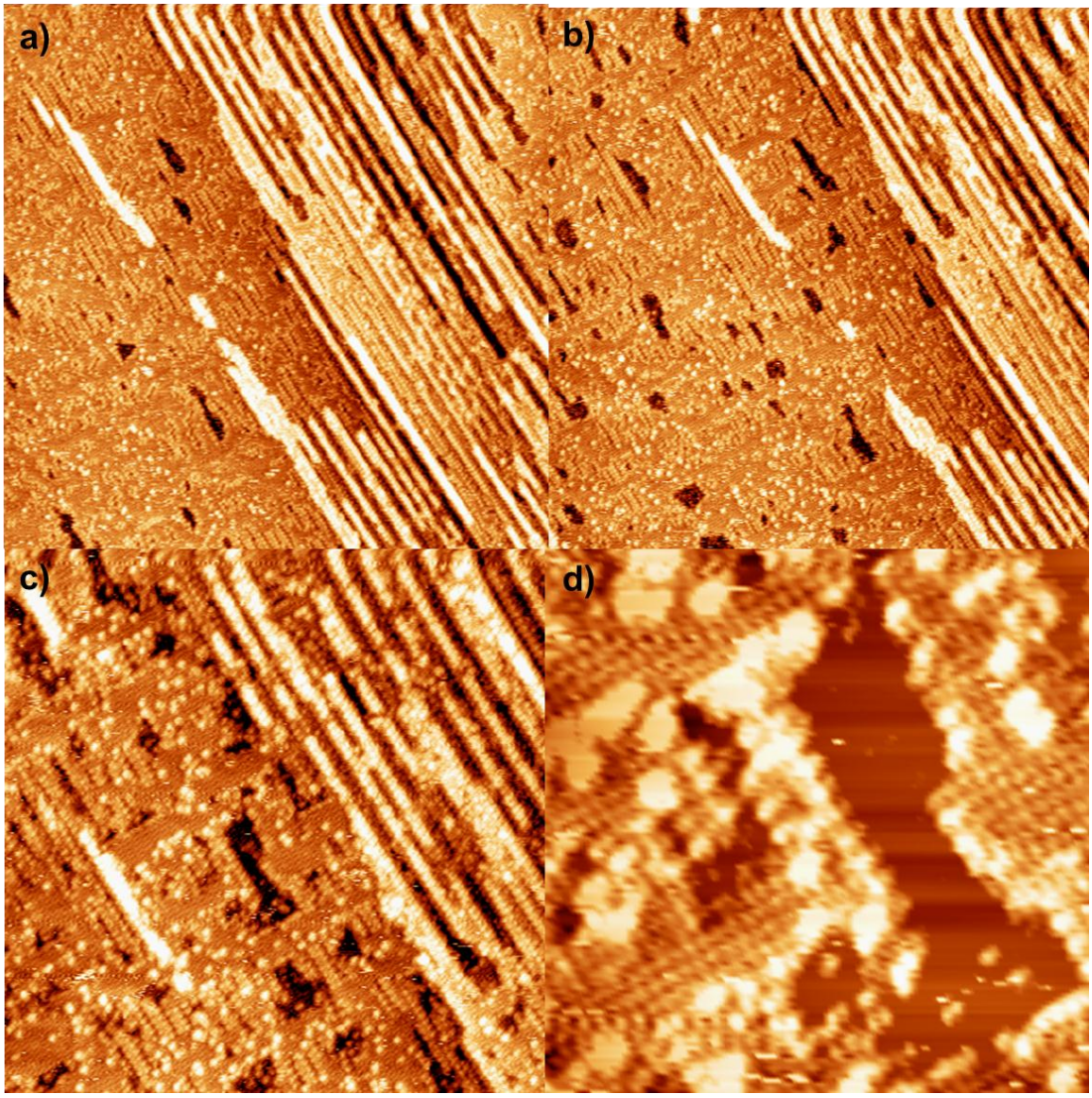

Fig 6.8: a) STM image at the beginning of the water exposure. The black regions are appearing, and new short chains are forming aligned to the previous molecular lines Size: 100 × 100 nm; Bias Voltage: 1.65 V and Set Point current: 1.0 μA; b) Topographic appearance of the surface 39 min after the Fig 6.8a. The black regions have increased, the original stripes have shortened, and there are more short lines on the surface. Size: 100 × 100 nm; Bias Voltage: 1.65 V and Set Point current: 1.0 μA; c) This picture corresponds to the surface 66min after 6.7a. The 2×1 reconstruction is easily observed, the stripes of Cu_4Cl_4 are shorter, and there are fewer amounts of them. White balls are distributed on the surface; they are rest of molecules. Size: 60 × 60 nm; Bias Voltage: 1.65 V and Set Point current: 1.0 μA; d) A close view of the surface in the same period of 6.7c. The reconstruction and the other elements

described before are observed. Size: 14 × 14 nm; Bias Voltage: 1.65 V and Set Point: 1.0 μA.

On the other hand, the reaction induced by water molecules does not stop in this step. We observe the evolution of the surface appearance, and eleven hours later, it is completely different. The water molecules, the ions from the water dissociation and the dark islands from the surface continue interacting with the stripes of molecules (the short new ones and the long and bright chains).

The LEED pattern has transformed into a kind of c (2×2) cell where the center spot is unfolded in four ones (Fig 6.9a). The copper unit cell is indicated with the pink dashed lines and in the down left corner has placed a representation of a c (2x2) cell. This scheme has obtained with the LEEDpat software[124]. This reconstruction is reported in the bibliography as a sulfur atoms organization on Cu (110) after the surface had interacted with oxygen atoms forming a p(2×1)[160,161]. So, we have reproduced this process. Thus, we can extract from this information that we have free sulfur atoms on the surface, and therefore our molecules broke and release them. Afterwards, they react with the oxygen from the surface.

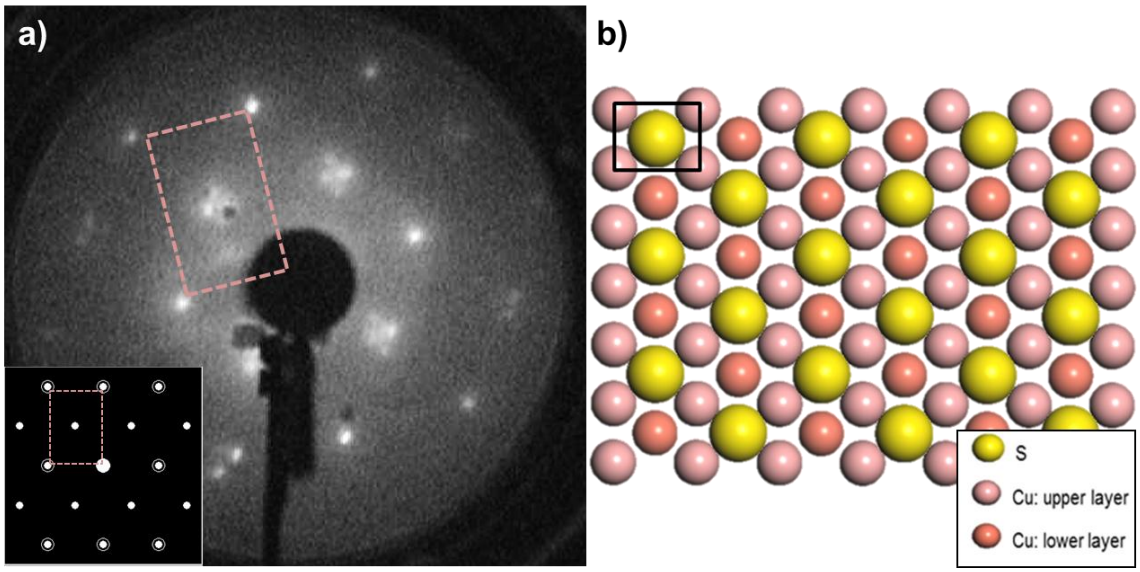

Fig 6.9: a) LEED pattern of a c(2×2) with the unfolded center spot in four ones. In the down, left corner the corresponding representation obtained with LEEDpat is placed. In both cases, the unit cell of Cu (110) is indicated with pink dashed lines. E = 67 eV; Scheme of the sulfur distribution on the Cu (110) in agreement with the literature and the LEED pattern. The copper unit cell is indicated by solid black lines.

The model related to the sulfur reconstruction on Cu (110) is illustrated in Fig 6.9b. The sulfur atoms are positioned in the center of a copper unit cell (indicated with black lines forming a rectangular shape), but they are not in all copper cells of the surface. This organization of the sulfur atoms is only obtained with an oxidized Cu (110) surface. This way, it is reported in the literature by several works related to this topic[160,161] where we can extract some conclusions: 1.) the sublimation of oxygen atoms on Cu (110) forms a p (2x1) structure as the model in Fig 6.7b. After that, a sublimation of sulfur atoms reorganizes the structure forming a c (2x2) as it is illustrated in Fig 6.9b; 2.) the sublimation of sulfur atoms on a clean Cu (110) surface do not make an organized structure, and the sulfur atoms form clusters on the surface; 3.) however, if oxygen atoms are sublimated on a Cu (110) with sulfur clusters on it, the sulfur atoms re-organize forming a c (2x2) as Fig 6.9b. Thus, the oxygen plays an essential role in this reaction.

On the other hand, the STM images show a different situation (Fig 6.10a). The stripes observed before water sublimation (section 6.2) have now less population and there are new chains distributed on the surface. The black areas have disappeared (Fig 6.8) and new chains are forming 60° with the brighter chains. Moreover, it is possible to observe rest of molecules as bright balls covering the areas between the chains. These rests of molecules began to appear from the beginning to the miliQ-water sublimation.

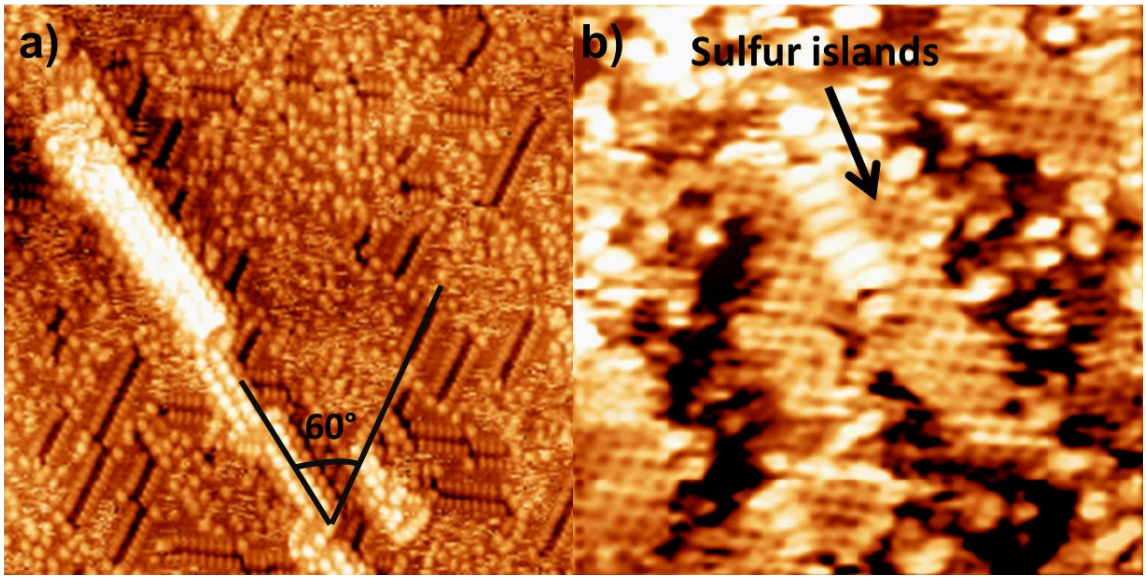

Fig 6.10: a) Topographic STM image showing the surface before water sublimation with molecular chains and other new ones with a different appearance. These new stripes form 60 ° with the first lines as it is indicated in the figure. Size: 30 × 30 nm; Bias Voltage: -1.6 V and Set Point current: 10.0 μA; b) STM picture showing sulfur islands. These islands cover the surface around the different chains and the bright balls observed on the surface. Size: 12 × 12 nm; Bias Voltage: -1.7 V and Set Point: 20 μA

Zoom images let us to observe between stripes and rest of molecules that the surface is covered by sulfur islands (Fig 6.10b). These islands are the reason for the new LEED pattern, showing an appearance in agreement with the geometrical model (Fig 6.9) and with other reported results[160,161].

It is useful to get a good characterization of these new stripes to understand the main differences with the original ones and elucidate how they can be formed. This idea leads us to compare the periodicity and the width of the two types of chains. In a simple view of an STM image (Fig 6.10a), the periodicity along the new chains is apparently lower, so the molecules are more packed. A comparison profile is performed along the new and original chains as shown in Fig 6.11a. The corresponding images are next to the graph, with arrows indicating where the profiles were taken. In the graph, the distance between six bumps of the first stripes corresponds to twelve bumps of the new chains approximately. So, the new stripes have a periodicity close to the half of the one of the stripes before water sublimation. In fact, the average distance between two bumps of the new chains is 0.45 nm (The periodicity of the original stripes is 0.76 nm as it is indicated above). This value has been obtained from an average of the profiles from different images and chains.

On the other hand, the width of the new and original stripes is also compared through transversal profiles (Fig 6.11b). The width of the original stripes was taken from the distance end-to-end of the chain (1.80 nm) and the distance between centers of the bumps (0.90 nm), but the width of the new stripes are characterized only by the heart of the bumps. The new chains are darker than the originals, and the transversal ends of them are diffused with respect to the other things on the surface, anyway the distance bump-to-bump is around 1nm and the total width of the stripes 1.9nm.

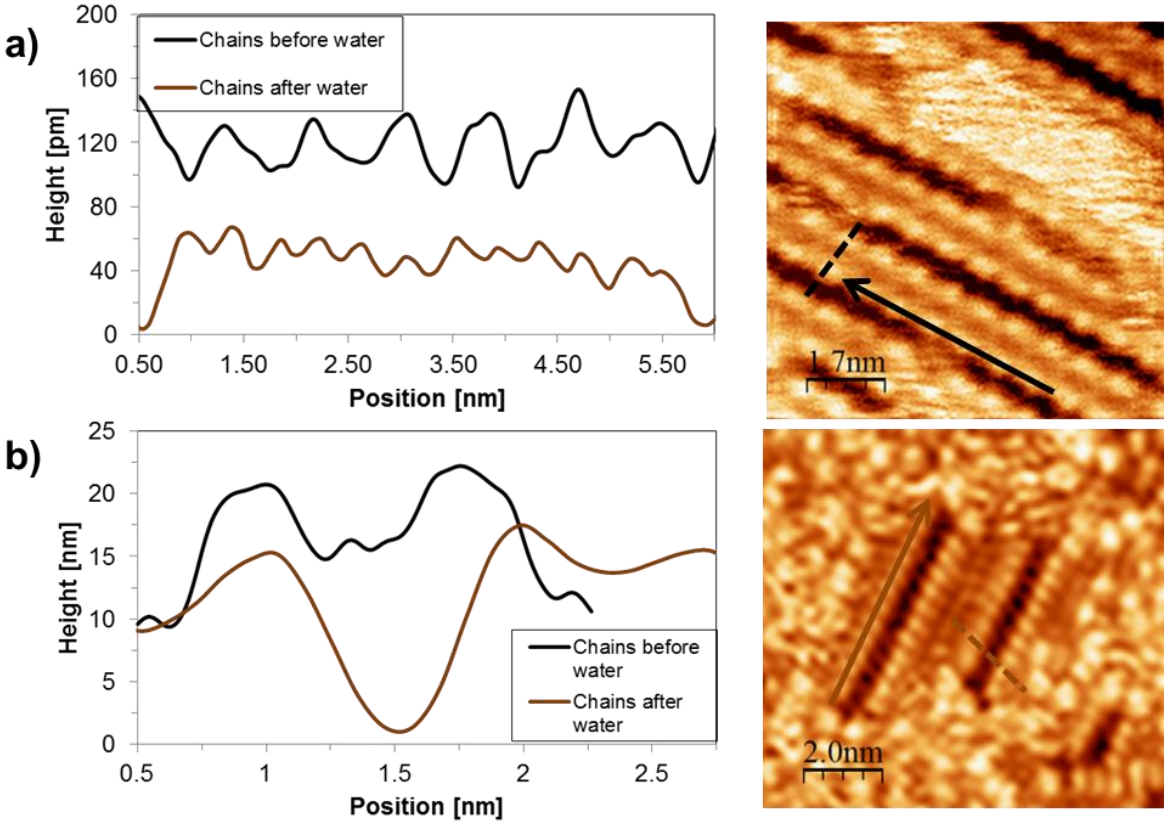

Fig 6.11 a a) Comparison of profiles along the two types of chains. The corresponding images to the profiles are placed on the right side with two arrows indicating the profile direction; b) Comparison of profiles of the width across the two types of chains. The corresponding images are next to the graph with two dashed lines indicating the profile direction.

The transversal profiles show that the new chains are slighty wider than the original stripes. The estimation from the average width of the new stripes is 1.00 nm (distance between the brightest zones of the bumps), so they are at around 0.10 nm wider than the first lines.

The two corresponding images of the transversal profile are placed next to the width comparison (Fig 6.11b), and a line on every image indicate the direction of the profiles.

The experimental results lead us to the idea that water molecules induce a reaction of the stripes of Cu_4Cl_4 molecules on the Cu (110) surface, in a way that the molecules break and release sulfur atoms. The resulting new molecules, without or with fewer sulfur atoms, organize on the Cu (110) to form new chains. On the other hand, DFT calculation determines that the self-organization of the molecules by π-interactions force the molecules to keep “stand up”, it means that there are two legs (di-pyrimidine disulfide) close to the Cu (110) surface and two other ones away.

We focus on the possible reactions which can be involved between these legs to clear up the structure of the molecule and forming the new stripes. Based on the literature[162] we have established several mechanisms of reaction to obtain three possible final structures. These mechanisms are showed according to the bond valence model, which is an easy way to represent a solid structure (Fig 6.12- Fig 6.14).

In all of these mechanisms, we have to consider that the copper from the surface links to the molecule as a metallic complex, but this is a weak interaction. Moreover, the reactions occur at the legs of the Cu4Cl4 (di-pyrimidine disulfide), so we have represented one of them as a way to simplify the scheme. This way, the rest of the molecule is represented as a red R. On the other hand, these mechanisms can be given by an asymmetric or a symmetric reaction. It means that the di-pyrimidine disulfide is a symmetric structure and the reaction can form in one part of it or two parts at the same time symmetrically.

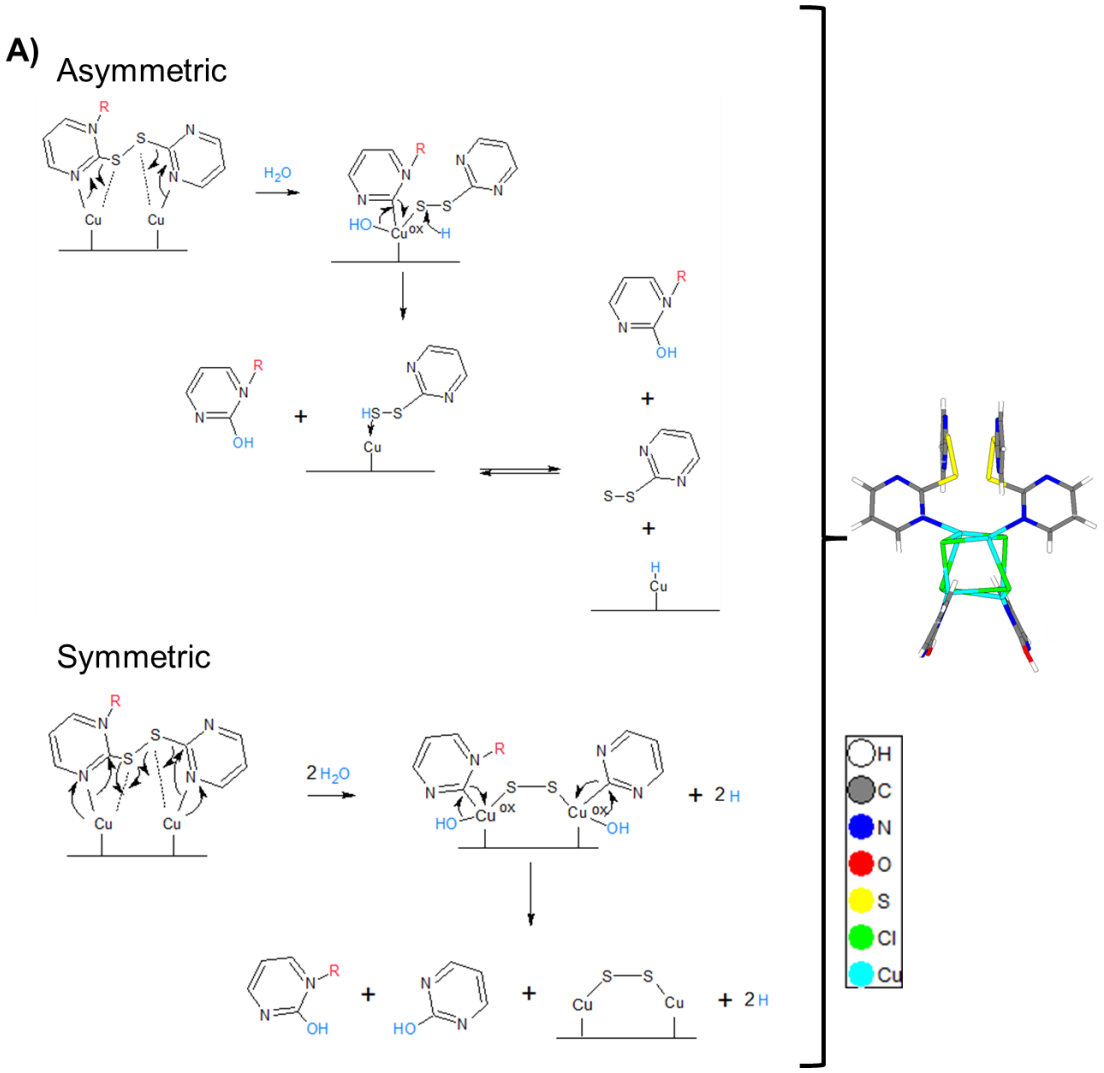

Fig 6.12: Scheme of two mechanisms of reaction which conclude in the same structure of the molecule (at the right side): the structure A.

The first structure (Fig 6.12) can be given through two different mechanisms, one symmetric and another one asymmetric. In the initial state, the leg of the molecule is interacting with the copper of the surface weakly. After water sublimation, the copper from the surface oxidizes, and the dissociated water molecules react with the molecule. In the asymmetric case, the OH^- links to the carbon of a ring and the rest of the di-pyrimidine disulfide breaks free, and in the symmetric case, two dissociated water molecules react at the same time with a carbon atom of the every ring. The final configuration for our molecule is the same, but the rests from

the reaction differ. In the symmetric case, the sulfur atoms are linked with the copper from the surface, and it can give an explanation of the sulfur islands formation, however, in the asymmetric case, the free part can continue reacting with the surface in subsequent events, and a similar final situation can be formed. Here, we have not gone deeper in that part. These two mechanisms have as result the colored molecule next to them.

The second structure (Fig 6.13) is the result of an asymmetric mechanism. Like the first case, the copper from the surface has a weak interaction with the leg of the molecule. After water sublimation, the bond between the two sulfur atoms breaks, in a way that one of them links to a hydrogen from the dissociated water and the other one links to the oxidized copper from the surface. Then, the OH^- links to the sulfur atom of the free part of the molecule. The new molecule obtained from this mechanism is placed next to it.

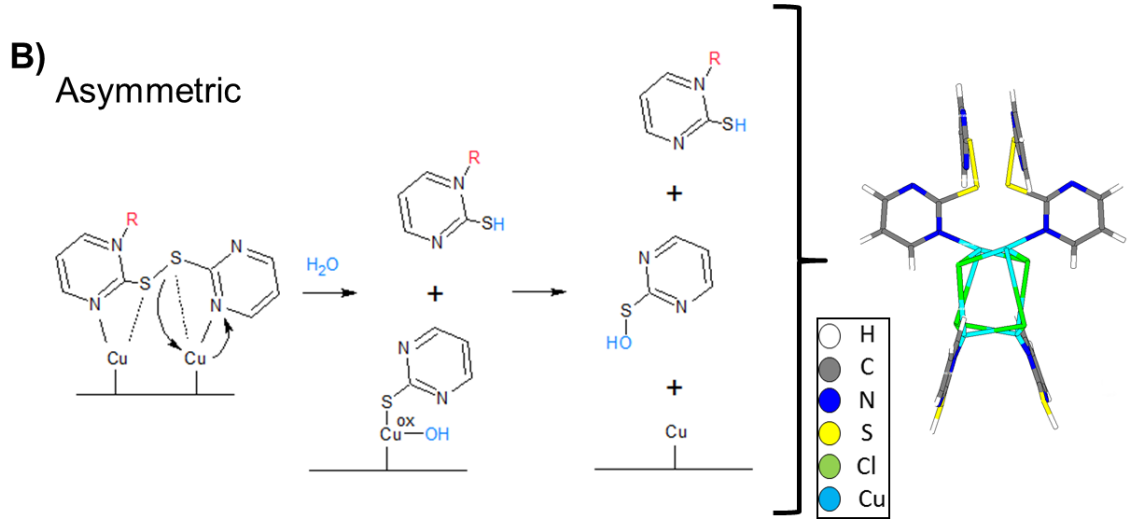

Fig 6.13: Structure B (at the right side) as one of the possible molecules that can be formed by water sublimation. It consists of asymmetric mechanism of the reaction.

The third possible structure (Fig 6.14) can be formed by two different mechanisms as the first, one asymmetric and another one symmetric. In both cases, the copper is interacting weakly with the legs of the molecule. After water sublimation, the copper substrate oxidizes. In the asymmetric scheme, the di-pyrimidine disulfide breaks between the two sulfur atoms, in a way that a sulfur atom link to hydrogen and this part release from the rest of the molecule. The other sulfur atom is connected to an OH^- at the end of the reaction. The symmetric mechanism allows the interaction of two dissociated water molecules with the sulfur atoms at the same time. In that way, the bond of the two sulfur atoms brakes and they link to two OH^-. In both mechanisms, the surface is involved in the reaction, but at the end, it keeps clean. In principle, the copper atoms do not link to another species at the end of the reaction. However, the free part of the original molecule can continue reacting with the surface until the formation of the sulfur islands. The complete obtained molecule from these mechanisms is situated at the right side of the schemes, and the color legend indicates its composition.

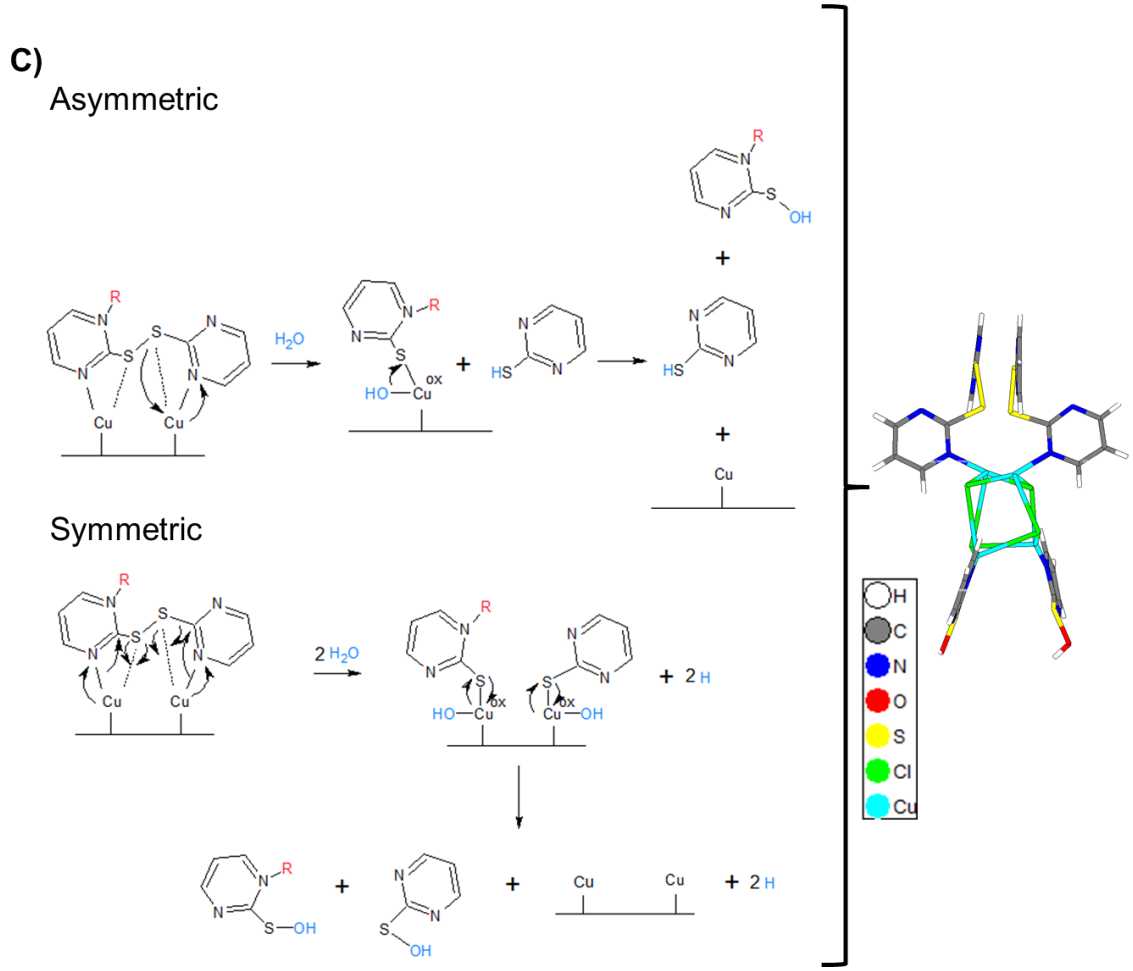

Fig 6.14: Structure C of the molecule (at the right side) and two different mechanisms to form it.

Consequently, we have performed the geometry optimization of these three structures to obtain which is the most energetically favorable transformation. The convergence parameters employed are the same as in section 4.4, including the exchange-correlation functional. The Monkhorst-Pack grid used is 1 × 1 × 1, and the calculations have been performed with the CASTEP code.

The molecules (the molecule before water sublimation and the three possible resultants) are compounded by a huge number of atoms (70-88). In addition, each molecule has to be separated in the cell without interacting with other molecules,

so we have used a Cu (110) supercell of 7x7. In a first moment, we placed each molecule on the copper surface but the systems are compounded by 315-333 atoms (molecules + 5 layers of copper atoms in a 7x7 supercell), so we find some troubles for the convergence process. The calculation was very slow, and we needed a lot of RAM memory and a number of processors for every calculation. On the other hand, the copper substrate affects to the activation energy of the reaction, but the initial and final energy of the molecule should be the same, so we have performed these calculations to obtain the transformation energy by using the molecules alone in the cells. Here, we consider the ions of the dissociated water for the transform energy calculation because the water has been broken with the copper interaction.

The energy of the each reaction is calculated from:

$$E = (E_A + E_{RA}) - (E_{Cu4Cl4} + 2E_{OH}) \quad \text{Eq (6.1)}$$

$$E = (E_B + E_{RB}) - (E_{Cu4Cl4} + 2E_H) \quad \text{Eq (6.2)}$$

$$E = (E_C + E_{RC}) - (E_{Cu4Cl4} + 2E_{OH}) \quad \text{Eq (6.3)}$$

Where E_A, E_B, and E_C are the energies for the structure A, B and C of the molecules respectively and $E_{RA,}$ E_{RB} and E_{RC} the energies for the corresponding free rests of each one. E_{Cu4Cl4} is the energy for the molecule before the water sublimation, and E_{OH}/ E_H is the energy of the dissociated water part involved in the structure of the last molecule (OH^- or H^+).

The values of the transforming energy are collected in Table 6.1. These values indicate that the energetically most favorable transformation is the change from the molecule before sublimation to the molecules with the A structure. The negative value is related to the exothermic nature of the transformation, and it denotes a spontaneous process.

	A	B	C
Energy [eV]	-14.64	-3.37	-11.12

Table 6.1: The table collects the values for the transforming energy from Cu_4Cl_4 to each one of these three. The values have been calculated with the equations 6.1 - 6.3.

On the other hand, the absolute value of -14.64 eV can be significant, so we focus on the break of a di-pyrimidine disulfide. We have isolated this compound and the two final products (2-pyrimidinol and pyrimidine disulfide) to obtain the energy involved in this transformation. Applying the above equations, we have calculated this energy with:

$$E = (E_{POH} + E_{P2S}) - (E_{2P2S} + E_{OH}) \qquad \text{Eq (6.4)}$$

where E_{POH}, E_{P2S}, and E_{2P2S} are the energies for the 2-pyrimidinol, the pyrimidine disulfide, and the di-pyrimidine disulfide respectively.

In this case, the final energy of this conversion is -7.37 eV. This value is almost half of the transformation energy of the whole molecule where two di-pyrimidine disulfides are implicated, so the result obtained from Eq(6.1) is due to the breaking of the two legs at the sulfur-carbon bond and creation of new bonds as the C-OH.

The Fig 6.15 illustrates these components to facilitate the identification with the Fig 6.12 and the comprehension of the energy from Eq (6.4).

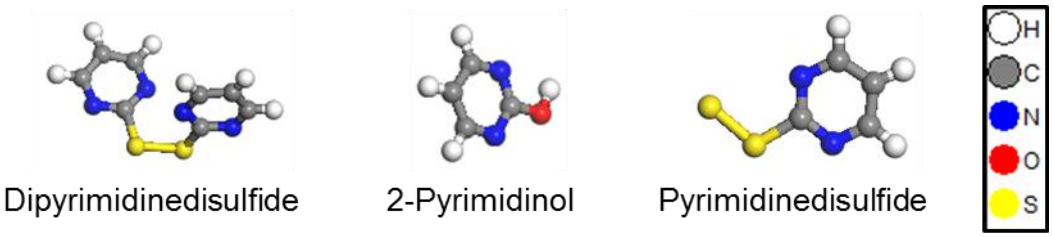

Fig 6.15: Illustration of the involved elements of the transformation to obtain the Structure A as a result of the reaction induced by the water in the Cu_4Cl_4 molecules.

In conclusion, the chemical mechanisms and the energetic calculation determine that the most energetically favorable transformation is the one from the structure of the molecule before water sublimation (Cu_4Cl_4) to the structure A (Fig 6.12). Thus, we have built a model of a molecular chain with the structure A and taken into account the distances observed in STM. Placing four units of this structure on two layers of the copper surface Cu(110) we have performed an STM simulation with CASTEP. The substrate has been previously optimized using a Cu (110) super-cell (10×10) as well as the geometric structure of the molecules on the surface with the same parameters as above.

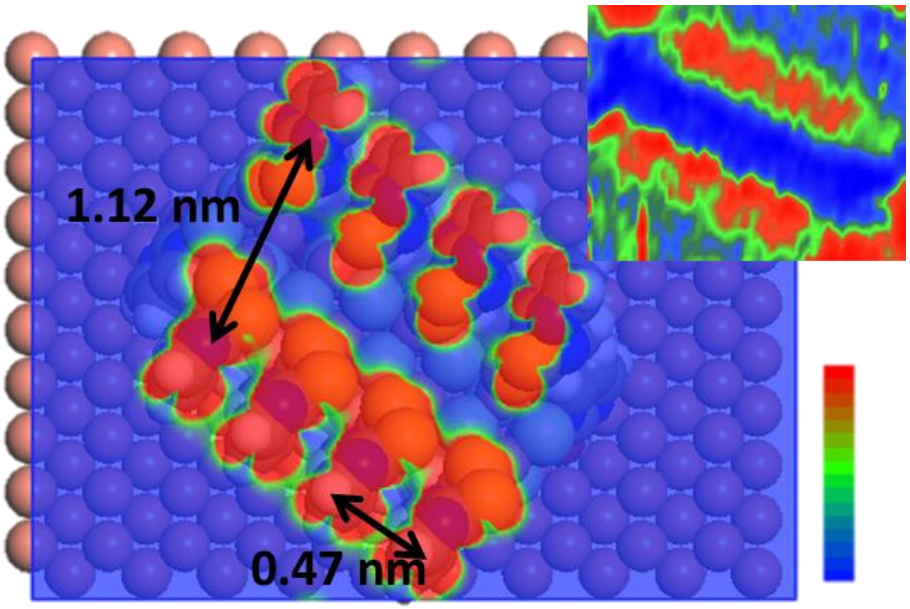

Fig 6.16: STM image simulation of four Structure A molecules on two Cu (110) layers.

Up, right is placed a corresponding experimental STM image to an easier comparison. The width and periodicity of the STM image are indicated on it.

Fig 6.16 shows the STM simulated image and the up, right corner displays an STM experimental image of the new chains observed after water sublimation. We have changed the color code of the experimental image for a better comparison between both. The model corresponds nicely with the periodicity and the width of the new chains: 0.47 nm and 1.12 nm respectively for the model, in good agreement with the experimental values of 0.45 nm and 1.00 nm. So the broken of the two di-pyrimidine disulfides close to the Cu (110) induces a molecular reorganization of the chains, in a way that the distance inter-molecular is almost half of the distance before water sublimation. The two other di-pyrimidine disulfides, far from the surface, extent their positions and increase the width of the chain.

6.4 Discussion

In this chapter, we have studied the transformation of a metal organic cluster on a Cu (110) surface induced by water. First, we analyze the self-assembly organization that the molecules acquire. The LEED and STM techniques and the DFT calculation determine that the molecules form stripes where the middle of the molecules give a dark contrast in the STM. The inter-molecular π interaction between the legs of the molecule (the di-pyrimidine disulfides) is the reason for this assembly. The width and periodicity of these chains are 1.8 and 0.76 nm respectively. These values correspond to the distance between 5 and 3 copper atoms of Cu (110) in the two directions, so it is in agreement with the LEED pattern observed (p (5×3)).

After water sublimation, the water molecules dissociate on the copper surface. The surface reconstructs with the oxygen forming a p(2×1) as it is reported[148,149]. At the end of the reaction, the black islands observed at the sublimation have disappeared, and the new short chains have changed to a different appearance. Now, they are less bright, wider (1.00 nm), with low periodicity (0.45 nm) and they form 60° respect to the original chains. It means that the new chains are placed along the [111] crystallographic direction of Cu (110). The differences between the width and the periodicity can be observed in Fig 6.10. Besides the two types of stripes, the surface shows a lot of rest of broken molecules with an appearance as bright balls. Under all this, the copper is covered by sulfur islands forming a c(2×2) ordered structure.

Regarding the mechanism of the reaction and due to the chemical nature of the elements involved, at least five different reactions can be given with three different molecules as resultant products. An estimation of the transformation energy establishes one of them as the most favorable (structure A, Fig 6.12). Even so, it is worth pointing out that the two structures with better values for the transforming energy are the two with the legs link to OH^-(structures A and C; Fig 6.12 and Fig 6.14). Thus, the OH^- helps to stabilize this molecule better than the hydrogen atom.

The analysis of the transformation of one isolated leg of Cu4Cl4 (di-pyrimidine disulfide) in 2-pyriminidol and pyrimidine disulfide (the products of the mechanism to obtain the structure A) establish that the break and the formation of the bonds C-S and C-OH is an exothermic process which invests -7.37 eV. That value is a half of the total energy implicated in the transformation energy from Cu4Cl4 to structure A. Thus, it indicates that the whole transformation energy is due to the changes with the two legs close to the copper surface.

On the other hand, the reason for the conversion of Cu_4Cl_4 to one specific molecule (structure A) is the most energetically favorable does not mean that it is the only molecule on the Cu (110) co-existing with the Cu_4Cl_4 ones. In fact, the most probable thing is that the two other molecules, or at least the structure C, have a presence, to a lesser degree, on the surface.

Moreover, we propose a model for the observed chains using units of the structure A. The STM image simulation of four molecules with structure A on Cu (110) (Fig 6.16) shows a similar appearance that the observed in the experimental images. Moreover, the characterization parameters as the width and the periodicity are in good agreement with the experimental ones.

So, in this chapter, we have faced to two different challenges: a) we have sublimated a huge molecule in ultra-high vacuum environment without molecular disruption; and b) we have analyzed the chemical reaction carried out on a copper surface.

7. General Conclusions

I. In this work, we show a new method to growth graphene. It is based on the direct sublimation of atoms or compounds made of carbon on a surface. This methodology can be summarized as a solid carbon source through which a current between 14.0 -18.0 A pass in a UHV environment. In our case, we have characterized that the used current in the graphene growth (14.0 A) sublimates atomic carbon as the main mass.

II. The Clausius-Clapeyron equation has allowed obtaining the specific latent heat of different species. The results reveal that the diatomic carbon is especially hard to sublimate in comparison with other ones. Even so, the diatomic carbon has much presence during sublimation, and it increases at higher temperatures.

III. Based on the values for the specific latent heat and the percentages of presence, we can conclude that the solid carbon filament is mainly made of mono- and di- atomic carbon species, and there are other ones in minor quantity.

IV. We have demonstrated the efficiency of our method in the growth of graphene on substrates with different characteristics: two metallic substrates (Pt (111) and Au (111)) and two different surfaces of diamond (C (111) and C (100)) doped with boron or nitrogen (they have a semiconductor behavior). We have annealed these substrates at lower temperatures that the reported in the literature to growth graphene. Those temperatures are G/Pt (111): 923 K; G/Au (111): 823 K; G/C (111) and G/C (100): 1273 K. The difference between the values of G/Pt (111) and G/Au (111) is due to

the diffusion barrier of one carbon atom on each surface. The carbon atom needs 60 K extra to jump from a cell to the neighbor one on platinum.

V. Graphene on Pt (111) covers large areas. The main graphene orientation is the moire of 19° (observed in the LEED pattern). However, it is hard to observe because the periodicity is small (7.1 Å approx.). On the other hand, there are other moirés easily identifiable as the moire of 2°. This orientation is the result of the rotation of 16.5° of the graphene layer respect to the substrate, and it exhibits a higher periodicity (18.8 Å).

VI. Graphene on Au (111) form dendritic shapes and growth from both sides of the steps or pinned by defects. There are two main orientations of graphene at 0° and 30°. An increase of the surface covering does not alter the dendritic shape. These “fingers” are the result of the carbon-carbon interaction prevailing over the carbon-gold one. The main difference with the G/Pt system is that the carbon atoms can diffuse more on platinum because this substrate is annealed at higher temperature.

VII. Calculations establish that if the number of carbon atoms increases, it is more complicated that they are adsorbed on a surface. In the Platinum case, the carbon atoms place in the positions of the platinum ones if they exist, occupying a fictitious platinum layer on the surface. However, the carbon atoms on the gold surface form compounds with each other bonded to the atoms of the surface. However, in the cases of six carbon atoms on the metallic surfaces, the behavior changes and the carbon atoms combine with the substrate atoms to form a hexagonal structure. On the other hand, the distance between the carbon atoms and the substrate increase with the number of carbons, so once the graphene layer is formed, that distance is the highest in both cases (between 3.0 Å and 4.0 Å).

VIII. Graphene on diamond C (111) forms nano-islands as patches on the surface with different orientations. The LEED and STM techniques identify a p(2×2) structure attributable to the graphene growth. Moreover, a displacement of the energy loss peak is observed, in a way that the distance of it with the elastic peak increases 9.0 eV. The theoretical calculation and the simulation of STM images help to determine that the p(2×2) structure is compounded by the graphene on a buffer layer of one carbon atom on the C (111) surface.

IX. In this work, graphene has growth on three hexagonal surfaces (Pt (111), Au (111) and C (111)) and another more with a square surface (C (100)). At first, the geometry of the surface should favor the formation of another hexagonal material like graphene, and it can be more complicated in a different geometry. In this case, graphene growth on C (100) forms a p (2×1) structure, and it is oriented in both directions of the diamond lattice. Despite the troubles with the quality of the surface and the insulating nature of the substrate, graphene has grown on the surface forming hexagonal islands linked with each other. The energy loss peak suffers a displacement in the same direction of the G/C (111) case, but now, the distance between it and the elastic peak increases only 4 eV.

X. On the other hand, we have been able to sublimate a large molecule on Cu (110) without it suffering damage. The Cu_4Cl_4 molecule has self-assembled on the surface forming long stripes in a p (5×3) structure. The DFT calculations have determined that the chains be formed by intermolecular π bonds. In that way, the molecule keeps “stand-up” on the surface, because two di-pyrimidine disulfides are placed close to the copper, and the other two at outlying areas.

XI. In a water molecules environment, a series of chemical reactions have been produced. They conclude with the formation of new stripes. They are less bright, shorter, wider and the bumps show higher periodicity than the stripes related to the Cu_4Cl_4 molecules. Due to the possible chemical mechanisms and the calculations, we conclude that the two di-pyrimidine disulfide of the Cu_4Cl_4 molecule close to the substrate has transformed into two 2-pyrimidinol. The transformation allows that the intermolecular distance reduces, so the periodicity in the stripes formed by the molecules after transformation is higher. This way, the corresponding simulated image of STM ratifies this fact.

XII. The chemical reaction produced on the copper surface changes the LEED pattern in every step. So, these schemes are not directly related to the stripes structure. At the begin of the reaction, the pattern shows a p (2×1) that corresponds to the well-known reconstruction of oxygen on the Cu (110) surface. Later, the scheme changes to a c (2×2) that is related to the organization of sulfur islands on the surface. Both structures are also observed in the STM images, covering the surface. So, that is the reason they have the major contribution in the LEED technique.

XIII. Due to the combination of experimental techniques, calculations, and an analysis of the chemical and physical processes can be involved, we have studied and understood in situ the chemical reaction on Cu (110) surface.

7. Conclusiones Generales

I. En este trabajo se presenta un nuevo método para crecer grafeno basado en la sublimación directa de átomos o compuestos de carbono sobre una superficie. Esta metodología se puede resumir como una fuente de carbono sólida por la que pasa una corriente de entre 14-18 A en un ambiente de Ultra Alto vacío. En nuestro caso, hemos caracterizado que a la corriente usada en los crecimientos de grafeno (14 A), la masa principal sublimada es carbono atómico.

II. Gracias a la ecuación de Clausius-Clapeyron, hemos podido determinar los calores latentes de fusión. Esto determina que las especies formadas por carbono di-atómico son especialmente difíciles de sublimar en comparación con otras. A pesar de eso, el carbono di-atómico es una de las especies más presentes durante la sublimación, pues incluso aumenta su cantidad con el incremento de temperatura.

III. Apoyándonos en los calores latentes de fusión y los porcentajes de presencia de cada compuesto, podemos concluir que el filamento de carbono sólido está principalmente formado por carbono mono- and di-atómico, aunque también hay cantidades de otras especies.

IV. Hemos demostrado la eficiencia de nuestro método creciendo grafeno en sustratos de diferentes características. Por un lado, en dos superficies metálicas, platino (Pt (111)) y oro (Au (111)); y por otro, dos superficies de diamante (C (111) y C (110)) dopados con boro o nitrógeno, por lo que se comportan como semiconductores. Para conseguir estos sistemas, hemos

calentado los sustratos usando temperaturas inferiores a las registradas en la bibliografía. Estas son: G/Pt (111): 923K; G/Au (111): 823K; G/C (111) y G/C (100): 1273K. La diferencia de temperatura entre los sistemas G/Pt y G/Au es debido a la barrera de difusión de un átomo de carbono sobre cada superficie, en el que de un sustrato a otro, el átomo de carbono necesita unos 60 K más para poder saltar de una celda a otra vecina del sustrato.

V. El grafeno sobre Pt (111) se extiende en todas las regiones planas. La orientación principal del grafeno forma el moire de 19°. Sin embargo, es un moire con una periodicidad muy pequeña (7,1 Å aprox.), por lo que es difícilmente observable en STM. Además, hay otros moires fácilmente reconocibles como el de 2°, formado por la rotación de 16,5° del grafeno respecto del sustrato con una periodicidad de 18,8Å.

VI. El grafeno sobre Au (111) tiene una apariencia dendrítica y crece a partir de defectos en la superficie o desde los extremos de los escalones. Sus orientaciones principales forman dos moires, de 0° y 30°. El incremento de recubrimiento de grafeno no cambia la forma dendrítica. Esta forma de "dedos" se debe a que la interacción carbono-carbono predomina con respecto a la interacción carbono-oro. La principal diferencia con el caso de G/Pt es que los átomos de carbono pueden difundir más en la superficie por los 100 K más de calentamiento del sustrato.

VII. Los cálculos teóricos establecen que a medida que aumenta el número de átomos de carbono en la superficie, son más difíciles de ser adsorbidos. En platino, en un principio, los átomos de carbono se organizan en la superficie de forma que intentan adquirir las posiciones que ocuparían los átomos del sustrato. En oro, sin embargo, los átomos de carbono forman compuestos entre ellos que se unen a los átomos del sustrato. A partir de seis átomos de carbono, se forma una estructura hexagonal combinándose con los

átomos del metal. Por otro lado, la distancia de los átomos de carbono aumenta con el número de éstos, de forma que al formar una capa de grafeno, éste se encuentra a mayor distancia del sustrato en ambos casos (entre 3,0 Å y 4,0 Å).

VIII. El grafeno sobre diamante C (111) forma nano islas sobre la superficie con distintas orientaciones. La posición principal de las islas forman una estructura p (2×2) que se observa con las técnicas LEED y STM. El crecimiento de grafeno sobre C (111) produce un desplazamiento del pico de pérdida de energía aumentando en 9 eV las distancia con el pico elástico. Con los cálculos teóricos y la simulación de imágenes de STM, hemos determinado que esta estructura (p (2×2)) se compone de un átomo de carbono (que ha sido previamente adsorbido) en una capa intermedia entre la superficie de diamante y el grafeno.

IX. El grafeno ha sido crecido sobre tres superficies hexagonales, que en principio favorecerían la formación de otro material hexagonal y sobre el diamante C (100) con una superficie cuadrada. En este caso, el grafeno forma una p (2×1) orientado en las dos direcciones de la red del sustrato. A pesar de los problemas por la calidad de la superficie y naturaleza de los diamantes, podemos comprobar la existencia de islas hexagonales de grafeno enlazadas entre sí sobre la superficie de C (100). El pico de pérdida de energía, en este caso, se desplaza en el mismo sentido que en el caso de G/C (111), pero en este caso, la distancia entre él y el pico elástico aumenta en 4 eV.

X. Por otro lado, hemos sido capaces de sublimar una gran molécula sobre una superficie de Cu (110) sin que ésta se haya roto. La molécula Cu_4Cl_4 se ha autoensamblado en la superficie formando largas cadenas organizadas en una estructura p (5×3). Los cálculos DFT han determinado que las

cadenas son el resultado de enlaces π intermoleculares que mantienen a la molécula “de pie” sobre la superficie, es decir, con dos di-pirimidinas di-sulfuro cercanos al cobre, y otras dos muy alejadas de él.

XI. En un ambiente con moléculas de agua, se producen una serie de reacciones químicas que culminan con la formación de nuevas cadenas en la superficie con diferente apariencia. Estas nuevas cadenas son menos brillantes, más cortas, más anchas y con las protuberancias que la forman más apiladas. A través de los posibles mecanismo químicos que se pueden haber dado, y los cálculos teóricos, determinamos que la molécula Cu_4Cl_4 ha sufrido una ruptura en las dos di-pirimidinas di-sulfuro cercanas al sustrato, de forma que han concluido en la formación de dos 2-pirimidinol. Esta ruptura ha permitido que las moléculas resultantes se acercaran más, aumentando así la periodicidad observada en las protuberancias con el STM. Este último hecho se ha podido comprobar simulando la imagen de STM.

XII. A lo largo de la reacción química en la superficie de cobre, los patrones de LEED cambian mostrando un esquema no directamente relacionado con la estructura de las cadena, como sí lo hacía antes de la sublimación de agua. Al principio de la reacción, el patrón de LEED forma una p (2×1) relacionaba con la bien conocida reconstrucción de la superficie de cobre por átomos de oxígeno. Posteriormente, el patrón cambia a una c (2×2) relacionada con la organización de islas de azufre sobre esa superficie. Ambas estructuras son observadas en las imágenes de STM, cubriendo toda la superficie, por lo que dan mayor contribución de señal que las cadenas para la difracción de electrones a baja energía.

XIII. Gracias a la combinación de técnicas experimentales de superficies, cálculos teóricos y el análisis de los procesos químicos y/o físicos que han

podido estar envueltos, hemos podido estudiar y entender in situ la reacción química producida en la superficie de cobre.

Bibliography

1. *Feynman, R. P. There's plenty of room at the bottom.* Eng. Sci. ***23,*** *22–36 (1960).*
2. *Eigler, D. M. & Schweizer, E. K. Positioning single atoms with a scanning tunnelling microscope.* Nature ***344,*** *524–526 (1990).*
3. *Binnig, G. & Rohrer, H. Scanning tunneling microscopy.* IBM J. Res. Dev. ***44,*** *279 (2000).*
4. *Binnig, G., Quate, C. F. & Gerber, C. Atomic force microscope.* Phys. Rev. Lett. ***56,*** *930 (1986).*
5. *Novoselov, K. S.* et al. *Electric field effect in atomically thin carbon films.* Science (80-.). ***306,*** *666–669 (2004).*
6. *Castro Neto, A. H., Guinea, F., Peres, N. M. R., Novoselov, K. S. & Geim, A. K. The electronic properties of graphene.* Rev. Mod. Phys. ***81,*** *109–162 (2009).*
7. *Geim, A. K. & Novoselov, K. S. The rise of graphene.* Nat. Mater. ***6,*** *183–191 (2007).*
8. *Neto, A. H. C. Charge density wave, superconductivity, and anomalous metallic behavior in 2D transition metal dichalcogenides.* Phys. Rev. Lett. ***86,*** *4382 (2001).*
9. *Lippert, G.* et al. *Direct graphene growth on insulator.* Phys. status solidi ***248,*** *2619–2622 (2011).*
10. *Park, J.* et al. *Epitaxial Graphene Growth by Carbon Molecular Beam Epitaxy (CMBE).* Adv. Mater. ***22,*** *4140–+ (2010).*
11. *Wurstbauer, U.* et al. *Molecular beam growth of graphene nanocrystals on dielectric substrates.* Carbon N. Y. ***50,*** *4822–4829 (2012).*

12. *Bartels, L. Tailoring molecular layers at metal surfaces.* Nat. Chem. ***2,*** *87–95 (2010).*

13. *Zwaneveld, N. A. A.* et al. *Organized formation of 2D extended covalent organic frameworks at surfaces.* J. Am. Chem. Soc. ***130,*** *6678–6679 (2008).*

14. *Mendez, J., Lopez, M. F. & Martin-Gago, J. A. On-surface synthesis of cyclic organic molecules.* Chem. Soc. Rev. ***40,*** *4578–4590 (2011).*

15. *Bieri, M.* et al. *Two-dimensional polymer formation on surfaces: insight into the roles of precursor mobility and reactivity.* J. Am. Chem. Soc. ***132,*** *16669–16676 (2010).*

16. *Gutzler, R.* et al. *Surface mediated synthesis of 2D covalent organic frameworks: 1, 3, 5-tris (4-bromophenyl) benzene on graphite (001), Cu (111), and Ag (110).* Chem. Commun. *4456–4458 (2009).*

17. *Ourdjini, O.* et al. *Substrate-mediated ordering and defect analysis of a surface covalent organic framework.* Phys. Rev. B ***84,*** *125421 (2011).*

18. *HTW Hochtemperatur-Werkstoffe GmbH. Sigadur ® G-type. Available at: http://www.htw-germany.com.*

19. *Horcas, I.* et al. *WSXM: A software for scanning probe microscopy and a tool for nanotechnology.* Rev. Sci. Instrum. ***78,*** *(2007).*

20. *Bardeen, J. Tunnelling from a many-particle point of view.* Phys. Rev. Lett. ***6,*** *57 (1961).*

21. *Chen, C. J.* Introduction to scanning tunneling microscopy. ***4,*** *(Oxford University Press on Demand, 1993).*

22. *Hansma, P. K. & Tersoff, J. Scanning tunneling microscopy.* J. Appl. Phys. ***61,*** *R1–R24 (1987).*

23. *Tersoff, J. & Hamann, D. R. Theory and application for the scanning tunneling microscope.* Phys. Rev. Lett. ***50,*** *1998 (1983).*

24. *Gottlieb, A. D. & Wesoloski, L. Bardeen's tunnelling theory as applied to scanning tunnelling microscopy: a technical guide to the traditional*

interpretation. Nanotechnology ***17,*** *R57 (2006).*

25. *Hohenberg, P. & Kohn, W. Inhomogeneous electron gas.* Phys. Rev. ***136,*** *B864 (1964).*

26. *Vosko, S. H., Wilk, L. & Nusair, M. ACCURATE SPIN-DEPENDENT ELECTRON LIQUID CORRELATION ENERGIES FOR LOCAL SPIN-DENSITY CALCULATIONS - A CRITICAL ANALYSIS.* Can. J. Phys. ***58,*** *1200–1211 (1980).*

27. *Perdew, J. P. & Wang, Y. ACCURATE AND SIMPLE ANALYTIC REPRESENTATION OF THE ELECTRON-GAS CORRELATION-ENERGY.* Phys. Rev. B ***45,*** *13244–13249 (1992).*

28. *Clark, S. J.* et al. *First principles methods using CASTEP.* Zeitschrift Fur Krist. ***220,*** *567–570 (2005).*

29. *Segall, M. D.* et al. *First-principles simulation: ideas, illustrations and the CASTEP code.* J. Phys. Condens. Matter ***14,*** *2717 (2002).*

30. *Perdew, J. P., Burke, K. & Ernzerhof, M. Generalized gradient approximation made simple.* Phys. Rev. Lett. ***77,*** *3865 (1996).*

31. *Hammer, B., Hansen, L. B. & Norskov, J. K. Improved adsorption energetics within density-functional theory using revised Perdew-Burke-Ernzerhof functionals.* Phys. Rev. B ***59,*** *7413–7421 (1999).*

32. *Stankovich, S.* et al. *Synthesis of graphene-based nanosheets via chemical reduction of exfoliated graphite oxide.* Carbon N. Y. ***45,*** *1558–1565 (2007).*

33. *Eda, G., Fanchini, G. & Chhowalla, M. Large-area ultrathin films of reduced graphene oxide as a transparent and flexible electronic material.* Nat. Nanotechnol. ***3,*** *270–274 (2008).*

34. *Kim, K. S.* et al. *Large-scale pattern growth of graphene films for stretchable transparent electrodes.* Nature ***457,*** *706–710 (2009).*

35. *Reina, A.* et al. *Large Area, Few-Layer Graphene Films on Arbitrary Substrates by Chemical Vapor Deposition.* Nano Lett. ***9,*** *30–35 (2009).*

36. *Mårtensson, P., Owman, F. & Johansson, L. I. Morphology, Atomic and Electronic Structure of 6H-SiC (0001) Surfaces.* Phys. status solidi ***202,*** *501–528 (1997).*

37. *Istrate, O. M.* et al. *Reinforcement in melt-processed polymer-graphene composites at extremely low graphene loading level.* Carbon N. Y. ***78,*** *243–249 (2014).*

38. *Garcia, J. M.* et al. *Multilayer graphene films grown by molecular beam deposition.* Solid State Commun. ***150,*** *809–811 (2010).*

39. *Garcia, J. M.* et al. *Graphene growth on h-BN by molecular beam epitaxy.* Solid State Commun. ***152,*** *975–978 (2012).*

40. *Martinez-Galera, A. J., Brihuega, I. & Gomez-Rodriguez, J. M. Ethylene Irradiation: A New Route to Grow Graphene on Low Reactivity Metals.* Nano Lett. ***11,*** *3576–3580 (2011).*

41. *Otero, G.* et al. *Ordered Vacancy Network Induced by the Growth of Epitaxial Graphene on Pt(111).* Phys. Rev. Lett. ***105,*** *(2010).*

42. *Nie, S.* et al. *Scanning tunneling microscopy study of graphene on Au(111): Growth mechanisms and substrate interactions.* Phys. Rev. B ***85,*** *(2012).*

43. *Kiraly, B.* et al. *Solid-source growth and atomic-scale characterization of graphene on Ag(111).* Nat. Commun. ***4,*** *(2013).*

44. *Lin, M.-Y.* et al. *Low-temperature grown graphene films by using molecular beam epitaxy.* Appl. Phys. Lett. ***101,*** *221911 (2012).*

45. *Moreau, E.* et al. *Graphene growth by molecular beam epitaxy on the carbon-face of SiC.* Appl. Phys. Lett. ***97,*** *(2010).*

46. *Jerng, S.-K.* et al. *Graphitic carbon growth on crystalline and amorphous oxide substrates using molecular beam epitaxy.* Nanoscale Res. Lett. ***6,*** *(2011).*

47. *Loginova, E., Bartelt, N. C., Feibelman, P. J. & McCarty, K. F. Evidence for graphene growth by C cluster attachment.* New J. Phys. ***10,*** *(2008).*

48. *Pfeiffer, L. N. & West, K. W. Deposition of carbon-containing layers using vitreous carbon source. (2008).*

49. *Harris, P. J. F. Structure of non-graphitising carbons.* Int. Mater. Rev. ***42,*** *206–218 (1997).*

50. *Garcia, J. M. & Pfeiffer, L. N. Devices with graphene layers. (2010).*

51. *Martinez, J. M. G. & Pinczuk, A. Systems and methods using a glassy carbon heater. (2013).*

52. *Chupka, W. A. & Inghram, M. G. Investigation of the heat of vaporization of carbon.* J. Chem. Phys. ***21,*** *371–372 (1953).*

53. *Weltner, W., Thompson, K. R. & DeKock, R. L. Spectroscopy of carbon molecules. IV. C4, C5, C6 (and C9).* J. Am. Chem. Soc. ***93,*** *4688–4695 (1971).*

54. *Zavitsanos, P. D. & Carlson, G. A. Experimental study of the sublimation of graphite at high temperatures.* J. Chem. Phys. ***59,*** *2966–2973 (1973).*

55. *Honig, R. E. Mass spectrometric study of the molecular sublimation of graphite.* J. Chem. Phys. ***22,*** *126–131 (1954).*

56. *Palmer, H. B. On the equilibrium vapor pressure of graphite and the temperature of the carbon arc.* Carbon N. Y. ***8,*** *243–244 (1970).*

57. *Land, T. A., Michely, T., Behm, R. J., Hemminger, J. C. & Comsa, G. STM INVESTIGATION OF SINGLE LAYER GRAPHITE STRUCTURES PRODUCED ON PT(111) BY HYDROCARBON DECOMPOSITION.* Surf. Sci. ***264,*** *261–270 (1992).*

58. *Bae, S.* et al. *Roll-to-roll production of 30-inch graphene films for transparent electrodes.* Nat. Nanotechnol. ***5,*** *574–578 (2010).*

59. *Lang, B. A LEED study of the deposition of carbon on platinum crystal surfaces.* Surf. Sci. ***53,*** *317–329 (1975).*

60. *Wintterlin, J. & Bocquet, M. L. Graphene on metal surfaces.* Surf. Sci. ***603,*** *1841–1852 (2009).*

61. *Gao, M.* et al. *Tunable interfacial properties of epitaxial graphene on metal substrates.* Appl. Phys. Lett. ***96,*** *(2010).*

62. *Dedkov, Y. S.* et al. *Intercalation of copper underneath a monolayer of graphite on Ni (111).* Phys. Rev. B ***64,*** *35405 (2001).*

63. *Grüneis, A. & Vyalikh, D. V. Tunable hybridization between electronic states of graphene and a metal surface.* Phys. Rev. B ***77,*** *193401 (2008).*

64. *Preobrajenski, A. B., Ng, M. L., Vinogradov, A. S. & Mårtensson, N. Controlling graphene corrugation on lattice-mismatched substrates.* Phys. Rev. B ***78,*** *73401 (2008).*

65. *Sutter, P. W., Flege, J.-I. & Sutter, E. A. Epitaxial graphene on ruthenium.* Nat. Mater. ***7,*** *406–411 (2008).*

66. *Pletikosić, I.* et al. *Dirac cones and minigaps for graphene on Ir (111).* Phys. Rev. Lett. ***102,*** *56808 (2009).*

67. *Coraux, J., N 'Diaye, A. T., Busse, C. & Michely, T. Structural coherency of graphene on Ir (111).* Nano Lett. ***8,*** *565–570 (2008).*

68. *Nemec, N., Tománek, D. & Cuniberti, G. Modeling extended contacts for nanotube and graphene devices.* Phys. Rev. B ***77,*** *125420 (2008).*

69. *Nemec, N., Tománek, D. & Cuniberti, G. Contact dependence of carrier injection in carbon nanotubes: an ab initio study.* Phys. Rev. Lett. ***96,*** *76802 (2006).*

70. *Giovannetti, G.* et al. *Doping graphene with metal contacts.* Phys. Rev. Lett. ***101,*** *26803 (2008).*

71. *Huard, B., Stander, N., Sulpizio, J. A. & Goldhaber-Gordon, D. Evidence of the role of contacts on the observed electron-hole asymmetry in graphene.* Phys. Rev. B ***78,*** *121402 (2008).*

72. *Wofford, J. M.* et al. *Extraordinary epitaxial alignment of graphene islands on Au(111).* New J. Phys. ***14,*** *(2012).*

73. *Kwon, S.-Y.* et al. *Growth of Semiconducting Graphene on Palladium.* Nano

Lett. ***9,*** *3985–3990 (2009).*

74. *Abel Quiroga, M. Growth of carbon structured over Pd, Pt and Ni: A comparative DFT study.* Appl. Surf. Sci. ***268,*** *11–15 (2013).*

75. *Saadi, S.* et al. *On the Role of Metal Step-Edges in Graphene Growth.* J. Phys. Chem. C ***114,*** *11221–11227 (2010).*

76. *Dedkov, Y. S., Fonin, M., Rüdiger, U. & Laubschat, C. Rashba effect in the graphene/Ni (111) system.* Phys. Rev. Lett. ***100,*** *107602 (2008).*

77. *Karpan, V. M.* et al. *Graphite and graphene as perfect spin filters.* Phys. Rev. Lett. ***99,*** *176602 (2007).*

78. *Marchini, S., Günther, S. & Wintterlin, J. Scanning tunneling microscopy of graphene on Ru (0001).* Phys. Rev. B ***76,*** *75429 (2007).*

79. *Sutter, P., Sadowski, J. T. & Sutter, E. Graphene on Pt(111): Growth and substrate interaction.* Phys. Rev. B ***80,*** *(2009).*

80. *Pauling Electronegativity of transition metal. Available at: https://en.wikipedia.org/wiki/Electronegativity.*

81. *Merino, P., Svec, M., Pinardi, A. L., Otero, G. & Martin-Gago, J. A. Strain-Driven Moire Superstructures of Epitaxial Graphene on Transition Metal Surfaces.* ACS Nano ***5,*** *5627–5634 (2011).*

82. *Ueta, H.* et al. *Highly oriented monolayer graphite formation on Pt (111) by a supersonic methane beam.* Surf. Sci. ***560,*** *183–190 (2004).*

83. *Cushing, G. W., Johanek, V., Navin, J. K. & Harrison, I. Graphene Growth on Pt(111) by Ethylene Chemical Vapor Deposition at Surface Temperatures near 1000 K.* J. Phys. Chem. C ***119,*** *4759–4768 (2015).*

84. *Fujita, T., Kobayashi, W. & Oshima, C. Novel structures of carbon layers on a Pt(111) surface.* Surf. Interface Anal. ***37,*** *120–123 (2005).*

85. *Gao, M.* et al. *Epitaxial growth and structural property of graphene on Pt(111).* Appl. Phys. Lett. ***98,*** *(2011).*

86. *Kang, B. J., Mun, J. H., Hwang, C. Y. & Cho, B. J. Monolayer graphene growth on sputtered thin film platinum.* J. Appl. Phys. ***106,*** *(2009).*

87. *Liang, Z., Khosravian, H., Uhl, A., Meyer, R. J. & Trenary, M. Graphene domain boundaries on Pt(111) as nucleation sites for Pt nanocluster formation.* Surf. Sci. ***606,*** *1643–1648 (2012).*

88. *Yao, W.* et al. *Monolayer charge-neutral graphene on platinum with extremely weak electron-phonon coupling.* Phys. Rev. B ***92,*** *(2015).*

89. *Blanco, J. M.* et al. *Origin of contrast in STM images of oxygen on Pd (111) and its dependence on tip structure and tunneling parameters.* Phys. Rev. B ***71,*** *113402 (2005).*

90. *Nicoara, N., Roman, E., Gomez-Rodriguez, J. M., Martin-Gago, J. A. & Mendez, J. Scanning tunneling and photoemission spectroscopies at the PTCDA/Au(111) interface.* Org. Electron. ***7,*** *287–294 (2006).*

91. *Parish, R. V. Organogold chemistry: I structure and synthesis.* Gold Bull. ***30,*** *3–12 (1997).*

92. *Croix, C.* et al. *Organogold (I) complexes: Synthesis, X-ray crystal structures and aurophilicity.* J. Organomet. Chem. ***690,*** *4835–4843 (2005).*

93. *Hashmi, A. S. K., Ramamurthi, T. D. & Rominger, F. Synthesis, structure and reactivity of organogold compounds of relevance to homogeneous gold catalysis.* J. Organomet. Chem. ***694,*** *592–597 (2009).*

94. *Tat'yana, V. B., Kuz'mina, L. G., Lemenovskii, D. A. & Blumenfel'd, A. L. New organogold (I) complexes: Synthesis, structure, and dynamic behavior of the polynuclear organogold diphenylmethane and diphenylethane derivatives.* J. Organomet. Chem. ***530,*** *27–38 (1997).*

95. *Martinez, J. I.* et al. *Role of the Pinning Points in epitaxial Graphene Moire Superstructures on the Pt(111) Surface.* Sci. Rep. ***6,*** *(2016).*

96. *Wu, Y.* et al. *High-frequency, scaled graphene transistors on diamond-like carbon.* Nature ***472,*** *74–78 (2011).*

97. *Lin, Y.-M.* et al. *100-GHz transistors from wafer-scale epitaxial graphene.* Science (80-.). ***327,*** *662 (2010).*

98. *Berger, C.* et al. *Electronic confinement and coherence in patterned epitaxial graphene.* Science (80-.). ***312,*** *1191–1196 (2006).*

99. *Emtsev, K. V* et al. *Towards wafer-size graphene layers by atmospheric pressure graphitization of silicon carbide.* Nat. Mater. ***8,*** *203–207 (2009).*

100. *Bunch, J. S.* et al. *Electromechanical resonators from graphene sheets.* Science (80-.). ***315,*** *490–493 (2007).*

101. *Chen, J.-H., Jang, C., Xiao, S., Ishigami, M. & Fuhrer, M. S. Intrinsic and extrinsic performance limits of graphene devices on SiO2.* Nat. Nanotechnol. ***3,*** *206–209 (2008).*

102. *Yu, J., Liu, G. X., Sumant, A. V, Goyal, V. & Balandin, A. A. Graphene-on-Diamond Devices with Increased Current-Carrying Capacity: Carbon sp(2)-on-sp(3) Technology.* Nano Lett. ***12,*** *1603–1608 (2012).*

103. *Ando, T. Screening effect and impurity scattering in monolayer graphene.* J. Phys. Soc. Japan ***75,*** *74716 (2006).*

104. *Hwang, E. H., Adam, S. & Sarma, S. Das. Carrier transport in two-dimensional graphene layers.* Phys. Rev. Lett. ***98,*** *186806 (2007).*

105. *Fratini, S. & Guinea, F. Substrate-limited electron dynamics in graphene.* Phys. Rev. B ***77,*** *195415 (2008).*

106. *Ishigami, M., Chen, J. H., Cullen, W. G., Fuhrer, M. S. & Williams, E. D. Atomic structure of graphene on SiO2.* Nano Lett. ***7,*** *1643–1648 (2007).*

107. *Pate, B. B. The diamond surface: atomic and electronic structure.* Surf. Sci. ***165,*** *83–142 (1986).*

108. *Ogawa, S.* et al. *Vacuum Annealing Formation of Graphene on Diamond C(111) Surfaces Studied by Real-Time Photoelectron Spectroscopy.* Jpn. J. Appl. Phys. ***51,*** *7 (2012).*

109. *Wang, Y.* et al. *Electronic properties of nanodiamond decorated graphene.*

ACS Nano ***6,*** *1018–1025 (2012).*

110. *Varshney, D.* et al. *Free standing graphene-diamond hybrid films and their electron emission properties.* J. Appl. Phys. ***110,*** *44324 (2011).*

111. *Ma, Y. D., Dai, Y., Guo, M. & Huang, B. B. Graphene-diamond interface: Gap opening and electronic spin injection.* Phys. Rev. B ***85,*** *5 (2012).*

112. *Shiga, T.* et al. *Graphene-diamond hybrid structure as spin-polarized conducting wire with thermally efficient heat sinks.* Appl. Phys. Lett. ***100,*** *233101 (2012).*

113. *Hu, W., Li, Z. & Yang, J. Structural, electronic, and optical properties of hybrid silicene and graphene nanocomposite.* J. Chem. Phys. ***139,*** *154704 (2013).*

114. *Li, L. & Zhao, X. Dangling bond-induced graphitization process on the (111) surface of diamond nanoparticles.* J. Chem. Phys. ***134,*** *44711 (2011).*

115. *Seal, M. Graphitization of diamond.* Nature ***185,*** *522–523 (1960).*

116. *Yan, Y., Zhang, S. B. & Al-Jassim, M. M. Graphite-like surface reconstructions on C {111} and their implication for n-type diamond.* Phys. Rev. B ***66,*** *201401 (2002).*

117. *Tokuda, N.* et al. *Formation of Graphene-on-Diamond Structure by Graphitization of Atomically Flat Diamond (111) Surface.* Jpn. J. Appl. Phys. ***52,*** *4 (2013).*

118. *De Vita, A., Galli, G., Canning, A. & Car, R. A microscopic model for surface-induced diamond-to-graphite transitions.* Nature ***379,*** *523 (1996).*

119. *Selli, D.* et al. *Theoretical investigation of the electronic structure and quantum transport in the graphene-C(111) diamond surface system.* J. Physics-Condensed Matter ***25,*** *(2013).*

120. *Cooil, S. P.* et al. *Controlling the growth of epitaxial graphene on metalized diamond (111) surface.* Appl. Phys. Lett. ***107,*** *(2015).*

121. *Cooil, S. P.* et al. *Iron-mediated growth of epitaxial graphene on SiC and*

diamond. Carbon N. Y. ***50,*** *5099–5105 (2012).*

122. *Gu, C.* et al. *Graphene grown out of diamond.* Appl. Phys. Lett. ***109,*** *(2016).*

123. *Lee, J.-K.* et al. *The growth of AA graphite on (111) diamond.* J. Chem. Phys. ***129,*** *(2008).*

124. *Klaus E. Hermann (FHI) and Michael A. Van Hove (HKBU). The software utility LEEDpat, Version 4.2. (2014).*

125. *Martin-Gago, J. A., Fraxedas, J., Ferrer, S. & Comin, F. Electron loss spectroscopy study of the growth by laser ablation of ultra-thin diamond-like films on Si (100).* Surf. Sci. ***260,*** *L17–L23 (1992).*

126. *Bruley, J., Williams, D. B., Cuomo, J. J. & Pappas, D. P. Quantitative near-edge structure analysis of diamond-like carbon in the electron microscope using a two-window method.* J. Microsc. ***180,*** *22–32 (1995).*

127. *Wan, D. & Komvopoulos, K. Transmission electron microscopy and electron energy loss spectroscopy analysis of ultrathin amorphous carbon films.* J. Mater. Res. ***19,*** *2131–2136 (2004).*

128. *Lehn, J.-M. Toward complex matter: supramolecular chemistry and self-organization.* Proc. Natl. Acad. Sci. ***99,*** *4763–4768 (2002).*

129. *Lehn, J.-M. Toward self-organization and complex matter.* Science (80-.). ***295,*** *2400–2403 (2002).*

130. *Barth, J. V, Costantini, G. & Kern, K. Engineering atomic and molecular nanostructures at surfaces.* Nature ***437,*** *671–679 (2005).*

131. *Cook, T. R., Zheng, Y.-R. & Stang, P. J. Metal–organic frameworks and self-assembled supramolecular coordination complexes: comparing and contrasting the design, synthesis, and functionality of metal–organic materials.* Chem. Rev. ***113,*** *734–777 (2012).*

132. *Li, S.-S., Northrop, B. H., Yuan, Q.-H., Wan, L.-J. & Stang, P. J. Surface confined metallosupramolecular architectures: Formation and scanning tunneling microscopy characterization.* Acc. Chem. Res. ***42,*** *249–259 (2008).*

133. *Lin, N., Stepanow, S., Ruben, M. & Barth, J. V. Surface-confined supramolecular coordination chemistry. in* Templates in Chemistry III *1–44 (Springer, 2008).*

134. *Barth, J. V. Molecular architectonic on metal surfaces.* Annu. Rev. Phys. Chem. ***58,*** *375–407 (2007).*

135. *Cornia, A., Mannini, M., Sainctavit, P. & Sessoli, R. Chemical strategies and characterization tools for the organization of single molecule magnets on surfaces.* Chem. Soc. Rev. ***40,*** *3076–3091 (2011).*

136. *Rodriguez-Douton, M. J.* et al. *One-step covalent grafting of Fe 4 single-molecule magnet monolayers on gold.* Chem. Commun. ***47,*** *1467–1469 (2011).*

137. *Mannini, M.* et al. *Magnetic memory of a single-molecule quantum magnet wired to a gold surface.* Nat. Mater. ***8,*** *194–197 (2009).*

138. *Saywell, A.* et al. *Single molecule magnets on a gold surface: in situ electrospray deposition, x-ray absorption and photoemission.* Nanotechnology ***22,*** *75704 (2011).*

139. *Saywell, A.* et al. *Self-assembled aggregates formed by single-molecule magnets on a gold surface.* Nat. Commun. ***1,*** *75 (2010).*

140. *Otero, G.* et al. *Morphological investigation of Mn12 single-molecule magnets adsorbed on Au (111).* Langmuir ***25,*** *10107–10115 (2009).*

141. *Vitali, L.* et al. *Electronic structure of surface-supported bis (phthalocyaninato) terbium (III) single molecular magnets.* Nano Lett. ***8,*** *3364–3368 (2008).*

142. *Gallego, A.* et al. *Solvent‐Induced Delamination of a Multifunctional Two Dimensional Coordination Polymer.* Adv. Mater. ***25,*** *2141–2146 (2013).*

143. *Otero-Irurueta, G.* et al. *On-surface self-organization of a robust metal-organic cluster based on copper(I) with chloride and organosulphur ligands.* Chem. Commun. ***51,*** *3243–3246 (2015).*

144. *Lewis, J. P.* et al. *Advances and applications in the FIREBALLab initio tight-binding molecular-dynamics formalism.* Phys. status solidi ***248,*** *1989–2007 (2011).*

145. *Giannozzi, P.* et al. *QUANTUM ESPRESSO: a modular and open-source software project for quantum simulations of materials.* J. Phys. Condens. matter ***21,*** *395502 (2009).*

146. *Blanco, J. M.* et al. *First-principles simulations of STM images: From tunneling to the contact regime.* Phys. Rev. B ***70,*** *85405 (2004).*

147. *Blanco, J. M., Flores, F. & Pérez, R. STM-theory: Image potential, chemistry and surface relaxation.* Prog. Surf. Sci. ***81,*** *403–443 (2006).*

148. *Crew, W. W. & Madix, R. J. MONITORING SURFACE-REACTIONS WITH SCANNING-TUNNELING-MICROSCOPY - CO OXIDATION ON P(2X1)-O PRE-COVERED CU(11O) AT 400-K.* Surf. Sci. ***319,*** *L34–L40 (1994).*

149. *Kishimoto, S., Kageshima, M., Naitoh, Y., Li, Y. J. & Sugawara, Y. Study of oxidized Cu(110) surface using noncontact atomic force microscopy.* Surf. Sci. ***602,*** *2175–2182 (2008).*

150. *Hodgson, A. & Haq, S. Water adsorption and the wetting of metal surfaces.* Surf. Sci. Rep. ***64,*** *381–451 (2009).*

151. *Ito, M. Structures of water at electrified interfaces: Microscopic understanding of electrode potential in electric double layers on electrode surfaces.* Surf. Sci. Rep. ***63,*** *329–389 (2008).*

152. *Bange, K., Grider, D. E., Madey, T. E. & Sass, J. K. The surface chemistry of H2O on clean and oxygen-covered Cu (110).* Surf. Sci. ***137,*** *38–64 (1984).*

153. *Spitzer, A. & Lüth, H. An XPS study of the water adsorption on Cu (110).* Surf. Sci. ***160,*** *353–361 (1985).*

154. *Spitzer, A. & Lüth, H. The adsorption of water on clean and oxygen covered Cu (110).* Surf. Sci. ***120,*** *376–388 (1982).*

155. *Bensebaa, F. & Ellis, T. H. Water at surfaces: What can we learn from*

vibrational spectroscopy? Prog. Surf. Sci. ***50,*** *173–185 (1995).*

156. *Lackey, D., Schott, J., Straehler, B. & Sass, J. K. Water adsorption on clean and caesium covered Cu {110}.* J. Chem. Phys. ***91,*** *1365–1373 (1989).*

157. *Mariani, C. & Horn, K. Orientation of water adsorbed on Cu (110).* Surf. Sci. ***126,*** *279–285 (1983).*

158. *Polak, M. On the structure and bonding of H2O adsorbed on Cu (110).* Surf. Sci. ***321,*** *249–260 (1994).*

159. *Morgenstern, K. & Rieder, K.-H. Formation of the cyclic ice hexamer via excitation of vibrational molecular modes by the scanning tunneling microscope.* J. Chem. Phys. ***116,*** *5746–5752 (2002).*

160. *Carley, A. F.* et al. *The structure of sulfur adlayers at Cu(110) surfaces: an STM and XPS study.* Surf. Sci. ***447,*** *39–50 (2000).*

161. *Carley, A. F.* et al. *Structural aspects of chemisorption at Cu(110) revealed at the atomic level.* Top. Catal. ***11,*** *299–306 (2000).*

162. *Wei, K.-J., Quan, Z., Zhang, Z., Da, Y. & Wang, X. Copper (i) chloride promoted Csp 2–N cross-coupling of 1, 2-di (pyrimidin-2-yl) disulfides with amines: an efficient approach to obtain C2-amino functionalized pyrimidines.* Org. Biomol. Chem. ***14,*** *2395–2398 (2016).*